



TECHNISCHE UNIVERSITÄT MÜNCHEN

Physik Department E21 (Lehrstuhl für Experimentalphysik III)

Radiography with Polarised Neutrons

Dipl. Phys. (Univ.) Michael L. Schulz

Vollständiger Abdruck der von der Fakultät für Physik der Technischen Universität München zur Erlangung des akademischen Grades eines

Doktors der Naturwissenschaften (Dr. rer. nat.)

genehmigten Dissertation.

Vorsitzender: Univ.-Prof. Dr. Roland Netz

Prüfer der Dissertation: 1. Univ.-Prof. Dr. Peter Böni
2. Univ.-Prof. Dr. Dirk Grundler

Die Dissertation wurde am 26.02.2010 an der Technischen Universität München eingereicht und durch die Fakultät für Physik am 20.08.2010 angenommen.

Abstract

In this thesis I present a new technique for the spatially resolved investigation of the magnetic properties of bulk samples. Standard one dimensional neutron depolarisation analysis is combined with neutron radiography to a method we call Neutron Depolarisation Imaging (NDI).

The experimental setup which was installed at the neutron radiography beam line ANTARES at FRM II consists of a double crystal monochromator, neutron polariser, spin flipper, polarisation analyser and a position sensitive CCD detector. A comprehensive discussion of the requirements for these components is given and the limitations of the method are shown. The maximum spatial resolution which can be achieved with a neutron radiography setup is determined by the collimation of the neutron beam and the distance between sample and detector. In this context it is most important for the components of the setup to maintain the collimation of the beam. Furthermore, the polarisation analyser after the sample should be as compact as possible in order to decrease the distance between sample and detector. Different types of polarisers have been tested and their advantages and disadvantages are discussed.

A double crystal monochromator and a new type of polariser employing polarising neutron supermirrors based on the principle of an optical periscope were developed and tested during this work. The construction of these components is shown and a detailed analysis of their performance in NDI is given.

Furthermore, NDI measurements on various samples of the weakly ferromagnetic materials $\text{Pd}_{1-x}\text{Ni}_x$ and Ni_3Al are presented. These experiments prove that NDI is an extremely powerful tool to assess the quality and homogeneity of ferromagnetic samples. This is especially important for the material systems studied here since their magnetic properties depend crucially on the concentration of their constituents. Neutron depolarisation radiography and tomography measurements were conducted with a spatial resolution as high as 0.3 mm on $\text{Pd}_{1-x}\text{Ni}_x$ and Ni_3Al samples. The results prove that samples of high quality are extremely rare. Even samples which have already been used in neutron scattering experiments and were found to be of high quality by residual resistivity measurements were found to show strong variations of the ordering temperature. This fact may have lead to a misinterpretation of the neutron scattering data.

The feasibility of NDI experiments under hydrostatic pressures up to 10kbar was shown on a sample of Ni_3Al using a modified Cu:Be clamp cell. A decrease of the ordering temperature by 2K under hydrostatic pressure was determined from the NDI measurements and shows the potential of the method for further high pressure experiments.

Additionally a method was developed which in principle allows to obtain the intrinsic dependence of the ordering temperature T_C on the ordered moment M_s from NDI measurements on inhomogeneous samples containing regions with different ordering temperatures. This dependence reveals whether the phase transition remains second order for $T_C \rightarrow 0$, implying a quantum critical point in the system or changes to first order instead. This procedure was tested on one $\text{Pd}_{1-x}\text{Ni}_x$ sample and the results were compared with simulations of the temperature dependence of the neutron beam depolarisation by an inhomogeneous sample. However, for this particular sample it is not possible to unambiguously deduce the intrinsic behaviour of the sample from the measurements mainly due to the lack of regions in the sample showing very low ordering temperatures. Furthermore, the counting statistics need to be increased.

As a result from these simulations a criterion was developed to assess the amount of heterogeneity in

a sample from the shape of the temperature dependence of the beam polarisation after transmission of the sample. It is found from simulations that increasing the heterogeneity in the sample leads to a rounding of the signature of the phase transition in the depolarisation data. With this criterion NDI can in the future be developed into a valuable tool to test whether the presence of heterogeneities in a sample is responsible for the formation of new magnetic order in systems close to ferromagnetic quantum criticality.

NDI has several advantages compared to other techniques which can yield similar information about the sample. Most importantly, NDI is a non-destructive technique which can be performed on large samples without the need of time consuming preparation of samples of a defined shape or size. Furthermore, the measurement of the distribution of the magnetic properties over the entire sample in a single measurement, yielding a large amount of data on a small length scale, makes NDI a very fast method. In contrast to that, standard bulk measurement methods require time consuming subsequent measurements of the magnetic properties on small samples prepared from a large and inhomogeneous sample.

Zusammenfassung

In dieser Arbeit stelle ich eine neue Technik zur orts aufgelösten Untersuchung von magnetischen Eigenschaften großer Proben vor. Gewöhnliche eindimensionale Neutronendepolarisationsanalyse wird hierbei mit Neutronenradiographie zu einer Methode kombiniert, die wir Neutron Depolarisation Imaging (NDI) nennen.

Der experimentelle Aufbau, der an der Neutronenradiographie Beam Line ANTARES am FRM II installiert wurde, besteht aus einem Doppelkristallmonochromator, Neutronenpolarisator, Spin Flipper, Analysator und einem ortsauflösenden CCD-Detektor. Es wird eine umfassende Diskussion der Anforderungen an diese Komponenten und der Grenzen der Methode durchgeführt. Die maximale Ortsauflösung, die mit einem Neutronenradiographie-Aufbau erreicht werden kann, wird von der Kollimation des Strahls und der Distanz zwischen Objekt und Detektor bestimmt. In diesem Zusammenhang ist es besonders wichtig, dass die Komponenten des Aufbaus die Kollimation des Strahls erhalten. Außerdem sollte der Analysator nach der Probe so kompakt wie möglich sein, um den Abstand zwischen Probe und Detektor zu verkleinern. Es wurden verschiedene Arten von Polarisatoren getestet und deren Vor- und Nachteile werden diskutiert.

Ein Doppelkristallmonochromator und ein neuartiger Polarisator basierend auf dem Prinzip eines optischen Periskops wurden im Rahmen dieser Arbeit entwickelt und getestet. Es wird die Konstruktion dieser Komponenten aufgezeigt und eine detaillierte Analyse ihrer Leistungsfähigkeit durchgeführt.

Außerdem wurden NDI Messungen an verschiedenen Proben der schwach ferromagnetischen Materialien $\text{Pd}_{1-x}\text{Ni}_x$ und Ni_3Al vorgestellt. Diese Experimente beweisen, dass NDI eine wertvolle Methode zur Beurteilung der Qualität und Homogenität von ferromagnetischen Proben darstellt. Diese ist für die hier untersuchten Materialsysteme besonders wichtig, da ihre magnetischen Eigenschaften empfindlich von der Konzentration ihrer Bestandteile abhängen. Es wurden Neutronendepolarisations-Radiographie und -Tomographie Messungen mit einer Ortsauflösung von bis zu 0.3 mm an $\text{Pd}_{1-x}\text{Ni}_x$ und Ni_3Al Proben durchgeführt, deren Ergebnisse beweisen, dass Proben von hoher Qualität extrem selten sind. Selbst Proben, die bereits in Neutronenstreuexperimenten verwendet wurden, und für die aufgrund von Restwiderstandsmessungen eine hohe Qualität festgestellt wurde, zeigten starke Variationen in der Ordnungstemperatur. Diese Tatsache hat möglicherweise zu einer Fehlinterpretation der Neutronenstreudaten geführt.

Die Machbarkeit von NDI Messungen unter hydrostatischem Druck von bis zu 10 kbar wurde unter Verwendung einer modifizierten Cu:Be Druckzelle an einer Ni_3Al Probe demonstriert. Es wurde eine Erniedrigung der Ordnungstemperatur um 2 K unter hydrostatischem Druck aus den NDI Messungen bestimmt, was das Potential der Methode für zukünftige Experimente unter hohem Druck zeigt.

Des Weiteren wurde eine Methode entwickelt, die es prinzipiell ermöglicht, die intrinsische Abhängigkeit der Ordnungstemperatur T_C vom geordneten Moment M_s aus NDI Messungen an inhomogenen Proben zu erhalten, die aus Regionen mit unterschiedlicher Ordnungstemperatur bestehen. Diese Abhängigkeit zeigt, ob der Phasenübergang für $T_C \rightarrow 0$ zweiter Ordnung bleibt und deshalb einen Quantenkritischen Punkt in dem System impliziert, oder ob er statt dessen zu einem Übergang erster Ordnung wird. Diese Vorgehensweise wurde an einer $\text{Pd}_{1-x}\text{Ni}_x$ Probe getestet und die Ergebnisse mit Simulationen der Temperaturabhängigkeit der Depolarisation des Strahls durch eine inhomogene Probe verglichen. Jedoch ist es, hauptsächlich wegen des Fehlens von Bereichen in der Probe mit sehr niedrigen Ord-

nungstemperaturen, für diese spezielle Probe nicht möglich, eindeutig auf ihr intrinsisches Verhalten zu schließen. Außerdem müsste die Zählstatistik verbessert werden.

Als Ergebnis dieser Simulationen wurde ein Kriterium entwickelt das es ermöglicht, die Stärke der Heterogenität einer Probe anhand der Form der Temperaturabhängigkeit der Strahdepolarisation nach Transmission der Probe zu bestimmen. Simulationen zeigen, dass Heterogenitäten in der Probe zu einer Verrundung der Signatur des Phasenübergangs in den Depolarisationsdaten führen. Mit diesem Kriterium kann NDI in Zukunft zu einer wertvollen Methode entwickelt werden um zu überprüfen ob das Vorhandensein von Heterogenitäten in einer Probe verantwortlich ist für die Entstehung neuer magnetischer Ordnung in Systemen in der Nähe ferromagnetischer Quantenkritikalität.

NDI hat mehrere Vorteile gegenüber anderen Methoden, die ähnliche Informationen über die Probe liefern können. Am Wichtigsten ist, dass es sich bei NDI um eine zerstörungsfreie Methode handelt, die an großen Proben ohne die Notwendigkeit einer zeitaufwändigen Präparation von Proben mit definierter Form oder Größe durchgeführt werden kann. Außerdem liefert die Messung der Verteilung der magnetischen Eigenschaften über die ganze Probe eine Vielzahl an Datenpunkten auf einer kleinen Längenskala, was NDI zu einer sehr schnellen Methode macht. Im Gegensatz dazu benötigen normale Bulk-Messmethoden zeitaufwändige, aufeinanderfolgende Messungen an kleinen Proben, die aus der großen und inhomogenen Probe präpariert werden müssen.

Contents

1	Introduction	9
1.1	Motivation: Quantum Phase Transitions and Quantum Criticality	9
1.2	Weak Itinerant Ferromagnetism	12
1.2.1	Stoner Model	14
1.2.2	Self-Consistent Ginzburg-Landau-Theory	15
1.3	Ferromagnetic Quantum Criticality?	19
1.3.1	ZrZn ₂ , UGe ₂ , MnSi	20
1.3.2	Pd _{1-x} Ni _x	22
1.3.3	Ni ₃ Al	25
1.3.4	CeSi _{1.81} and CePd _{1-x} Rh _x	27
2	Theoretical Background of Experimental Techniques	29
2.1	Properties of the Neutron and its Interaction with Matter	29
2.2	Neutron Imaging	31
2.2.1	Attenuation Radiography	31
2.2.2	Attenuation Tomography	32
2.3	Polarised Neutrons	33
2.4	1D and 3D Neutron Depolarisation Technique	34
2.5	Neutron Depolarisation Imaging	39
2.6	Neutron Depolarisation Tomography	42
3	The Neutron Depolarisation Setup	45
3.1	Monochromatic Neutron Radiography	47
3.1.1	Monochromatising Techniques	47
3.1.2	Double Crystal Monochromator	49
3.1.3	Characterisation of the Double Crystal Monochromator	51

3.2	Polariser and Analyser	54
3.2.1	^3He Spin Filter Cells	55
3.2.2	Standard Benders	57
3.2.3	Solid State Benders	58
3.2.4	Polarising Neutron Periscope	58
3.2.5	Summary & Conclusion	65
3.3	Spin Flippers	66
3.4	Detector	68
4	Data Acquisition and Evaluation	71
4.1	Measurement Procedure	71
4.2	Experimental Setups	76
4.3	Magnetisation Measurements	79
4.4	Determination of M_s from Depolarisation Data	80
5	Experimental Results	93
5.1	First Proof of Principle Measurements on MIRA	93
5.2	Measurements on Weakly Ferromagnetic Materials	98
5.2.1	$\text{Pd}_{1-x}\text{Ni}_x$	98
5.2.2	Ni_3Al	116
5.2.3	Pressure Dependence of Ferromagnetism	127
5.2.4	Tomographic Measurements	129
6	Conclusion & Outlook	135
7	Acknowledgements	137
8	List of Publications	141
A	Further Experiments	143
A.1	Visualisation of magnetic field integrals	143
A.2	Magnetostriction in Ni foils	145
	Bibliography	147

Chapter 1

Introduction

1.1 Motivation: Quantum Phase Transitions and Quantum Criticality

Conventional phase transitions like the melting of ice or the more complex transition from the ferromagnetic to the paramagnetic phase are driven by temperature induced fluctuations. Therefore, these are generally known as *thermal phase transitions*. In the past 20 years phase transitions driven by quantum fluctuations have become a topic of great physical interest. These transitions can be controlled via non-thermal parameters like pressure p , magnetic field B or compositional doping x . To account for their non-thermal nature, such phase transitions are called *quantum phase transitions* (QPT).

All phase transitions can be distinguished by their order n in the Ehrenfest classification, which is equivalent to the order of the derivative of the free energy which is discontinuous. In the case of a *second order phase transition* ($n = 2$) the order parameter (magnetisation in the case of a ferromagnet) vanishes continuously whereas for a *first order phase transition* ($n = 1$) it vanishes discontinuously. A second order quantum phase transition at $T = 0$ is called a *quantum critical point* (QCP).

Let us consider a system in the vicinity of a second order quantum phase transition, where the order parameter vanishes continuously as shown in Fig. 1.1.1. Approaching the phase boundary at $T = 0$ from the disordered side leads to an increase of the correlation length ζ of the fluctuations of the order parameter. This correlation length ζ diverges with $\zeta \propto r^\nu$, where ν is the critical exponent and r is the dimensionless distance from the quantum critical point. At the same time, the correlation time τ_c of the fluctuations diverges with the dynamical critical exponent z as $\tau_c \propto \zeta^z \propto r^{\nu z}$ [1, 2].

Therefore, at a quantum critical point, the correlation length as well as the correlation time are diverging, making a simple mean-field theory like the Stoner-model for ferromagnets inapplicable. Furthermore at $T = 0$ spatial and temporal fluctuations can no longer be separated and completely new physical behaviour arises. Quantum fluctuations do not only play a role at low temperatures. Above the QCP, extending to high temperatures, a region in the phase diagram in Fig 1.1.1 arises, where the energy of the quantum fluctuations $\hbar\omega$ is higher than the thermal energy $k_B T$.

Hertz [1] and Millis [2] showed that systems close to a QCP can be treated with an effective dimension $d_{\text{eff}} = d + z$, where d is the spatial dimension of the system and z is the dynamical scaling exponent introduced above. For $d_{\text{eff}} > 4$ it is possible to treat the fluctuations in an effective mean-field theory. This is always the case for cubic ferromagnetic metals since $d = 3$ and $z = 3$ for clean systems and $z = 4$

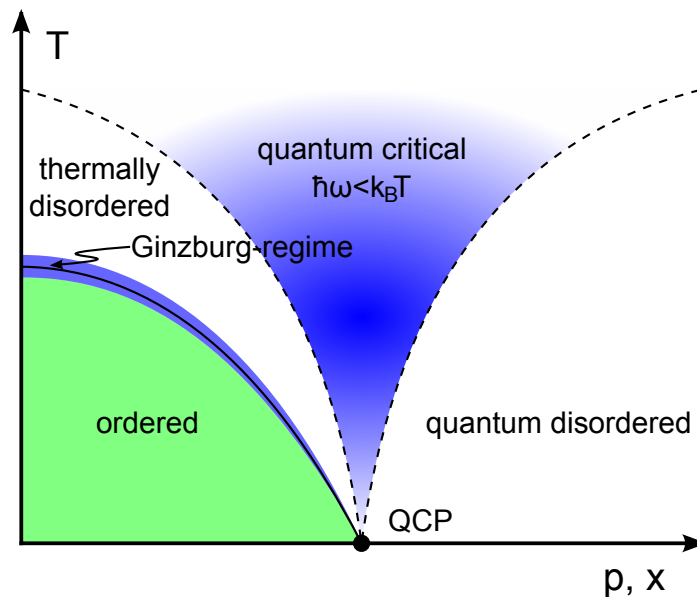


Figure 1.1.1: Schematic phase diagram for a three dimensional magnetic quantum critical point (QCP) in a metal. A QCP is a second order phase transition at $T = 0$, which is driven by quantum fluctuations. At finite temperatures, the phase transition is driven by classical thermal fluctuations and the phase boundary lies within the Ginzburg-regime, which has a width given by the thermal energy $k_B T$.

for disordered systems. Therefore, a self consistently renormalised Ginzburg-Landau (SCR) theory is used, which will be discussed in 1.2.2.

In contrast, magnetic phase transitions at finite temperatures can not be described by mean field theories, because $d_{\text{eff}} = 3$. Classical thermal fluctuations dominate the behaviour of the system in a region of width $k_B T$ around the phase transition, which is called the Ginzburg-regime. These fluctuations slow down the more the system approaches the ordered state, which leads to the classical critical slowing-down (c.f. critical opalescence). Renormalisation group theories are necessary to describe the behaviour of a system in the Ginzburg-regime. The width of the Ginzburg-regime, however, collapses at $T = 0$.

Most metals can be described in a Fermi liquid theory (FL) which allows to make predictions about the bulk properties of the material. For a paramagnetic system one obtains a linear increase of the electronic heat capacity C_{el} with temperature $C_{\text{el}} = \gamma T$ and a quadratic increase of the electronic part of the resistivity $\rho_{\text{el}} = AT^2$, as well as a constant susceptibility $\chi = \text{const}$. The material specific parameters A and γ depend on the effective mass of the conduction electrons and their scattering cross section, respectively.

Close to a QCP, both the correlation length ζ and the correlation time τ_c are diverging which also leads to a divergence of A and γ as well as the effective mass of the electrons and their scattering cross section. This is in conflict with the fundamental assumptions of the Fermi-liquid theory. Consequently any behaviour of a system that is not consistent with the expectations of the Fermi-liquid theory is called non-Fermi-liquid (NFL) behaviour.

The phenomenological SCR model introduced by Lonzarich, Taillefer [3] and Moriya [4] and described in 1.2.2 yields the following predictions for a system in the vicinity of a three dimensional ferromagnetic QCP:

- a logarithmic divergence of $C_{\text{el}}/T \propto -\log T$,

- a diverging susceptibility $\Delta\chi \propto T^{-4/3}$
- a 5/3 power law for the specific resistivity $\rho \propto T^{5/3}$.

Clearly, QCPs can exist in non-magnetic substances, as well. However, magnetic systems turn out to be very convenient to study QCPs, since magnetisation – which is the order parameter of a ferromagnetic QPT – is an experimentally easily accessible property of the systems, which is often decoupled from the lattice degrees of freedom. In several antiferromagnetic systems QCPs have been found [5], however there is up to now, no doubtless evidence for a ferromagnetic QCP. Ferromagnetic QCPs were proposed in several systems but in all pure systems studied to date, the phase transition was found to be first-order instead of second-order. The most prominent examples are ZrZn_2 [6], UGe_2 [7], CoS_2 [8] and Ni_3Al [9]. For all of these substances, which will be discussed in more detail in 1.3, the ordering temperature was found to vanish discontinuously as a function of applied hydrostatic pressure.

It has been a great challenge for researchers in the past 20 years to find a ferromagnetic system, which shows a second order quantum phase transition at $T = 0$ (i.e. a QCP). Measurement techniques involved in solving this problem were mainly bulk techniques like heat capacity, electronic transport and magnetisation measurements as well as neutron scattering studies to identify the spin fluctuations in the ferromagnetic systems. All of these techniques imply an averaging process over the sample volume. Especially in neutron scattering experiments, large samples are used to increase the scattered neutron flux. At this point, quite naturally the question about the quality and homogeneity of the samples arises.

In this thesis, we will present a new method which uses the combination of neutron radiography and neutron depolarisation to obtain spatially resolved information about the magnetic properties of a sample. This method will in the following be called **Neutron Depolarisation Imaging (NDI)**. Measurements made with this newly developed technique during this thesis show that many ferromagnetic samples which have been used for bulk and neutron scattering measurements to investigate the properties of QPTs turn out to be highly inhomogeneous on a macroscopic scale.

The inhomogeneity of the samples directly raises the question whether the conclusions drawn from bulk and neutron scattering measurements on these samples represent the true physical behaviour of the sample or might rather arise from averaging over regions with different magnetic properties within a sample. Especially an observed second order phase transition may indeed be an intrinsic first order phase transition, which becomes smeared by inhomogeneities of the sample. In this context NDI may be developed into a valuable tool for the investigation of quantum phase transitions.

Neutron depolarisation imaging has been developed during this thesis as a new method to investigate ferromagnetic samples. On the one hand it can be used to obtain information about the homogeneity and therefore the quality of the sample. However, on the other hand, neutron depolarisation imaging also offers the possibility to obtain information about the distribution of magnetic properties over an inhomogeneous sample. This information may eventually be equivalent to the information obtained by performing time consuming bulk measurements on a large number of small and homogeneous samples, which could be prepared from an inhomogeneous sample. Thus, NDI has the potential to be of great help in the proof or disproof of the existence of a QCP in many substances.

Structure of this Thesis

This thesis is organised in six chapters. In this first chapter a theoretical introduction to quantum phase transitions and quantum criticality is given. Since weakly ferromagnetic systems are in many ways ideal to study the effects of quantum critical phenomena, section 1.2 gives an overview of the observed magnetic properties of this material class and shows the current theoretical approach to describe these properties in the framework of a mean field theory. In the last section of this chapter an overview of the current status of research on weakly ferromagnetic materials is given, with special emphasis on the systems $\text{Pd}_{1-x}\text{Ni}_x$ and Ni_3Al , which have been extensively studied in this thesis.

The second chapter deals with the theoretical background of the employed experimental techniques. An introduction to standard neutron radiography is given as well as to the standard neutron depolarisation technique. It is furthermore shown how to combine both techniques to the newly developed neutron depolarisation imaging method in order to obtain spatially resolved information about the magnetic properties of a sample.

Chapter 3 is focused on the components of the experimental setup for neutron depolarisation imaging measurements, some of which have been specially built during this thesis, and others have been adapted as to meet the requirements also discussed in this chapter. First, an overview of the entire setup is given and subsequently the components of this setup and their performance are discussed.

Chapter 4 explains the general measurement procedure for the determination of the spatially resolved depolarisation of a neutron beam after transmission of the sample and shows how the data can be evaluated. Furthermore, an overview of the various setups that have been used for the measurements described in this thesis is shown and the advantages and disadvantages of each setup are discussed.

Our experimental results are shown and discussed in chapter 5. First, proof-of-principle measurements made on a neutron scattering instrument at FRM II are shown. The second part of this chapter focuses on measurements on the weakly ferromagnetic substances $\text{Pd}_{1-x}\text{Ni}_x$ and Ni_3Al on which extensive studies have been performed. In addition to the standard NDI measurements, tomographic measurements were made on $\text{Pd}_{1-x}\text{Ni}_x$, and pressure studies using a Cu:Be clamp cell were performed on Ni_3Al .

In chapter 6 a conclusion is drawn from the experimental results and an outlook towards further development of the experimental method as well as further possible applications of the technique developed in this thesis is given.

1.2 Weak Itinerant Ferromagnetism

The class of weak itinerant ferromagnetic compounds shows magnetism on a very small and well defined unique energy scale, which makes them an interesting group of substances to study the fundamentals of ferromagnetism. Weak itinerant ferromagnets have the following typical properties:

- a low Curie temperature T_C of the order of several 10 K or below,
- a small ordered moment m_s of only several tenths of μ_B , which shows the following temperature dependence below T_C :

$$m_s^2(T) = m_s^2(0) \left(1 - \left(\frac{T}{T_C} \right)^2 \right), \quad (1.2.1)$$

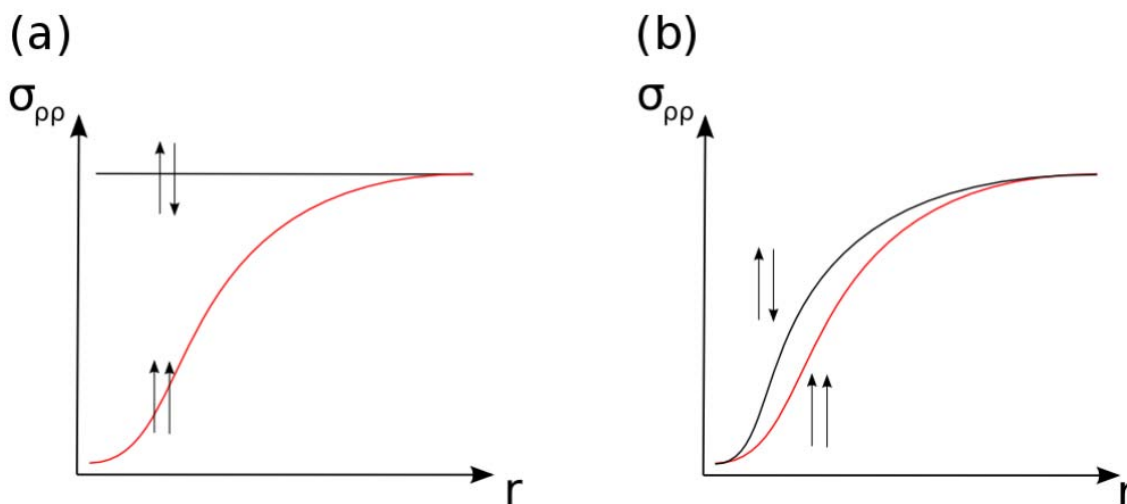


Figure 1.2.1: Pair correlation function $\sigma_{\rho\rho}$ for two electrons with spins parallel and antiparallel as a function of their distance r . (a) shows the correlation ignoring and (b) accounting for the Coulomb repulsion.

- a strongly unsaturated field dependence of the magnetisation $M(T \rightarrow 0, B)$, which shows a linear behaviour in plots of $B/M(T, B)$ vs. $M^2(T, B)$ (called Arrot plots [10]) over a wide temperature and field range,
- a Curie-Weiss behaviour of the susceptibility over a wide temperature range above T_C with an effective Curie-Weiss moment m_{cw} , which is much larger than the ordered moment ($m_{cw}/m_s \gg 1$).

Weak itinerant ferromagnetism can qualitatively be understood as a result of the coaction of the Coulomb repulsion and the Pauli-principle of the conduction electrons, which have a high mobility in metals. Let us first consider only the Pauli-principle and neglect the Coulomb repulsion. The Pauli principle leads to a repulsion of electrons with parallel spins, since it tends to arrange Fermions with their spins being antiparallel. This repulsion leads to a pronounced minimum in the pair correlation function of two electrons with parallel spins at a distance $r = 0$. In contrast, electrons with antiparallel spins can occupy any position with equal probability (see Fig. 1.2.1 (a)). Thus, electrons with parallel spins have, on the temporal average, a larger distance from each other. Their larger distance automatically leads to a reduction of their potential energy in the Coulomb potential. As a result, it is energetically favourable for electrons to arrange their spins in parallel with each other due to the reduction of their energy in the Coulomb potential. However, the Coulomb repulsion also acts on electrons with antiparallel spins, which reduces the energy gain of the parallel arrangement compared to the antiparallel one (see Fig. 1.2.1 (b)). Furthermore, since the total number of electrons is conserved, the number of quantum states is also conserved. This means that the parallel electrons have to occupy states with higher quantum numbers in k -space which have a higher kinetic energy. This energy loss competes with the energy gain due to the Pauli principle and the Coulomb repulsion. The difference in energy between the two possible orientations of two electrons is small, which makes it difficult to calculate it numerically. However, there exist phenomenological models which account for the correlation between all electrons that allow to successfully describe the properties of ferromagnetic materials. We will discuss these models in more detail in the following sections.

1.2.1 Stoner Model

The Stoner model [11], which was developed in the 1930s, is a phenomenological model that is an extension to the molecular field model developed by Pierre Weiss [12]. It was elaborated to describe metallic band ferromagnets like iron, nickel and cobalt and is based on the description of the interaction of a single conduction electron with all other conduction electrons in the material via a molecular field λM inherited from the Weiss model. Here, λ is a temperature-independent coupling constant resulting from the exchange interaction and M is the magnetisation. The conduction band is spin-split by the molecular field and one treats excitations from one band to the other as excitations of uncorrelated particle-hole pairs in the molecular field λM . This way one can write the electronic free energy as¹

$$F(M) = F_0(M) + \Delta F(M). \quad (1.2.2)$$

Here $F_0(M)$ is the free energy resulting from the one-particle density of states $N(E)$ without interaction with the other electrons. A correction to the free energy resulting from the interaction with the molecular field is introduced by

$$\Delta F(M) = -\frac{1}{2}\lambda VM^2 + \dots, \quad (1.2.3)$$

where V is the volume of the material. For small magnetisations M , the first term of the free energy in (1.2.2) can be expanded in powers of M [13]. Time inversion symmetry requires that only even powers of M appear in this expansion:

$$F_0(M) = F_0(0) + \frac{1}{2}Va_0M^2 + \frac{1}{4}b_0M^4 + \dots \quad (1.2.4)$$

The parameters a_0 and b_0 are given by

$$a_0 = \frac{1}{\chi_p} \left(1 + s_F \frac{T^2}{T_F^2} + \dots \right) \quad (1.2.5)$$

$$b_0 = \left(\frac{\mu_B^2}{2\chi_p^3} \right) \left\{ \left(\frac{N'_F}{N_F} \right)^2 - \frac{N''_F}{3N_F} \right\}, \quad (1.2.6)$$

where the factor s_F is the sign of the expression in brackets on the right-hand side of (1.2.6):

$$s_F = \text{sgn} \left(\left(\frac{N'_F}{N_F} \right)^2 - \frac{N''_F}{3N_F} \right). \quad (1.2.7)$$

The parameter a_0 furthermore contains the Pauli-susceptibility χ_p at $T = 0$:

$$\chi_p = \frac{2\mu_B^2 N_a N_F}{V}. \quad (1.2.8)$$

$N_F = N(E_F)$ is the density of states at the Fermi-energy per spin per atom, N_a is equal to the number of atoms, N'_F and N''_F are the first and second derivative of the density of states at the Fermi-energy and T_F is the Fermi degeneracy temperature which may be approximated as $T_F \approx E_F/k_B$ for a parabolic band

¹Following the publication of Lonzarich and Taillefer [3] all equations will in the following be based on the cgs unit system.

structure. More accurately it is given by

$$T_F = \left| \frac{1}{6} \pi^2 k_B^2 \left(\left(\frac{N'_F}{N_F} \right)^2 - \frac{N''_F}{3N_F} \right) \right|^{-1/2}. \quad (1.2.9)$$

In any case $T \ll T_F$ holds, which is why (1.2.5) and (1.2.6) have only been expanded to first order in T . The parameter a_0 is always positive for a ferromagnetically ordered system. In case $b_0 < 0$ one has to consider higher order terms of M in (1.2.4) to obtain a magnetically stable state.

With the parameters introduced above one can obtain a magnetic equation of state from the free energy defined in (1.2.2) as

$$B = \frac{1}{V} \frac{\partial F(M)}{\partial M} = (a_0 - \lambda)M + b_0 M^3 + \dots, \quad (1.2.10)$$

which yields the linear behaviour in the Arrot plots B/M vs. M^2 observed over a wide temperature and field range. One can define:

$$A(T) = a_0 - \lambda = \frac{1 - \lambda \chi_p}{\chi_p} \left(1 + \frac{s_F T^2}{T_F^2 (1 - \lambda \chi_p)} + \dots \right) \quad (1.2.11)$$

Here $S = (1 - \lambda \chi_p)^{-1}$ is known as the Stoner factor with a dimensionless parameter $\lambda \chi_p$, that defines the magnetic state of the system. In the case of $\lambda \chi_p > 1$, $A(T)$ becomes negative and the material is ferromagnetic with a spontaneous magnetisation in zero-field

$$M(T, 0) = \left(-\frac{A(T)}{b_0} \right)^{1/2}. \quad (1.2.12)$$

For $\lambda \chi_p < 1$ and thus $A(T) > 0$ the system is paramagnetic with a susceptibility given by $\chi = 1/A$.

For nearly ferromagnetic materials like palladium with $\lambda \chi_p < 1$ and $\lambda \chi_p \approx 1$ the Stoner factor becomes very large, which leads to an increase of the susceptibility and its temperature dependence. This is why such a system is entitled as Stoner enhanced paramagnet with a susceptibility

$$\chi(T) = A(T)^{-1} = S \chi_p \left(1 - \frac{s_F S T^2}{T_F^2} + \dots \right). \quad (1.2.13)$$

Under the assumption that λ is temperature-independent, that $s_F = +1$, and $T \ll T_F$ one can calculate a Curie temperature for a Stoner ferromagnet from $A(T_0) = 0$, which is given by

$$T_0 = T_F (\lambda \chi_p - 1)^{1/2}. \quad (1.2.14)$$

However, this Curie temperature is typically an order of magnitude larger than the experimentally observed ordering temperature. The Stoner model succeeds in qualitatively describing the temperature and field behaviour for weak ferromagnets, however it fails in quantitative calculations like that of the Curie temperature shown above.

1.2.2 Self-Consistent Ginzburg-Landau-Theory

The Stoner model discussed above fails to quantitatively describe the temperature dependence of the susceptibility for most metals. An extension to this theory is a self-consistent Ginzburg-Landau-Theory

(SCR) developed by Lonzarich and Taillefer [3], which additionally takes into account slow and long-wavelength fluctuations of the magnetisation. Longitudinal and transverse fluctuations are treated separately in this model. This phenomenological theory succeeds in quantitatively describing the experimentally observed behaviour for weak ferromagnets making use of four material specific parameters, which can be either determined from band structure calculations or from magnetisation and neutron scattering measurements, respectively. These parameters are the inverse initial susceptibility a , the mode-coupling parameter b , the spin-wave stiffness c , and the energy width of the spin fluctuations γ . In the following we will discuss this theory following the article by Lonzarich [3].

We start by defining a slowly varying local magnetisation $\mathbf{M} + \mathbf{m}(\mathbf{r}, t)$, where \mathbf{M} represents the statistical average of the magnetisation and $\mathbf{m}(\mathbf{r}, t)$ is its slowly varying fluctuation, which on the average is zero. The power spectrum of this magnetisation is given by the fluctuation-dissipation-theorem [14]:

$$\langle |m_v(\mathbf{q}, \omega)|^2 \rangle = 2\hbar V \Theta \left(\frac{1}{2} + n(\omega) \right) \text{Im}\chi_v(\mathbf{q}, \omega) \quad (1.2.15)$$

V is the (large) volume and Θ is the (long) time interval over which the given Fourier transform is performed, $n(\omega) = \left(\exp\left(\frac{\hbar\omega}{k_B T}\right) - 1 \right)^{-1}$ is the Bose factor and $\chi_v(\mathbf{q}, \omega)$ is the diagonal component of the generalised dynamical susceptibility. $\langle |m_v(\mathbf{q}, \omega)|^2 \rangle$ represents a quantum statistical average of the ensemble, in which the term $\frac{1}{2}$ covers the zero-point fluctuations and $n(\omega)$ are the thermally excited contributions. In our case we can neglect the zero-point fluctuations since the thermally excited fluctuations generally have small \mathbf{q} inside the first Brillouin-zone, which leads to $n(\omega) \gg \frac{1}{2}$. Thus, (1.2.15) reduces to

$$\langle |m_v(\mathbf{q}, \omega)|^2 \rangle = 2\hbar V \Theta n(\omega) \text{Im}\chi_v(\mathbf{q}, \omega), \quad (1.2.16)$$

where v represents the component perpendicular (\perp) and parallel (\parallel) to \mathbf{M} . We can integrate (1.2.16) over ω and \mathbf{q} since it represents the variance per unit wave number $q/2\pi$ and unit frequency $\omega/2\pi$ and obtain

$$\langle |m_v(\mathbf{q})|^2 \rangle = 4\hbar V \int \frac{d\omega}{2\pi} n(\omega) \text{Im}\chi_v(\mathbf{q}, \omega) \quad (1.2.17)$$

and

$$\langle m_v^2 \rangle = 4\hbar \int \frac{d^3\mathbf{q}}{(2\pi)^3} \int_0^\infty \frac{d\omega}{2\pi} n(\omega) \text{Im}\chi_v(\mathbf{q}, \omega), \quad (1.2.18)$$

where the integral over \mathbf{q} goes over the first Brillouin-zone. The obtained mean-square value of the fluctuation amplitude only depends on the Bose-factor and the imaginary part of the dynamical susceptibility, which means that in equilibrium it is independent of t and for low temperature and in weakly ferromagnetic materials it is also independent of \mathbf{r} . The inclusion of the thermal variance of the local magnetisation $\langle m_v^2 \rangle$ is the main difference between the Stoner-model and this Ginburg-Landau model and yields the temperature dependence of the parameter A .

We may assume that the local free energy $f(\mathbf{r})$ is an analytic function of a small and slowly varying classical order parameter $\mathbf{M} + \mathbf{m}^c(\mathbf{r})$, which is composed of the static magnetisation \mathbf{M} and its fluctuation $\mathbf{m}^c(\mathbf{r})$ with zero mean. Thus it can be expressed in a series expansion as

$$f(\mathbf{r}) = f_0 + \frac{a}{2} |\mathbf{M} + \mathbf{m}^c(\mathbf{r})|^2 + \frac{b}{4} |\mathbf{M} + \mathbf{m}^c(\mathbf{r})|^4 + \frac{c}{4} \sum_{\mathbf{v}} |\nabla \mathbf{m}_{\mathbf{v}}^c(\mathbf{r})|^2 \quad (1.2.19)$$

with

$$\mathbf{m}^c(\mathbf{r}) = \frac{1}{V} \sum_{\mathbf{q}} \mathbf{m}^c(\mathbf{q}) e^{i\mathbf{q}\cdot\mathbf{r}}. \quad (1.2.20)$$

Here $\mathbf{m}^c(\mathbf{q}) = \mathbf{m}(\mathbf{q})$ as defined in (1.2.17) for $q < q_c$ and $\mathbf{m}^c(\mathbf{q}) = 0$ otherwise, with an elaborately chosen cut-off wave vector \mathbf{q}_c . The expansion coefficients a, b and c are the coefficients introduced above, which are, for small \mathbf{M} and a cubic lattice, independent of \mathbf{v} but in general depend on \mathbf{q}_c . The fourth parameter γ defined above is essentially q_c and will be given below.

Integration of the local free energy $f(\mathbf{r})/V$ over the volume V yields the total free energy of one specific spatial magnetic configuration:

$$\begin{aligned} \frac{F(\mathbf{M}, \mathbf{m}^c(\mathbf{q}))}{V} &= \int d^3\mathbf{r} f(\mathbf{r})/V = \\ &= f_0 + \frac{a}{2} M^2 + \frac{b}{4} M^4 + \frac{1}{2V^2} \sum_{\mathbf{q}} |m_{\mathbf{v}}^c(\mathbf{q})|^2 (a + bM^2(1 + 2\delta_{\mathbf{v}\parallel}) + cq^2) \\ &\quad + \int \frac{d^3\mathbf{r}}{V} \frac{b}{4} |\mathbf{m}^c(\mathbf{r})|^4 + \dots \end{aligned} \quad (1.2.21)$$

where the vector product $\mathbf{m}_{\mathbf{v}}^c(\mathbf{r}) \cdot \mathbf{M}$ in (1.2.19) yields $\delta_{\mathbf{v}\parallel} = 1$ for the component parallel to \mathbf{M} and 0 for the component perpendicular to \mathbf{M} . Since we deal with a classical local order parameter, the joint probability distribution of its Fourier components is proportional to

$$\exp\left(-\frac{F(\mathbf{M}, \mathbf{m}^c(\mathbf{q}))}{k_B T}\right). \quad (1.2.22)$$

The quadratic term $b|m_{\mathbf{v}}^c(\mathbf{q})|^2 M^2$ and the fourth order term in (1.2.21) lead to a statistical dependence in the joint probability distribution due to cross products, i.e. a coupling of the modes. We will first neglect the fourth order term, which is possible for very low temperatures or a small mode coupling parameter b only. The effect of this term will later be taken into account by a self-consistent renormalisation of the susceptibility obtained from the magnetic equation of state that will follow from (1.2.21). Neglecting the fourth order term, we obtain a Gaussian probability distribution for each component $m_{\mathbf{v}}^c(\mathbf{q})$ (not so for $M_{\mathbf{v}}$) with zero-mean $\langle m_{\mathbf{v}}^c(\mathbf{q}) \rangle = 0$ and a variance of

$$\langle |m_{\mathbf{v}}^c(\mathbf{q})|^2 \rangle = V k_B T \chi_{\mathbf{v}}^{-1}(\mathbf{q}) \quad (1.2.23)$$

for $q < q_c$, otherwise $\langle |m_{\mathbf{v}}^c(\mathbf{q})|^2 \rangle = 0$. The inverse static susceptibility is given by

$$\chi_{\mathbf{v}}^{-1}(\mathbf{q}) = \chi_{\mathbf{v}}^{-1} + cq^2 \quad (1.2.24)$$

$$\chi_{\mathbf{v}}^{-1} = a + bM^2(1 + 2\delta_{\mathbf{v}\parallel}). \quad (1.2.25)$$

Since $m_{\mathbf{v}}^c(\mathbf{q})$ is a classical order parameter, the Kramers-Kronig relation states that (1.2.23) and (1.2.17) are fully equivalent for $q < q_c$, which is the basis for the self-consistency argument of this theory.

Integrating the joint probability distribution of (1.2.22) over all variables with $\mathbf{q} \neq 0$ yields an expression

for the free energy $F(M)$

$$\frac{F(M)}{V} = \frac{F(0)}{V} + \frac{a}{2}M^2 + \frac{b}{4}M^4 + \frac{k_B T}{2V} \sum_{\mathbf{v}, q < q_c} \ln \chi_{\mathbf{v}}^{-1}(\mathbf{q}), \quad (1.2.26)$$

where $F(0)$ is independent of M . Taking the derivative of the free energy with respect to the magnetisation M gives a magnetic equation of state for the magnetisation stabilised by an applied field B

$$B = \frac{1}{V} \frac{\partial F(M)}{\partial M} = AM + bM^3 \quad (1.2.27)$$

which looks similar to the equation of state (1.2.10) obtained from the Stoner model, however here we have a different definition of A :

$$A = a + b \left(3 \left\langle (m_{\parallel}^c)^2 \right\rangle + 2 \left\langle (m_{\perp}^c)^2 \right\rangle \right) \quad (1.2.28)$$

$$\left\langle (m_{\mathbf{v}}^c)^2 \right\rangle = \frac{k_B T}{V} \sum_{q < q_c} \chi_{\mathbf{v}}(\mathbf{q}) \quad (1.2.29)$$

Thus, for this model A depends on M and the first term in (1.2.27) may be of higher than first order in M . For systems in the vicinity of the ferromagnetic instability ($\lambda \chi_p \approx 1$) and not too close to T_C one obtains $a \approx a_0 - \lambda$ and $b \approx b_0$ as defined above.

Having neglected the fourth order term $b|m^c(\mathbf{r})|^4$ in (1.2.21) leads to a difference between the susceptibility obtained from (1.2.27) and (1.2.28) from the susceptibility in (1.2.25). In order to account for this fourth order term the susceptibility in the latter equation has to be replaced self-consistently by the following expressions

$$\chi_{\parallel}^{-1} = \frac{\partial B_{\parallel}}{\partial M_{\parallel}} = \frac{\partial B}{\partial M} = A + M \frac{\partial A}{\partial M} + 3bM^2 \quad (1.2.30)$$

$$\chi_{\perp}^{-1} = \frac{\partial B_{\perp}}{\partial M_{\perp}} = \frac{B}{M} = A + bM^2, \quad (1.2.31)$$

where A is defined in (1.2.28). Equations (1.2.24) and (1.2.27) to (1.2.31) describe a complete set of self-consistent equations that define the magnetic equation of state in terms of the four parameters a, b, c and γ which has not yet been introduced but basically depends on q_c . These four parameters can either be obtained from calculations from the underlying band structure or – more reliably – be determined experimentally. In this case a and b can be found from magnetisation measurements and c and γ can be found from inelastic neutron scattering on magnons and paramagnetic scattering, respectively.

In contrast to the Stoner model, for which the entire temperature dependence comes from $A(T)$ and is relatively weak, in the SCR model the additional term $3 \left\langle (m_{\parallel}^c)^2 \right\rangle + 2 \left\langle (m_{\perp}^c)^2 \right\rangle$ in (1.2.28) is also temperature dependent. The corrections introduced by this term, resulting from thermal spin fluctuations, become important due to the only weak temperature dependence of $A(T)$. In this manner the temperature dependence of the magnetic properties of weak ferromagnets can be explained

For further quantitative evaluation a specific form of the dynamical susceptibility has to be introduced. In the Fermi-Liquid theory for a paramagnet, the dynamical susceptibility can be expanded in terms of

the static susceptibility $\chi_v^{-1}(\mathbf{q})$ (cf. (1.2.24))

$$\chi_v^{-1}(\mathbf{q}, \omega) = \chi_v^{-1}(\mathbf{q}) \left(1 - \frac{i\omega}{\Gamma_v(\mathbf{q})} \right) \quad (1.2.32)$$

with a relaxation rate $\Gamma_v(\mathbf{q})$ of a spin fluctuation with wave vector \mathbf{q} given by

$$\Gamma_v(\mathbf{q}) = \gamma q \chi_v^{-1}(\mathbf{q}) = \gamma q (\chi_v^{-1} + cq^2 + \dots) \quad (1.2.33)$$

The energy width γ of the spin fluctuations is the fourth parameter of this model for weak ferromagnets introduced above. For the parameter c and γ at $T = 0$ and for isotropic but not necessarily parabolic bands in lowest order in $\langle m^2 \rangle$ one finds

$$c = \frac{1}{9\chi_p k_F^2} \left(1 - \frac{3nN'_F}{2N_F^2} + \frac{9}{8} \left(\frac{nN'_F}{N_F^2} \right)^2 - \frac{9}{16} \frac{n^2 N''_F}{N_F^3} \right) + \dots \quad (1.2.34)$$

$$\gamma = \frac{2}{\pi} \chi_p v_F + \dots, \quad (1.2.35)$$

where $k_F = (3\pi^2 n N_a / V)^{1/3}$ is the Fermi wave vector and $v_F = 3n(2\hbar k_F N_F)^{-1}$ is the Fermi velocity.

In contrast to the Stoner model in this self-consistent Ginzburg-Landau model the temperature dependence of the behaviour of weak ferromagnets can be determined quantitatively in good agreement with experiment. For the Curie-temperature one obtains the expression

$$T_C = 2.387 c M_0^{3/2} \frac{(\hbar\gamma)^{1/4}}{k_B}, \quad (1.2.36)$$

where $M_0 = (-a/b)^{1/2}$ is the spontaneous magnetisation extrapolated towards $T = 0$.

1.3 Ferromagnetic Quantum Criticality?

The self-consistently renormalised spin fluctuation theory (SCR) discussed above has been a major breakthrough in the theoretical description of weakly ferromagnetic materials. It succeeds in quantitatively modelling the properties of many materials and the excellent agreement of the calculated Curie temperatures with experimental values shows that the theory correctly incorporates the dynamics accompanying the ferromagnetic spin alignment in terms of exchange-enhanced spin fluctuations of the conduction electrons. However, since at a quantum phase transition strong effects are balanced, effects on weaker energy scales which are not included in the SCR theory may become significant.

As discussed in 1.1, QCPs have been identified in several antiferromagnetic systems [5], but the existence of QCPs in ferromagnets is up to now still an open question. Despite being proposed in various weakly ferromagnetic materials, QCPs were never identified free of doubt. In contrast, the phase transitions were found to be first-order instead of second-order for all pure systems studied to date.

These observations lead to a generic phase diagram for ferromagnetic QPTs which is currently being discussed as shown in Fig 1.3.1. For sufficiently high temperatures it shows a second-order transition with increasing order parameter δ . However at a certain temperature a tricritical point (TCP) is reached, below which the phase transition becomes first-order. If additionally a magnetic field is applied, a

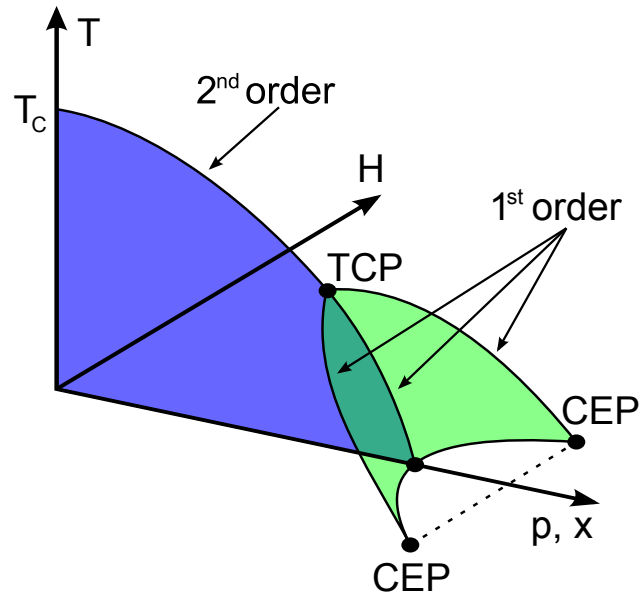


Figure 1.3.1: Generic phase diagram for ferromagnetic quantum phase transitions. Below a certain temperature the second order phase transition turns first order beginning in a tricritical point (TCP). The application of an external magnetic field leads to a first order metamagnetic transition which ends in critical endpoints (CEP) at $T = 0$.

metamagnetic transition is induced, which is first-order as well and which ends in critical endpoints (CEP) for $T \rightarrow 0$. This phase diagram suggests that in ferromagnetic systems no QCP can exist since a second-order phase transition for $T \rightarrow 0$ is not observed. Such a proposal was also made by Belitz *et al.* [15] who showed in a theoretical analysis that at low temperatures the phase transition in weak itinerant ferromagnets is generically first order in pure systems. This result comes from long-wavelength correlations based on the underlying phase transition and it is independent of the band structure.

In the following we will discuss in some detail the experimental results obtained from several candidate substances for a ferromagnetic QCP and show inconsistencies with the theoretical predictions.

1.3.1 ZrZn_2 , UGe_2 , MnSi

Historically these substances were the first promising candidates for a quantum critical point to be studied. A huge body of investigation exists, revealing that all three substances show complex magnetic behaviour and a first order phase transition for $T \rightarrow 0$, which is in contradiction with the expectation for a QCP. UGe_2 was the first substances for which a coexistence of ferromagnetism and superconductivity was observed. MnSi shows a similarly complex phase diagram due to its helical structure, which also avoids a QCP.

ZrZn_2

The itinerant ferromagnet ZrZn_2 , which crystallises in the cubic C15 structure, has for long time been considered as the most promising substance to show ferromagnetic quantum criticality. The material shows a low Curie temperature of $T_C = 28.5 \text{ K}$ and has an ordered moment of $M = 0.17 \mu_B/\text{f.u.}$, which are both of typical magnitude for weak itinerant ferromagnets. Early high pressure studies on ZrZn_2

found the phase transition with increasing pressure to be second order, which is generally in agreement with a QCP [16, 17, 18].

However, these studies were disproved by Uhlarz *et al.* [6] who reported high pressure magnetisation studies on high purity single crystals of ZrZn_2 showing that the magnetisation vanishes discontinuously at a critical pressure of $p_c = 16.5$ kbar. In contrast to that, the magnetisation shows a second order phase transition as a function of temperature at ambient pressure. By additional application of a magnetic field, a first order metamagnetic transition can be induced. All of these observations are consistent with the phase diagram proposed in Fig. 1.3.1 and therefore not in agreement with a QCP. Furthermore the authors report multiple first order QPTs between two different ferromagnetic phases at ambient pressure as a function of applied magnetic field, which are consistent with de Haas van Alphen measurements reported by Kimura *et al.* [19].

UGe₂

UGe₂ is a uniaxial ferromagnet with a strong magnetocrystalline anisotropy, which crystallises in the orthorhombic (Cmmm) ZrGa_2 crystal structure. The ordering temperature at ambient pressure is $T_C = 52$ K and an ordered moment of $1.4 \mu_B/\text{U}$ along the a axis is observed. Furthermore, a first order phase transition from a weakly (FM1) to a strongly polarised phase (FM2) is found at ambient pressure at $T_X = 25$ K [7]. Application of pressure leads to a monotonic decrease of the ordering temperature, which vanishes in a first order phase transition at $p_c = 15.8$ kbar [20] and is therefore not consistent with the requirements of a QCP. Also the transition between the phases FM1 and FM2 is first order in the low temperature limit and therefore also inconsistent with a QCP, which was proposed for this phase transition [7].

Being the first ferromagnetic material for which a coexistence of ferromagnetism and superconductivity was found [21, 22], the compound has attracted much attention. Superconductivity was observed in a limited pressure range between $p_x = 12.2$ kbar and p_c with a maximum critical temperature of 850 mK. The origin of superconductivity in UGe₂ has been extensively discussed after these findings.

Nishioka *et al.* [23, 24] found regular jumps in the magnetisation which they attributed to field-induced tunnelling between quantum states and lead them to propose a magnetic domain size of the order of 40 \AA . In contrast to that, the Cooper-pair correlation length ξ was estimated to be of the order of $130 - 200 \text{ \AA}$. Such a ferromagnetic domain size which is very small compared to the correlation length would lead to the cancellation of the magnetic field at the length scale of the Cooper-pair correlation. However, this thesis was disproved by 3D neutron depolarisation analysis using the technique described in 2.4 yielding a domain size of the order of $10 \mu\text{m}$, which is much larger than the correlation length ξ [25].

MnSi

Another candidate, which was under consideration for a QCP is the transition-metal compound MnSi. The magnetic properties of MnSi have therefore been extensively studied. The present understanding of the complex phase diagram of MnSi shows that the compound exhibits very interesting and previously unknown magnetic behaviour which is, however, not consistent with a QCP.

MnSi is a helical ferromagnet in which interactions on three distinct, hierarchical energy scales coexist, leading to a complex magnetic phase diagram. First, on the largest energy scale a ferromagnetic coupling with an ordering temperature of $T_C = 29.5$ K and an ordered moment of $0.4 \mu_B/\text{Mn}$ is observed. The second and much weaker energy scale is the Dzyaloshinskii-Moriya (DM) interaction, which favours a perpendicular alignment of neighbouring magnetic moments [26, 27]. The competition of this interaction with the stronger ferromagnetic ordering leads to an incommensurate helical structure of the magnetic moments with a wavelength of $\lambda \approx 180 \text{ \AA}$. The third and weakest energy scale is the magnetocrystalline anisotropy resulting in a pinning of the propagation vectors \mathbf{k} of the helices along the cubic $\langle 111 \rangle$ axes.

If an applied magnetic field exceeds these three energy scales, respectively, a different magnetic order of the system is observed. Below T_C and at lowest fields below $B_{c,1} \approx 0.1$ T for $T \rightarrow 0$, MnSi is in the helical phase which shows a structure with four degenerate helices which are pinned along the cubic $\langle 111 \rangle$ axes [28, 29]. Increasing the field above $B_{c,1}$ leads to an unpinning of the helices and a preferred alignment of their propagation vectors in parallel to the applied magnetic field in a regime, which is called conical phase. A completely field polarised state is achieved at $B_{c,2} \approx 0.6$ T for $T \rightarrow 0$ [28]. Recently a third phase, called A-phase, occurring close to the transition temperature T_C and at an applied field of $B \approx \frac{1}{2} B_{c,2}$ was identified to show a previously unknown magnetic order with topological knots of the magnetisation, called a Skyrmion lattice [30].

Application of hydrostatic pressure leads to a reduction of the Curie temperature, which reaches $T_C = 0$ at a critical pressure of $p_c = 15$ kbar. The phase transition changes from second order to weakly first order at a pressure $p^* = 12$ kbar [31, 32]. Above this pressure p^* a region of partial magnetic order is found, which survives up to $p > p_c$ [33], where additionally an extended region of NFL behaviour is observed for pressures as high as 30 kbar and a temperature a large temperature range from several mK to 12 K [34, 35].

In conclusion, MnSi shows a very complex and exciting phase diagram which exhibits completely new magnetic order but is not consistent with a QCP.

1.3.2 $\text{Pd}_{1-x}\text{Ni}_x$

Pd is a metal, which crystallises in a face centred cubic (fcc) structure. Pure Pd is paramagnetic, however it shows a strongly Stoner enhanced paramagnetic susceptibility and in fact, the Stoner factor S for Pd is the highest of all pure elements. In Pd, which is on the border of ferromagnetism, ferromagnetic order can be induced by doping with small amounts of Ni. At a critical concentration of $x_c = 0.026$ the material becomes ferromagnetic and shows a strong dependence of the Curie temperature T_C on the Nickel content x as shown in the diagram in Fig. 1.3.2, for which most of the experimental data obtained up to 1999 was compiled by Nicklas *et al.* [36].

$\text{Pd}_{1-x}\text{Ni}_x$ is a system for which a ferromagnetic quantum critical point was proposed at a critical concentration² of $x = 0.025$ [36]. The system is non stoichiometric and falls in the class of disordered weak

²The critical concentration for the QCP was proposed to be $x_c = 0.025 \pm 0.002$ by Nicklas *et al.*, which gives the best agreement with all their experimental data obtained with different bulk measurement techniques. The data of the concentration dependence of the Curie temperature was best fit to $x_c = 0.026$ by the authors. In the following we will use $x_c = 0.025$ when referring to this article.

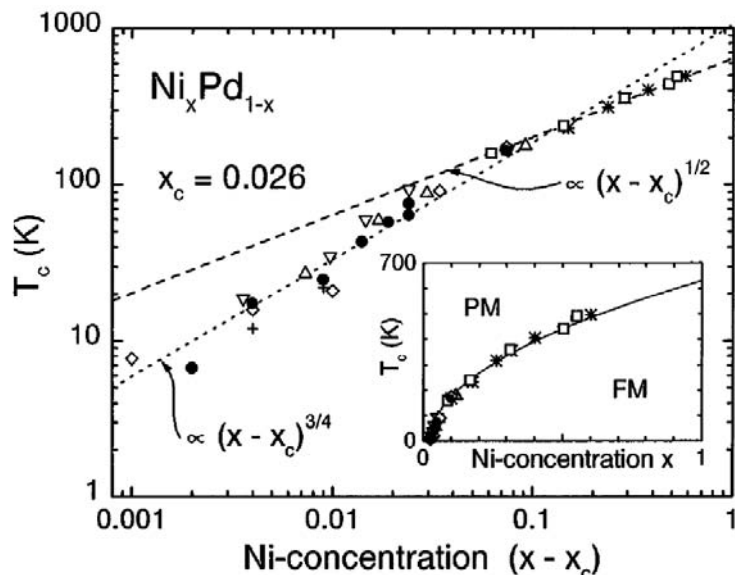


Figure 1.3.2: Concentration dependence of the ordering temperature for $\text{Pd}_{1-x}\text{Ni}_x$ taken from [36]. Most of the published experimental data available up to the year 1999 has been compiled in this diagram. Nicklas proposed a critical concentration $x_c = 0.026$.

ferromagnets. Historically $\text{Pd}_{1-x}\text{Ni}_x$ has been extensively studied, and we will now give an overview of the experimental results on the material.

First measurements on $\text{Pd}_{1-x}\text{Ni}_x$ were reported by Gerstenberg [37] in 1958 who performed susceptibility measurements on Pd doped with various transition metals and found an effective moment $\mu_{\text{eff}} = 4.79 \mu_B$ for a Ni concentration of $x = 0.03$. These measurements were extended to temperatures as low as 1.4 K by Shaltiel *et al.* [38] in 1964 who investigated the susceptibility of various $\text{Pd}_{1-x}\text{Ni}_x$ crystals with $x = 0.002$ to $x = 0.035$ and found an effective moment of $\mu_{\text{eff}} = 7.0 \pm 0.3 \mu_B$ for $x = 0.035$, with a Curie temperature of $T_C = 45$ K. However, these authors admit that their samples might have contained impurities.

For this reason Chouteau *et al.* [39] in 1968 reinvestigated samples in a very wide concentration range from $x = 0.002$ to $x = 0.1$. Their susceptibility measurements show a maximum in the ratio of the susceptibility of the alloy to the susceptibility of pure Pd at a Ni concentration of $x = 0.025$. An increase of the saturation magnetisation is already found to take place from $x > 0.015$. In 1970 Aldred *et al.* [40] used diffuse magnetic neutron scattering to determine the polarisation effect of various Ni concentrations on the Pd matrix. The experiments were carried out at a temperature of $T = 4.2$ K and revealed a long-range polarisation of the Pd matrix by the Ni atoms. However only the excess amount of Ni above the critical concentration seemed to contribute to this polarisation. The authors discussed the possibilities that either a large distance between single Ni atoms prevents ferromagnetic ordering or that the Pd matrix could only be polarised by clusters of Ni atoms.

Electrical resistivity measurements on samples close to the critical concentration were performed in 1974 by Tari *et al.* [41]. The temperature dependent resistivity was fit to the function

$$\rho(T) = \rho_0 + AT^n \quad (1.3.1)$$

and a deviation of the exponent from $n = 2$ was found. The critical concentration x_c was determined

from a pronounced peak of the parameter $A(x)$ to be $x_c = 2.32 \pm 0.03\%$. These results were confirmed by Murani *et al.* [42] in the same year on samples obtained from the same ingots as the ones used by Tari. Murani furthermore performed magnetisation measurements on these samples and found strongly curved Arrott plots [10]. The authors compared different methods to find the critical concentration (electrical resistivity, specific heat, magnetisation and paramagnetic susceptibility) and found – within experimental errors – the same critical concentration of $x_c = 0.023$ for all methods. It was furthermore pointed out in this article that the magnetisation close to the critical concentration seems to be highly inhomogeneous on a microscopic scale.

Similarly curved Arrot plots below T_C were observed by Beille *et al.* [43]. Above the ordering temperature the susceptibility was found to follow a Curie-Weiss behaviour. In 1975 Beille and Tournier [44] studied the effect of pressure on the magnetisation of $\text{Pd}_{1-x}\text{Ni}_x$. From these measurements additional proof was found of a theory of localised giant moments that are constituted of groups of 3 or more neighbouring Ni atoms proposed by one of the authors – an idea already discussed in the article by Aldred in 1970. These measurements were extended by the authors to samples with higher Ni concentrations up to $x = 0.40$ in 1976 [45] and further confirmation of the existence of giant moments was found.

Another article dating from 1976 by Fujiwara *et al.* [46] deals with the pressure dependence of the Curie temperature for various Ni alloys. However, only higher concentration samples of $\text{Pd}_{1-x}\text{Ni}_x$ with $x > 0.20$ were investigated.

The question of the existence of giant moments was pursued in more detail in 1978 by Sain and Kouvel [47] who compared their magnetisation measurements on paramagnetic $\text{Pd}_{1-x}\text{Ni}_x$ samples with concentrations $x < 0.019$ with theoretical calculations and found three or more Ni atoms forming clusters with giant magnetic moments of $18 \mu_B$. Single Ni atoms and pairs of nearest neighbouring Ni atoms were found to contribute only a temperature independent part to the paramagnetic susceptibility. The measurements were made in a temperature range between 2.4K and 100K and in fields up to 56kOe. Such measurements were extended to samples with Ni concentrations between 2% and 3%, i.e. also above the proposed critical concentration by Cheung *et al.* [48] in 1981 for which they also found clusters of three or more Ni atoms. These authors pointed out that the major part of the giant magnetic moments of $17 \mu_B$ for a cluster of three Ni atoms must come from the polarised Pd matrix surrounding the cluster. However, since they only found spin values of $S = 2$, the polarisation of the Pd matrix must be tightly coupled to the Ni cluster and have no independent degrees of freedom.

Nicklas *et al.* [36] reported a ferromagnetic quantum critical point in $\text{Pd}_{1-x}\text{Ni}_x$ at a concentration of $x = 0.025 \pm 0.002$. Evidence for this is drawn from measurements of the electrical resistivity, the magnetic susceptibility and the specific heat on polycrystals with Ni concentrations between $x = 0.00$ and $x = 0.10$. The concentration dependence of the Curie temperature of these samples and of all other published data was identified to follow the relation $(x - x_c)^{3/4}$ for $(x - x_c) < 0.1$, which is in agreement with the predictions for a QCP. Furthermore the electrical resistivity exactly follows a $T^{5/3}$ law only in a very narrow range around the critical concentration. A logarithmic divergence of the specific heat $C/T \propto \ln \frac{T}{T_0}$ is found over a wider concentration range from $x = 0.022$ to $x = 0.028$, while the prefactor of the Non-Fermi Liquid (NFL) contribution to the heat capacity peaks at the critical concentration. Finally the article shows the DC susceptibility for several concentrations around the critical concentration. The authors admit that these data are the least convincing of the data shown. And indeed, even though the susceptibility follows a $T^{3/4}$ law for more than one decade, deviations are found for temperatures below 5K. All of the properties described above fulfil the predictions for a clean ferromagnetic QCP despite

the inevitable existence of disorder in the system. Two of the samples used by Nicklas have also been investigated in this thesis and the results will be discussed in 5.2.1.

Shortly after this publication in 2000 Yamada and Tanda also confirmed the existence of a ferromagnetic QCP in $\text{Pd}_{1-x}\text{Ni}_x$ in two short articles [49, 50]. They determined the dependence of the Curie temperature on the Ni concentration for samples with a Ni content between $x = 0.00$ and $x = 0.032$ by magnetisation measurements at temperatures between 2 K and 400 K. T_C was obtained from Arrott plots and a critical concentration of $x_c = 0.022$ was found, which is slightly lower than what Nicklas reported. NFL-behaviour of T_C was found for $(x - x_c) < 0.1$ with an exponent of $z\nu = 1.6$. For higher Ni concentrations $(x - x_c) \gg 0.1$ the expected Fermi-Liquid (FL) behaviour $T_C \propto (x - x_c)^{1/2}$ was confirmed. The transition between NFL and FL behaviour is reported to take place at $x = 0.10$.

In the year 2003, theoretical predictions on the behaviour of the Grüneisen ratio upon approaching a QCP were made by Zhu *et al.* [51]. The Grüneisen ratio Γ , which is the ratio of the thermal expansion α to the specific heat c_p , was found to universally diverge for any QCP as

$$\Gamma \propto T^{-1/\nu z}, \quad (1.3.2)$$

where ν and z are the critical exponents introduced in 1.1. Measuring the Grüneisen ratio for a specific system can consequently reveal details about the critical exponents and thus the dimensionality of a system at a QCP.

These predictions were very recently used by KÜchler *et al.* [52] in 2006 to test some systems for which a QCP had been proposed for their compatibility with the divergence of the Grüneisen ratio. Among the materials investigated by the authors was the same sample of $\text{Pd}_{1-x}\text{Ni}_x$ with $x = 0.024$ investigated by Nicklas in 1999. The Grüneisen ratio was found to be constant within experimental errors for temperatures below 2 K, which is incompatible with a ferromagnetic QCP in $\text{Pd}_{1-x}\text{Ni}_x$.

A recent diploma thesis by Franz [53] dealt with more detailed magnetisation measurements on four $\text{Pd}_{1-x}\text{Ni}_x$ samples with nominal concentrations close to the critical concentration. The magnetisation measurements were evaluated using Arrott plots (B/M vs. M^2), which were found to be linear for high fields and high temperatures. However, at low fields and low temperatures a region with deviations from these linear Arrott plots was found, which suggests that there are additional terms to the free energy not covered by the SCR theory of Lonzarich (cf. eq. (1.2.27)). The regions were found to extend to higher fields and temperatures for samples with lower T_C (i.e. samples closer to the critical concentration). A phase diagram obtained from these results is shown in Fig. 1.3.3. The shaded areas show the regions for which non-linear behaviour of the Arrott plots is observed for four different samples, respectively, whereas outside of these areas linear Arrott plots are observed.

1.3.3 Ni_3Al

The weak itinerant ferromagnet Ni_3Al is a stoichiometric system which crystallises in the fcc Cu_3Au -structure. In contrast to $\text{Pd}_{1-x}\text{Ni}_x$ where disorder might introduce physical behaviour which is not incorporated in the SCR theory, the absence of disorder in Ni_3Al makes it an ideal candidate to study quantum phase transitions and to verify the predictions of the SCR theory. The phase transition from ferromagnetism to paramagnetism can be tuned via hydrostatic pressure and was reported to reach $T_C = 0$

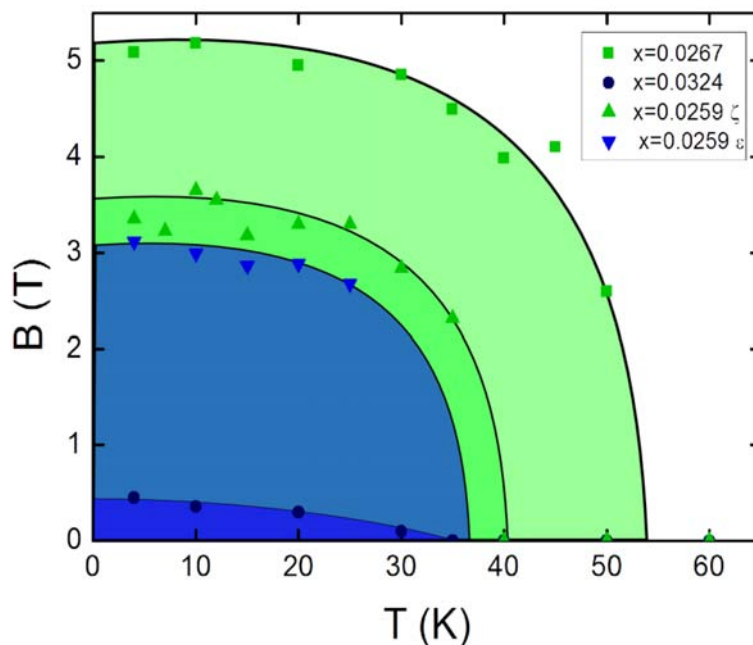


Figure 1.3.3: Phase diagram obtained by C. Franz for four different samples of $\text{Pd}_{1-x}\text{Ni}_x$. The coloured areas are the regions for which a more complicated behaviour than what is described by the SCR theory introduced by Lonzarich is found. The regions are larger for samples closer to the critical concentration. Outside of these regions, linear Arrot plot are found.

at a critical pressure of $p_c \approx 81$ kbar [9] as shown in Fig. 1.3.4 in contrast to an ambient pressure value of $T_C = 42$ K.

At the same time compositional doping has a strong influence on the ordering temperature. It has been found that only small amounts $x = 0.4$ of excess Al in $\text{Ni}_{75-x}\text{Al}_x$ can reduce the ordering temperature to zero. Therefore, both compositional doping and the application hydrostatic pressure are useful to tune the ordering temperature of $\text{Ni}_{75-x}\text{Al}_x$.

Historically Ni_3Al is one of the most extensively studied ordered weak itinerant ferromagnets for which a large variety of experimental techniques has been used [54, 55, 56, 57, 58, 59, 60, 61, 62, 63, 64, 65, 66, 67]. Chronologically, the concentration dependence of the magnetic properties of the material have been investigated before their pressure dependence [64, 57, 9]. All of these results show that spin fluctuations have to be taken into account to be able to theoretically describe the magnetic behaviour of Ni_3Al [68, 69].

There exist somewhat contradictory results on the composition dependence of the ordering temperature, which may be attributed to the complex metallurgy of the material and consequently the exact way the samples are prepared. Bremer *et al.* [70] performed a detailed analysis of the binary phase diagram around the stoichiometric composition and it turned out to be difficult to grow extended crystals of Ni_3Al of a defined composition from a melt. The data on the phase diagram obtained by Bremer has been put together with new data by Okamoto *et al.* [71] in a new phase diagram. However, the experimental uncertainties are too large to exactly determine the position of the peritectic point of the system.

All published data of resistivity measurements are generally consistent in the temperature region from 1 K to 30 K in that a deviation from the T^2 behaviour expected from FL theory is found. As a result from these measurements, the temperature dependence of the resistivity is to first order best described

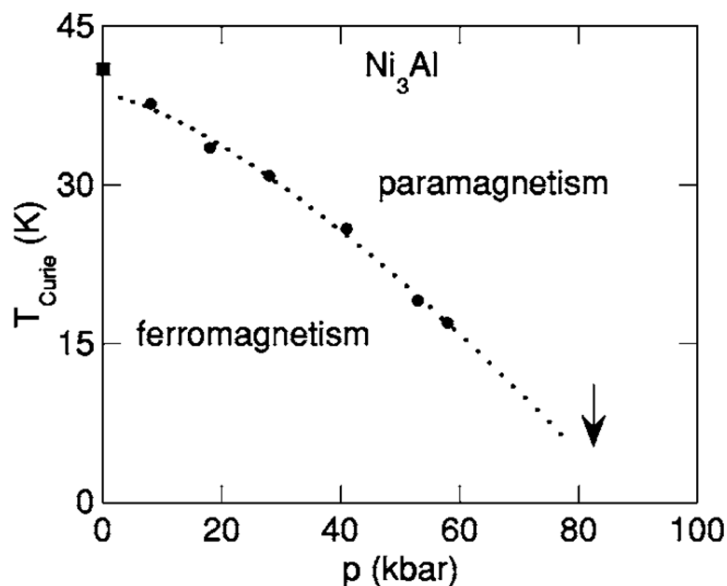


Figure 1.3.4: Pressure dependence of the ordering temperature for Ni_3Al taken from [9]. The Curie temperature T_C decreases monotonically with increasing pressure and was proposed to vanish at a critical pressure $p_c = 81$ kbar.

by a power law with an exponent around $3/2$. At temperatures below 1 K, however, discrepancies between the different publications are found. Steiner *et al.* [66] found variations in the low temperature behaviour of the resistivity for different stoichiometric Ni_3Al samples, which gives evidence that the low temperature behaviour of the resistivity is extremely sensitive to the way the samples are prepared and might consequently not reflect the behaviour of an ideally ordered sample. Fluitman *et al.* [56] find that the exponent of $3/2$ stays constant down to $T = 200$ mK, whereas Niklowitz *et al.* [9] report a T^2 behaviour of the resistivity below a characteristic temperature T_{FL} , which has a negative pressure dependence. As T_{FL} remains finite at the critical pressure p_c , the authors argue that the phase transition might be first order and consequently not in agreement with a QCP.

1.3.4 $\text{CeSi}_{1.81}$ and $\text{CePd}_{1-x}\text{Rh}_x$

As discussed in the previous paragraphs all systems for which a QCP was proposed so far turned out to show a first order phase transition for $T \rightarrow 0$ after more detailed investigation. However, the search for ever new systems which might exhibit quantum criticality goes on and a wide range of substances is being studied for their low temperature behaviour.

$\text{CePd}_{1-x}\text{Rh}_x$

Several f -electron based antiferromagnetic Kondo lattice (KL) systems have recently been shown to exhibit a QCP by tuning of concentration or hydrostatic pressure [5]. In contrast to that, there exist only a few ferromagnetic KL systems [72]. However, these systems are also candidates to show a QCP. For this reason the magnetic properties of $\text{CePd}_{1-x}\text{Rh}_x$ have been studied close to $T = 0$.

Pure CePd orders ferromagnetically at a Curie temperature of $T_C = 6.6$ K. The transition temperature can be decreased by doping with Rh and is found to vanish at $x_c \approx 0.87$ and the system crystallises in

the orthorhombic CrBr structure independent of the Rh concentration. The $T_C(x)$ phase diagram shows a change in curvature from negative to positive and a long tail for $x \rightarrow x_c$, which might, however, be caused by smearing of the phase transition due to the disorder present in the system as proposed by theoretical calculations [73].

Pronounced NFL behaviour of the specific heat, thermal expansion, magnetisation and susceptibility are found [74, 75], however, the Grüneisen ratio Γ does not diverge for $T \rightarrow 0$ as would be expected for the case of a QCP [75]. Instead a new type of ferromagnetic order appears near quantum criticality at $x \geq 0.65$: A Kondo-cluster-glass, which embodies the formation of ferromagnetic clusters as a result of the disorder in the system. These clusters undergo a glassy freezing at low temperatures and hence show a magnetically inhomogeneous state at mesoscopic scales. It has been proposed that these clusters are the manifestation of a quantum Griffiths phase [76].

CeSi_{1.81}

Depending on the Si concentration x , the heavy fermion system CeSi _{x} changes from an antiferromagnetic ground state for $x = 1$ via a ferromagnetic ground state just below $x = 1.85$ to paramagnetism for $1.85 < x < 2$ [77]. In the ferromagnetic regime CeSi _{x} crystallises in the orthorhombic structure, whereas a transition to a tetragonal structure is found for $x < 1.75$ [78]. The magnetisation of single crystalline samples of the ferrimagnetic CeSi_{1.81} has been studied by Drotziger *et al.* [79] and Löhneysen *et al.* [80]. At ambient pressure CeSi_{1.81} exhibits ferromagnetic order below 9.5 K. By application of hydrostatic pressure the ordering temperature can be reduced and is found to vanish presumably in a second order manner at a critical pressure of $p_c \approx 13$ kbar.

Of all systems discussed so far, CeSi_{1.81} is the only remaining candidate for a QCP. However, the pressure studies discussed above have been performed at lowest temperatures of 1.7 K which is – on the energy scale of weak ferromagnetism – still far away from absolute zero. Lacking studies at lower temperatures currently inhibit the doubtless identification of a QCP. Furthermore, Löhneysen *et al.* [80] report on step-like features in the hysteresis curves which vanish at higher temperature and higher pressures. These features might indicate that the ferromagnetic order at low temperatures is more complicated and shows another example of new magnetic textures.

Chapter 2

Theoretical Background of Experimental Techniques

In this chapter a brief overview of the fundamental physical properties of the neutron and the resulting interaction with matter will be given. One method that makes use of this interaction is neutron attenuation radiography. In addition to the nuclear interaction the neutron has a magnetic moment, which gives rise to a magnetic interaction of a polarised neutron beam with magnetic fields or magnetic samples. We will discuss the principle of the neutron depolarisation technique - a method based on the analysis of the polarisation of a neutron beam transmitted through a ferromagnetic sample. Combining the two methods – neutron radiography and neutron depolarisation – will finally lead us to the neutron depolarisation imaging technique (NDI), which can give information on the variation of the magnetic properties of a sample on a sub-millimetre length scale. By additionally rotating the sample one can furthermore perform neutron depolarisation tomography, which will be shown at the end of this chapter.

2.1 Properties of the Neutron and its Interaction with Matter

The neutron is a spin-1/2 particle with a zero net charge, a mass of $m = 1.67495 \cdot 10^{-27}$ kg and a magnetic moment of $\mu_n = -1.913$ nuclear magnetons. Due to some favourable fundamental properties – in particular the zero charge – neutrons are nowadays a widely established probe for the investigation of condensed matter.

Neutron beams are typically produced in either research reactors or spallation neutron sources. Both of these produce high energy neutrons in the MeV regime, which are then moderated down to thermal or cold energies, where their kinetic energy is comparable to the thermal energy of particles with a temperature of ≈ 300 K or ≈ 30 K, respectively. Thermal neutrons have a velocity v of typically several thousands of metres per second, which can be calculated from their energy E by $v = \sqrt{2E/m}$. This is slow enough to be monochromatised or chopped with mechanical devices like velocity selectors or choppers, which will be discussed in (3.1.1).

Of even greater importance is the fact, that the deBroglie wavelength $\lambda = h/mv = h\sqrt{2mE}$ of such low energy neutrons is of the order of magnitude of the interatomic distances in condensed matter, giving rise to interference effects in scattering experiments, which can help to reveal the structure of a sample.

At the same time, dynamics (i.e. collective excitations like phonons and magnons) in condensed matter often have the same energy scale as thermal neutrons. This makes neutrons an ideally suited probe for the investigation of structure and dynamics of condensed matter.

As stated above, the neutron has a zero net charge, and consequently it does not interact with the Coulomb potential of an atom, which leads to a high penetration of neutrons in many materials. In contrast to that, photons – which also have zero charge – interact with the charge of the nucleus and the electrons via their electromagnetic field. This interaction is based on scattering of the photons on the charge density of the electrons around the nucleus. The scattering cross section of photons increases monotonically with increasing atomic number Z and is proportional to Z^2 . Therefore, the penetration of photons decreases with increasing atomic number.

The interaction between the neutron and an atom via the nuclear interaction has a very short range compared to the Coulomb interaction, which therefore leads to a high penetration depth of neutrons in many materials. Furthermore, the absorption coefficient for neutrons rather depends on the constitution of the nucleus than on the atomic number Z . As a consequence, the neutron absorption coefficient shows strong variations even for isotopes of the same element. As an example, the neutron absorption coefficient of hydrogen ${}^1_1\text{H}$ for thermal neutrons is approximately 650 times larger than for deuterium ${}^2_1\text{H}$.

Even though the neutron does not have a net charge it consists of three charged quarks and consequently has a nuclear magnetic moment. The interaction of this magnetic moment with the spins of the unpaired electrons in magnetic substances can be used to reveal information about the magnetic properties of a sample. Such information can either be obtained from polarised neutron scattering experiments or from the alteration of the polarisation of a neutron beam after transmission of a sample.

Exponential Attenuation Law

The interaction of neutrons with matter leads to a decrease of the intensity in the direct beam transmitted through the sample. Upon the transmission of an infinitesimally thin piece of matter a neutron beam of intensity I will be attenuated by a factor dI , which is proportional to the incoming intensity and the thickness dx

$$dI = -\mu I dx. \quad (2.1.1)$$

The factor μ , which depends on the isotope and the wavelength of the neutrons is called total attenuation coefficient. Integrating this equation within the boundaries I_0 to I and 0 to d one obtains the exponential attenuation law, which relates the intensities of the beam before and after transmission of a sample

$$I = I_0 \exp(-\mu d). \quad (2.1.2)$$

It follows that the intensity transmitted through the compound decreases exponentially with its thickness in the most simple case.

Total Mass Attenuation Coefficient

Relating the decrease of intensity to the mass, one can define the so called total mass attenuation coefficient, which is defined as $\mu_m = \mu/\rho$. With this coefficient the exponential attenuation law reads

$$I = I_0 \exp(-\mu_m \rho d) = I_0 \exp(-\mu_m \frac{m}{Ad}) = I_0 \exp(-\mu_m \rho_f), \quad (2.1.3)$$

where A is the area of the cross section and $\rho_f = \frac{m}{A}$ is the mass per area. This description has the advantage that the mass attenuation coefficient is independent of the physical condition of the absorbing material, i.e it does not matter whether it is in the gaseous or solid state or which temperature it has.

If the absorber is not a single isotope, the total mass attenuation coefficient is additively composed of the contributions of the isotopes in the absorber. If a compound is composed of N isotopes, each isotope i of which has a mass fraction α_i of the compound, the total mass attenuation coefficient is

$$\mu_m = \sum_{i=1}^N \alpha_i \mu_{m_i}, \quad (2.1.4)$$

with $\sum_{i=1}^N \alpha_i = 1$.

The total mass attenuation coefficient of a single isotope is additively composed of the contributions of different physical mechanisms of interaction. The most significant contributions for neutron radiography are the scattering coefficient μ_{sc} and the absorption coefficient μ_{abs} , which again are composed of different parts which depend strongly on the energy of the neutrons as well as on their polarisation. The scattering coefficient consists of the nuclear and the magnetic scattering cross section, both of which have a coherent and an incoherent part.

2.2 Neutron Imaging

Descriptively spoken, radiography is the recording of transmission images of an object under and irradiation angle θ , where the object has a spatial distribution of the attenuation coefficient $\mu(x, y)$. By recording a sufficient number of projections under different projection angles θ it is possible to reconstruct a 2D model of $\mu(x, y)$. This technique is called tomography.

2.2.1 Attenuation Radiography

The resulting transmission of the neutron beam through a sample is given by the line integral of the neutron attenuation coefficient along the transmission path through the sample.

Let us first consider the radiation to be monoenergetic, that is we neglect the energy dependence of μ . Additionally we assume a parallel beam geometry. One measures the transmission I/I_0 of the beam along a straight line s through an object as shown in Fig. 2.2.1 (left). This can be calculated from the integral of the attenuation of the beam along the trajectory s .

$$\frac{I}{I_0} = \exp\left(-\int_s \mu(x, y) ds\right) \quad (2.2.1)$$

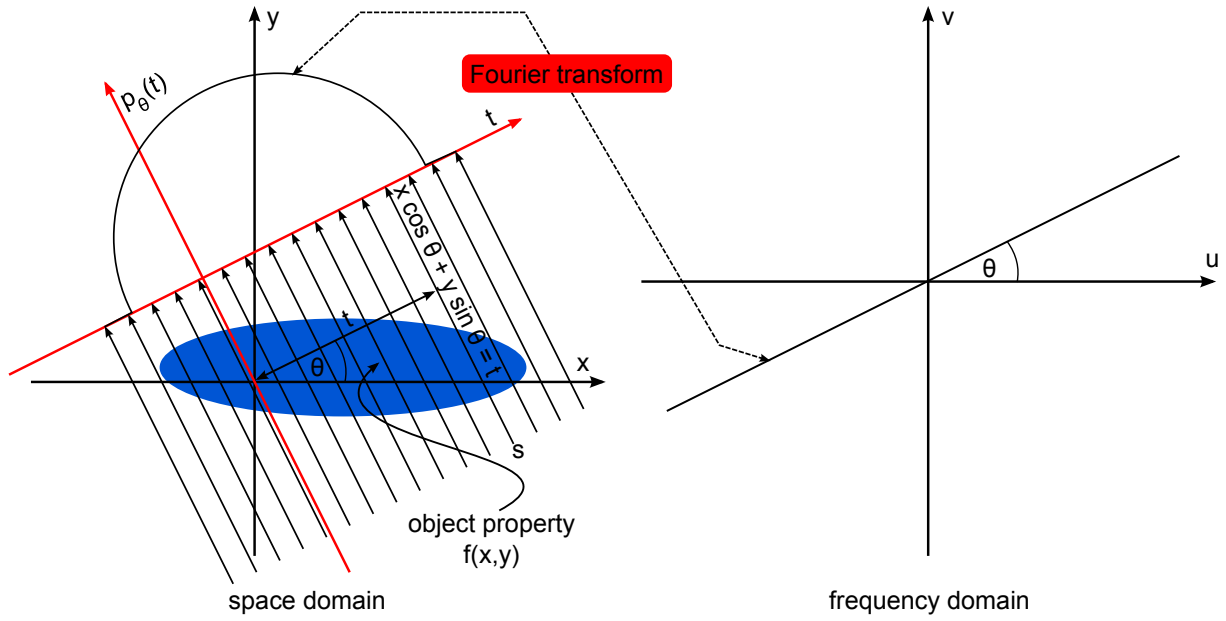


Figure 2.2.1: The geometry for recording a projection $p_\theta(t)$ under the angle θ in a parallel beam geometry along the line s (left). The Fourier Slice Theorem says that the 1D Fourier transform of this projection corresponds to a line in the frequency domain of the 2D Fourier transform of the object property $f(x,y)$ (right).

Taking the logarithm of this formula, the measured value is the integral of the attenuation coefficient along line s .

$$\lambda = -\ln \frac{I}{I_0} = \int_s \mu(x,y) ds \quad (2.2.2)$$

All points for which $x \cos \theta + y \sin \theta = t$ applies, with θ being the angle between the beam and the x -axis and t the distance of the beam from the origin, lie on this line. Measuring the value of λ for all values of t for a certain projection angle θ yields the projection of the attenuation coefficient $\mu(x,y)$ under the angle θ . Using the Dirac delta function this can be written as

$$p_\theta(t) = \lambda(\theta, t) = \iint_{-\infty}^{\infty} \mu(x,y) \delta(x \cos \theta + y \sin \theta - t) dx dy. \quad (2.2.3)$$

Of course this implies the loss of all information about the variation of the attenuation coefficient μ along the line s . The expression on the right side of equation (2.2.3) is called *radon transformation* of $\mu(x,y)$. Consequently the process of measuring a projection $p_\theta(t) = \lambda(\theta, t)$ is equivalent to performing the radon transformation of the attenuation coefficient $\mu(x,y)$.

2.2.2 Attenuation Tomography

Tomography is based on the measurement of many projections $p_\theta(t)$ of an object property $f(x,y)$ under different angles θ . As will be discussed in 2.6, this object property does not necessarily have to be the attenuation coefficient $\mu(x,y)$. From the knowledge of an infinite number of projections $p_\theta(t)$

under all angles θ the information about the variation of $\mu(x, y)$, which is lost by performing the radon transformation, can be retrieved.

Mathematically this is based on the *Fourier Slice Theorem*, which correlates the projections under all angles with the spatial distribution of the object property $f(x, y)$ [81]. More accurately the Fourier Slice Theorem reads:

The one-dimensional Fourier transform $P_\theta(w)$ of a parallel projection $p_\theta(t)$ of an object property $f(x, y)$ under an angle θ represents a line in the two-dimensional Fourier transform $F(u, v)$ of the object property, which includes an angle θ with the u -axis.

This is shown more descriptively in Fig. 2.2.1 (right). This theorem means that if all projections under all angles θ are known, then all lines under all angles in the 2D Fourier transform of the object property are known as well. This is equivalent to the complete knowledge of this 2D Fourier transform. In formulae the Fourier-slice-theorem reads:

$$P_\theta(w) = \mathcal{F}_{1D}(p_\theta(t)) = F(u, v) = \mathcal{F}_{2D}(f(x, y)) \quad (2.2.4)$$

The spatial distribution of $f(x, y)$ can thus be simply obtained by performing the inverse 2D Fourier transform of $P_\theta(w)$.

$$f(x, y) = \mathcal{F}_{2D}^{-1}(\mathcal{F}_{1D}(p_\theta(t))) \quad (2.2.5)$$

In a real experiment one can of course never measure an infinite number of projections. However, by determining the value of the projections at a sufficient number of pixels and under a sufficient amount of angles one can replace the Fourier transform in (2.2.5) by a discrete Fourier transform. Special care has to be taken in this case when the coordinate transformation of the measured projections to a quadratic grid is performed to account for the higher information density in the center of the coordinate system shown in Fig. 2.2.1 (right), which represents low spatial frequency. This procedure is called *filtered back projection*. A more detailed and very informative discussion of the fundamental principles of computerised tomography can be found in [81].

2.3 Polarised Neutrons

The neutron is a particle with a spin quantum number $s = 1/2$. The spin can be described as a vector operator \vec{s} for which only one component along an arbitrary coordinate axis can be determined independently. However, for a neutron beam composed of a large number of neutrons one can obtain the expectation value $\langle \vec{s} \rangle$ of the neutron spin in all three spatial directions by successive measurement of the three independent components. If this expectation value for a neutron beam differs from zero one calls the neutron beam polarised. The polarisation vector \vec{P} of the beam is then defined as the expectation value of the neutron spin divided by its maximum value

$$\vec{P} = \frac{\langle \vec{s} \rangle}{1/2} = 2 \left(\langle s_x \rangle \vec{i}_x + \langle s_y \rangle \vec{i}_y + \langle s_z \rangle \vec{i}_z \right), \quad (2.3.1)$$

where \vec{i}_x, \vec{i}_y and \vec{i}_z are unit vectors along the three coordinate axes of an arbitrary coordinate system. The polarisation of a beam along one coordinate axis can be determined by measuring the intensities I_+ of the neutrons with a positive and I_- with a negative spin component along this direction. The polarisation

along this direction i is then given by

$$P_i = \frac{I_{i+} - I_{i-}}{I_{i+} + I_{i-}}. \quad (2.3.2)$$

As a measure of the polarising efficiency of a polarised neutron setup without a sample in place one frequently uses the flipping ratio, which is defined as

$$R = \frac{1 + P}{1 - P}. \quad (2.3.3)$$

If a neutron passes through a homogeneous magnetic field \vec{B} , the direction of the neutron spin is changed and obeys the classical equation of motion of a magnetic moment in a homogeneous magnetic field

$$\frac{d\vec{s}}{dt} = \gamma (\vec{s} \times \vec{B}), \quad (2.3.4)$$

where γ is the gyromagnetic ratio of the neutron and is given by $\gamma = g_n \mu_o \mu_B = 1.83 \cdot 10^8 \text{ s}^{-1} \text{ T}^{-1}$. This equation is also valid for the expectation value of the spin $\langle \vec{s} \rangle$ and thus also for the polarisation \vec{P}

$$\frac{d\vec{P}}{dt} = \gamma (\vec{P} \times \vec{B}). \quad (2.3.5)$$

The solution for this equation of motion is a precession of the polarisation vector \vec{P} around the direction of the magnetic field \vec{B} in the plane perpendicular to the magnetic field. This means that the component of the polarisation vector which is parallel to \vec{B} is conserved, while the component of \vec{P} which is perpendicular to \vec{B} rotates around the field vector in a plane perpendicular to the field. The neutron spin precession is shown in Fig. 2.4.1 (left). The frequency ω of the precession is called the Larmor frequency and is given by $\omega = \gamma B$. The solution for this differential equation, which gives the time and field dependence of the polarisation vector reads

$$\vec{P}(t) = \vec{P}(0) \cos \omega t - (\vec{P}(0) \times \vec{n}) \sin \omega t + (\vec{P}(0) \cdot \vec{n}) \vec{n} (1 - \cos \omega t). \quad (2.3.6)$$

Here \vec{n} is a unit vector pointing in the direction of the magnetic field $\vec{n} = \vec{B}/B$.

2.4 1D and 3D Neutron Depolarisation Technique

When a beam of polarised neutrons is transmitted through an unmagnetised, ferromagnetic material it will generally be depolarised due to the Larmor precession of the neutron spin in the local magnetic field inside the domains of random orientation within the sample. In polarised neutron scattering experiments this depolarisation is an unwanted effect. However, important information about the magnetic properties of a sample can be obtained by analysing the amount of depolarisation the beam suffers after transmission of the sample. Halpern and Holstein [82] developed a theory already in 1941 which describes the depolarisation of a neutron beam due to the transmission through ferromagnets. The authors only dealt with the analysis of the polarisation in one spatial dimension and predicted that the results of such neutron depolarisation measurements would reveal information about the mean domain sizes and the type of domain structure in the material. First experiments with this method were published by Burgy *et al.* in 1950 [83].

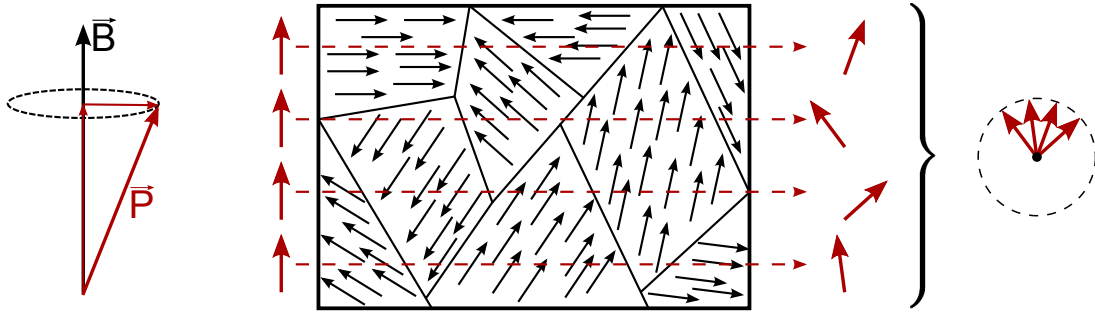


Figure 2.4.1: Schematic view of the precession of the beam polarisation \vec{P} around a magnetic field \vec{B} (left). Descriptive picture of the neutron depolarisation on transmission of a ferromagnet with randomly oriented domains (right). Each neutron sees a different field constellation during the transmission of the material which leads to an effective precession angle. Spatially averaging over the different transmission paths leads to an effective depolarisation of the beam.

The depolarisation technique was extended to the analysis of the depolarisation of the beam in all three spatial directions by Rekveldt *et al.* in 1973 [84]. Such 3D neutron depolarisation experiments additionally provide directional information about the domain structure of the sample, i. e. the mean direction cosines of the local magnetisation and the direction of a net magnetisation of the sample.

A descriptive picture of the effect of neutron depolarisation due to the transmission of a ferromagnetic material with randomly oriented domains is given in Fig. 2.4.1. The polarised beam penetrates the sample from left to right. In each domain the neutron spin precesses around the local magnetic field vector. Along its transmission path through the sample, each neutron sees a particular field sequence which leads to a certain precession angle of the neutron spin after the sample. Spatially averaging over the various transmission paths results in an effective depolarisation of the beam as indicated at the right-hand side of the bracket.

In the following we will first discuss the principle of the 1D neutron depolarisation technique, which is the basis for the NDI technique introduced in this thesis. After that an overview of the 3D technique will be given, which can generally be extended as well to provide spatially resolved information about the sample. However this procedure would require very long experiment times due to the measurement of the beam polarisation in all three spatial directions. Furthermore, the spatial resolution would be limited by the minimum length of additional polarisation manipulators between sample and detector.

Neutron Depolarisation in one Dimension

In this paragraph the neutron depolarisation in one spatial dimension will be discussed following the theory of Halpern and Holstein [82]. In their classical approach they treated the ferromagnetic sample as a sequence of domains ($1 \dots i \dots n$), each of which has a local magnetic field \vec{B}_i , which is constant in direction and magnitude. As shown in 2.3 the classical equation of motion for a neutron spin \vec{s} in a magnetic field is given by

$$d\vec{s}_i/dt = \gamma \vec{s}_i \times \vec{B}_i(\vec{r}) \quad (2.4.1)$$

and describes the precession of the spin around the magnetic field inside the domain. This means that the component of the spin $\vec{s}_{\parallel,i}$ parallel to the magnetic field is conserved ($\vec{s}_{\parallel,i} = \vec{s}_{\parallel,i-1}$), whereas the component $\vec{s}_{\perp,i}$ of the spin perpendicular to the field rotates in a plane perpendicular to the magnetic

field vector with the angular velocity $\omega = \gamma B_i$. Here $B_i = \sqrt{\vec{B}_i \cdot \vec{B}_i}$. This rotation can be written as

$$\vec{s}_{\perp,i} = \vec{s}_{\perp,i-1} \cos(\gamma B_i t_i) + \vec{s}_{\perp,i-1} \times \vec{B}_i / B_i \sin \gamma B_i t_i, \quad (2.4.2)$$

where t_i is the time the neutron spends in the i th domain. Writing

$$\vec{s}_{\parallel,i-1} = (\vec{s}_{i-1} \cdot \vec{B}_i) \cdot \vec{B}_i / B_i^2 \quad \text{and} \quad \vec{s}_{\perp,i-1} = \vec{s}_{i-1} - \underbrace{(\vec{s}_{i-1} \cdot \vec{B}_i) \cdot \vec{B}_i / B_i^2}_{\vec{s}_{\parallel,i-1}} \quad (2.4.3)$$

yields a simple expression for $\vec{s}_i = A_i \vec{s}_{i-1}$, with the dyadic A_i

$$A_i = \frac{\vec{B}_i \vec{B}_i}{B_i^2} + \left(1 - \frac{\vec{B}_i \vec{B}_i}{B_i^2}\right) \cos(\gamma B_i t_i) - \sin \gamma B_i t_i \frac{\vec{B}_i \times}{B_i}. \quad (2.4.4)$$

In order to find the resulting rotation of the spin \vec{s}_f after transmission of the sample along one specific path, one has to calculate the effective rotation of the spin by the sequence of the domains ($1 \dots i \dots n$) along this path. Using the dyadic formalism developed above this can simply be written as $\vec{s}_f = A_n \dots A_i \dots A_1 \vec{s}_0$. This only describes a rotation of the spin, whereas the magnitude of the spin is conserved. The depolarisation of the beam results from averaging over the effective rotations of the spin along different transmission paths through the sample (cf. Fig. 2.4.1). This averaging process can only be evaluated analytically if some assumptions on the domain structure are made. If one assumes that there is no statistical interconnection between the different \vec{B}_i in the domains and that they are randomly oriented one can independently average over all A_i and finds

$$\langle A_i \rangle = \frac{1}{3} + \frac{2}{3} \cos(\gamma B_i t_i) = 1 - \frac{4}{3} \sin^2\left(\frac{1}{2} \gamma B_i t_i\right) \quad (2.4.5)$$

and

$$\vec{s}_f = \langle A_n \rangle \dots \langle A_0 \rangle \vec{s}_0 = \prod_i \left(1 - \frac{4}{3} \sin^2\left(\frac{1}{2} \gamma B_i t_i\right)\right) \vec{s}_0. \quad (2.4.6)$$

Now there exist two limiting cases for which eq. 2.4.6 can be solved analytically. These depend on the domain sizes and therefore the precession angle of the spin within the single domains.

a) $\frac{1}{2} \gamma B_i t_i \ll 1$

In this case one can use the series expansion of the sine and obtains

$$\prod_i \left(1 - \frac{4}{3} \sin^2\left(\frac{1}{2} \gamma B_i t_i\right)\right) \simeq \prod_i \left(1 - \frac{1}{3} \gamma^2 B_i^2 t_i^2\right) \simeq \exp\left(-\frac{1}{3} \gamma^2 \sum_i B_i^2 t_i^2\right), \quad (2.4.7)$$

which yields for the component of \vec{s}_f parallel to the analysing direction

$$s_f = s_0 \exp\left(-\frac{1}{3} \gamma^2 \langle B^2 \rangle T t\right), \quad (2.4.8)$$

where T is the total time spent in the sample and t is the average time the neutron spends in a single domain. Rewriting this in terms of the transmission length d of the sample, the average domain size δ

and the neutron velocity v this expression reads

$$s_f = s_0 \exp\left(-\frac{1}{3}\gamma^2 \langle B^2 \rangle \frac{d\delta}{v^2}\right) \quad (2.4.9)$$

b) $\frac{1}{2}\gamma B_i t_i \geq 1$

In this case the order of magnitude without regarding numerical factors is given by

$$s_f = \prod_i \left(1 - \frac{4}{3} \sin^2\left(\frac{1}{2}\gamma B_i t_i\right)\right) s_0 \simeq \left(1 - \frac{4}{3} \sin^2\left(\frac{1}{2}\gamma B_i t_i\right)\right)^{T/t_{Av}} s_0 \simeq \left(\frac{1}{3}\right)^{T/t} s_0 \simeq e^{-d/\delta} s_0. \quad (2.4.10)$$

Halpern and Holstein state “The physical distinction between the two cases arises from the fact that, when $\frac{1}{2}\gamma B_i t_i \ll 1$, the depolarisation is produced by a succession of small rotations the magnitude of which is given by the quantity $\gamma B_i t_i$ whereas, when $\frac{1}{2}\gamma B_i t_i > 1$, the rotation in each domain is so large that the component of the initial spin perpendicular to B_i , $\vec{s}_{\perp,i-1}$, averages out to zero, leaving only the parallel component $\vec{s}_{\parallel,i}$, the magnitude of which is independent of $\gamma B_i t_i$. Since the average of $\vec{s}_{\parallel,i-1}$ over all directions of the field is $\frac{1}{3}s_{i-1}$ the depolarisation factor is $\frac{1}{3}$ per domain or $3^{-n} = 3^{-d/\delta}$ for the whole specimen.”

Neutron Depolarisation in Three Dimensions

Even though all measurements in this thesis were done with the one dimensional neutron depolarisation technique, we will briefly discuss its extension to the determination of the neutron depolarisation in all three spatial directions. This means that the initial beam polarisation before the sample must be aligned parallel to all three coordinate axes, respectively by means of a polarisation rotator and the polarisation after the sample is then analysed in all three spatial directions with a similar rotator. This method yields a 3×3 depolarisation matrix from which much more detailed information about the magnetic properties of the sample can be obtained than from the one dimensional method. However, for this method, one needs a space consuming zero field region and polarisation rotators around the sample. As we will see in section 2.5, the spatial resolution of our method is limited by the distance between sample and detector, which would be drastically increased by the zero field region and polarisation rotators. Furthermore, for the measurement of all elements of the 3×3 depolarisation matrix, the measurement times would be increased by a factor of nine.

The three dimensional neutron depolarisation technique was developed by T. Rekveldt in 1972 [85, 84] and will be briefly introduced here¹ following a discussion in [25].

The 3×3 depolarisation matrix D gives the relation between the polarisation \vec{P}_0 before and \vec{P}_1 after transmission of the sample:

$$\vec{P}_1 = D\vec{P}_0 \quad (2.4.11)$$

As said above the polarisation rotators before and after the sample can turn the polarisation vector parallel and antiparallel to each of the coordinate axes x, y and z respectively. The matrix element D_{ij}

¹It should be noted that this approach describes the depolarisation of the beam in terms of a classical precession of the neutron spin within the domains in the sample. Another approach is to use a quantum mechanical description of the depolarisation as a result from small angle scattering by magnetic inhomogeneities [86, 87]. Both approaches yield the same results and were proven to be equivalent [88].

(where i, j can be x, y or z respectively) of the depolarisation matrix can then be calculated from the measured intensities with

$$D_{ij} = \frac{1}{P_0} \frac{I_S - I_{ij}}{I_S}, \quad (2.4.12)$$

where P_0 is the polarisation measured without the sample in place and I_{ij} are the intensities measured at the detector with the polarisation before the sample being rotated to the i -direction and being analysed in the j -direction behind the sample. The so called shim intensity I_S is the intensity of the unpolarised beam, which can be determined from

$$I_S = \frac{I_{ij} + I_{-ij}}{2}. \quad (2.4.13)$$

We will now discuss the relation between the measured elements D_{ij} and the magnetic properties of the sample. Therefore we define the correlation matrix

$$\alpha_{ij} = \left\langle \int_0^d dx' \Delta B_i(x, y, z) \Delta B_j(x', y, z) \right\rangle, \quad (2.4.14)$$

where $\Delta \vec{B}(\vec{r}) = \vec{B}(\vec{r}) - \langle \vec{B} \rangle$ is the variation of the local magnetic induction and the integral goes over the transmission length d of the neutron through the sample. The angular brackets are a spatial average over the sample volume and result from an averaging process comparable to the one used in (2.4.6). The correlation functions α_{ij} describe the mean correlation between $\Delta B_i(\vec{r})$ and $\Delta B_j(\vec{r})$ along the transmission path of the neutron through the sample averaged over the cross section of the beam.

If we assume that $\alpha_{ij} = 0$ for $i \neq j$ (if this is not the case, α must be diagonalised first) we can furthermore define a correlation function ξ as the trace of α :

$$\xi = \text{Tr}(\alpha) = \sum_i \alpha_{ii}. \quad (2.4.15)$$

The correlation function ξ is proportional to the mean correlation length along the neutron path.

If $\langle \vec{B} \rangle = 0$, which means that there is no macroscopic magnetisation of the sample, it can be shown that the depolarisation matrix is diagonal and reads

$$D_{ii} = \exp\left(-(\gamma^2/v^2)d\{\xi - \alpha_{ii}\}\right), \quad i = x, y, z \quad (2.4.16)$$

with $\gamma = 1.83 \cdot 10^8 \text{ s}^{-1} \text{ T}^{-1}$ being the gyromagnetic ratio of the neutron and v its velocity. This is of similar form as the result obtained in (2.4.9) for the one dimensional case, where effectively only D_{zz} is measured.

For the case of a non-zero net magnetisation of the sample ($\langle \vec{B} \rangle \neq 0$), the polarisation vector additionally undergoes a rotation in the plane perpendicular to the direction of the mean magnetisation. The angle of rotation ϕ is obtained from the net magnetisation $\langle M \rangle$ by

$$\phi = \frac{\gamma}{v} L \mu_0 \langle M \rangle = \frac{\gamma}{v} d \mu_0 M_S \langle m \rangle, \quad (2.4.17)$$

where $\langle m \rangle$ is the reduced magnetisation of the sample, which is given by the ratio between the net magnetisation $\langle M \rangle$ of the sample and the saturation magnetisation M_S by $\langle m \rangle = \langle M \rangle / M_S$. To explicitly write down the matrix elements, let us now assume that the mean magnetisation of the sample $\langle M \rangle$ is aligned along the z direction. In this case and with assuming $\phi \ll (\gamma/v)^2 |\alpha_{xx} - \alpha_{yy}| d/2$ (the weak

damping limit) the elements of the depolarisation matrix read

$$\begin{aligned}
 D_{xx} = D_{yy} &= e^{-(\gamma^2/v^2)d\{\xi - (\alpha_{xx} + \alpha_{yy})/2\}} \cos \phi \\
 D_{xy} = -D_{yx} &= e^{-(\gamma^2/v^2)d\{\xi - (\alpha_{xx} + \alpha_{yy})/2\}} \sin \phi \\
 D_{zz} &= e^{-(\gamma^2/v^2)d\{\xi - \alpha_{zz}\}} \\
 D_{xz} = D_{zx} = D_{zy} = D_{yz} &= 0.
 \end{aligned} \tag{2.4.18}$$

With these measured values the angle ϕ of the rotation of the beam polarisation can be calculated from

$$\phi = \arctan \left(\frac{D_{xy} - D_{yx}}{D_{xx} + D_{yy}} \right) \tag{2.4.19}$$

and ξ is obtained from

$$\xi = -v^2 \ln \{ \det D \} / 2\gamma^2 d. \tag{2.4.20}$$

Another very important information that can be obtained about the sample from 3D depolarisation measurements are the mean-square direction cosines γ_i ($i = x, y, z$) of the orientation of the magnetic induction vector inside the domains. This means that from these quantities a preferred orientation (i.e. an easy axis) of the magnetisation in the domains can be found. These direction cosines can be calculated from $\gamma_i = \alpha_{ii}/\xi$ and are given by

$$\gamma_i = 1 - 2 \ln D_{ii} / \ln \{ \det D \}. \tag{2.4.21}$$

However, this equation only holds for those directions that have no net rotation of the beam polarisation.

The big advantage of the 3D depolarisation technique is that it can be applied to samples with a net magnetisation and that a **rotation** of the spin can be **distinguished** from **depolarisation**, which is not easily possible with the 1D method. Furthermore it yields more detailed information about the domain structure of the sample, namely not only the mean domain size but also the mean-square direction cosines of the orientation of the domains.

2.5 Neutron Depolarisation Imaging

We will now describe the setup of a standard neutron radiography facility and show how it can be modified to allow for a spatially resolved measurement of the neutron depolarisation after transmission of the sample. With this extension one can measure the attenuation and the depolarisation of the beam at the same time.

As described in 2.2.1, neutron radiography is based on the measurement of the attenuation of a neutron beam along a straight line through the sample in a parallel beam geometry. However, in a practical setup one has to consider the fact that the neutron source, which is typically a reactor or a spallation source, is a more or less homogeneous source with a broad divergence of the beam. To achieve a quasi parallel beam with a reasonable intensity instead of a parallel beam, most facilities use a small pinhole close to the neutron source in combination with a long flight tube for the neutrons. This is called collimation of the beam. A schematic of a typical radiography setup is shown in Fig. 2.5.1 and consists of a collimator, a flight path, the sample position and a position sensitive detector.

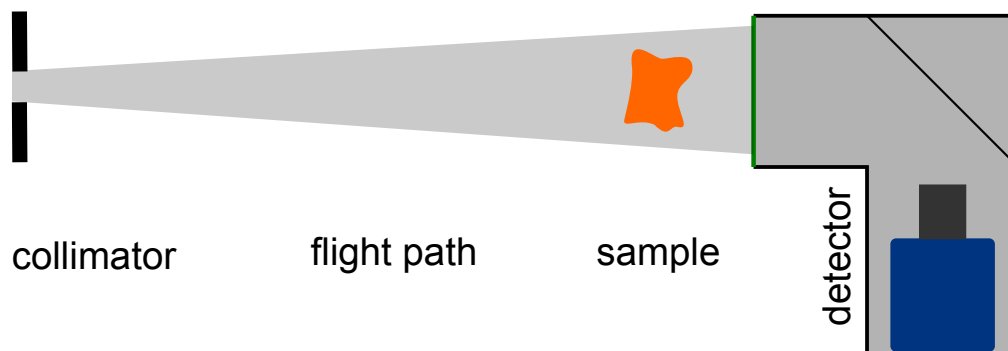


Figure 2.5.1: Schematic of the typical components of a neutron radiography facility. The setup consists of a collimator, a flight path, the sample and a position sensitive detector.

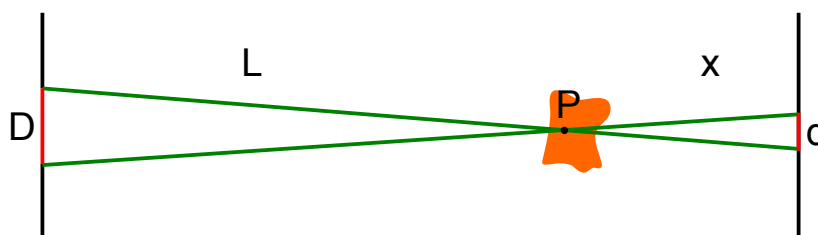


Figure 2.5.2: A point P in the sample is imaged on an area d at the detector due to the finite size D of the pinhole.

Due to the fact that a not perfectly parallel beam is used, a certain blurring is introduced in the transmission images recorded at the detector. As can be seen in Fig 2.5.2, a point P in the sample will be imaged onto a circular area² with a diameter d at the detector due to the finite diameter D of the pinhole. The resulting blurring at the detector can easily be calculated to be

$$d = x/(L/D), \quad (2.5.1)$$

where L is the length of the flight path between the pinhole and the sample, and x is the distance between sample and detector. The term generally known as L/D -ratio is frequently used as a measure for the collimation of the beam in a neutron radiography facility. Higher L/D -ratios mean better collimation and thus less blurring at the detector. Typical L/D -ratios at current facilities are in the range of 400...1000 [89, 90, 91, 92, 93]. One can see that the distance x between sample and detector must be kept reasonably small in order to achieve good resolution. This will become important for polarised neutron radiography, since a polarisation analyser and maybe even a polarisation rotator have to be placed between the sample and the detector, thus limiting the minimum distance x .

In order to extend a radiography setup to perform one dimensional polarisation analysis as shown in Fig 2.5.3, a neutron polariser, an analyser, a spin flipper and some guide fields have to be added. Ideally none of these devices should have an influence on the beam collimation, however this is not possible with most types of polarisers. The ideal choice of polarising and analysing devices will be discussed in 3.2. Since the depolarisation formulae derived in 2.4 are wavelength-dependent, it may additionally be desired to have a monochromatic neutron beam in order to obtain quantitative information about the mean domain sizes. Therefore, a monochromator or a neutron velocity selector needs to be installed

²The area is actually only circular in the case of a circular pinhole.

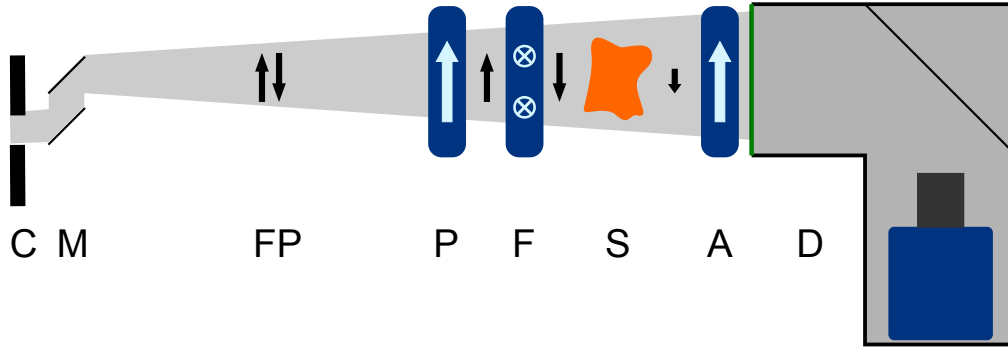


Figure 2.5.3: Schematic of a standard radiography setup extended for one dimensional polarisation analysis. The components are C: collimator, M: monochromator, FP: flight path, P: polariser, F: spin flipper, S: sample, A: analyser, D: detector.

before the polariser. This is the type of setup which was installed at the ANTARES beam line at FRM II. If a dedicated beam line were to be built, one could try to polarise and monochromatise the beam before the collimation. However, it must be considered that a polariser in the uncollimated beam leads to a severe gamma contamination due to the absorption of more than 50% of the neutron intensity. Furthermore, only a transmission polariser can be used since the structure of a reflection polariser would be imaged on the detector due to the pre-collimation of the beam introduced by the polariser. Further details on the polarisers will be discussed in 3.2.

With such a setup the intensities $I_+(x,y)$ and $I_-(x,y)$ of the neutron beam with polarisation parallel and antiparallel to the incoming beam polarisation can be measured at each pixel of the detector. Here $I_+(x,y)$ and $I_-(x,y)$ are the intensities measured with the spin flipper turned off and on, respectively. The spatial distribution of the beam polarisation after transmission of the sample is then calculated to be

$$P(x,y) = \frac{1}{P_0(x,y)} \frac{I_+(x,y) - I_-(x,y)}{I_+(x,y) + I_-(x,y)}, \quad (2.5.2)$$

where $P_0(x,y)$ is the polarisation of the beam measured without the sample in place. From this equation one can also determine the projection of the precession angle of the neutron polarisation in magnetic fields on the analysing direction. This method was used by Kardjilov et. al [94] to measure the field integral of the magnetic field of complex solenoids, as well as the precession of the neutron spin in trapped magnetic flux in superconductors. In the present work mainly the depolarisation of the beam due to the subsequent transmission of domains of different orientation in ferromagnetic materials was measured. Herefore it is important to note that the formulae developed in 2.4 imply a spatial average over the beam cross section. In the case of the NDI method this means that the cross section of one pixel (over which the beam polarisation will be averaged in the measurement) must be much larger than the average domain size. Such an averaging process is necessary to determine the depolarisation of the beam. If the pixel size were of similar size as the average domain size in the sample, only a rotation of the neutron spin but no depolarisation could be measured, since the depolarisation results from the average over different transmission paths through the sample. This fact might eventually limit the maximum spatial resolution, which is achievable with this method.

In principle it is also possible to extend the setup described above to a 3D depolarisation setup. As discussed in 2.4, three dimensional polarisation analysis requires the beam polarisation to be set to and analysed in all three spatial directions. Therefore, this technique additionally requires polarisation

rotators before and after the sample instead of only one π spin flipper before the sample as for a 1D setup. With these polarisation rotators the direction of the polarisation before the sample can be set parallel or antiparallel to all three coordinate axes, respectively. The rotator after the sample allows to analyse the polarisation in all three spatial directions. With these modifications, a spatially resolved measurement of the entire 3×3 depolarisation matrix D_{ij} from eq. (2.4.12) would be possible.

However, such a setup where the polarisation vector can have an arbitrary orientation with respect to the coordinate system does not allow for the installation of a guide field to conserve the direction of the beam polarisation as the neutrons travel through the instrument. This is not possible, since the neutron polarisation would precess around the direction of a constant guide field as soon as this is not parallel to the beam polarisation. Therefore, additionally a field free region around the sample and the polarisation rotators is required, in which the direction of the neutron polarisation is conserved independently of its orientation.

To measure all elements of this matrix, the required beam time would of course be increased by a factor of nine. What is even more important is that the field free region around the sample together with the polarisation rotators can at present not be built very compact for extended beam diameters. In practice this means that the minimum distance from sample to detector would in such a setup be increased to $x \approx 0.75$ m (for a comparable setup see i.e. the MUPAD polarimeter [95]). Such a large object to detector distance results in severe blurring of the images at the detector. With an L/D -ratio of 400 the blurring would be $d = 750 \text{ mm}/400 = 1.9 \text{ mm}$.

2.6 Neutron Depolarisation Tomography

An extremely interesting application of polarised neutron tomography would be the possibility to reconstruct the orientation of all domains within a sample. In contrast to standard absorption tomography, where a scalar quantity (the neutron attenuation coefficient) is reconstructed, this method requires the reconstruction of a vector quantity. This is not easily possible since the rotations of the neutron spin within the single domains do not commute, i.e. a different sequence of the same domains yields a different total rotation of the neutron spin. However, a modified algebraic reconstruction technique algorithm (ART) has been developed by Jericha *et al.* [96], which succeeds in reconstructing the orientation of a limited number of domains of a pre-defined shape for simulated data. In practice a major problem of this technique is that it requires the spatial resolution of the detector to be better than the domain size (typically several μm). However, current radiography setups (especially with polarisation analysis) do not fulfil this requirement.

In contrast to the reconstruction of the orientation of the domains within a sample, we will describe a method which succeeds in reconstructing the spatial distribution of the neutron depolarisation density ρ , which will be defined below and is a measure of the spin-flip probability. This technique does not require such a high spatial resolution and does furthermore not show the mathematical problems discussed above.

Standard neutron absorption tomography measures the integral of the neutron attenuation coefficient along the trajectory of the beam through the sample under many different projection angles θ .

$$p_{\theta}(t) = -\ln \frac{I}{I_0} = \int_s \mu(x, y) \, ds \quad (2.6.1)$$

Based on the Fourier-slice-theorem, which was discussed in (2.2.2), by the measurement of a sufficient amount of projections of $\mu(x,y)$ one can retrieve the information about the variation of $\mu(x,y)$ along the transmission path of the neutron. There exist standard algorithms which perform fast and accurate reconstruction of the 2D information about $\mu(x,y)$ from a set of measured projections.

We will now show that neutron depolarisation information can be reconstructed with the same algorithms if certain assumptions are made. Under the assumption that Eq. (2.4.9) is valid, the neutron beam polarisation shows an exponential decrease with sample thickness d .

$$P = P_0 \exp\left(-\frac{1}{3}\gamma^2 \langle B^2 \rangle \frac{\delta}{v^2} d\right) \quad (2.6.2)$$

By defining a neutron depolarisation density $\rho(x,y) := \frac{1}{3}\gamma^2 \langle B^2 \rangle \frac{\delta}{v^2}$ (equivalent to the neutron absorption coefficient $\mu(x,y)$ in the case of neutron absorption tomography) this equation is similar to the exponential attenuation law

$$\frac{P}{P_0} = \exp\left(-\int_s \rho(x,y) ds\right). \quad (2.6.3)$$

Just as above a projection of the neutron depolarisation can be measured under a certain angle θ

$$p_\theta(t) = -\ln \frac{P}{P_0} = \exp\left(-\int_s \rho(x,y) ds\right). \quad (2.6.4)$$

Therefore, the object property $\rho(x,y)$ can be reconstructed from the measured projections in exactly the same way as the neutron absorption coefficient. The main assumptions for the validity of Eq. (2.4.9) were that the rotation within the single domains of the sample is much smaller than 360° and that the orientation of the domains with respect to each other is random. However, the latter assumption is not very crucial since e.g. the existence of an easing axis in the sample only changes the pre-factor in the exponent in (2.4.9). Furthermore this equation contains a spatial average over the size of one pixel, which needs to be much larger than the average domain size as discussed in 2.5.

The depolarisation density $\rho(x,y)$ contains two variables. First, the average magnetic field inside the domains and thus the Larmor frequency of the spin precession may change from domain to domain. Second, the average domain size may vary over the sample volume, which in turn also influences the precession angle inside the domains. Consequently, only the product of both properties can be reconstructed.

In standard absorption tomography measurements one has to avoid the condition of zero-transmission, which happens when the intensity transmitted through the sample becomes too small to be detected. In this case, information about the magnitude of the attenuation coefficient is lost, which leads to artifacts in the reconstruction of the data. A similar condition occurs in neutron depolarisation tomography when the transmitted beam polarisation is zero, leading to the loss of information about the magnitude of the depolarisation density. In practice total depolarisation of the beam by the sample must therefore be avoided under all projection angles. In the measurements described in 5.2.4, this has been achieved by selecting a sufficiently high sample temperature, where the magnetisation m_s of the sample is small enough to avoid total depolarisation of the beam.

Chapter 3

The Neutron Depolarisation Setup

In this chapter all components of the setup used for polarised neutron imaging will be shown and their performance and application will be discussed. Most of the neutron depolarisation imaging experiments described in this work were performed at the radiography beam line ANTARES, which is not optimally suited for this type of measurements. A major problem at ANTARES is the high gamma contamination of the primary beam, which gives a large background especially in the case of low intensity monochromatic and polarised neutron imaging. This background manifests in white spots on the CCD detector which are mainly caused by scattered gamma radiation coming from the primary beam. The intensity of secondary gamma radiation generated by the sample, detector and beam stop is negligible in comparison to the primary gamma flux [97].

The ANTARES beam line consists of a collimator, which is partly inside and partly outside the biological shielding of the reactor. It is followed by an evacuated flight tube, which serves as a flight path for the neutrons to the sample position. This flight tube has a length of approximately 12m after which the neutrons enter the sample area, where the sample manipulator and detector are installed. An overview of the beam line and the installed components is shown in Fig. 3.0.1.

This setup was extended by several components to adapt it to the requirements for polarised neutron imaging. A monochromator was installed in the remaining space of approximately 80cm between the collimator and the flight tube. At this position several other instruments like beam filters, multi aperture holes and an x-ray tube had already been installed, making the installation of the monochromator very difficult due to the extremely limited space. The construction and performance of the monochromator will be discussed in detail in 3.1.

The entire neutron depolarisation setup consists of polariser, analyser, spin flipper, cryostat and detector and was installed inside the sample area (cf. Fig. 2.5.3 for a schematic of all components of the setup). It would have been beneficial to install the polariser as close as possible to the monochromator and install guide fields to the sample area, however, this could not be realised due to the limited space at the monochromator position. The components of the neutron depolarisation setup will be discussed in detail in 3.2 to 3.4.

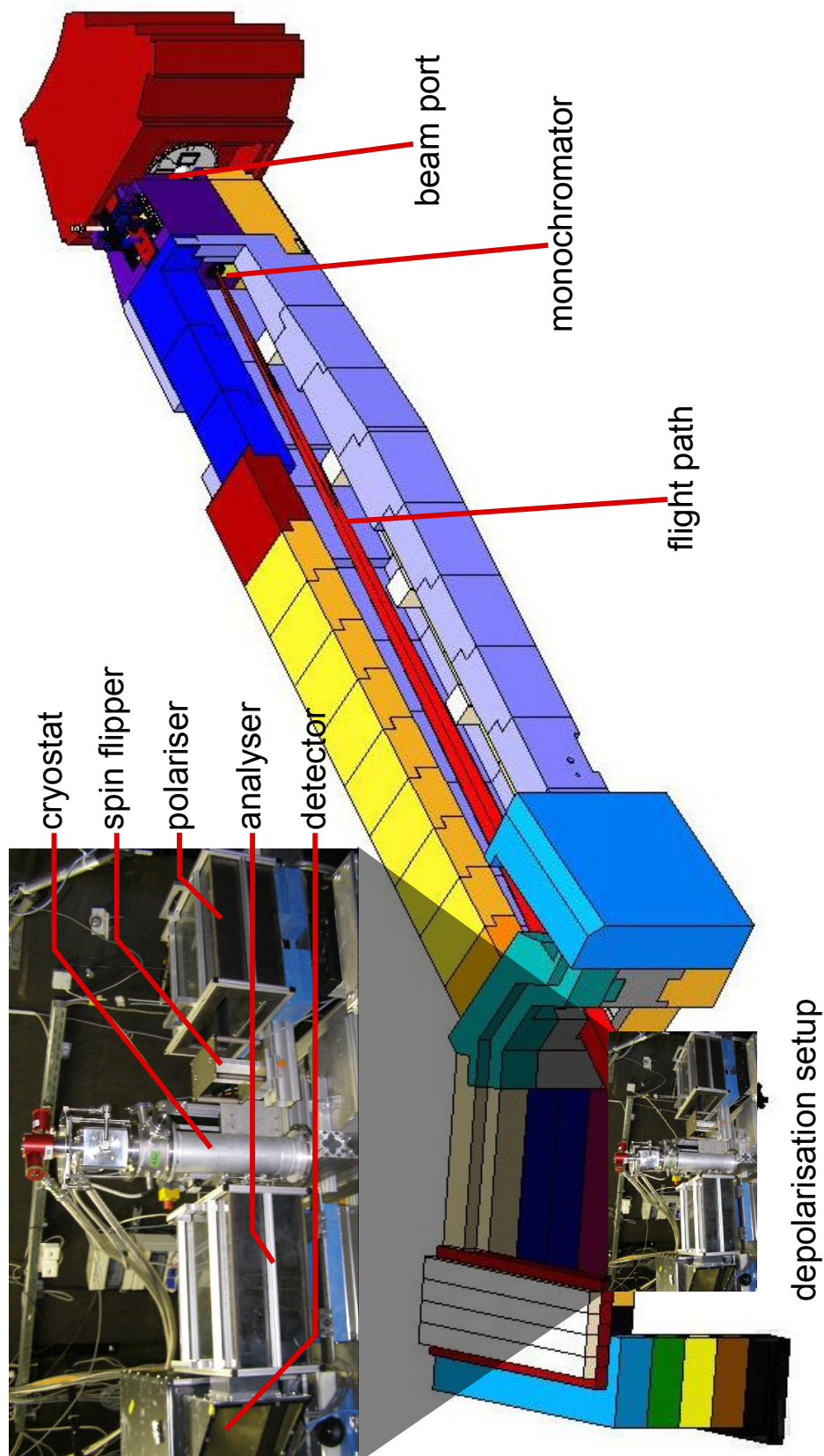


Figure 3.0.1: Technical view of the ANTARES beam line with opened shielding. The neutrons emerge from the beam port to the right, pass the monochromator and the flight tube and enter the sample area, where the entire neutron depolarisation setup with polariser, sample and analyser was installed as shown in the inset.

3.1 Monochromatic Neutron Radiography

Standard neutron radiography typically uses a polychromatic (“white”) thermal or cold neutron beam to obtain high neutron flux and thus low exposure times [98]. This implies an averaging over the wavelength dependence of the mass attenuation coefficient introduced in (2.1.3). However, some wavelength dependent effects – like the strong variation of the neutron absorption cross section at Bragg edges – only become visible with a monochromatic neutron beam [99, 100]. Furthermore, as shown in 2.4 the depolarisation of a neutron beam after transmission of a ferromagnetic sample is wavelength-dependent (most of the neutron depolarisation measurements described in this thesis have indeed been made with monochromatic neutrons). So it was desired to have a monochromatic neutron beam of adjustable wavelength at the ANTARES beam line in order to perform neutron depolarisation measurements and to reveal energy dependent effects in a sample. Such a monochromatisation of the beam is of course only possible at the cost of losing a major part of the original beam intensity.

One further advantage of using a monochromatic neutron beam is to avoid the effect of beam hardening [101], which comes from the variation of the mass attenuation coefficient of a sample over the wavelength range used. The absence of beam hardening allows the quantitative measurement of material thickness in radiographs. Additionally setting the wavelength to a point where the mass attenuation coefficient has a local minimum for a given sample (i.e. above a Bragg edge) allows penetration of samples of larger thickness without encountering the effect of zero transmission which can be extremely harmful especially for tomographic reconstructions, where this effect leads to strong artifacts. It is also possible to identify materials – even without acquiring a tomography – by locating their Bragg edge, which depends on the lattice parameters and is therefore characteristic for every material.

3.1.1 Monochromatising Techniques

There are several requirements that have to be fulfilled to make a monochromator suitable for neutron imaging. Most important at an existing facility is that the beam direction may not be altered. Neutron radiography setups usually consist of a massive concrete shielding around a flight tube which can not be moved easily [89, 91, 93]. Therefore, the monochromatic beam must go in the same direction as the primary, polychromatic beam. Additionally the monochromator must either conserve the beam collimation or be installed far upstream from the sample position so as to act as a small pinhole source itself. The design goals for the monochromator at ANTARES were to achieve a wavelength resolution $\Delta\lambda/\lambda < 5\%$ in a wavelength interval from 3.0 \AA to 6.0 \AA , a collimation ratio $L/D \geq 400$ and a transmission for the selected wavelength $T \geq 80\%$.

There are many different ways to monochromatise a neutron beam. The probably most obvious method is to determine the neutron’s velocity by measuring its time-of-flight. For a pulsed neutron source, where all neutrons of one pulse are emitted nearly at the same time, this is a very practical method. One only needs to measure the time the neutron travels from the source to the detector (the energy of the neutrons transmitted through the sample is unchanged) to determine its wavelength. Especially for radiography, where 2D detectors are used, this requires a very fast detector readout to make use of most neutron energies within one neutron pulse with a typical duration of $100\text{ }\mu\text{s}$. Using this technique at a continuous source requires choppers to interrupt the neutron beam in order to form pulses, which leads

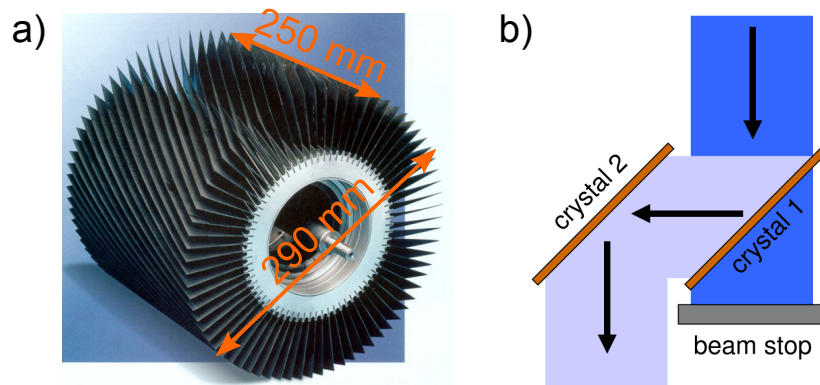


Figure 3.1.1: (a) Photo of the rotor of a neutron velocity selector with a diameter of 290 mm. The bent channels through which the neutrons travel are clearly seen. To allow for high rotation speeds of up to 29,000 rpm this rotor is mounted in an evacuated case for operation. (b) Principle of operation of a Double Crystal Monochromator. The polychromatic beam coming from the top hits the first monochromator crystal and the selected wavelength is reflected towards the second crystal, where it is reflected back into the original beam direction. The remaining polychromatic beam transmitted through the first crystal is stopped by a beam stop.

to the loss of a major part of the beam intensity. For this reason, this method was not pursued for the ANTARES beam line at FRM II.

Another promising option, which is also based on a time-of-flight method, but has higher transmission at a continuous source is a neutron velocity selector (NVS) [102, 103]. Such a device has already been successfully used for energy selective neutron imaging [104, 105, 106]. A NVS is a rotating, turbine-like device as shown in Fig 3.1.1 (a), which has channels through which only neutrons of a certain wavelength band are transmitted, while the neutrons with higher or lower wavelength hit the walls of the channels and are absorbed. In order to obtain a reasonable beam size at the detector position, the NVS has to be installed close to the pinhole aperture, where the beam is still small enough to fit into the beam window of the NVS, which has typical dimensions of 80 mm \times 50 mm. The typical maximum divergence of 1° which can be transmitted through a NVS is large enough to form a beam size of approximately 25 \times 25 cm² at a distance of 14 m from the NVS. Within this area the collimation of the beam will be conserved. A NVS yields a rather coarse wavelength resolution with a $\Delta\lambda/\lambda$ typically ranging between 10% and 20% depending on the number of the lamellae and their skew angle (which in turn is one of the limiting components for the minimum transmitted wavelength). A maximum of 144 lamellae, which is nowadays feasible, and a minimum wavelength of $\lambda_{\min} = 3.5 \text{ \AA}$, limited by the maximum rotation speed of the selector, yield a resolution $\Delta\lambda/\lambda = 11\%$ for a beam divergence of 1°. The peak transmittance is of the order of $T_m \geq 68\%$ [103]. These characteristics lead to higher beam intensities when compared to those obtained with crystal monochromators. However, for the study of most effects of interest in radiography (e.g. the lattice distortion due to mechanical stress), the achieved wavelength resolution is not fine enough. Additionally, due to the inclination of the absorbing blades inside the NVS with respect to the beam direction, the mean wavelength depends on the position within the beam.

A double crystal monochromator (DCM) uses a double Bragg reflection from two monochromator crystals. The wavelength is selected with the first crystal and reflected out of the original beam direction. In order to reflect the beam back into its original direction, a second crystal is additionally mounted on

a linear stage. Setting it to the correct linear position and the same Bragg angle as the first crystal, a zigzag reflection of the monochromatic beam is achieved with the outgoing beam shifted in parallel to the original beam as shown in Fig. (b). The remaining polychromatic beam transmitted through the first crystal is stopped by a beam stop. In order to obtain a sufficiently high neutron flux, crystals with a mosaic spread adapted to the beam divergence have to be used. The reflection from a mosaic crystal, however, increases the beam divergence. Thus, in order to obtain a well collimated beam, the monochromator must be installed a long distance away from the detector position so as to act as a pinhole source itself.

A certain wavelength band is reflected by the crystal as a result of the mosaic spread of the crystal and the beam divergence. The reflected mean wavelength is given by Bragg's law from the mean reflection angle $\overline{\theta_B}$.

$$\overline{\lambda} = 2d/n \sin \overline{\theta_B} \quad (3.1.1)$$

Depending on the mosaic spread of the monochromator crystal, one can obtain a very precise wavelength selection, which results from differentiation of (3.1.1).

$$\Delta \overline{\lambda} / \overline{\lambda} = \cot(\overline{\theta_B}) \Delta \overline{\theta_B}, \quad (3.1.2)$$

where $\Delta \overline{\theta_B}$ results from the full width at half maximum (FWHM) of the incident and the outgoing beam divergence α_1 and α_2 , respectively and the mosaic spread β of the crystal [107]

$$\Delta \overline{\theta_B} = \sqrt{\frac{\alpha_1^2 \alpha_2^2 + \alpha_1^2 \beta^2 + \alpha_2^2 \beta^2}{\alpha_1^2 + \alpha_2^2 + 4\beta^2}}. \quad (3.1.3)$$

High wavelength resolution can therefore be achieved by minimising the mosaic spread of the crystals or by maximising the Bragg angle (i.e. ideally going to backscattering $\theta_B \approx 90^\circ$).

The collimation of the beam will in fact be destroyed by the monochromator due to the large divergence introduced by the mosaic spread of the monochromator crystals. However, mounting the device close to the pinhole aperture results in essentially the same L/D ratio as without the monochromator.

3.1.2 Double Crystal Monochromator

Considering the advantages and disadvantages of the discussed options and also considering the financial effort for the realisation of the monochromator (the monochromator crystals were available to us at no cost) it was chosen to construct and install a DCM at the ANTARES facility [108]. In the following, the construction of the monochromator and first test measurements will be discussed.

Two pyrolytic graphite (002) monochromator crystals with a mosaic spread of 0.7° and 1.0° , respectively, and a size of approx. $6 \times 10 \text{ cm}^2$ were used to build the DCM. Both crystals have sufficient thickness to give nearly 100% reflectivity in the desired wavelength interval. The mosaic spread of the crystals was determined from rocking curve measurements on the diffractometer HEIDI at FRM II [109] at different points of the crystals. The results of this measurement showed that the mosaic spread has only small variations of less than 0.1° over the size of the crystals.

An overview of the installed monochromator is shown in Fig. 3.1.2. For protection, the crystals are mounted in aluminium boxes with a front window thickness of 0.5 mm on a rotary stage. The second

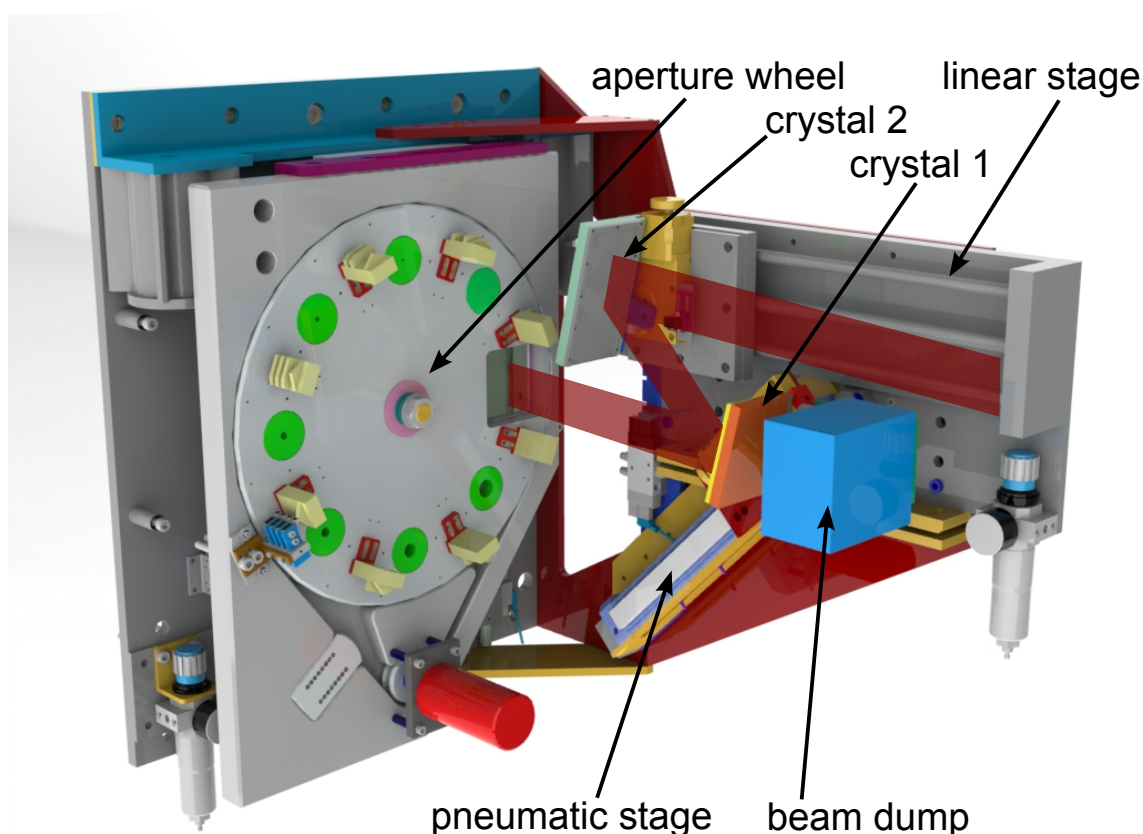


Figure 3.1.2: The double crystal monochromator as installed after the aperture selection wheel before the entrance to the flight tube of the ANTARES beam line. The beam path from the opening of the aperture wheel over the two crystals is indicated in red. The two pyrolytic graphite crystals are contained in aluminium cases, which are each mounted on a rotary stage. The second crystal is additionally mounted on a linear stage, whereas the first crystal is mounted on a pneumatic cylinder to be able to move the crystal together with the beam stop out of the direct beam if the monochromator is not in use. The flight tube begins directly downstream of the setup to right hand side of the image.

rotary stage is mounted on a linear stage so that the second crystal can be moved into the beam reflected by the first crystal. The first one is mounted on a pneumatic cylinder together with the beam stop for the primary beam in order to allow to move this crystal completely out of the beam. Thus, no attenuation of the beam occurs when the monochromator is not in use. The beam stop for the primary beam is made of borated polyethylene of 10 cm thickness and coated with a 5 mm layer of borated rubber. This is sufficient to stop all thermal neutrons, however, fast neutrons and gamma radiation are transmitted through the beam stop. Therefore, the monochromatic beam has essentially the same gamma and fast neutron background as the polychromatic beam. This leads to a significant decrease of the signal to noise ratio (i.e. thermal neutrons to fast neutrons and gammas), since the thermal neutron flux is at the same time decreased by a factor of approximately 150. However, since the neutron flight tube begins directly after the monochromator setup it was not possible to build a more massive beam stop (i.e. of Pb or Fe) to additionally shield the gamma and fast neutron background (cf. Fig 3.1.2).

The monochromator module was mounted only a small distance behind the collimator in front of the entrance of the flight tube of ANTARES. No modifications to the flight tube were necessary, since it was large enough to cover the monochromatic beam, which is shifted upwards by 105 mm with respect to the primary beam. With this setup, any wavelength between 2.7 \AA and 6.5 \AA can be selected. The resulting

$\bar{\lambda}$ [Å]	2.7	3.0	3.5	4.0	4.5	5.0	5.5	6.0	6.5
$\Delta\lambda/\lambda$ [%]	4.1	3.6	3.1	2.9	2.5	2.0	1.6	1.3	0.8
2 nd order/1 st order	0.07	0.09	0.18	0.24	0.45	0.61	0.90	1.43	2.34

Table 3.1: Results of the Time Of Flight Measurements at PSI for the different wavelengths given in the first row. The second row gives the wavelength spread as determined from the FWHM of the peaks fitted with a Gaussian and the third row gives the ratio of the area under the second-order peak to the area under the first-order peak. It can be clearly seen that higher-order contamination increases drastically with increasing wavelength.

beam size at the detector position is $20 \times 20 \text{ cm}^2$.

3.1.3 Characterisation of the Double Crystal Monochromator

Time of Flight Measurements

Due to the good accessibility of the beam close to the pinhole aperture at the ICON facility [90] at Paul Scherrer Institute, Switzerland (PSI), this instrument was chosen as a test bed for alignment and first measurements with the DCM. ICON is a cold neutron radiography beam line with a spectrum which is very similar to that of the ANTARES beam line [110], where the monochromator was eventually installed. The mechanics of the monochromator had to be slightly adapted to match the beam geometry at ICON, where it was then installed some 2 m after the pinhole aperture. After alignment of the setup, Time of Flight (TOF) measurements were performed to measure the resulting wavelength spectrum of the monochromatic beam in order to assess the wavelength distribution $\Delta\lambda/\lambda$ and the amount of higher order contaminations ($\lambda/2, \lambda/3, \dots$) of the beam. The flight distance between the chopper wheel and the detector was $L = 6.35 \text{ m}$. The spectra were measured for different wavelength settings in the range between 2.7 Å and 6.5 Å and are shown in Fig 3.1.3 with Gaussian fits of the peaks. The results for all measured wavelengths are given in Table 3.1. The second row shows that the measured wavelength spread (FWHM) ranges between $\approx 4\%$ at $\lambda = 2.7 \text{ Å}$ and $\approx 1\%$ at $\lambda = 6.5 \text{ Å}$, which is a good compromise between beam intensity and wavelength resolution resulting from the choice of the mosaic spread of the monochromator crystals. In the third row the area under the second order wavelength peak is compared to that under the first order peak. One can see that for $\lambda > 4 \text{ Å}$ the higher order contamination becomes severe and the intensity of the higher order peaks can be higher than the intensity of the selected wavelength itself. This increase of the second order compared to the first order peak is due to the steep decrease of the primary intensity at higher wavelengths. To avoid this effect, a Be filter is now used at the ANTARES facility in combination with the DCM for $\lambda > 4 \text{ Å}$. This cuts down the intensity of the spectrum below 4 Å by at least a factor of 10 [111].

Intensity of the Monochromatic Beam

Further measurements were performed after installation of the monochromator at the ANTARES facility at FRM II to assess the intensity of the monochromatic neutron beam and to compare it with the intensity of the primary, white beam. The results provide a measure of the typical exposure times compared to radiography with polychromatic neutrons. Furthermore, as discussed above, the gamma and fast neutron

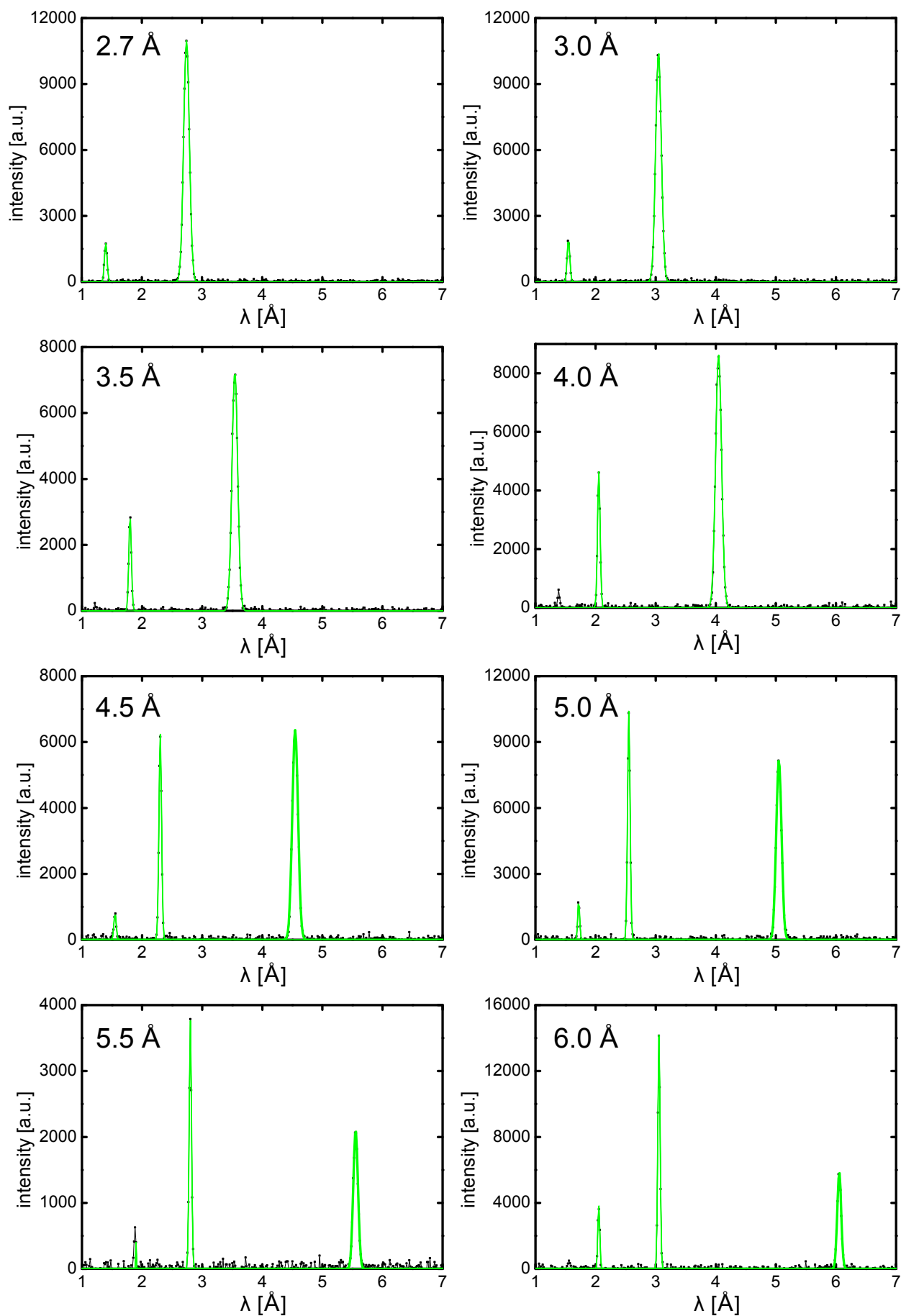


Figure 3.1.3: Measured spectra with the monochromator set to wavelengths from 2.7 Å to 6.0 Å. The second-order peak at half wavelength, which becomes more pronounced with increasing wavelength, can clearly be identified. Even a small third-order peak is observed for long wavelengths.

flux is not attenuated by the monochromator. Therefore the loss of cold or thermal neutron intensity also implies a decrease of the ratio of signal to background.

Since no counting detector was available for the experiment the standard CCD detector at ANTARES was used to measure the beam intensity. This detector is not capable of counting single neutrons, but the detected intensity (measured in grey levels) is on the average proportional to the light output of the neutron sensitive scintillator. However, the sensitivity of the scintillator depends on the neutron velocity v and generally shows a $1/v$ behaviour. Thus, it is not easily possible, without prior calibration, to calculate a neutron flux from the detected intensity on the CCD detector. Therefore, we have only used the intensity at the CCD detector as a measure of the beam intensity and not the neutron flux.

Flat field images at various wavelengths were acquired and the mean grey level values were calculated over the same, homogeneous area for all images. Thus one can obtain the number of grey levels per second (GL/s) as a measure for the beam intensity (see Fig. 3.1.4). The measurements were made with two different pinhole sizes ($L/D = 800$ and $L/D = 400$) with and without a 10 mm Pb filter in the beam. The Pb filter is used as a low-energy gamma filter, which attenuates the neutron beam intensity by approximately 15%. We find that the intensity of the monochromatised beam observed with $L/D = 400$ is approximately three times higher than for $L/D = 800$. In contrast to that, the primary intensity increases by a factor of 4 when decreasing the collimation from $L/D = 800$ to $L/D = 400$. The smaller increase of the intensity of the monochromatic beam occurs because the mosaic spread of the monochromator crystals is too small to fully reflect the larger beam divergence at $L/D = 400$.

The maximum intensity is observed at a wavelength of 3.2 \AA with approx. 32 GL/s. This maximum occurs due to the combination of two effects: First, at lower wavelengths, the Bragg angles are very small. Since the monochromator crystals are not big enough to cover the entire beam at these small angles, only a part of the beam is reflected by the monochromator. This effect leads to an increase of the intensity with increasing wavelength. Second, the intensity in the primary spectrum decreases with increasing wavelength. Both of these effect together cause the maximum at 3.2 \AA . The step at $\lambda = 4 \text{ \AA}$ occurs due to the use of the Be filter for $\lambda > 4 \text{ \AA}$. An approximately linear decrease of the beam intensity with increasing wavelength is observed for $\lambda > 3.5 \text{ \AA}$, which results from the decrease of the primary intensity. No simple explanation was found for the dip at $\lambda = 3.0 \text{ \AA}$.

With the same detector setting, and after removing the monochromator from the beam, the intensity of the polychromatic beam was measured to be approx. 4300 GL/s for $L/D = 400$, which is a factor of 134 more than the maximum intensity observed with the monochromator. This already shows that in order to have good neutron counting statistics in the monochromatic mode, very long exposure times and even integration over several images are necessary.

Exposure times for monochromatic radiographs are of the order of 300 s. Here the high gamma contamination of the beam becomes a severe problem since it produces white spots on the CCD chip with an intensity comparable to that of the neutron signal. These white spots can however be drastically reduced by using a 10 mm Pb filter in the primary beam before the monochromator to stop the low energy gammas while at the same time attenuating the neutron flux by only approx. 15% (see Fig. 3.1.4, red and green curves).

Since the amount of gamma spots produced in the images is relatively high, exposure times were limited to 60 s in most measurements. In this case $\approx 5\%$ of all detector pixels are affected by gamma spots, which increase the intensity measured in these pixels. This is low enough to use a search & replace strategy to

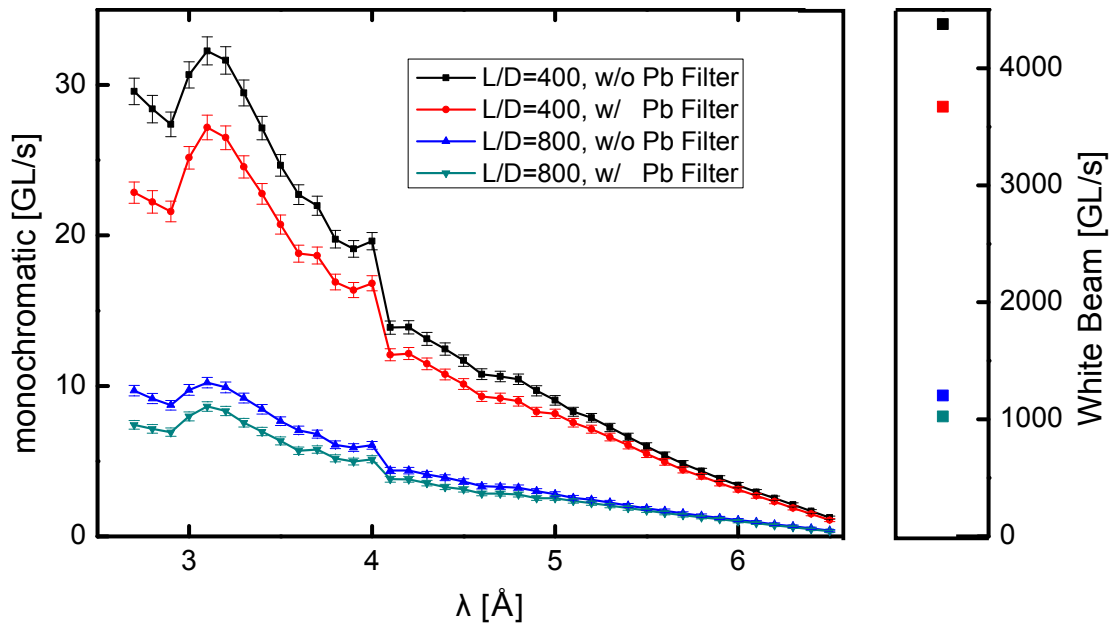


Figure 3.1.4: Dependence of the intensity (in greylevels / s) on the wavelength measured using different pinhole sizes ($L/D = 800$ and $L/D = 400$). The points on the right hand side (separate scale) give a comparison with the intensity measured with the polychromatic beam.

replace the value of the affected pixels by the mean value of their neighbouring pixels. This procedure is described in more detail in [112] and in 4.1. In order to obtain good neutron counting statistics, several filtered images with short exposure times have to be summed up.

3.2 Polariser and Analyser

Of major importance for the success of polarised neutron imaging experiments is the choice of the polarising and analysing devices. Here we will briefly discuss the requirements for these devices. Up to now, most measurements with polarised neutrons have been performed using polarising equipment that has been taken from neutron scattering experiments, where the homogeneity of the beam was no issue. However, for neutron imaging polarisers with a high polarisation providing beams with a high spatial homogeneity are mandatory. Moreover, after the sample, the polarising analysers should be as compact as possible to reduce the blurring d of the images due to the increased sample to detector distance as given by (2.5.1).

Since for the measurements at the ANTARES facility at FRM II, where most of the experiments described in this thesis were made, the polariser had to be placed in the sample area after the flight tube, it was an additional prerequisite for the polariser to conserve the beam collimation as much as possible. However, most standard polarising systems like neutron guides or benders destroy the initial collimation by a large number of reflections, while at the same time introducing intensity inhomogeneities either by the segment joints of a guide, by the multiple plate structure of a bender or by the waviness of the substrates.

We have therefore tested various combinations of conventional polarisers and analysers as shown in Fig. 3.2.1 to determine the ideal conditions, without special efforts to adapt these techniques to the

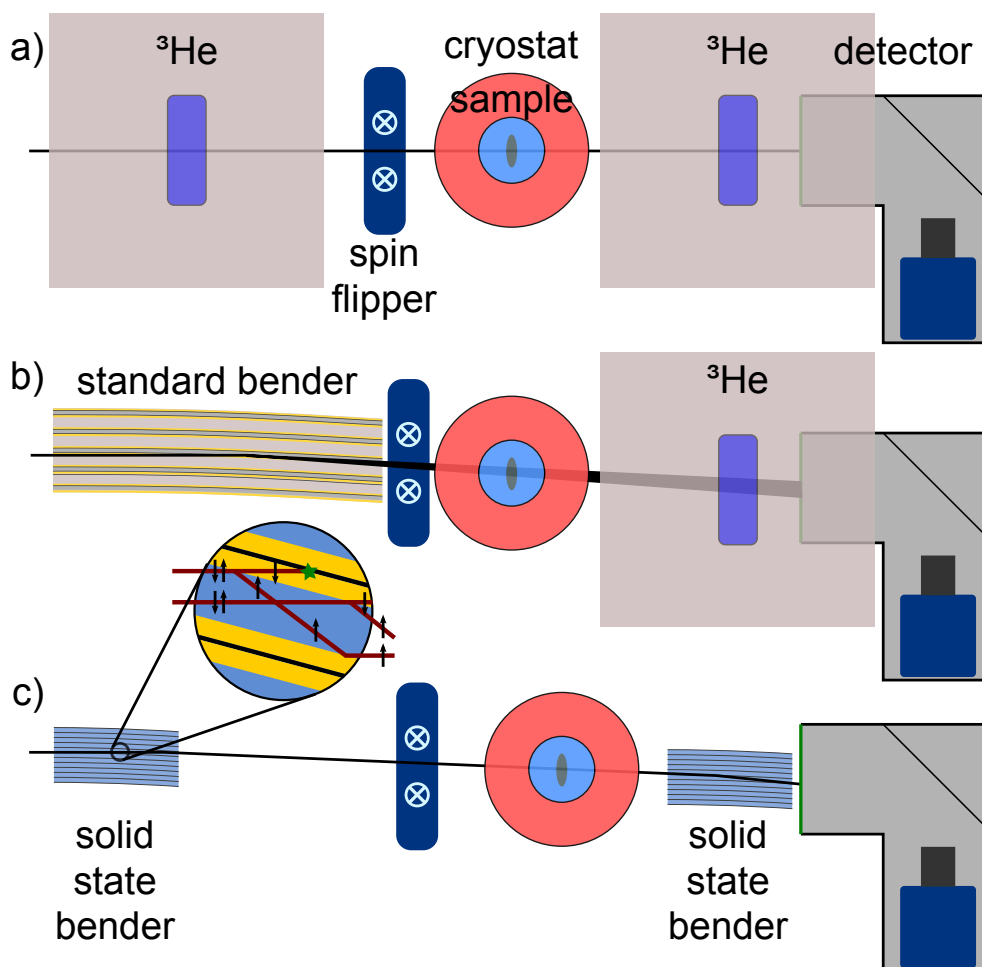


Figure 3.2.1: Various setups for neutron imaging with polarised neutrons. The setups (a) and (b) involving ^3He filters and setup (c) using solid state benders have been used at the ANTARES (FRM II) and CONRAD (HZB) beam lines, respectively.

special requirements of the pinhole setup used in radiography. Furthermore a new type of polariser was introduced. In the following we compare the properties of these setups for neutron imaging.

The basic setup used for all measurements consists of a neutron polariser, followed by a spin flipper, a polarisation analyser, and a position sensitive CCD detector that records the image of a neutron sensitive scintillator, which is placed behind the analyser. The sample was attached to the cold head of a closed-cycle refrigerator and the depolarisation of the transmitted neutrons was measured for various inhomogeneous ferromagnetic samples. The measurements using ^3He spin filters were carried out at the ANTARES beam line at FRM II, Munich, and those with solid state benders were made at the CONRAD beam line at HZB, Berlin.

3.2.1 ^3He Spin Filter Cells

^3He spin filters make use of the strong polarisation dependence of the neutron absorption cross section of ^3He gas. In order to use this method to polarise a neutron beam, the nuclei of the ^3He gas have to be polarised. At FRM II, the ^3He gas is polarised at low pressure based on the Metastability Exchange Optical Pumping (MEOP) method using the optical pumping facility HELIOS [113, 114]. After polarisation of the gas, it is filled into quartz glass cells. The polarisation of a neutron beam that can be

achieved with such a spin filter cell is given by [115]

$$P = \tanh(\eta P_{\text{He}}), \quad (3.2.1)$$

while the transmission of the cell is found to be

$$T = T_0 e^{-\eta} \cosh(\eta P_{\text{He}}). \quad (3.2.2)$$

Here P_{He} is the polarisation of the ^3He gas used in the cell, T_0 is the transmission of an evacuated cell and η is an opacity parameter of the cell which can be calculated from the spin-dependent and spin-independent part of the total cross section, the number of atoms per unit volume and the thickness of the cell. At room temperature the opacity of ^3He gas is

$$\eta = 7.32 \cdot 10^{-2} p(\text{bar}) d(\text{cm}) \lambda(\text{\AA}), \quad (3.2.3)$$

with the pressure of the gas p , the transmission length of the cell d and the neutron wavelength λ . After removing the ^3He cell from the polarising facility the gas will start to depolarise as

$$P_{\text{He}}(t) = P_{\text{He}}(0) \cdot e^{-t/\tau} \quad (3.2.4)$$

with a relaxation time τ , which is strongly dependent on the homogeneity of the magnetic field over the volume of the cell. Relaxation times of the order of 200h have been achieved with magnetostatic boxes made from MuMetal, where the magnetic field is either produced with permanent magnets or solenoids.

Using ^3He as a polariser has the advantage of leaving the beam collimation as well as the beam homogeneity unaffected, making it well suited for neutron imaging. However, the bulky magnetostatic box required to create a homogeneous field surrounding the ^3He cells leads to a large sample to detector distance (SDD) d_{SD} . Therefore, the spatial resolution is seriously reduced. A magnetic sample can not be placed inside the box since the magnetic field homogeneity in the box would suffer from the influence of the sample. To improve the setup, the non-magnetic scintillator was placed inside the box directly after the ^3He cell as discussed in 3.4, which decreases the SDD in our case to $d_{\text{SD}} \approx 30\text{cm}$.

The cells are transported from the filling station to the beam line and installed in the magnetostatic boxes. Due to the relaxation of the gas polarisation, a regular exchange of the ^3He cells is required. Using ^3He as a polariser and analyser as shown in Fig. 3.2.1(a) leads to a time dependence of the polarisation, which can, however, be corrected for. Moreover, the transmission of the cells is also time-dependent, leading to a loss in intensity with time. Currently, at the beam line ANTARES at FRM II the gas has to be exchanged every 24 – 48 hours. For typical applications one generally maximises the term $P^2 T$ from equations (3.2.1) and (3.2.2), which yields a beam polarisation P of up to 80% and a transmission T of $\approx 25\%$ for 3.2\AA neutrons for a cell of 5cm thickness at a pressure of 1.6bar depending on P_{He} , which is of the order of $P_{\text{He}} = 70\%$ for freshly polarised gas.

For most recent experiments, a RF spin flipper was integrated into the magnetostatic box that allowed to select the polarisation of the ^3He gas, thus allowing to use a broad wavelength band of neutrons, yielding a high neutron flux. For the polychromatic measurements, a Be-filter was inserted to remove neutrons with a wavelength $\lambda < 4\text{\AA}$ [111]. This way, the polarisation of the neutrons could be improved, i.e. for a ^3He polarisation of 80%, a flipping ratio (cf. eq. (2.3.3)) of 9.6 was obtained. The image shown

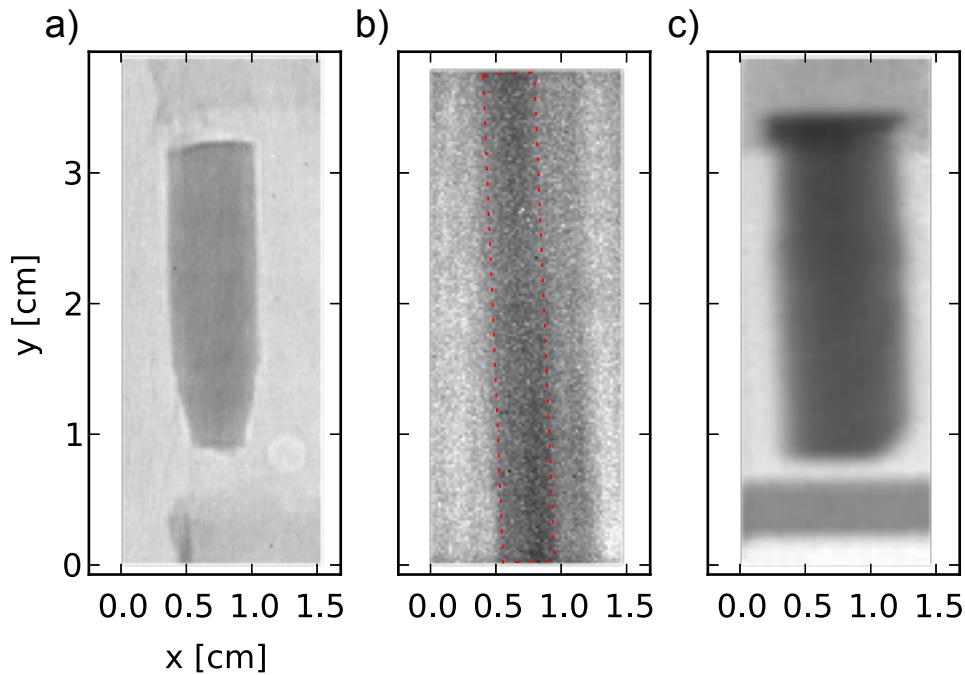


Figure 3.2.2: (a) - (c) Transmission images of different samples taken with the setups (a) through (c) shown in Fig. 3.2.1. The differences in image quality for the different methods are clearly visible. The samples are: (a) a NbFe_2 sample, (b) a Ni_3Al sample (the position of the sample is indicated with a red rectangle) and (c) a $\text{Pd}_{1-x}\text{Ni}_x$ sample. The details of the measurements are explained in the text.

in Fig. 3.2.2a has been recorded using this setup yielding a resolution of ≈ 0.3 mm. By reducing the size of the magnetostatic box, the resolution could be improved further. Of course, for a quantitative determination of the field integral as described in [94, 116], a polychromatic beam cannot be used. In this case, the dependence of the neutron's precession angle in the magnetic field on its velocity leads to a depolarisation of the beam.

3.2.2 Standard Benders

Benders as described in [117] make use of the polarisation dependence of the reflection of a neutron beam from a supermirror surface. Such a device is made from bent glass lamellae coated with a polarising supermirror such that there is no direct sight through the bender. Only neutrons with one spin polarisation are reflected at the surface, while neutrons with the opposite polarisation are transmitted through the coating and absorbed in a Gd layer below the supermirror coating. The reflected neutron beam has a high polarisation of $P \approx 0.96$.

For a setup using a standard bender as a polariser for neutron radiography as shown in Fig. 3.2.1(b) a poor spatial resolution is observed in the reflection plane, because the bender increases the beam divergence through the reflection of the beam on the curved channels, delivering an L/D -ratio of the order of $L/D \approx 60$ similar to that of a standard neutron guide [118]. Hence, the images are smeared in the horizontal direction. Moreover, the beam becomes inhomogeneous, showing a stripe structure. With $d_{\text{SD}} \approx 30$ cm, which was required by the ^3He analyser, no satisfactory images could be obtained (see Fig. 3.2.2(b)), i.e., the sample was completely smeared out in the horizontal direction. Even with a shorter d_{SD} , the image would still be severely blurred. A more favourable position for the bender would be to place it closely behind or even before the pinhole. However, if using the latter position for

the polariser, extreme care has to be taken to avoid imaging of the polariser structure onto the detector according to the pinhole camera principle. Such a setup was not feasible at the ANTARES beam line due to geometrical constraints. The divergence of the beam will still be increased but the cross section of the exit of the bender then represents a pinhole source, which defines the collimation of the beam.

3.2.3 Solid State Benders

The length of a bender can be significantly reduced by using a stack of thin, bent Si wafers coated with a polarising supermirror. The neutrons of one spin direction are guided through the Si, while neutrons with the opposite spin direction are transmitted through the supermirror coating and absorbed in a Gd layer below the coating as shown in the inset in Fig 3.2.1(c). Such a bender is mostly suited as an analyser, since it can be relatively compact. All neutrons entering one of the channels will also exit the same channel on the other side of the bender. If placed directly in front of the scintillator, the resolution obtained with a bender is therefore given by the width of the channels in the horizontal direction. The vertical component of the neutron direction is not altered by the reflection. Thus, the resolution in this direction is given by the geometrical blurring due to the finite distance between sample and detector, which is limited by the length of the bender. The secondary gamma radiation produced by the Gd layers in the bender is, in such a low flux measurement, small compared to the intensity of scattered gammas from the primary beam.

A setup using two such solid state benders as polariser and analyser was investigated at the radiography facility CONRAD at HZB, Berlin (see Fig. 3.2.1(c)). The performance of the polarisers has been evaluated as described in [119]. A high beam polarisation of $\approx 95\%$ was achieved, however, the beam profile was inhomogeneous exhibiting a pronounced stripe structure caused by imperfections of the wafers in the benders. However, these stripes are fixed for a fixed detector and polariser position and consequently they cancel out when the polarisation is evaluated from the raw images. For the benders used in this experiment, the wafer thickness was $250\ \mu\text{m}$ and the length was $\approx 80\text{mm}$, yielding a resolution of $\approx 0.5\text{mm}$ [94]. A radiograph taken with this setup is shown in Fig. 3.2.2(c). The resolution of the analyser can be improved by using thinner Si wafers, which would also allow to build a shorter polariser. This allows to decrease d_{SD} as well. Of course, the optimum position of a solid state polariser would be in front of the pinhole of the beam line.

3.2.4 Polarising Neutron Periscope

In the last few years significant advances have been made in increasing the critical angle of reflection θ_{max} of neutron supermirrors, which is typically expressed by a parameter m , giving the ratio of the critical reflection angle of the supermirror compared to a Ni surface. The critical angle for Ni can be calculated as [120]

$$\theta_c = \lambda \sqrt{\frac{\hbar^2 N b}{\pi}} \approx \lambda [\text{\AA}] \cdot 0.1^\circ, \quad (3.2.5)$$

where N is the number density of the scattering Ni atoms and b their bound coherent scattering amplitude. Thus, the critical angle θ_{max} of a supermirror increases linearly with m and λ and can be written as

$$\theta_{\text{max}} [^\circ] = 0.1 m \lambda [\text{\AA}]. \quad (3.2.6)$$

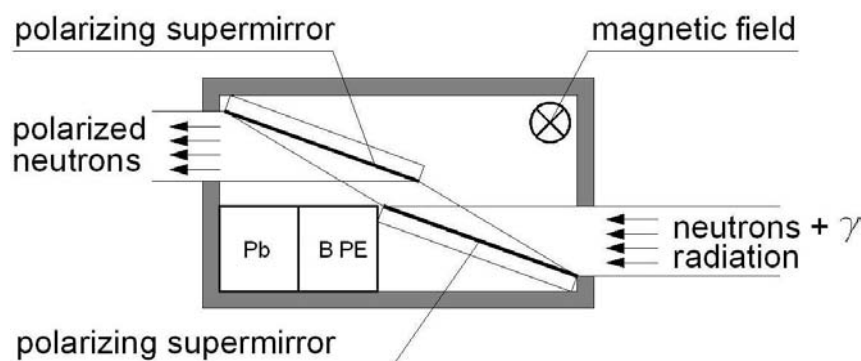


Figure 3.2.3: Schematic of the principle of operation of a polarising periscope. The neutrons enter the device from the right and are reflected from the first mirror towards the second mirror, which is parallel to the first one. This mirror reflects the beam back into its original direction. The direct beam and its gamma and fast neutron contamination can be stopped by a massive shielding behind the first mirror.

Therefore, higher m allows to reflect neutron beams of larger size with a given mirror size due to larger reflection angles. Currently non-polarising mirrors with m -values up to $m = 7$ and polarising mirrors with $m = 4.5$ are commercially available [121].

Principle

The neutron periscope is an arrangement of two parallel high- m supermirrors as shown in Fig. 3.2.3. If the supermirrors are positioned such that a zig zag double reflection results, the beam leaving the periscope is parallel to the incoming beam but shifted to the side. Also the beam geometry, i.e. the beam collimation is conserved [122]. This is especially important if the periscope is used with a collimated neutron beam for radiography and tomography experiments. In this case, the periscope can operate as a device to stop most of the gamma and fast neutron contamination of a thermal neutron beam by shifting the beam out of the direct sight to the beam nozzle and stopping the background radiation with shielding material within the periscope. Nowadays, high- m polarising supermirrors with $m = 4.5$ are available. This offers the possibility to build a neutron polariser with very high polarising efficiency $P > 99\%$ for large beams, leaving the beam collimation unaffected [123]. In the following, we show the construction of the polarising periscope and demonstrate its usability for radiography with polarised neutrons.

Construction

Four polarising FeSi supermirrors with $m = 3.88$ were used to build a first polarising version of the neutron periscope. They are of $500\text{ mm} \times 40\text{ mm}^2$ size each and have a thickness of 2 mm. The acceptance angle of the periscope was designed for a mean wavelength of 3.2 \AA since, as discussed in Chapter 3.1.3, at this wavelength the neutron flux of the monochromatic beam at the ANTARES facility has its maximum. The mirrors are inclined by an angle of 1° with respect to the incoming beam, allowing to reflect a neutron beam with $\lambda = 3.2\text{ \AA}$ and a divergence of 0.1° . The periscope setup has an overall length of approx. 180 cm. An overview of the entire periscope assembly together with the massive Pb and borated PE shielding as installed at ANTARES can be seen in Fig. 3.2.4. The magnetic field of 450 G necessary to magnetise the polarising supermirror coating was produced by 200 NdFeB permanent magnets which

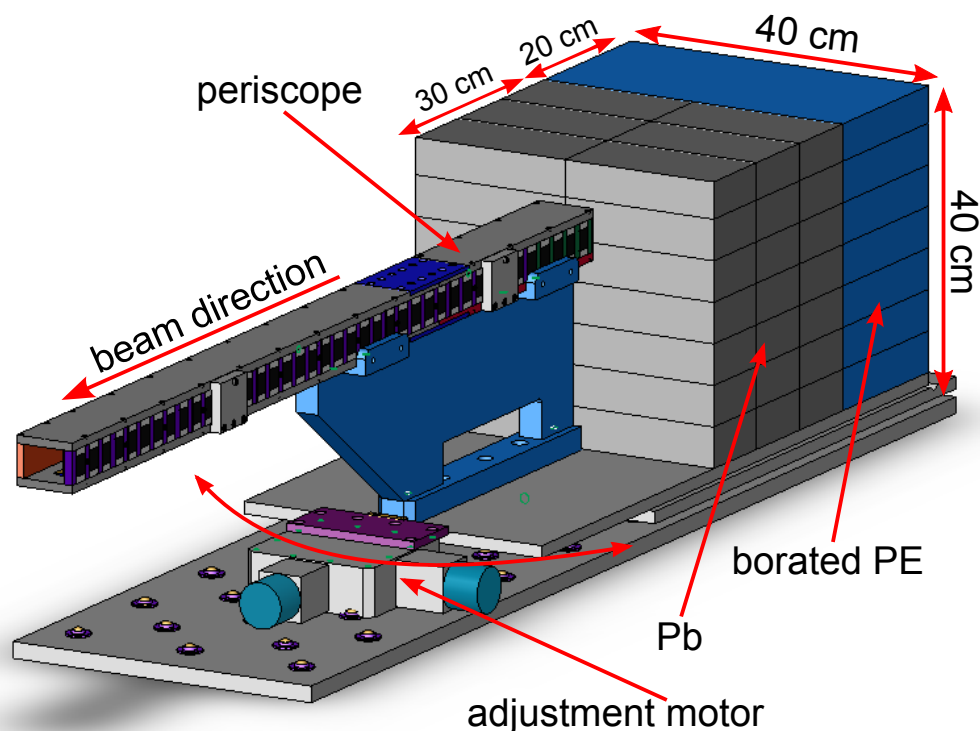


Figure 3.2.4: Technical drawing of the polarising periscope setup. The block on the right side is the massive shielding made of Pb and borated PE to stop the primary beam with its fast neutron and gamma contamination at the entrance of the sample area.

were arranged on both sides of the polariser housing, with their magnetisation pointing in the same direction. The top and bottom parts of the periscope are made of iron, which guides the return field of the permanent magnets to the space where the mirrors are mounted.

The unpolarised, collimated beam at the detector position of the ANTARES [92, 124] facility has a size of $400\text{ mm} \times 400\text{ mm}$. Since the useable beam area of the periscope is much smaller, we used a combination of borated polyethylene and Pb to stop the unused part of the primary beam, and thus we could severely cut down the gamma, epithermal neutron and fast neutron background. This setup significantly reduces the number of bright spots on the CCD detector which originate from gammas directly hitting the CCD chip.

For adjustment the entire setup was mounted on a plate with ball casters. The end of the periscope which is closer to the reactor is fixed by a pin around which the entire setup can be rotated using a linear stage at the other end. This setup allows to adjust the angle of the periscope with respect to the beam.

In the future, the periscope will be installed further upstream of the neutron beam to allow for an expansion of the beam dimensions due to its divergence when space becomes available during the ANTARES upgrade in 2010 [125]. This will require for a guide field along the entire length of the flight tube, which could, however, easily be realised by winding a longitudinal coil around the flight tube or by building a transverse guide field using permanent magnets.

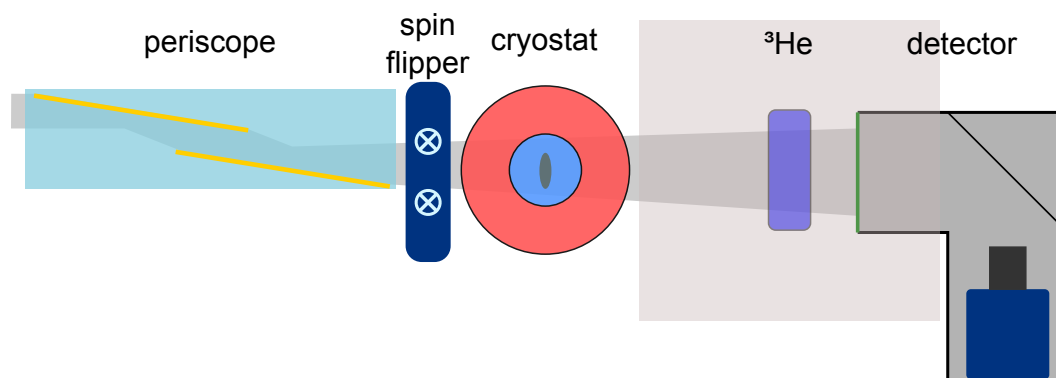


Figure 3.2.5: The setup used for the measurements described in this chapter consists of a periscope polariser and a ^3He analyser. By placing shielding material behind the upper reflecting mirror, the direct line of sight to the moderator can be interrupted.

Evaluation of the Beam Homogeneity

The conservation of the beam geometry is of great importance for radiographic experiments. To assess the performance of the polarising neutron periscope, several measurements have been performed at the ANTARES beam line at FRM II with a setup shown in Fig. 3.2.5 using a ^3He analyser. Due to geometrical constraints the periscope could only be installed close to the sample position, which restricted the beam to an area of approximately $17.5 \times 40\text{mm}$, where the height of the beam is only limited by the height of the mirrors. Most of the following measurements were performed with a polychromatic beam with a collimation ratio of $L/D = 800$, since the intensity of the monochromatic beam at 3.2Å is very low, which leads to long exposure times with poor S/N ratio. The collimation ratio $L/D = 800$ was preferred over $L/D = 400$ since the former yields better spatial resolution.

First, flat field images were taken with the periscope and – just as with the first version of the unpolarising neutron periscope – we observed a pronounced stripe structure in these images (see Fig. 3.2.6 (left)). As discussed below and in [122], this occurs due to a waviness of the mirror surface. As will be shown in the next paragraph, a waviness of only 0.1mrad – the typical waviness of supermirrors on float glass – can produce a stripe structure like the one we observed.

Fig. 3.2.7 shows a radiograph recorded with the unpolarised version of the periscope, which was normalised to an image with no sample in the beam to correct for intensity fluctuations reported in [122]. This figure shows the image quality which can be achieved by reducing the waviness of the mirrors. The polarising version did not yet reach the same perfection at the time of writing. A strong stripe structure with variations of the beam intensity was observed. Normalising the radiographs to the flat field images cancels the stripe structure but, due to the large intensity variations, the statistical noise is increased in areas with poor counting statistics. The origin of the blurring of the radiograph of a printed circuit board sample shown in Fig 3.2.6 (right) is mainly due to the large sample-detector distance of approx. 30cm . This leads to an inherent blurring of approx 0.4mm at $L/D = 800$. This large distance was necessary because of the bulky magnetostatic housing of the ^3He analyser.

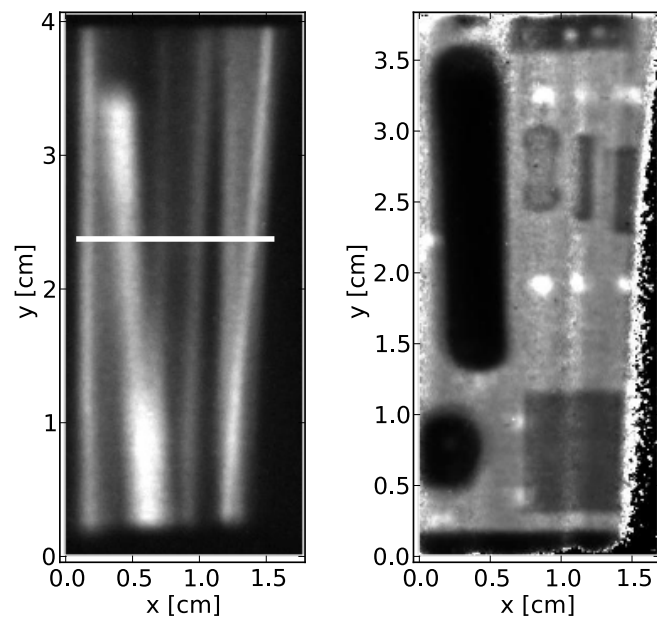


Figure 3.2.6: An open beam image that shows a strong stripe structure due to the waviness of the mirrors (left). Normalised radiograph of a printed circuit board (right).

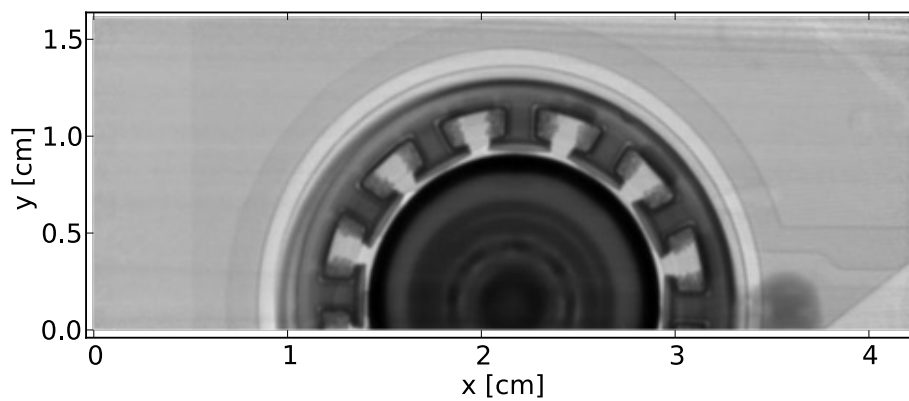


Figure 3.2.7: Normalised radiograph of a hard disk drive motor recorded with an unpolarising version of the periscope, with a distance of approximately 2 cm between sample and detector.

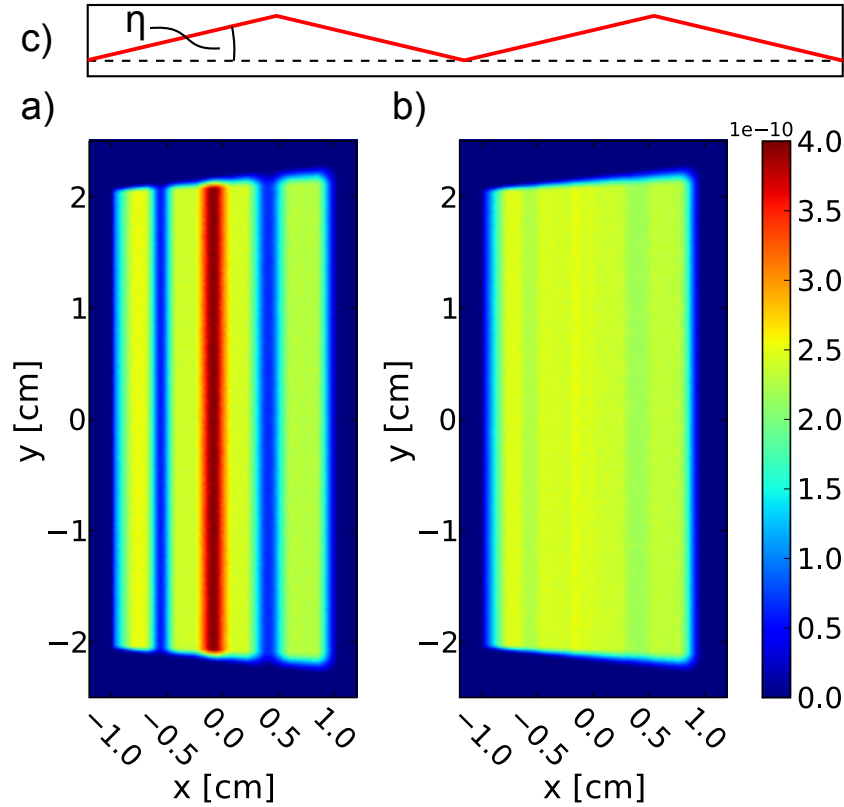


Figure 3.2.8: Results of the simulations for a waviness $\eta = 2 \cdot 10^{-4}$ rad (a) and $\eta = 2 \cdot 10^{-5}$ rad (b). Furthermore the simple model for the mirror waviness as two triangles with base angles η is sketched (c).

McStas Simulations of the Effect of the Mirror Waviness

To prove that the stripe structure observed in our measurements arises from the waviness of the supermirrors used in the periscope, a model of the polariser was simulated with the Monte Carlo simulation software McStas [126, 127]. The instrument was simulated with parameters resembling those of the real ANTARES facility as follows: The neutrons with a wavelength of $\lambda = 3.2 \pm 0.05 \text{ \AA}$ emerge from a pinhole with a diameter of 2 cm at a distance 4.3 m away from the source and follow a flight path of 13.8 m from the pinhole to the entrance of the periscope. For the periscope, non-polarising supermirrors with $m = 3.88$ were assumed, since the polarisation is not of importance for the stripe structure. The waviness of the mirrors on one side of the periscope was approximated by a profile composed of two triangles with a base angle of $2 \cdot 10^{-4}$ rad as sketched in Fig. 3.2.8 (c). This angle corresponds to the typical waviness of standard supermirrors on glass substrates. In a second simulation, a waviness $\eta = 2 \cdot 10^{-5}$ rad was used to assess the effect of using glass of higher surface quality (i.e. polished borkron glass, which has optical quality).

The intensity observed at the position sensitive detector at the exit of the periscope for both simulations is shown in Fig 3.2.8. We find a stripe structure that is in good qualitative agreement with the data shown in Fig. 3.2.6. Intensity variations of a factor of ≈ 4 are observed for a waviness $\eta = 2 \cdot 10^{-4}$ rad. Each of the triangles that was used for approximating the profile reproduces a sequence of regions with high and low intensity. If the frequency of the undulations of the profile is increased, the number of stripes increases as well. Actually, the wavelength Λ of the undulations of the profile is determined by the length L of the substrates. Typically, it turns out that $L/\Lambda = 0.5$ or 1. By pushing the mirrors against

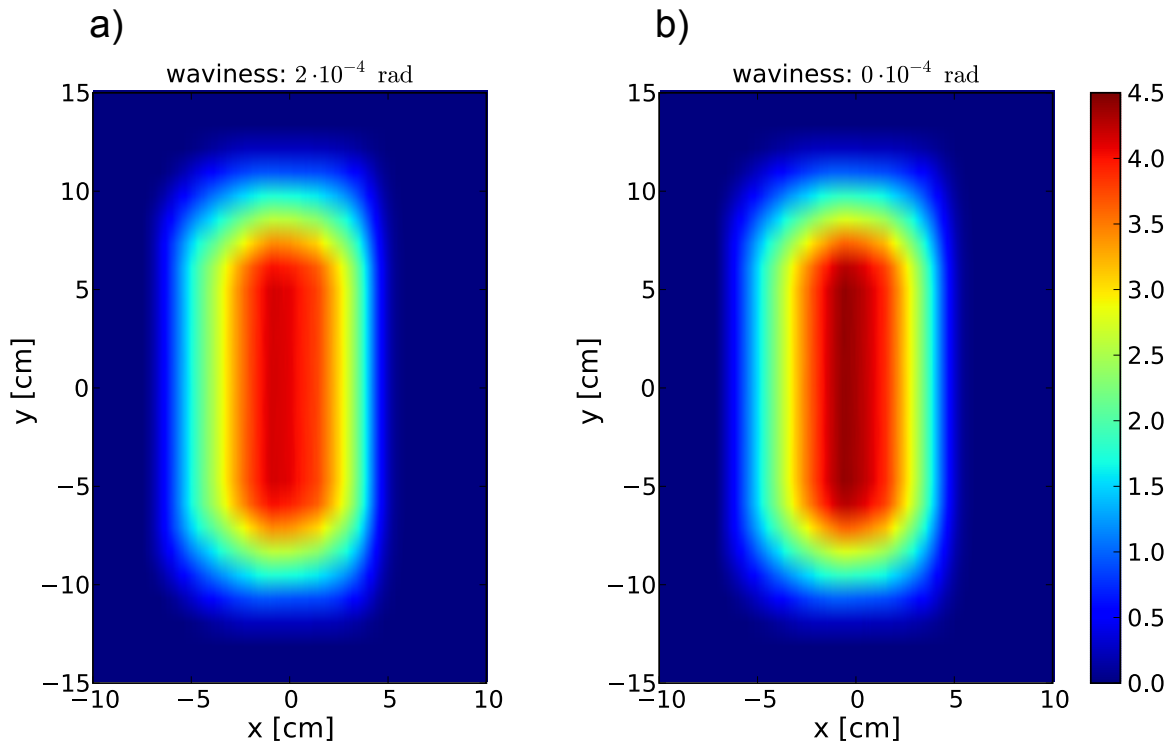


Figure 3.2.9: Results of the simulations of the periscope for a waviness $\eta = 2 \cdot 10^{-4}$ rad (a) and $\eta = 0$ rad (b). For both simulations the periscope was placed 3.7 m behind the pinhole allowing the beam to expand on a flight path of 10.1 m to the detector. The effect of the waviness of the mirrors is negligible at this large distance from the periscope.

a flat support structure, it should be possible to reduce η to $2 \cdot 10^{-5}$ rad leading to intensity variations of $\approx 25\%$, which is tolerable for neutron radiography. Using polished borkron glass, η can be reduced to even below $1 \cdot 10^{-5}$ rad, providing very homogeneous beams.

Further simulations with the periscope mounted closer to the pinhole were made to determine the resulting beam size at the detector position and the effect of the long flight path on the stripe structure. For these simulations, the periscope was placed 3.7 m behind the pinhole, which gives a flight path of 10.1 m from the periscope to the detector. If the first part of the flight tube of the ANTARES beam line were to be removed, the periscope could actually be installed at this position. The resulting beam size at the detector position was found to be $\approx 10 \times 20$ cm. As expected, the stripe structure in the beam profile was much diminished and the difference in variations between the two scenarios $\eta = 2 \cdot 10^{-4}$ rad and $\eta = 0$ rad was negligible.

The high image quality which can be obtained by positioning the periscope shortly after the collimator was shown in an additional test experiment at the ICON beam line at PSI, where the area after the collimator is easily accessible. The periscope was placed close to the collimator and 885 cm away from the sample position. For comparison two images with the same samples were acquired with and without the periscope. The resulting, normalised images are shown in Fig. 3.2.10 and prove that there is no visible difference in the image quality of both radiographs and no stripe structure is observed in the image acquired with the periscope.

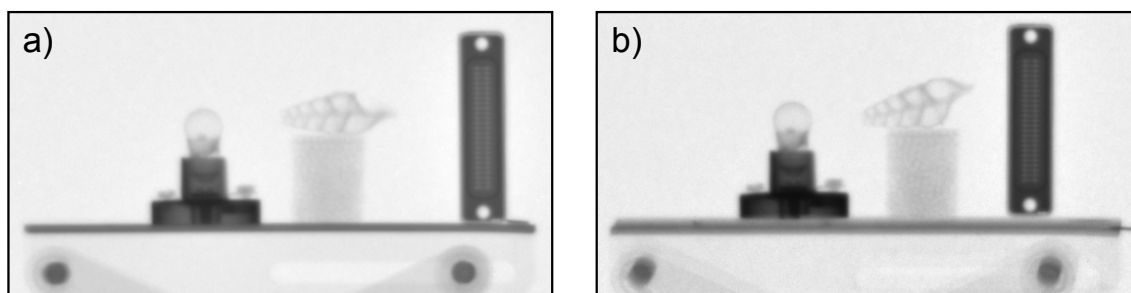


Figure 3.2.10: Comparison of the image quality obtained with the full beam (a) and with the periscope close to the collimator and 885 cm away from the sample (b). Both images show similar resolution and no stripe structure, which proves that the drawbacks of the periscope can be eliminated by positioning the device as close as possible to the collimator.

Polarising efficiency

To assess the polarising efficiency of such a polariser, a depolarising iron shim of 0.6 mm thickness, which depolarises the beam to $P < 1\%$, was put between polariser and analyser. The ratio of the intensity at the detector without and with the iron shim in place was measured. This ratio, generally known as shim-ratio R , determines the product of the polarising efficiency P_p and the analysing efficiency P_a by $P_p = \frac{1}{P_a} (1 - R)$ [120]. Knowing that the polarising efficiency of the ^3He analyser was $P_a = 0.76$ at the time of the measurement, one can then calculate the polarising efficiency of the periscope. Fig 3.2.11 shows a plot of the beam polarisation behind the periscope along the white line shown in Fig 3.2.6 (left). As seen in this plot, P_p lies roughly between $P_p = 0.75$ and $P_p = 0.96$ in most areas of the beam, with the stripes of low intensity in the image also having lowest polarisation. The left part of the plot shows significantly lower polarisation, which is probably a result of imperfect shielding of the primary and unpolarised beam at the entrance of the periscope. Due to the divergence of the beam, these unpolarised neutrons might transmit the periscope without reflection from the mirrors and thus contaminate the polarised beam.

This lets us conclude that improving the flatness of the supermirrors will also increase the polarising efficiency. From reflectometric measurements on the polarising mirrors used in the periscope we know that the beam polarisation after a single reflection by such a mirror should be $P_p \geq 0.96$. With two reflections it should be possible to obtain $P_p > 0.99$. This goal should also be achievable in the periscope setup by improving the mirror alignment.

3.2.5 Summary & Conclusion

The results of our experiments demonstrate that the combination of two ^3He cells, where the scintillator is placed directly behind the analyser cell inside the magnetostatic box (see Fig. 3.2.1a)) yields a resolution of ≈ 0.3 mm, which is the highest resolution of the setups tested so far. This resolution might also be achieved with an optimised version of the periscope which was, however, not yet available at the time of writing.

Our results indicate that an even higher resolution may be obtained if a ^3He spin filter as a polariser is combined with an optimised solid state bender as an analyser, if the setup has to be installed close to the sample area of an existing beam line for radiography. In this case the polariser would not affect the

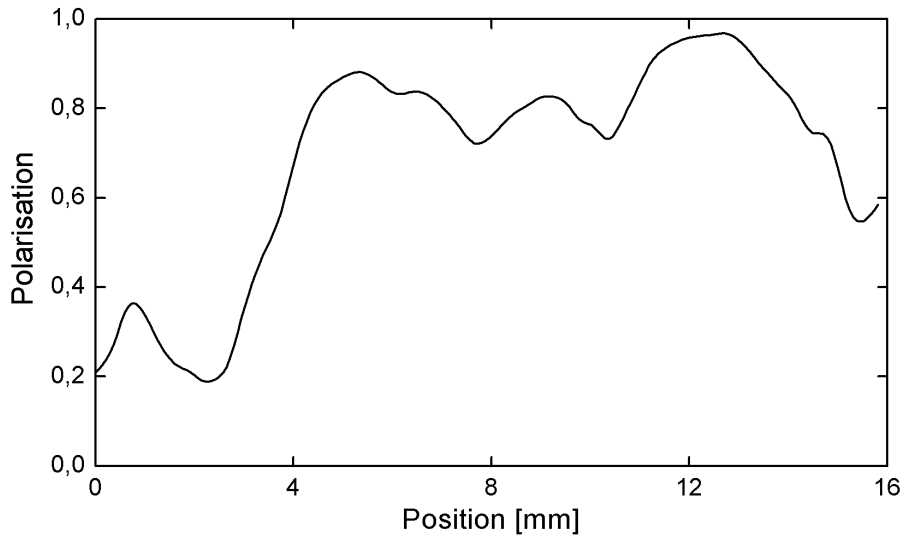


Figure 3.2.11: Beam polarisation along the white line shown in Fig 3.2.6 (left). In the right part of the plot, the beam polarisation varies between 75% and 96%, whereas in the left part it is significantly lower. This is probably a result of the imperfect shielding of the primary, unpolarised beam which transmits the periscope due to its divergence.

beam collimation and homogeneity at all and also the size of the magnetostatic box would not be crucial for this application. A solid state bender analyser could be manufactured with a Si wafer thickness of $100\ \mu\text{m}$ leading to an overall length of the analyser of only 5 cm or even less. At a collimation $L/D = 800$ as available at FRM II Munich this would result in a geometrical blurring of $< 100\ \mu\text{m}$ in the vertical direction and $100\ \mu\text{m}$ in the horizontal direction due to the wafer thickness. This would be a great step towards high resolution imaging with polarised neutrons.

If a dedicated beam line for polarised neutron imaging were to be built, the polariser should be installed before or shortly after the pinhole. This setup would relax the restriction for the polariser to conserve the beam collimation and thus would largely increase the choice of polarising devices. A good choice as a polariser would then be to install a periscope with which the background would be reduced significantly.

3.3 Spin Flippers

To measure both the intensity I_+ of the neutrons with spin in $+z$ direction and I_- with spin in $-z$ direction (see eq. (2.5.2)) it is necessary to rotate the polarisation of the neutron beam by 180° . This can either be done before or after the sample, since only the probability for a spin flip (i.e. the depolarisation of the beam) is measured. In order to decrease the distance between sample and detector as much as possible, the spin flipper was always installed before the sample in our experiments. The effect of a spin flipper on the polarisation P of a neutron beam can be written as a multiplicative factor

$$P^* = P(1 - 2f), \quad (3.3.1)$$

where P^* is the final polarisation and f is the flipping efficiency, which should be as close as possible to unity. Two different methods to change the polarisation direction of the beam were used.

Precession Coil Flippers

For the first measurements a precession coil spin flipper was used as introduced by Mezei [128]. This is a device based on the Larmor precession introduced in 2.3. Two rectangular coils are wound perpendicular to each other around an aluminium frame. Both coils produce a homogeneous field at their inside while the field outside of the coils is only slightly affected. The first coil produces a field which is exactly opposite to the guide field and results in an effective zero-field inside the flipper. The second coil produces a field which is perpendicular to the polarisation direction of the neutron beam. The neutrons enter the region inside the flipper non-adiabatically and start to precess around the magnetic field. The precession angle of the neutron spin after transmission of the spin flipper is given by $\phi = \gamma BL/v$, where γ is the gyromagnetic ratio, B is the magnetic field inside the flipper, L is the transmission length of the device and v is the neutron velocity. By adjusting the current in the second coil, the magnetic field can be tuned such that the precession angle ϕ inside the flipper is exactly 180° for a certain neutron velocity v . As a result the neutrons exiting the flipper have a polarisation which is exactly opposite to the incoming polarisation. From the dependence of ϕ on the neutron velocity it is easily seen that such a spin flipper only works well for a monochromatic neutron beam. This was a main reason for installing a monochromator at the ANTARES beam line. However, Hayter [129] showed that the flipping efficiency of such a spin flipper is not very sensitive to a small wavelength spread. For the dependence of the flipping efficiency f on the wavelength spread $\Delta\lambda/\lambda$ in case of a triangle-shaped wavelength distribution Hayter finds

$$f = 0.5 + (1 - \cos \pi\delta)/(\pi^2 \delta^2), \quad (3.3.2)$$

where $\delta = \Delta\lambda/\lambda$. A plot of this equation, shown in Fig 3.3.1, yields that e.g. at a wavelength spread of $\Delta\lambda/\lambda = 10\%$, which is typical for a velocity selector, a flipping efficiency $f > 0.99$ can be expected.

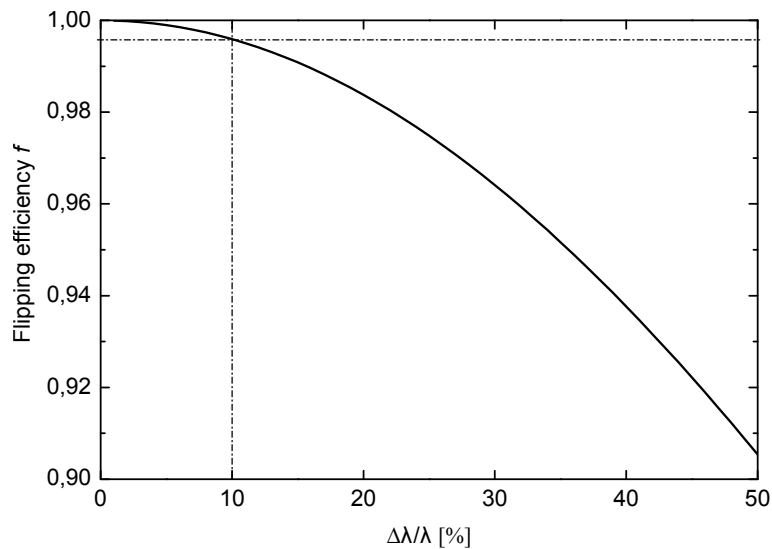


Figure 3.3.1: Flipping efficiency f of a precession coil spin flipper as a function of wavelength spread $\Delta\lambda/\lambda$ for a triangular wavelength distribution.

AFP Flippers

For the measurements after April 2009 a new magnetostatic box became available at FRM II, which has an integrated RF flipper that allows to flip the polarisation of the ^3He gas instead of the polarisation of

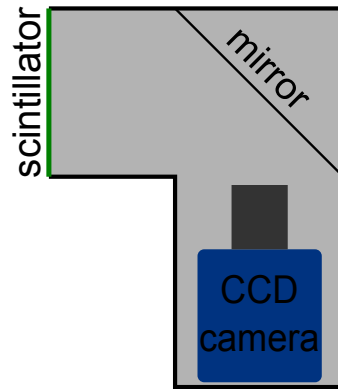


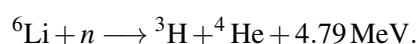
Figure 3.4.1: Schematic drawing of the detector consisting of a cooled CCD camera, which records the image on the scintillator via a single-lens reflex (SLR) camera lens and a 45° mirror.

the neutron beam [130]. This flipper is based on the AFP (adiabatic fast passage) technique, for which a constant permanent magnetic field B_0 is combined with an RF field B_1 rotating in the plane perpendicular to B_0 . By sweeping the frequency of the RF field for a duration of several ms, the polarisation of the ^3He gas can be flipped with a polarisation loss of less than 2×10^{-5} per flip. Flipping the polarisation of the gas has the big advantage that it is also possible to flip the polarisation of a polychromatic beam. However, as shown in eq. (3.2.1), the polarisation of a neutron beam polarised with ^3He depends on the wavelength and decreases with decreasing wavelength. To obtain a high beam polarisation for polychromatic measurements at ANTARES, a polycrystalline Be-filter was placed into the beam, which cuts down the intensity of neutrons with a wavelength $\lambda < 4\text{\AA}$ by more than a factor 10 as described in [111], resulting in a beam with $\bar{\lambda} > 4\text{\AA}$ neutrons. With ^3He filling parameters optimised for $\lambda \geq 3.2\text{\AA}$ as described in 3.2.1, the resulting beam polarisation was measured to be $P \approx 90\%$.

3.4 Detector

The detector used for the experiments in this thesis is a standard CCD detector as generally used for neutron imaging, which has been adapted slightly to meet the requirements for polarised neutron imaging. A schematic of the detector is shown in Fig 3.4.1. The neutrons are detected on a scintillating screen, which emits light in the green spectral range. The intensity of the emitted light is proportional to the intensity of the neutron beam. This generates a 2D image of the transmission of the sample on the scintillator, which is then recorded with a low noise CCD detector and digitally read out. The CCD detector records the image via a standard camera lens which looks at the image on the screen under reflection by a 45° mirror, allowing to place the CCD detector outside of the direct beam coming from the reactor. The reason for this is that the scintillator has an efficiency in the range of only 20% for thermal neutrons and the remaining neutrons transmitted through the scintillator would quickly destroy the CCD detector if placed in the direct beam. In the following we briefly discuss the components of the detector.

The scintillator used in this detector is a $^6\text{LiF/ZnS}$ screen, which is probably the most common type of scintillator for the detection of thermal neutrons. The neutrons are mainly absorbed by the ^6Li nuclei due to their high absorption cross section via the reaction



The energy of 4.79 MeV is transformed into kinetic energy of the tritium and the α particle. These particles are then stopped in the scintillator, exciting the ZnS, which then emits approximately $1.77 \cdot 10^5$ photons in the green spectral range per detected neutron [118]. The mean range of the charged particles in the scintillator and its thickness define the maximum resolution of the screen. Since this range is typically larger than the thickness of the scintillator the resolution is mostly governed by the thickness of the screen. For our experiments a $200 \mu\text{m}$ thick scintillator was used, which absorbs $\approx 20\%$ of the incoming neutrons.

The heart of the detector is an ANDOR DW436 16bit CCD camera with a CCD detector of 2048×2048 pixels, which can be thermoelectrically cooled down to -70°C , decreasing the CCD dark current and noise to values which are absolutely negligible for this application. The CCD detector is a back illuminated type with a peak quantum efficiency of $> 96\%$, which lies in the green spectral range where the scintillator has its maximum light output. One detected photon on the CCD chip produces approximately one electron-hole pair in the CCD chip, which is then digitised into approximately one grey level (GL). This shows the high sensitivity of this CCD detector which is in principle capable of detecting single photons (however, the noise level in the chip is typically larger than the signal obtained from a single photon). The CCD chip is coupled to a high end Leica 100mm single-lens reflex (SLR) camera lens with an F number of $F = 2.8$. The maximum optical resolution achieved with this lens in other experiments was of the order of $30 \mu\text{m}$, however, such high resolution was not necessary for polarised neutron imaging due to the limitation of the geometric resolution of the beam to $\approx 300 \mu\text{m}$. Considering the efficiency of the CCD chip, the lens and the mirror, one detected neutron produces a signal of several ten GL in the digital image, which is read out from the camera. The exact value of grey levels per neutron, however, depends strongly on the selected lens and the field of view of the camera.

For most of the measurements a ^3He analyser was used, which has to be placed inside a bulky magnetostatic box as described in 3.2.1. To be able to place the scintillator directly behind the ^3He -filled cavity inside this box, an extension to the camera box containing the CCD detector was built which fits inside the magnetostatic box and holds the scintillator.

Chapter 4

Data Acquisition and Evaluation

For most measurements described in chapter 5, a common procedure of data acquisition and evaluation has been used. This chapter focuses on the measurement procedure, the experimental setups used for the measurements and the data evaluation. Where appropriate, we will refer to this discussion when presenting the experimental results in chapter 5.

In 4.1 we will describe the general measurement procedure used to obtain the neutron depolarisation after transmission of the sample from the measured intensities at the detector position. Furthermore the process of data evaluation and the determination of the Curie temperature from the measured beam depolarisation will be discussed.

Several different experimental setups have been used for the measurements described in chapter 5. An overview of these setups and a discussion of their advantages and disadvantages will be given in 4.2.

In addition to the neutron depolarisation measurements, magnetisation measurements have been performed on several samples using a Quantum Design Physical Property Measurement System (PPMS). The evaluation of the magnetisation data and the determination of the ordered moment m_s and the ordering temperature T_C from these data will be described in 4.3.

Finally, a method was developed to determine the saturation magnetisation from the temperature dependence of the neutron depolarisation. This offers the possibility to investigate inhomogeneous samples in a single measurement without having to prepare several small and homogeneous samples for bulk measurements. The determination of M_s from the depolarisation data will be shown in 4.4.

4.1 Measurement Procedure

The general principle of neutron depolarisation imaging (NDI) measurements is to determine the beam polarisation after transmission of a sample as a function of position. To evaluate the effect of external parameters like temperature T , hydrostatic pressure p or mechanical strain σ on the magnetic properties of the sample, these parameters have to be tuned while the depolarisation of the beam is measured as a function of these parameters. In this section we will discuss this procedure in a more technical approach and go into further detail about the data evaluation and problems encountered during the measurements.

To determine the beam polarisation from the intensity observed at the detector there are in general two possibilities. If a spin flipper is available, the most effective way to determine the beam polarisation is

to measure the intensities I_+ and I_- of the beam at the detector with the flipper turned “off” and “on”, respectively¹. The beam polarisation P_B can then be calculated as

$$P_B = (I_+ - I_-) / (I_+ + I_-). \quad (4.1.1)$$

If no spin flipper is available, which was the case for our first measurements carried out at HZB Berlin, and the sample has a low Curie temperature, such that the sample can easily be heated to the paramagnetic state, the polarisation can also be determined from the measurement of the intensity $I_+(T)$ at the desired temperature and an additional measurement of $I_{+,PM}$ in the paramagnetic state. The beam polarisation is then calculated as

$$P_B = 2(I_+(T) / I_{+,PM}) - 1. \quad (4.1.2)$$

However, one has to assure that the sample is entirely paramagnetic for the measurement of $I_{+,PM}$, which was only achieved at room temperature for several of the investigated samples. In this case the large temperature difference leads to a significant thermal expansion of cold head and sample, which has to be corrected in order to maintain the correct position of each pixel on the sample. Consequently, whenever possible, we used a spin flipper to determine the beam polarisation.

For all of the following experiments CCD detectors with a 16bit digitisation (i.e. 65535 possible grey levels (GL)) were used. However, the intensity measured by a CCD detector is not immediately proportional to the beam intensity. The built-in analog to digital converter (ADC) adds an offset value to the measured value in order to avoid negative values in the digitisation process, which could occur due to statistical noise. This offset depends on the readout speed and amplification set in the CCD detector and is of the order of 1000 GL. Furthermore, some additional pseudo-intensity is generated on the detector by thermally induced particle-hole pairs in the CCD chip. However, at typical operating temperatures of -70°C this effect is only very small ($\approx 10^{-4}$ GL/s).

To account for both of these effects, additionally the intensity I_{dc} with closed optical shutter of the detector is determined, which is known as “dark current measurement”. To obtain the true intensity of the neutron beam, this intensity I_{dc} has to be subtracted from the measured intensity I_m

$$I = I_m - I_{dc}. \quad (4.1.3)$$

When the intensities I_+ and I_- are measured, for a polarised and sometimes even monochromatic beam, one is confronted with a very low neutron beam intensity compared to a relatively high gamma background. This is especially the case at the ANTARES beam line since, in order to obtain a high beam collimation and homogeneity, no neutron guides were used in the design of the facility [92, 93, 124]. As a consequence the instrument has direct sight to the aluminium beam nozzle close to the reactor core, which is an intense source of gamma radiation. As explained in 3.1.2 there was not enough space available to construct a massive beam stop after the monochromator to stop this gamma contamination of the primary beam. Consequently a monochromatic beam has much lower neutron flux than a polychromatic beam but the gamma flux is only reduced by a small amount.

Despite the comparatively low sensitivity of the neutron scintillator to gamma radiation, scattered or secondary gammas can cause bright spots directly on the CCD chip by ionisation. In a standard, un-

¹In fact we are talking about a spatially resolved measurement of the intensities (i.e images) here. In the following we will use a short notation for this, where e.g. $I_+ \triangleq I_+(x,y)$. All calculations discussed in the following therefore have to be evaluated pixelwise as $P_B(x_0,y_0) = (I_+(x_0,y_0) - I_-(x_0,y_0)) / (I_+(x_0,y_0) + I_-(x_0,y_0))$.

polarised measurement with an exposure time of 7s and fully open beam channel, approximately 86% of all pixels in the detector are affected by gamma radiation, which raises their intensity by more than 100GL. A typical histogram of a dark image with closed optical shutter of the detector but open neutron shutter is shown in Fig. 4.1.1. The constant offset and dark current were subtracted from this histogram to show only the gamma-induced intensity. From the histogram it can be seen that there is a pronounced maximum of gamma spots with an intensity between 10GL and 100GL, however there exist some ultra bright spots that come close to a value of 10000GL.

Being produced directly on the CCD chip, gamma spots are not blurred by the optical imaging procedure of the lens and are sharper than the image recorded from the scintillator. This fact makes it relatively easy to distinguish gamma spots from structure of the sample by their sharpness. There exist many different techniques for filtering images and reducing the amount of spots. In this work a search & replace algorithm was used, which identifies the gamma spots and replaces the value of the affected pixel(s) with the mean value of its/their neighbouring pixels [112].

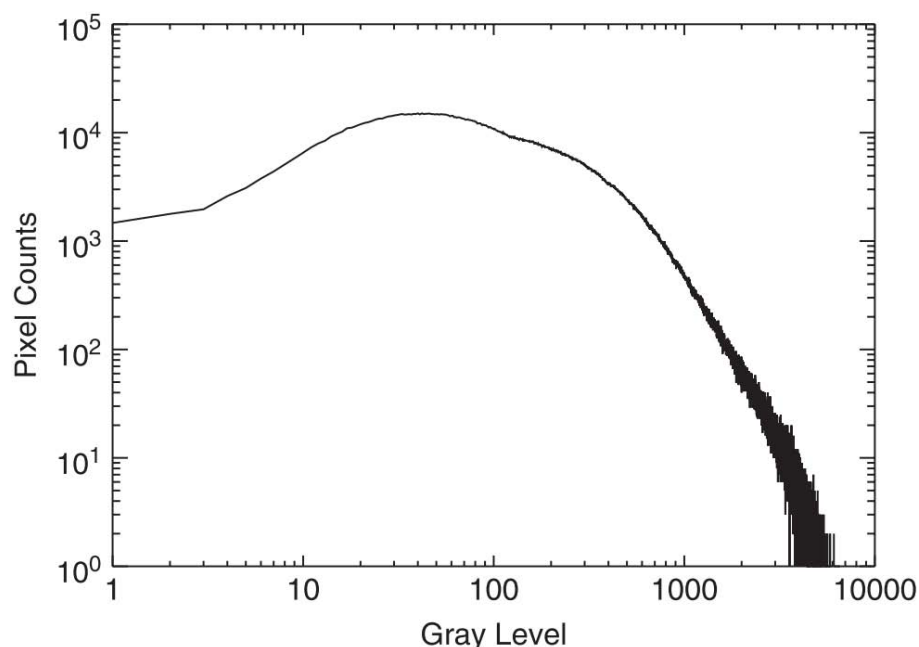


Figure 4.1.1: Histogram of a dark image acquired with closed optical shutter of the detector but open neutron beam and an exposure time of 7s. The dark current and offset were subtracted to only show the gamma-induced intensity. The value of most pixels is raised by 10 – 100GL. Furthermore, there exist some ultra bright spots with intensities up to 10000GL. A total of 86% of all pixels are affected by gamma spots.

Due to the even longer exposure times of typically 60s for polarised or monochromatic measurements, essentially all pixels of the CCD detector would be affected by at least one gamma spot, which consequently takes away the possibility of removing these spots with the search & replace strategy described above.

The gamma flux at the detector position could, however, be significantly reduced by the installation of a massive beam stop inside the entrance channel to the sample area at ANTARES. This channel has a cross section of $40 \times 40 \text{ cm}^2$, which was designed for experiments with large samples. Since the samples used in our polarised neutron radiography experiments were comparatively small, the installed beam stop transmits only a beam cross section of $7 \times 7 \text{ cm}^2$, while the remaining part of the beam is stopped in a

shielding of 20 cm of borated polyethylene and 30 cm of lead. Thus, it was possible to reduce the amount of gamma spots to a level that allows the application of a gamma spot filter even for an exposure time of 60 s. However, to improve the neutron counting statistics, it is necessary to record several images with this exposure time and sum up their intensities after spot removal.

Including the gamma filtering algorithm, the beam polarisation at the detector can thus be written as

$$P_D = \frac{\sum_i (G(I_{+,i}) - I_{dc}) - \sum_i (G(I_{-,i}) - I_{dc})}{\sum_i (G(I_{+,i}) - I_{dc}) + \sum_i (G(I_{-,i}) - I_{dc})}, \quad (4.1.4)$$

where $I_{\pm,i}$ are the single images with the spin flipper “on” and “off” and $G(I)$ is the gamma filtering function. To correct for the polarising efficiency of the polariser and analyser P_0 , the polarisation P_D can be measured in an area where the beam is not depolarised by the sample (i.e. an area outside the sample). To reduce the statistical uncertainty of the value of P_0 , it is calculated as the mean value of P_D over a larger region in the image, where the beam polarisation is not altered by the sample.

$$P_0 = \text{mean}(P_D |_{\text{nosample}}) \quad (4.1.5)$$

This yields the final procedure from which the polarisation of the beam P after transmission of the sample is obtained

$$P = \frac{1}{P_0} \frac{\sum_i (G(I_{+,i}) - I_{dc}) - \sum_i (G(I_{-,i}) - I_{dc})}{\sum_i (G(I_{+,i}) - I_{dc}) + \sum_i (G(I_{-,i}) - I_{dc})}. \quad (4.1.6)$$

In all of the experiments described in chapter 5, this procedure was used to calculate P from the measured intensities.

It should be remarked that the polarisation dependence of the scattering cross section does not influence the neutron beam polarisation of the transmitted neutrons as long as the sample is close to magnetic saturation. In an unsaturated sample the polarisation of the nuclei is on the average equal to zero. Therefore, the orientation of the magnetic moments of the atoms is random with respect to the neutron polarisation, leading to an isotropic scattering of both polarisation components. As a consequence, the beam polarisation is not affected by magnetic scattering.

Determination of the Curie Temperature

To determine the Curie temperature of the sample, for many of the experiments, the depolarisation of the beam by the sample was measured as a function of temperature. Typically the sample was cooled in a small guide field of ≈ 10 G below the Curie temperature and then neutron depolarisation measurements with increasing temperature were performed. In the following, the procedure to obtain the Curie temperature from the neutron depolarisation measurements at different temperatures will be discussed briefly.

Generally the beam polarisation is conserved on transmission of the sample if it is in the paramagnetic state. Decreasing the temperature below the Curie temperature leads to the formation of magnetic domains in the sample which depolarise the neutron beam. Due to the increase of the magnetic moment $M(T)$ with decreasing temperature, the precession inside the domains increases, resulting in a stronger depolarisation of the beam. Consequently the Curie temperature can be determined from the onset of beam depolarisation. The typical dependence of the beam polarisation at one pixel is shown as a func-

tion of temperature in Fig 4.1.2. Two methods were used to determine the temperature where the sample starts to depolarise the beam.

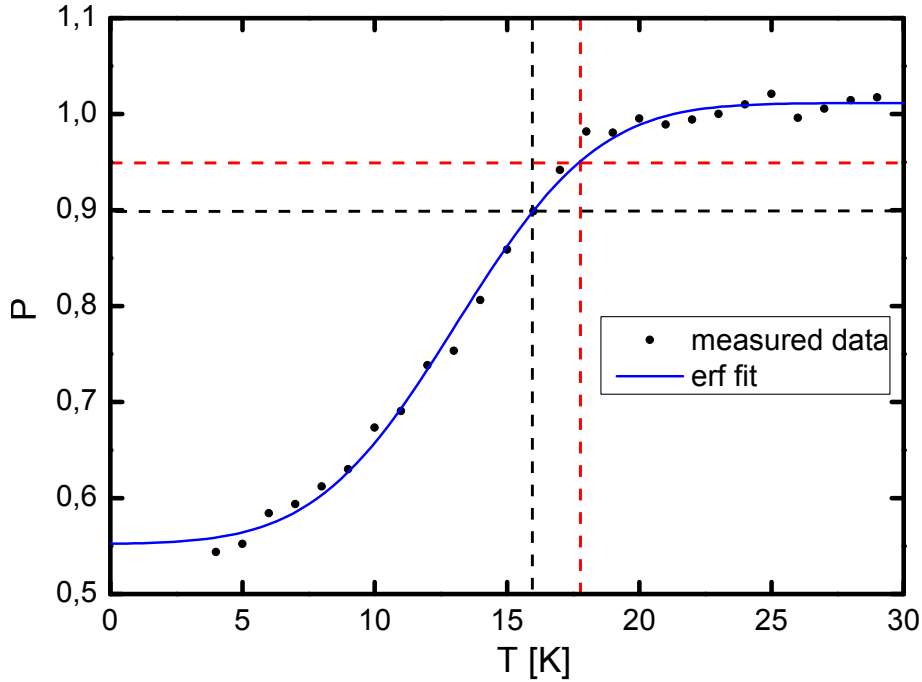


Figure 4.1.2: Typical temperature dependence of the beam polarisation after transmission of a ferromagnetic sample. Different methods of finding the Curie temperature of the sample are discussed in the text and indicated by the fit and the dashed lines.

The first method is based on fitting the polarisation $P(T)$ for each pixel with an appropriate function and finding the Curie temperature from this fit. As an advantage, this method is not so sensitive to statistical errors in single data points. However, if the polarisation has not been measured over a sufficiently large temperature interval, it is often difficult to find a good fit. Good agreement of the observed temperature dependence of the beam polarisation was found with a step function. The data was fitted making use of an error function as shown by the blue line in Fig. 4.1.2

$$P(T) = P(0) + \frac{A}{2} (\text{erf}(\sigma(T - T_{10})) + 1). \quad (4.1.7)$$

Here, $P(0)$ is the beam polarisation extrapolated to zero temperature, A the amplitude, σ a measure for the steepness of the step function and T_{10} is the temperature at which the polarisation is reduced by 10%. These parameters were determined from a Levenberg-Marquardt least squares fit of the measured temperature dependence of the depolarisation data for each pixel. The Curie temperature was defined as the temperature at which the beam polarisation is reduced by 5% (i.e $P = 0.95$) as shown by the dashed red lines in Fig. 4.1.2. This temperature is actually a little lower than the true Curie temperature, however the fit function is very flat in the range between 90% and 100% and the uncertainty in the Curie temperature by imperfect fits would be drastically increased by using a higher threshold for the Curie temperature.

As a second and very simple method, the measured data was compared with a threshold value. The Curie temperature was defined as the highest temperature at which the measured beam polarisation sinks below a certain threshold value. This method is, however, sensitive to noise in single data points, but yields more stable results if the beam polarisation is only measured in a small temperature interval around T_C .

In contrast to that, in the method discussed above, the small temperature interval would lead to severe uncertainties in the steepness σ of an error function fit and therefore to large uncertainties in T_C . An example of this method is shown in Fig. 4.1.2 by the dashed black lines with a threshold of $P < 0.9$. This method yields a slightly lower T_C than the method discussed above. Furthermore, we were obliged to use threshold values as small as 0.6 in several measurements with poor neutron counting statistics (i.e. monochromatic measurements), leading to the determination of an even lower value for T_C . This was necessary because a higher threshold in the flat part of the $P(T)$ plot yields very inaccurate values for T_C for noisy data.

Stray fields

Especially around the edges of the samples, distortions of the magnetic guide field by the sample affect the beam polarisation. The polarisation vector rotates around the locally distorted field, resulting in areas around the sample showing decreased or even negative beam polarisation. This effect is strongest very close to the edges of the sample. An example of this effect is shown in Fig. 4.1.3. The figure shows two images of I_+ at $T = 24\text{ K}$ and $T = 59\text{ K}$ of a $\text{Pd}_{1-x}\text{Ni}_x$ sample. Especially at the positions indicated by the arrows, the image at lower temperature shows significant distortions of the guide field around the sample, which are not present at $T = 59\text{ K}$, where the sample is paramagnetic. This effect was reduced in later measurements by applying a small field in parallel to the guide field by a pair of Helmholtz coils around the sample. These distortions of the guide field generally hinder the correct evaluation of the Curie temperature of the sample especially at the edges of the sample. If field distortions are present, the observed loss in beam polarisation can not be unambiguously attributed either to the effect of depolarisation due to the domains in the sample or to the stray field effects around the sample.

4.2 Experimental Setups

Neutron depolarisation imaging is a new method which was developed during this thesis. Therefore, different experimental setups – each of which has its advantages and drawbacks – have been tested during the measurements described in this thesis. We will at this point give a brief description of the employed setups and their particular properties. An overview of these setups in their chronological order of application is given in Table 4.1, and they will be referenced in the further discussion by the numbers given in the first column of this table.

Setup #1: Solid State Benders at HZB

The very first NDI measurements were performed on $\text{Pd}_{1-x}\text{Ni}_x$ crystals I – IV by the author at HZB, Berlin at the neutron radiography instrument CONRAD [91] in collaboration with N. Kardjilov and A. Hilger.

For this beam time two solid state benders with a beam cross section of $25 \times 50\text{ mm}^2$ were available at the instrument. A schematic drawing of the experimental setup is given in Fig. 3.2.1 (c). The benders consisted of a stack of bent $250\text{ }\mu\text{m}$ thick and 75 mm long Si wafers with an $m = 2$ supermirror coating [119]. The polarising efficiency was determined by the shim method to be $P_b \approx 95\%$. As discussed

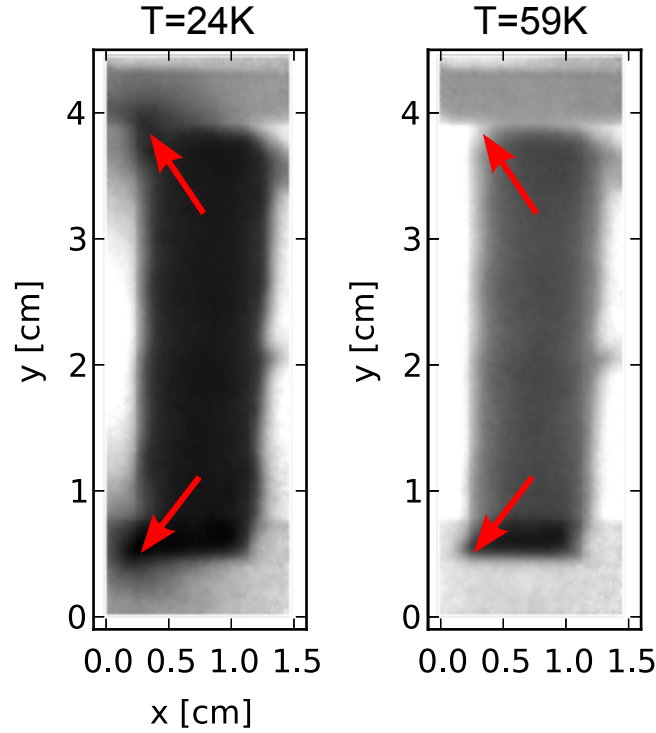


Figure 4.1.3: Images of the intensity I_+ at $T = 24$ K (left) and $T = 59$ K (right) for crystal I. The effect of distortions of the guide field by the sample can be observed for the lower temperature at the positions indicated by the arrows. The distortions are not present at the higher temperature, where the sample is entirely paramagnetic. At the bottom of the images, the sample holder and at the top of the thermal shield of the cryostat – both made of Al – are visible.

in 3.2.3, benders increase the beam divergence and thus deteriorate the spatial resolution of the radiography setup. However an $L/D \approx 100$ was achieved with the polariser being placed approximately 2 m before the sample. In combination with the analyser, the spatial resolution obtained with this setup was ≈ 0.75 mm. A monochromatic beam with a wavelength of $\lambda = 3.5 \text{ \AA}$ was obtained with a double crystal monochromator available at the instrument [99]. For the first measurements on crystals I, II and IV, no spin flipper was used, but for measurements on crystals I and III a precession coil spin flipper was later installed in front of the sample.

The sample was placed in a closed cycle cryostat reaching a base temperature of 5 K. Due to the lack of the possibility to address the cryostat from the instrument software which was used for the measurements, the temperature of the cryostat had to be set on an external computer which had no possibility to interact with the instrument control software. Temperature scans were realised by programming the temperature steps (1 K for most measurements) in the cryostat software in appropriate time intervals. During the run of the temperature scans the detector continuously acquired data with an exposure time of 296 s per image and a readout time of 4 s, which sums up to a total time per image of 300 s. To account for the time the cryostat needed to ramp from one temperature to the next and to afterwards stabilise the temperature, depending on the temperature steps, the first one or two images at each temperature were discarded in the data analysis. The remaining images were summed up to obtain better counting statistics. One thermometer was mounted at the cold head of the cryostat and a second one was mounted at the remote end of the sample. During the measurement a temperature difference between these two thermometers of $\Delta T < 1$ K could be maintained. At temperatures below 20 K this difference was even below $\Delta T < 0.5$ K, even though the sample was not mounted in a closed container with exchange gas.

Nr.	Reactor	Polariser	Analyser	Wavelength		Flipper	Res.	Remarks
				mono	poly			
1	HZB	SSB	SSB	3.5 Å	–	–/PC	0.75 mm	flipper not available for all measurements
2	FRM II	periscope	³ He	3.2 Å	✓	PC	0.5 mm	stripe structure due to mirror waviness
3	FRM II	³ He	³ He	3.2 Å	–	PC	0.4 mm	high beam homogeneity, good spatial res.
4	FRM II	³ He + AFP	³ He	3.2 Å	✓	AFP	0.3 mm	polychromatic measurements with Be filter, very good spatial res.

Table 4.1: Overview of the properties of the different experimental setups used for the neutron depolarisation measurements. Res.: spatial resolution; PC: precession coil spin flipper; AFP: Adiabatic fast passage (RF-flipper for ³He polarisation), SSB: Solid state bender

Setup #2: Periscope Polariser and ³He Analyser

The polarising periscope – a new type of polariser – is described in detail in 3.2.4 and the setup in which it was applied for neutron depolarisation measurements together with a ³He analyser is sketched in Fig. 3.2.5. Ideally, being used as a polariser, the periscope does not alter the beam geometry and the beam collimation is conserved. However, due to the waviness of the mirrors used in the present setup, a stripe structure arises, which on the one hand deteriorates the spatial resolution and on the other hand turns out to affect the beam polarisation. Consequently, the achieved spatial resolution is only of the order of 0.5 mm.

Most measurements with this setup were made on Ni₃Al samples using a polychromatic beam. In combination with a precession coil spin flipper, which only works well with a monochromatic beam, this could only be done due to the following two reasons: On the one hand, the periscope was designed to reflect wavelengths larger than $\lambda = 3.2 \text{ \AA}$, while smaller wavelengths are transmitted through the supermirrors and absorbed in a beam stop inside the periscope. On the other hand, the intensity of the primary beam rapidly decreases for $\lambda > 4.0 \text{ \AA}$. The combination of these two facts leads to a pronounced peak of the intensity in the wavelength interval between 3.2 and 4.0 Å, resulting in a $\Delta\lambda/\lambda \approx 17\%$. According to Fig. 3.3.1, this yields a reasonably high flipping efficiency of $f \approx 0.98$.

Setup #3: ³He Polariser and Analyser + Precession Coil Spin Flipper

In a further step of development the imperfectly functioning periscope was replaced by a ³He spin filter. As discussed in 3.2.1 a setup using two ³He spin filter cells as shown in Fig. 3.2.1 (a) yields very high spatial resolution of $\approx 0.4 \text{ mm}$ and excellent beam homogeneity. This setup was used with a monochromatic beam of $\lambda = 3.2 \text{ \AA}$ only, since a precession coil spin flipper was used. In contrast to the periscope, ³He spin filters also transmit small wavelengths and the use of a polychromatic beam would thus lead to a broad wavelength band which severely affects the performance of the spin flipper.

Setup #4: ^3He Polariser with AFP Flipper and ^3He Analyser

In the beam time in April 2009, for the first time a new ^3He magnetostatic box with an integrated RF spin flipper as described in 3.3 was available at FRM II. This spin flipper allows to flip the nuclear polarisation of the ^3He gas and consequently the beam polarisation. As a major advantage, this method also works with a polychromatic beam. Since the polarising efficiency of a ^3He cell depends on the wavelength of the neutron beam and is smaller at lower wavelengths [115], in order to obtain a high beam polarisation, the wavelength band of the neutron beam was restricted to $\lambda > 4.0\text{\AA}$ by means of a polycrystalline Be filter which was placed in the beam shortly after the pinhole. With this setup and with freshly polarised ^3He gas, flipping ratios of $R \approx 10$ could be achieved. Furthermore due to the larger mean wavelength compared to a monochromatic beam of $\lambda = 3.2\text{\AA}$ and increasing depolarisation of the beam with increasing wavelength (cf. eq. (2.4.9)), higher depolarisation of the beam by the sample was observed. This was especially advantageous for the thin and low T_C slices of $\text{Pd}_{1-x}\text{Ni}_x$ that were investigated and facilitated the determination of T_C .

Most measurements were performed at $L/D = 800$, which results in a maximum possible spatial resolution of approximately $350\text{ }\mu\text{m}$. This is significantly better than what can be obtained with a monochromatic beam, since the monochromator decreases the beam collimation.

4.3 Magnetisation Measurements

Magnetisation measurements on several $\text{Pd}_{1-x}\text{Ni}_x$ and Ni_3Al samples have been performed using a Quantum Design Physical Property Measurement System. This instrument allows to measure the field-dependence of the magnetisation in external fields of up to 9 T. The data obtained have been evaluated using Arrott plots [10] (B/M vs. M^2).

As discussed in 1.2, for materials that comply with SCR theory, Arrott plots should be linear. This behaviour follows from the magnetic equation of state (eq. (1.2.27) in 1.2.2)

$$\frac{B}{M} = A + bM^2 \quad (4.3.1)$$

derived in SCR theory. Deviations from a linear behaviour suggest that there must exist additional contributions to the free energy which have not been considered in the SCR framework, altering the magnetic equation of state. Such contributions complicate the evaluation of the data by introducing nonlinearities in the Arrott plot.

From such Arrott plots, the ordered moment M_s as well as the Curie temperature T_C can be determined. Parameter A is given as the y -value of the intersection of a linear extrapolation of the initial slope of the data towards $M^2 = 0$. In the units used in this thesis, A represents the inverse susceptibility χ^{-1} . The Curie temperature can be determined as the temperature at which $A = 0$. The ordered moment $M_s^2(T)$ can be determined from extrapolation of the low-temperature data towards the x -axis. Finally, b can be found from the slope of the linear fit of the high field data. An example of the determination of these parameters is shown for one data set in Fig. 4.3.1. In contrast to the evaluation of the NDI data shown below, especially the ordered moment obtained from Arrott plots is an extrapolation of the high-field behaviour towards low fields.

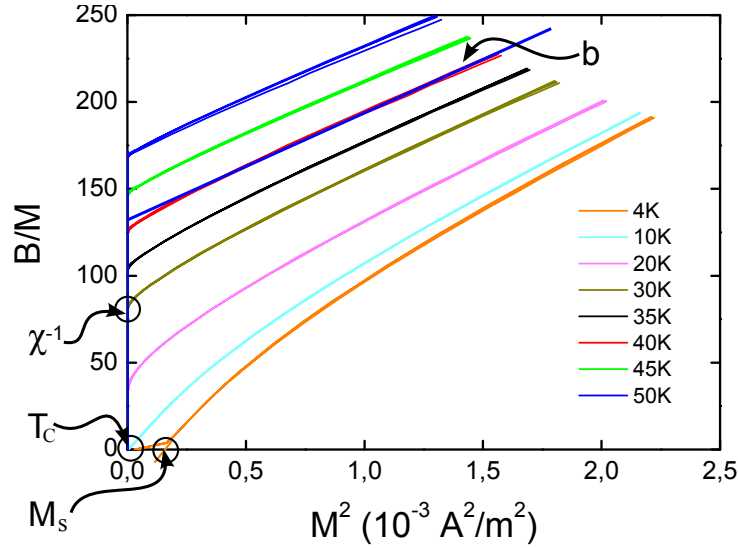


Figure 4.3.1: Determination of the parameters $A = \chi^{-1}$, b , T_C and M_s from Arrott plots.

4.4 Determination of M_s from Depolarisation Data

An extremely helpful application of NDI is to obtain a spatially resolved map of M_s vs. T_C over an inhomogeneous sample. This data can then be evaluated in a plot, giving all values of M_s and T_C over the entire sample in a single measurement. The dependence of M_s on T_C provides information on the nature of the underlying phase transition. Compared to bulk measurements where samples with different magnetic properties have to be prepared in a time consuming procedure and experiments have to be performed on all of these samples separately, the evaluation of M_s and T_C from NDI data is an elegant and time-saving method.

In this section we discuss the evaluation of the NDI data and the determination of the value of M_s from these data. We furthermore show by means of simulations that inhomogeneities lead to a smearing of the phase transition in the temperature dependence of the depolarisation and to an ambiguity in the determination of dependence of the ordered moment $M_s(T_C)$. A comparison of simulated data with the measured data is made and we find that we can reproduce and explain the shape of our measured data plot from our simulations. It, however, turns out that the particular sample we have investigated is too inhomogeneous to determine the intrinsic dependence of M_s on T_C from our measured data.

Calculation of M_s from $P(T)$

The determination of T_C from the neutron depolarisation data was already discussed in 4.1. Therefore, we additionally tried to find a way to obtain the value of M_s from the depolarisation data. An advantage of the determination of M_s from NDI data is that these data are acquired in low magnetic field (i.e. only the applied guide field of approximately 10^{-3} T) and no extrapolation towards low fields has to be made. In so far NDI offers a more direct possibility of determining the ordered moment. According to eq. (2.4.9) the beam polarisation after transmission of a ferromagnetic sample with random orientation of the domains is given by

$$P = P_0 \exp\left(-\frac{1}{3}\gamma^2 \mu_0^2 M^2 \frac{d\delta}{v^2}\right). \quad (4.4.1)$$

Here, d is the sample thickness, δ the average domain size, v the neutron velocity and M is the magnetisation inside the single domains. Using this relation, the value of $M(T)$ can be determined from the beam polarisation as

$$M^2(T) = -\frac{1}{\alpha} \ln \frac{P(T)}{P_0}, \quad (4.4.2)$$

where $\alpha := \frac{1}{3}\gamma^2\mu_0^2d\delta/v^2$ is only independent of temperature in the case of constant domain size, which was assumed for evaluation of the data.

If the temperature dependence of $M(T)$ is known, the value of $M_s = M(T=0)$ can be found as the extrapolation of $M(T)$ for $T \rightarrow 0$ derived from the depolarisation data according to eq. (4.4.2). The intrinsic behaviour of $M(T)$ which is generally found for weak itinerant ferromagnets was given in eq. (1.2.1) in 1.2 and is described by a quadratic temperature dependence of $M_s^2(T)$:

$$M^2(T) = M_s^2 \left(1 - \left(\frac{T}{T_C} \right)^2 \right). \quad (4.4.3)$$

In contrast to this intrinsic behaviour, the experimentally observed temperature dependence of $M(T)$ of our particular $\text{Pd}_{1-x}\text{Ni}_x$ sample rather follows a linear dependence of $M(T)$ on T^2 :

$$M(T) = M_s \left(1 - \left(\frac{T}{T_C} \right)^2 \right) \quad (4.4.4)$$

In the following we show that the subsequent transmission of several fractions of a sample with different M_s and T_C , each of which show the intrinsic behaviour of $M(T)$ as described by eq. (4.4.3), yields exactly the observed linear behaviour given in eq. (4.4.4). This will be of great importance for the interpretation of the neutron depolarisation data acquired on $\text{Pd}_{1-x}\text{Ni}_x$.

To prove this statement, simulations of the resulting beam polarisation after transmission of these regions were made. It was assumed that the observed beam polarisation is a product of the depolarisation resulting from all regions traversed by the neutron beam²:

$$P = \prod_{i=1}^N P_i = P_0 \prod_{i=1}^N \exp(-\beta M_i^2(T) d_i), \quad (4.4.5)$$

where N is the number of regions, $\beta = \frac{1}{3}\gamma^2\mu_0^2\frac{\delta}{v^2}$ is assumed to be constant, d_i is the transmission length of the i th region (which was assumed to be constant for all regions, i.e. $d_i = d/N$) and $M_i^2(T)$ is the temperature dependent magnetisation of the i th region given by eq. (4.4.3). Additionally a linear dependence $M_s(T_C) = bT_C + c$ was assumed for each of the regions.

Effect of inhomogeneities on $P(T)$

Using these relations the resulting beam polarisation was calculated as a function of temperature for different arrangements of regions with different magnetic properties in a sample. The schematic results of this procedure are indicated in Fig. 4.4.1 for three subsequent regions. In panel (a) four different configurations of regions named A to D are introduced. Here, the different magnetic properties are

²Note that this assumption is only valid if the size of the regions is much larger than the average domain size. This is because only in this case, the depolarisation formulae are valid.

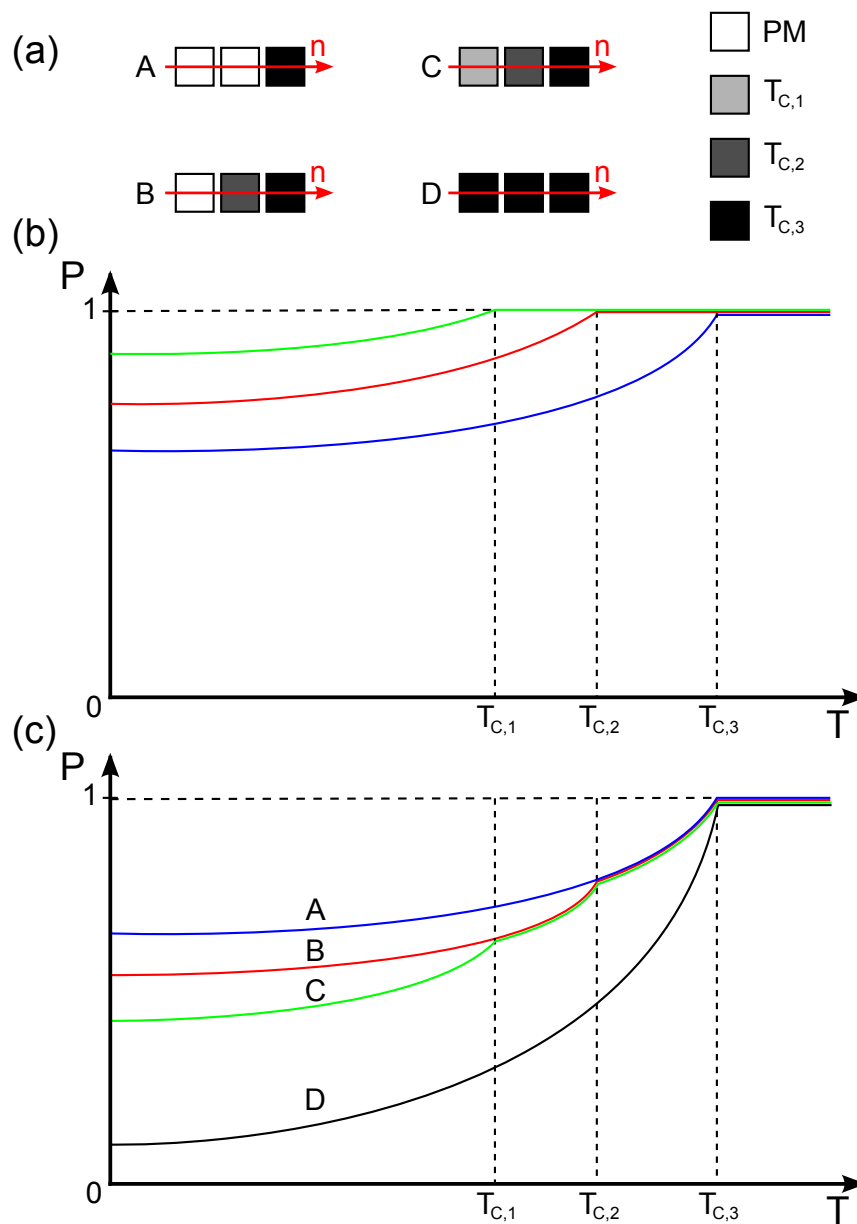


Figure 4.4.1: Schematic description of the depolarisation of a neutron beam through an inhomogeneous sample. In image (a) four different arrangements of regions A to D are defined consisting of three regions with different ordering temperature. Figure (b) shows the depolarisation of the beam as a function of temperature for each of the three ferromagnetic regions, respectively. The paramagnetic region (PM) does not affect the beam polarisation. In image (c) the resulting total depolarisation of the beam for the four different arrangement A to D are shown. All of these curves yield the same value for the ordering temperature ($T_C = T_{C,3}$) but different values for $P(T = 0)$ and therefore different values of M_S .

symbolised by a colour code from white to black, where white depicts a paramagnetic region and black a strongly ferromagnetic region with a high T_C and therefore a high M_s . We will in the following call a sample inhomogeneous if it consists of several regions with different T_C values. In contrast to that a homogeneous sample consists of only a single region with a single ordering temperature.

Panel (b) shows the schematic temperature dependence of the neutron beam polarisation after transmission of a single ferromagnetic region of thickness $d_i = d/3$ with Curie temperatures of $T_{C,1} < T_{C,2} < T_{C,3}$. Above T_C the polarisation has a constant value of 1 and a sharp edge appears at T_C , where the polarisation starts to drop with decreasing temperature and reaches a saturation value essentially defined by M_s for $T = 0$.

As discussed above the polarisation after transmission of the entire sample containing three subsequent regions is given by the product of the polarisations resulting from transmission of the single regions. This result is depicted in panel (c) of the figure for the cases A to D defined above. The curve for case A is drawn in blue. The two paramagnetic regions do not contribute any depolarisation of the beam and the resulting polarisation is given by the single ferromagnetic region with $T_{C,3}$. In contrast to this result, a lower beam polarisation is observed for case D, which involves three strongly ferromagnetic regions with the same $T_{C,3}$. According to eq. (4.4.5) the resulting beam polarisation is the polarisation observed for case A to the third power. These two curves already show that different polarisation is observed for $P(T = 0)$ for both cases even though an analysis of the high temperature depolarisation data will yield essentially the same T_C for both cases³. As the value of M_s can be determined from the value of $P(T = 0)$ according to eq. (4.4.2), an inhomogeneous sample composed of regions with different T_C but the same maximum $T_{C,max}$ will lead to different values of M_s for one value of $T_C = T_{C,max}$.

This fact is further illustrated for cases B and C, where regions of lower ordering temperature and therefore also lower M_s contribute to the depolarisation of the beam at lower temperatures. Here the neutron depolarisation data at high temperatures still yields a Curie temperature of $T_{C,3}$ but the low-temperature data gives intermediate values of M_s compared to cases A and D. This happens because the observed ordering temperature is always the highest ordering temperature of all regions contributing to the depolarisation (i.e. only one region defines the value of T_C). In contrast to that, the value of M_s is defined by the contribution of all ferromagnetic regions for $T \rightarrow 0$.

Furthermore a flattening of the polarisation curves with a higher value of $P(T = 0)$ is observed for inhomogeneous samples in comparison to a homogeneous sample with an ordering temperature $T_{C,3}$. The calculation of M_s from $P(T = 0)$ therefore always leads to a lower value of M_s than for the homogeneous case. This ambiguity will be discussed in more detail below in the context of the evaluation of the $M_s(T_C)$ diagram obtained from the depolarisation data on $\text{Pd}_{1-x}\text{Ni}_x$.

A simulation of the beam polarisation after transmission of an arrangement of 2000 regions with a random distribution of ordering temperatures $0 \leq T_{C,i} \leq 18 \text{ K}$ and a maximum ordering temperature of $T_{C,max} = 18 \text{ K}$ is shown by the blue line in Fig. 4.4.2. For comparison, the green line in this plot shows the beam polarisation as a function of temperature for the case of a homogeneous sample of equal thickness consisting of a single region with a similar ordering temperature of $T_C = 18 \text{ K}$. It is clearly observed that the shape of the curve for the inhomogeneous sample is rounded and the phase transition is smeared out by the inhomogeneity. It should be noted that in the case of a smaller number of transmitted regions

³The effect of the threshold which is used to define T_C on the exact value of the ordering temperature will be discussed below.

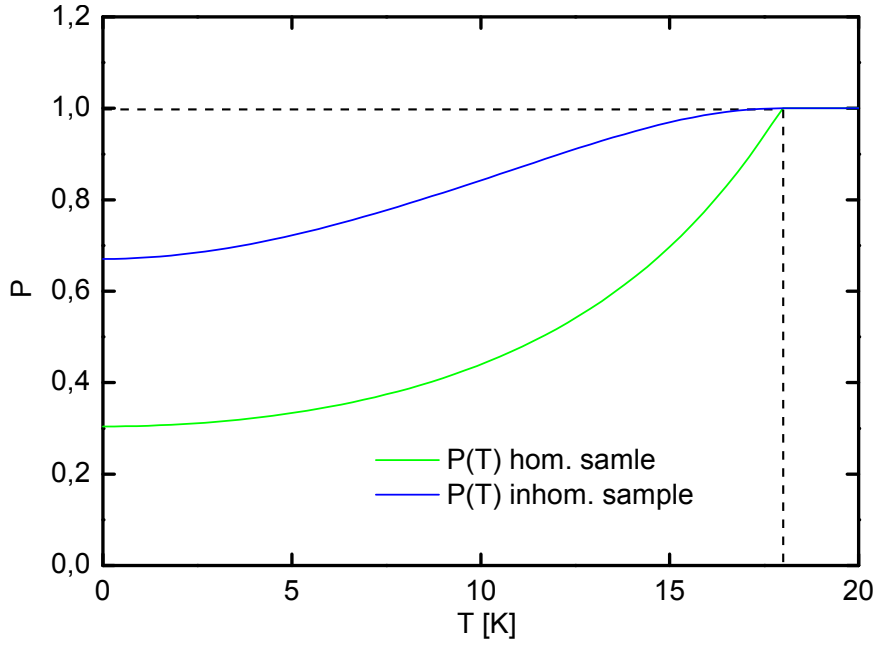


Figure 4.4.2: Simulated temperature dependence of the beam polarisation after transmission of an inhomogeneous sample consisting of 2000 subsequent regions with random ordering temperatures (blue) compared with the depolarisation caused by a homogeneous sample (green) with an ordering temperature which is equal to the maximum T_C found in the inhomogeneous sample.

(i.e. only 20 regions), the rounding of the curve is slightly decreased but the general shape of the curve remains. This large number of regions was only used to smooth the curve.

The curve of the inhomogeneous sample resembles the shape of the measured curve for a $\text{Pd}_{1-x}\text{Ni}_x$ sample, which was shown in Fig. 4.1.2 much more than the curve of the homogeneous sample. On the one hand, this justifies the use of an error function fit to determine the ordering temperature from the depolarisation data. On the other hand and more importantly, this result shows that the measured depolarisation results from the transmission of an inhomogeneous sample. Furthermore, this observation allows to establish the rounding of the $P(T)$ curves as a measure of inhomogeneity in the sample. Additionally the good agreements of the measured data with the simulations gives further proof that the decrease of spin polarisation after traversal of the sample results from true depolarisation of the beam and not from a rotation of the polarisation vector around locally inhomogeneous stray fields around the sample.

Effect of inhomogeneities on $M_s(T)$

The effect of inhomogeneities on the determination of the temperature dependence of $M(T)$ from the depolarisation data according to eq. (4.4.2) was studied in more detail. As discussed above, the intrinsic behaviour of weak itinerant ferromagnets shows a $M^2(T) \propto -T^2$ dependence, whereas the measured dependence of our $\text{Pd}_{1-x}\text{Ni}_x$ samples is in good agreement with a $M(T) \propto -T^2$ dependence. It can be verified from our simulations, that the transmission of an inhomogeneous sample yields exactly this result. Using eq. (4.4.2), M_s was calculated from the simulated depolarisation data as a function of temperature and plotted in Fig. 4.4.3 for a homogeneous sample (green) and an inhomogeneous sample again consisting of 2000 random regions (blue). In the inset we show the linear behaviour of

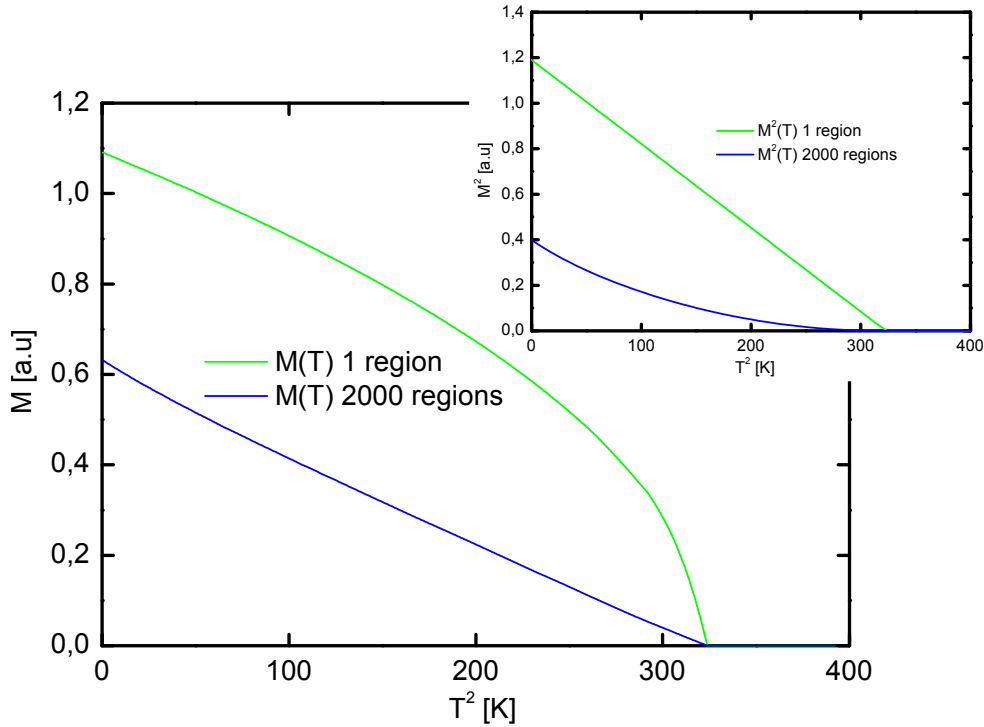


Figure 4.4.3: Simulated temperature dependence of $M(T)$ for an inhomogeneous sample consisting of 2000 subsequent regions (blue) and a homogeneous sample (green). The inset shows the intrinsic linear behaviour of $M^2(T^2)$ for a homogeneous sample. In contrast to that the inhomogeneous sample is in good agreement with a linear behaviour of $M(T^2)$, which is also consistent with the measured data on $\text{Pd}_{1-x}\text{Ni}_x$.

the homogeneous sample in a $M^2(T)$ vs. T^2 plot. Such a linear behaviour – however, with a random distribution of M_s values – was also assumed for all regions of the inhomogeneous sample. It is nicely observed in the main panel of the plot that the inhomogeneous sample yields a linear behaviour when plotting $M(T)$ vs. T^2 .

Dependence of M_s on T_C

A major goal of our NDI experiments was to find a way to obtain the intrinsic dependence of M_s on T_C for $\text{Pd}_{1-x}\text{Ni}_x$. This dependence, which is to date not exactly known, yields valuable information on the underlying phase transition. If the ordered moment M_s – which is the order parameter of the phase transition – vanishes discontinuously for $T_C \rightarrow 0$, the phase transition is first order and no QCP can exist in the material. For a QCP one would expect the ordering temperature to track the ordered moment M_s down to zero, providing evidence for a second order phase transition. Therefore we have tried to obtain spatially resolved information on the distribution of the values of M_s and T_C for an inhomogeneous sample.

As discussed above, the value of M_s was determined from the extrapolation of the ordered moment obtained from the depolarisation data towards low temperature using eq. (4.4.2). During the evaluation of the data we found that the observed $M(T)$ behaviour complies with eq. (4.4.4) rather than with eq. (4.4.3), which is why a linear dependence of M on T^2 was assumed for the extrapolation towards $T = 0$. However, as shown above, this behaviour gives evidence for inhomogeneities along the transmission

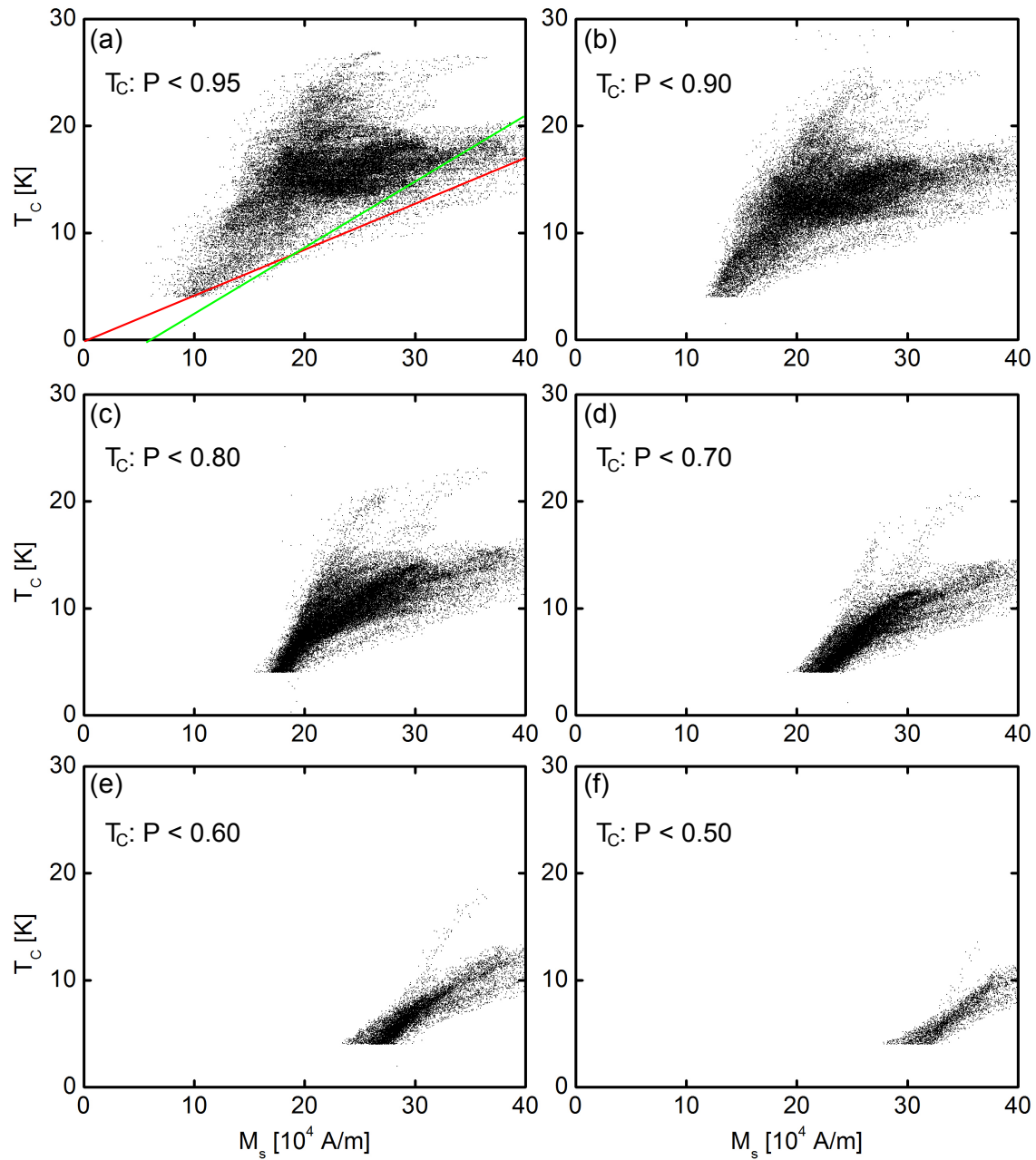


Figure 4.4.4: Dependence of the ordered moment M_s on the ordering temperature T_C for slice #1 of our $\text{Pd}_{1-x}\text{Ni}_x$ samples evaluated from the NDI data. Figure (a) was evaluated with a threshold of 0.95 for the determination of T_C . Decreasing this threshold leads to a shift of the data towards lower T_C which might lead to the false identification of a first order phase transition in $\text{Pd}_{1-x}\text{Ni}_x$.

path of the neutrons through the sample. A plot of all extrapolated values of M_s and their corresponding T_C values is shown in Fig. 4.4.4 (a). Here each point represents a pixel in the depolarisation images, for which the ordered moment as well as the ordering temperature were determined. The value of T_C was in this case determined with the threshold method described in 4.1 using a threshold of $P < 0.95$. This threshold was chosen in the following way. The standard deviation σ of the polarisation above T_C was measured and the threshold was set to $P_{\text{thr}} = 1 - 3\sigma$.

The image shows that no obvious relation between M_s and T_C is observed at a first glance for this sample and that there exists a large bandwidth of M_s values for one T_C value. Most of the observed ordering temperatures lie between 15K and 20K. There are only a few points which extend upwards of this region to a maximum T_C of 28K in this sample. The lowest temperature in the measurements was 4K, which is therefore also the lowest ordering temperature we could detect. For this reason, the plot is cut off towards lower temperatures. Similar to the high temperature end of the plot there exists a smaller number of points at the low temperature end.

Simulation of the $M_s(T_C)$ plots

The simulations already used to obtain the temperature dependence of the depolarisation and the ordered moment can also help to understand and interpret these data. Let us again use the schematic picture introduced in Fig. 4.4.1 where we already showed that in the case of an inhomogeneous sample the extrapolation of the depolarisation data for $T \rightarrow 0$ can yield different polarisation values, and therefore also different values of M_s for one T_C value. The intrinsic M_s corresponding to the measured T_C will only be found in case D, where the sample is homogeneous. In this case the lowest polarisation for $T \rightarrow 0$ of all possible cases with the same T_C will be measured. The value of M_s calculated from this polarisation using eq. (4.4.4) will therefore yield the highest of all possible M_s values for this T_C . All inhomogeneous cases will yield a lower M_s . For a given T_C the highest of all M_s values therefore represents the homogeneous case and consequently the intrinsic behaviour. In the plot in Fig. 4.4.4 (a) the highest M_s values for each T_C are found at the right edge of the cloud of points.

To further illustrate the effect of inhomogeneities on the resulting plots, additional simulations were performed. Two different possible intrinsic dependencies of M_s on T_C were assumed in these simulations. The plots shown in Fig. 4.4.5 were obtained using an intrinsic quantum critical dependence

$$M_s(T_C) = aT_C, \quad (4.4.6)$$

whereas the plots in Fig. 4.4.6 are based on the non quantum critical dependence

$$M_s(T_C) = bT_C + c, \quad (4.4.7)$$

where a , b and c are positive constants. These intrinsic relations are indicated by the red lines in all of the plots. For both figures the sample was simulated as a sequence of two regions with random T_C and corresponding M_s ⁴. The temperature dependence of the beam polarisation was simulated for a large number of random arrangements (up to 10^6) of these two regions. The ordered moment was determined from the value of $P(T = 0)$ using eq. (4.4.2) and the value of the ordering temperature was found as the

⁴The effect of assuming a larger number of transmitted regions leads to a broadening of the plots which will be discussed below. The overall shape of the plots remains, however, unaffected.

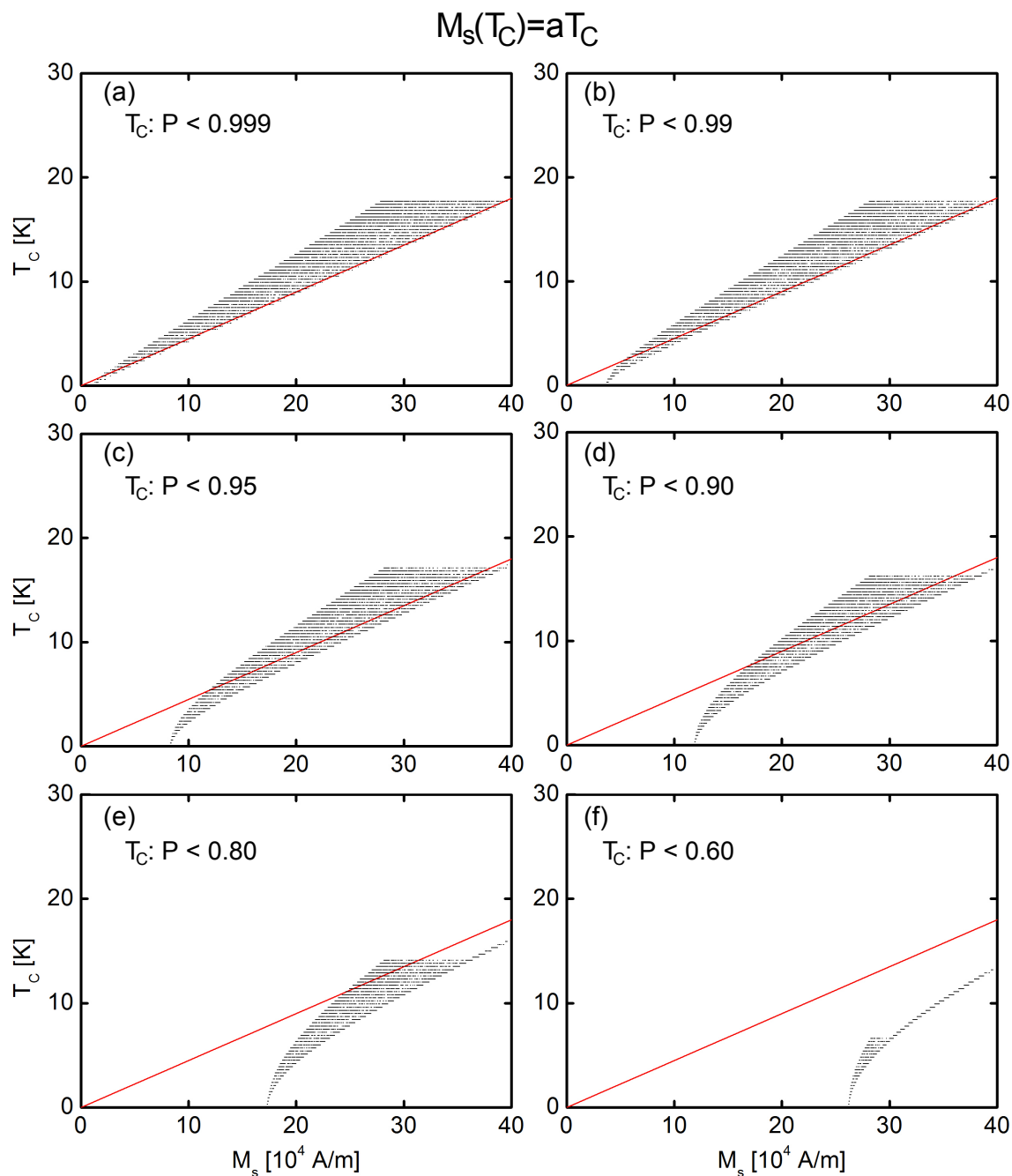


Figure 4.4.5: Simulated relation between M_S and T_C for an inhomogeneous sample consisting of 2 regions with random ordering temperatures. An intrinsic quantum critical relation indicated by the red line was assumed for each of the regions. The variation of the threshold to determine T_C was studied in images (a) to (f). A shift of the curves towards lower values of T_C is observed especially at the low- T_C end of the plot, which increases the resemblance of these plots to the non quantum critical plots shown in Fig. 4.4.6. This effect eventually hinders the determination of the intrinsic behaviour from our measured data.

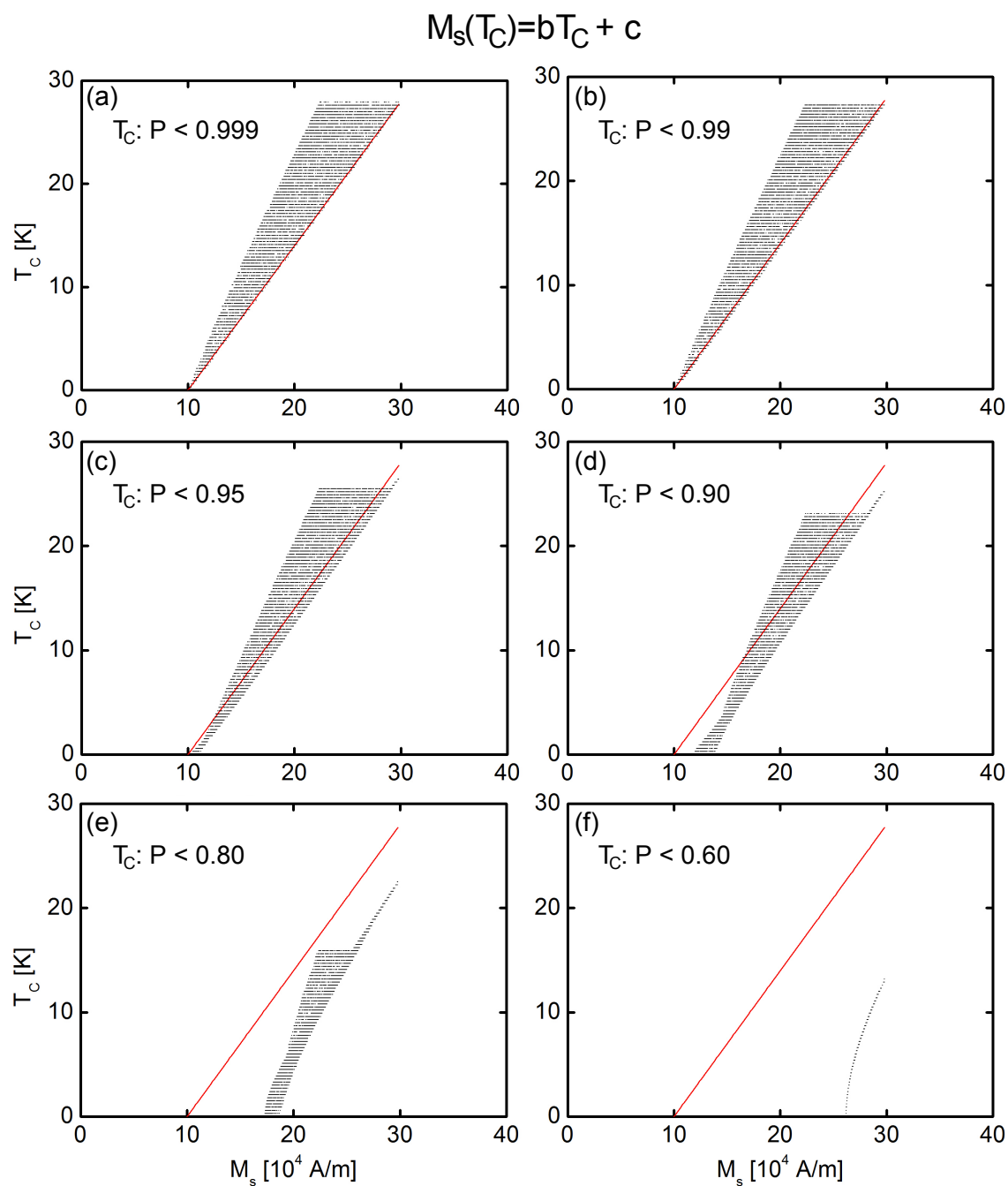


Figure 4.4.6: Simulated relation between M_s and T_C for an inhomogeneous sample consisting of 2 regions with random ordering temperatures. An intrinsic non quantum critical relation indicated by the red line was assumed for each of the regions. The variation of the threshold to determine T_C was studied in images (a) to (f). A shift of the curves towards lower values of T_C is observed especially at the low- T_C end of the plot. However, this effect is smaller than for the quantum critical relation shown in Fig. 4.4.5.

temperature for which the beam polarisation falls below a certain threshold. The effect of changing this threshold from 0.999 to 0.60 is shown in the different plots of the figures.

Let us first assume that the ordering temperature can be determined very accurately, which is equivalent to using a very high threshold value. This has been done in the panels (a) of both figures, where the threshold for the determination of T_C was set to $P < 0.999$. In this case both assumptions yield the intrinsic behaviour only if both regions have the same ordering temperature (i.e. if the sample is homogeneous). For all other cases where one region has a lower ordering temperature than the other, a lower value of M_s is found. As stated above, the intrinsic behaviour – which corresponds to the red line – is found at the right hand edge of the point cloud. It is worth noting that a sharp edge is also observed at the left side of the plot, which results from the case where one of the two regions is paramagnetic (i.e. $T_C = 0$). The width of the plot increases with increasing number of regions in the sample and will be discussed below.

Effect of changing the threshold to determine T_C

The effect of using a smaller threshold was studied in the simulations shown in panels (b) to (f) in Figs. 4.4.5 and 4.4.6. It can be seen that decreasing the threshold has the effect of shifting the points towards smaller T_C values. This effect is most prominent for very flat $P(T)$ curves, i.e. curves with a very small value of M_s (c.f. curve A in Fig. 4.4.1 (c)). Here, the choice of a smaller threshold leads to the determination of a much smaller T_C . In contrast to that, the effect of employing a smaller threshold on curve D in the figure is not so strong, since the curve is steeper. This means that especially low- T_C curves are affected. As a result of this effect the point clouds in the $M_s(T_C)$ plots are shifted towards lower T_C values, especially at the lower end. Furthermore the shape of the clouds for the quantum critical behaviour in Fig. 4.4.5 becomes more and more similar to the shape of the non quantum critical clouds in Fig. 4.4.6. This resemblance prevents the exact determination of the intrinsic behaviour from the measured data, since for thresholds of 0.95 or smaller, the quantum critical plots indicate a first order phase transition.

Effect of the number of regions

We furthermore studied the effect of the number of subsequent regions the beam transmits on the shape of the $M_s(T_C)$ plots. For these simulations the sample thickness was held constant and the sample was divided into different numbers of regions. The results in Fig. 4.4.7 were obtained using a threshold of 0.95 for the determination of the ordering temperature. We find that increasing the number of transmitted regions from 2 to 5 as shown in panels (a) to (d) increases the width of the plot. Furthermore, the edges of the plot become less sharp, which can be explained as a statistical effect. Using a larger number of random regions dramatically decreases the probability of obtaining the extreme cases of a completely homogeneous sample (right edge of the plot) or a sample where only a single region is ferromagnetic and all other regions are paramagnetic (left edge of the plot). No further increase of the width of the plot was observed for a number of regions larger than 5. However, this result may as well be attributed to the same statistical effect which decreases the probability of the extreme cases defining the boundaries of the plot. Comparing our data in Fig. 4.4.4 with these simulations we can say that our $\text{Pd}_{1-x}\text{Ni}_x$ sample consists on the average of more than 5 subsequent regions.

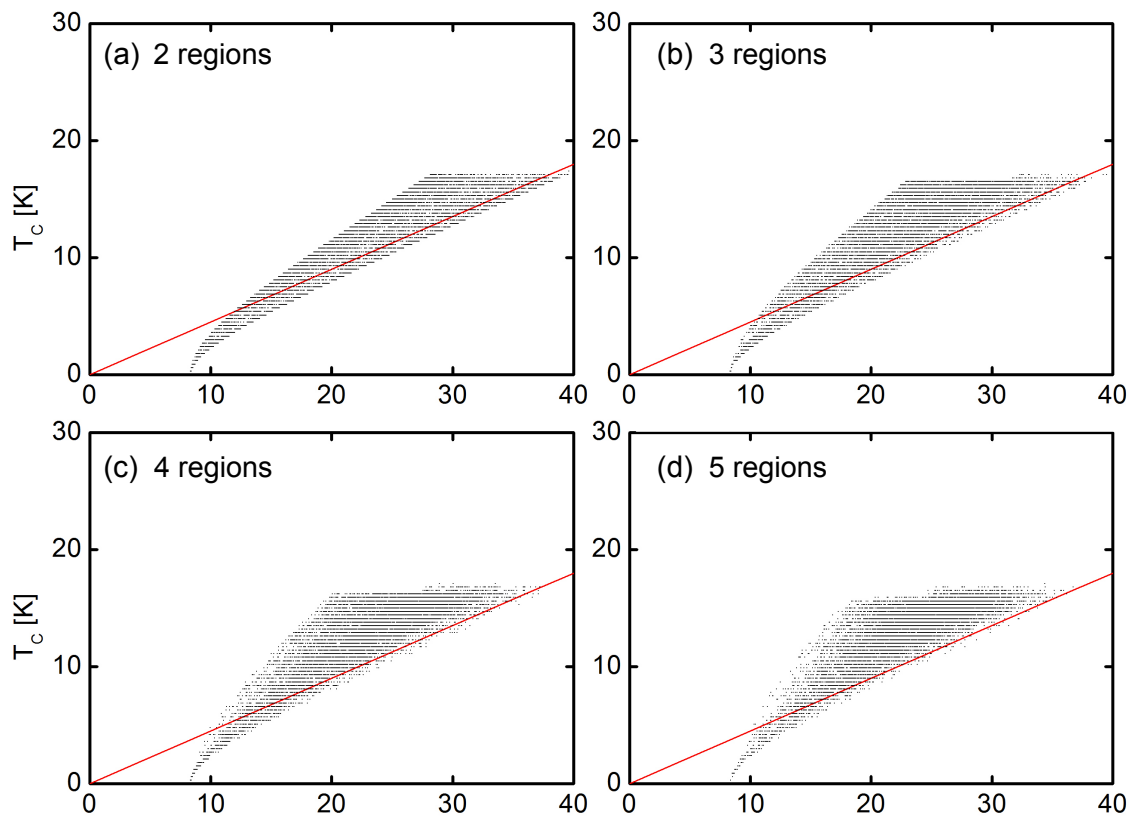


Figure 4.4.7: Simulation of the effect of a variation of the number of transmitted regions of different ordering temperature in an inhomogeneous sample on the relation between M_s and T_C . Increasing the number of regions increases the width of the plot. Furthermore the probability of obtaining a completely homogeneous sample (right edge of the plot) and a sample consisting of only one ferromagnetic region, while all other regions are paramagnetic (left edge) decreases with increasing number of regions. This leads to a decrease of the point density at the edges of the plot.

Conclusions

To conclude, these simulations have shown that all features of the M_s vs. T_C plot obtained from the NDI data can be understood in terms of (i) inhomogeneities of the sample along the transmission path and (ii) the threshold for the determination of T_C . We have shown that the width of the plots increases with increasing number of traversed regions with different ordering temperature. Furthermore we have proven that the decrease of the threshold value used to determine the ordering temperature leads to a shift of the data points towards lower T_C values especially at the low- T_C end of the plot, which may indicate a first order phase transition even though the sample is intrinsically quantum critical.

Tests of changing the threshold for T_C were performed with the measured data as shown in Fig. 4.4.4 (a) to (f). Here the noise in the data prevented the choice of a threshold larger than 0.95. Decreasing this threshold leads to a similar shift of the points towards lower T_C values as for the simulations shown above. Especially the fact that there are not many data points with very low T_C for this particular sample, circumvents the exact determination of the low temperature behaviour of the sample from the right edge of the point cloud. One might as well see a quantum critical behaviour as indicated by the red line in Fig. 4.4.4 (a) as a non quantum critical one as suggested by the green line. However, we can deduce from our simulations that the sample consists on the average of at least five different regions along the sample thickness of 1 mm.

Chapter 5

Experimental Results

This chapter is dedicated to the presentation and discussion of the experimental results obtained with the neutron depolarisation imaging (NDI) technique developed in this thesis.

In section 5.1, first proof of principle measurements performed at the instrument MIRA, FRM II will be shown. This instrument was already equipped with a position sensitive detector and polarisation analysis. Spatially resolved measurements of the magnetisation of Ni and Fe samples in different external fields will be shown.

Section 5.2 will present results obtained on the weakly ferromagnetic materials $\text{Pd}_{1-x}\text{Ni}_x$ and Ni_3Al . The first experiments were performed at the CONRAD beam line at HZB, Berlin. However, most of the presented data was obtained with a neutron depolarisation setup installed at the ANTARES beam line at FRM II.

5.1 First Proof of Principle Measurements on MIRA

To prove the feasibility of radiographic measurements with polarised neutrons, the instrument MIRA at FRM II was used as a test bed. Being located at the end of a neutron guide, MIRA was already equipped with a polarising bandpass supermirror, delivering a wavelength $\lambda \approx 10 \text{ \AA}$ and a polarisation of $P = 0.94$. Inside the monochromator shielding a pinhole can be set to define the beam collimation. Furthermore, a highly efficient position sensitive counting detector with a spatial resolution of $\approx 2 \text{ mm}$ was available at the instrument. Together with spin handling equipment like spin flippers, guide fields, etc. all prerequisites for first spatially resolved proof of principle measurements with polarised neutrons at low spatial resolution were fulfilled.

Setup

In this experiment the instrument MIRA was used to measure the beam polarisation transmitted through a ferromagnetic sample composed of Ni and Fe. An overview of the setup is shown in Fig. 5.1.1. All the experiments were carried out at a wavelength of 10 \AA where no Bragg scattering in the materials Ni and Fe is possible, which also eliminates the effect of magnetic Bragg scattering. The aperture installed directly after the monochromator was set to a size of $5 \times 5 \text{ mm}^2$, which – together with a flight path length

to the sample of $L \approx 280$ cm – yields an L/D ratio of 560 (see 2.5). The resulting geometrical resolution of 1.4 mm at the detector position is well matched to the 2 mm spatial resolution of the position sensitive detector (PSD) available on MIRA. Using a position sensitive detector to image the depolarisation of the beam over the area of the sample yields 2D information about the macroscopic magnetisation of the sample.

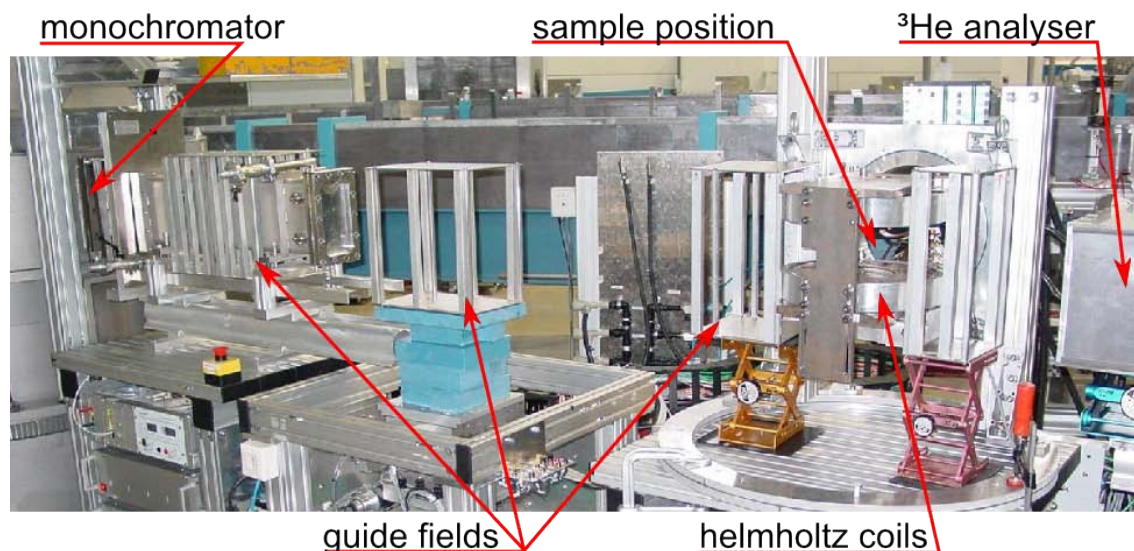


Figure 5.1.1: Photo of the setup used for the first proof of principle measurements on MIRA showing the monochromator housing, the guide fields, the Helmholtz magnet at the sample position and the housing of the ^3He analyser. The spin flipper in front of the sample position was not yet installed.

Between the aperture and the detector, guide fields were installed to conserve the beam polarisation. Furthermore, a spin flipper was used to change the sign of the beam polarisation. As a polarisation analyser a ^3He cell was used, which did not affect the geometrical resolution of the instrument. However, the bulky magnetic housing of the ^3He cell required a sample to detector distance of $d_{sd} \approx 800$ mm.

At the sample position a pair of water cooled Helmholtz coils was available. These could produce fields up to ≈ 3 kG parallel to the direction of the neutron polarisation. The maximum field used in the experiment was, however, only 1.4 kG since higher fields produced severe stray fields outside the sample area that depolarised the beam. The incoming beam polarisation was determined to be $P = 0.94$. The flipping efficiency f of the spin flipper was found to be $f > 0.99$ and will therefore be neglected in the further discussion.

Experiments

As a sample, a Ni slab of 3.5 mm thickness which had a smaller slab of iron of 3 mm thickness mounted on its side was used as shown in Fig. 5.1.2 (left). The sample could be magnetised with the Helmholtz magnet. Since the permeability μ of iron is much bigger than that of Ni, a major part of the magnetic flux is bypassed through the iron slab in the middle of the sample. This leads to a lower magnetisation M in the Ni slab in this region. Iron, however, does not come close to saturation in the applied fields.

Magnetising the sample in external fields of different magnitude made it possible to vary the local magnetisation in the sample. The state of magnetisation was then imaged by recording the beam polarisation transmitted by the sample for different applied magnetic fields.

The sample was magnetised in four different external fields from $400\text{G} < B < 1400\text{G}$. The beam polarisation P_S transmitted through the sample was calculated from I_+ and I_- for each of these fields with

$$P_S = \frac{1}{PP_A} \frac{I_+ - I_-}{I_+ + I_-}, \quad (5.1.1)$$

where P_A is the analysing efficiency. Due to the small pinhole aperture and the long neutron wavelength of 10\AA the flux at the detector was very low. This made it necessary to integrate the intensities on the PSD for several hours (typically 10h for one image of the polarisation P_S). During this time, due to the relaxation of the ^3He gas polarisation, the analysing efficiency P_A was continuously decreasing. In contrast, P was constant, since a supermirror was used to polarise the beam. To minimise the errors introduced in the measured beam polarisation, single images of I_+ and I_- with 900s exposure time were recorded. The polarisation was calculated from each of these images, which were then averaged after correction for the variation of P_A . The analysing efficiency was monitored in an area where there was no object in the beam, making it possible to correct for the relaxation of the ^3He polarisation in the data analysis.

Results and Discussion

The resulting beam polarisation is shown in false colour images in Fig. 5.1.2 for the different fields. The rounded edges at the top of the images at 400G and 1100G are due to the circular ^3He cells which were used for these images, in contrast to the rectangular cells used for the other two images. The Fe slab at the left side completely depolarises the beam in all of the four applied fields. For the Ni slab the beam polarisation after the sample strongly depends on the applied field. At the lowest field of 400G the transmitted beam polarisation is approximately 25% above and below the position of the Fe slab, while at the position of the Fe slab the beam is still completely depolarised. The polarisation in both regions increases with applied magnetic field and reaches a maximum of 80% in the bottom region and 75% at the side of the Fe slab.

Let us consider two extreme cases to explain the results we observed. First let the sample be completely demagnetised. In this case the magnetisation of the different domains is randomly oriented, which leads to a complete depolarisation of the beam at the given sample thickness.

Second, if the sample is fully saturated there exists only one macroscopic domain which is magnetised in the direction of the neutron polarisation. In this case the component of the magnetisation perpendicular to the neutron beam polarisation vanishes and therefore the polarisation after transmission of the sample is conserved.

The images shown are in agreement with the expectation that the Fe slab on the left side bypasses a certain part of the magnetic flux due to its higher permeability μ . As a result the magnetic flux density in the Ni slab and therefore its magnetisation at this position decreases. This decrease of the magnetisation leads to a higher depolarisation of the beam. What can also be seen is that the lower the external magnetic field, the lower is the magnetisation of the bulk material above and below the Fe slab, which also leads to a higher depolarisation of the beam. As said above, iron is far from saturation even at an external field of 1400G. This is why it completely depolarises the beam in all images. In Fig. 5.1.3, vertical plots of the polarisation after transmission of the Ni sample along the red arrow indicated in the image on the right-hand side are shown for different applied magnetic fields. These plots also show the

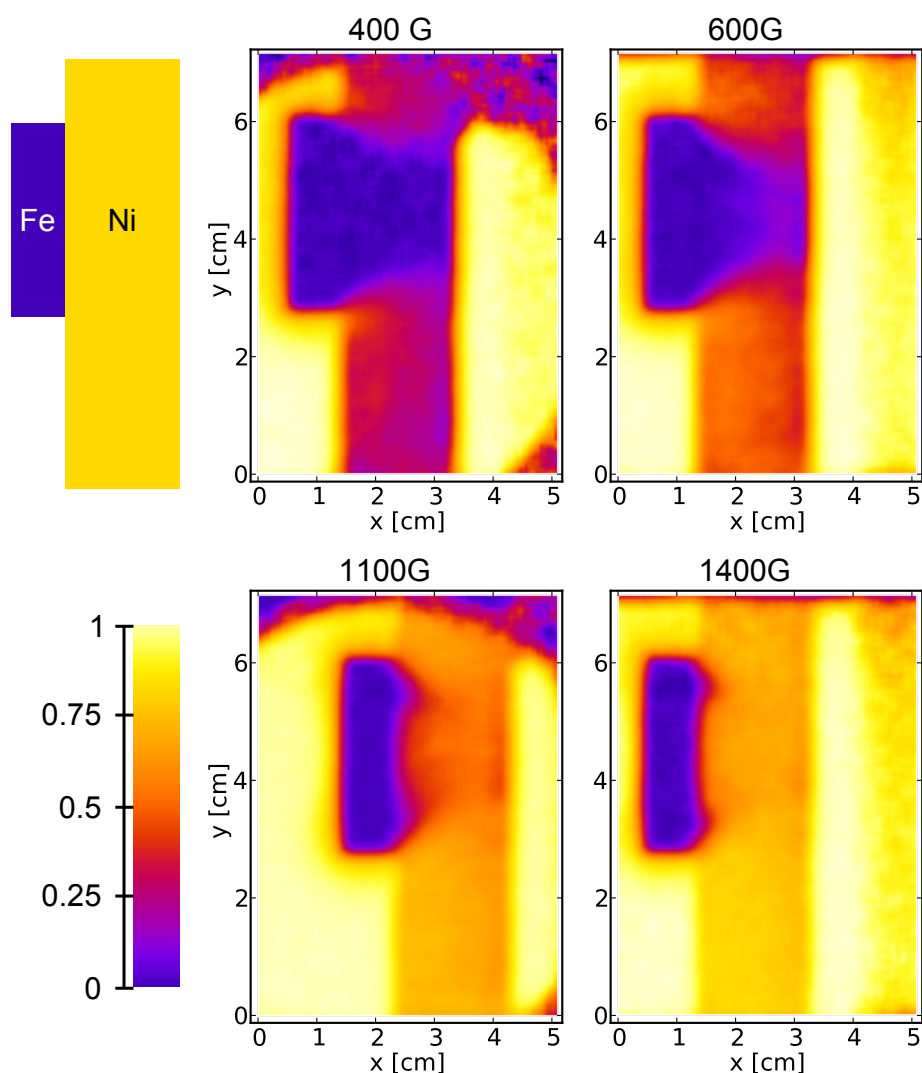


Figure 5.1.2: Beam polarisation after transmission of the sample in false colours (see colour bar) at different magnetic fields from $B = 400\text{ G}$ to $B = 1400\text{ G}$ at the sample position. As seen in the top left image, the rectangle on the left side is the Fe slab, which depolarises the beam completely at all applied fields. The slab to the right is made of Ni for which the depolarisation of the beam depends on the applied magnetic field.

increasing beam polarisation with increasing field strength due to the preferred alignment of the domains parallel to the applied magnetic field and therefore also parallel to the beam polarisation.

Conclusion

This first experiment has proven the feasibility to image the depolarisation of a neutron beam by a ferromagnetic sample. Spatially resolved information about the magnetisation of the sample was obtained, which makes this technique extremely useful to characterise material properties over the whole sample in a single measurement.

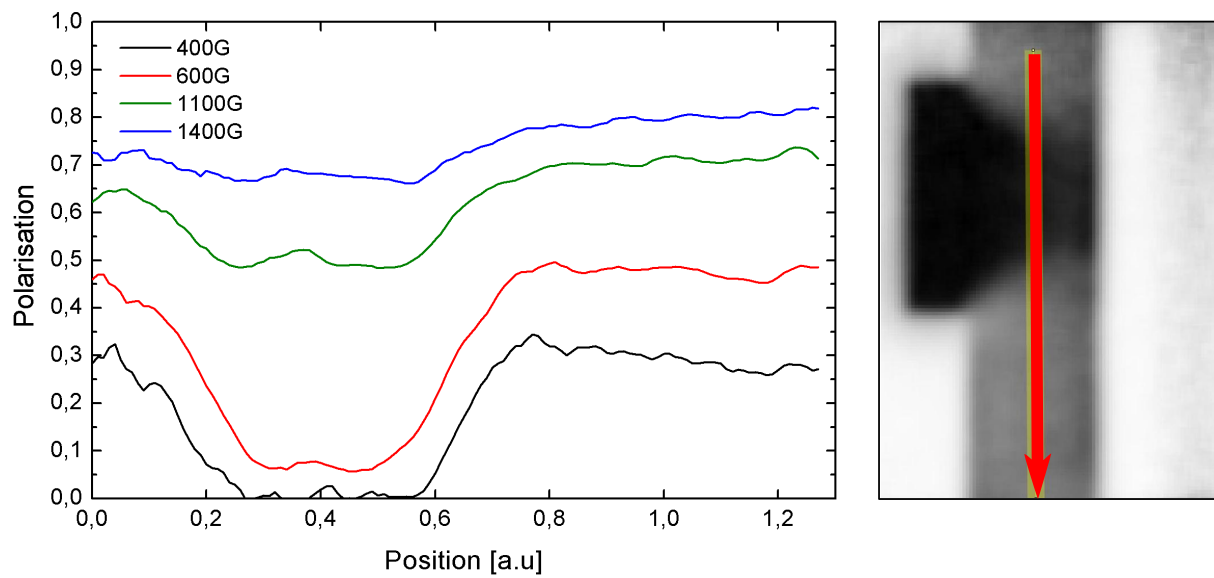


Figure 5.1.3: Beam polarisation after transmission of the Ni slab along the red arrow (from top to bottom) indicated in the right image at different external magnetic fields.

5.2 Measurements on Weakly Ferromagnetic Materials

In the following sections, experiments on the weakly ferromagnetic materials $\text{Pd}_{1-x}\text{Ni}_x$ and Ni_3Al will be presented. As discussed in 1.3, both of these substances have been subject to detailed investigation for many years. In the beginning the intention of our NDI measurements was to verify the homogeneity of the samples, which were to be used for bulk measurements and neutron scattering experiments. However, NDI has proven to be a helpful tool not only for the determination of the sample quality but also for the determination of magnetic properties of the samples as a function of temperature and hydrostatic pressure.

5.2.1 $\text{Pd}_{1-x}\text{Ni}_x$

In the following experiments, several $\text{Pd}_{1-x}\text{Ni}_x$ samples were studied. Four crystals were obtained from the company Mateck [131] with nominal Ni concentrations of 3.14% (crystal I), 2.67% (crystal II), 3.24% (crystal III) and 2.59% (crystal IV)¹, all lying close to the critical concentration of $x_c = 2.6\%$ [36, 49, 50]. Consequently all crystals except crystal IV should order ferromagnetically at a sufficiently low temperature. Crystal IV should be very close to the critical concentration. However, the nominal concentrations of the samples were determined from the amount of Ni in the Pd melt and are therefore not representative for the true concentration of the sample. The final concentration may depend on the growth conditions like growth velocity, temperature, or special features (i.e. peritectic points) in the phase diagram of the material. The crystals were grown by the Czochralski technique and have a diameter of $\approx 10\text{mm}$ and lengths of 26 – 35 mm. A photo of the samples is shown in Fig. 5.2.1. Neutron diffraction measurements on the single crystal diffractometer RESI at FRM II [132] revealed that only one of the four crystals, namely crystal IV with $x = 2.59\%$, is a single crystal, while the other samples are polycrystalline.



Figure 5.2.1: Photo of the four $\text{Pd}_{1-x}\text{Ni}_x$ crystals from Mateck grown by the Czochralski technique. These samples have a cylindrical shape with a diameter of $\approx 10\text{mm}$ and lengths between 26 mm and 35 mm. The crystals will in the following be referenced by their numbers I to IV.

Two slices of 1 mm thickness were cut out of the middle of crystal II along the cylinder axis after investigation of the whole crystal. These two slices have a size of $1 \times 10 \times 26\text{mm}^3$, each and are shown in Fig. 5.2.2. It was chosen to cut crystal II because this crystal is very inhomogeneous and contains a wide range of regions with different Curie temperatures, which gives the possibility to investigate

¹The crystals will in the following be referenced by their numbers I to IV.

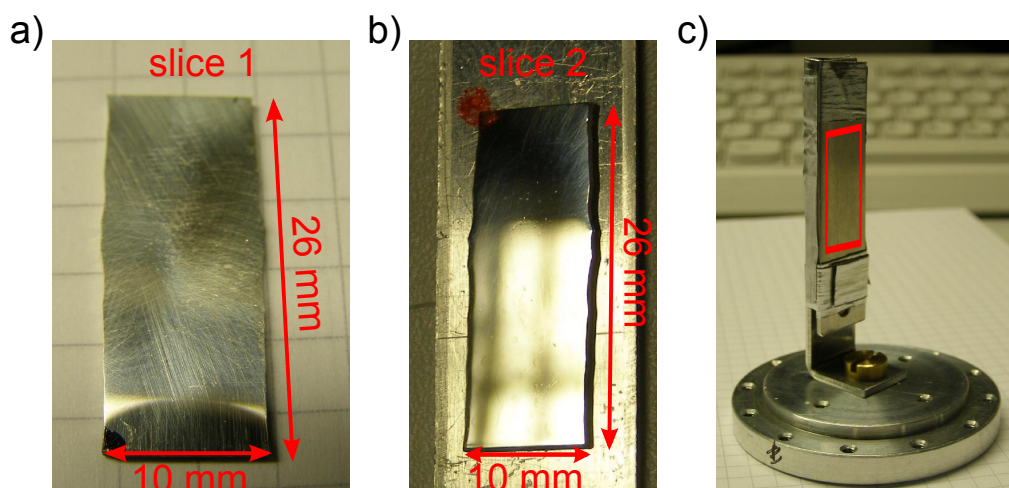


Figure 5.2.2: Photos of slice 1 (a) and slice 2 (b) cut out of the middle of $\text{Pd}_{1-x}\text{Ni}_x$ crystal II along the cylinder axis by spark erosion. After cutting and polishing, the samples were placed between two Al plates which were held together with Al tape (c). This setup was mounted in the sample container filled with He exchange gas and placed in the cryostat.

different magnetic properties within a single sample. Both slices were investigated with neutron depolarisation techniques, and afterwards, ten small samples of 1 mm^3 were cut from slice 1 for magnetisation measurements in a Quantum Design Physical Property Measurement System.

Furthermore, depolarisation measurements were made on two polycrystalline samples from the University of Augsburg, which have been prepared by A. Krimmel by arc melting in argon in exactly the same way as the samples investigated for the publication by Nicklas *et al.* [36]. These samples, which have a Ni concentration of 2.5% (sample A2.5) and 5.0% (sample A5.0) respectively, were used for comparison of the homogeneity of our Czochralski grown crystals with polycrystalline material.

An overview of all experiments on these samples together with a summary of the obtained results is given in Table 5.1

First experiments at HZB, Berlin

The very first NDI measurements were performed on $\text{Pd}_{1-x}\text{Ni}_x$ crystals I – IV by the author at HZB, Berlin at the neutron radiography instrument CONRAD [91] in collaboration with N. Kardjilov and A. Hilger. The object of this experiment was to assess the quality and homogeneity of the four crystals obtained from Mateck. Some of these samples had already been characterised by X-ray Laue imaging and found not to be single crystals. Crystal IV had at that time not yet been characterised by any other method, however, was later found to be the only single crystal.

Since the Curie temperatures of the samples were not exactly known, a coarse measurement with temperature steps of 5 K or 10 K was made before each measurement to roughly determine the Curie temperature of the sample and thus the appropriate temperature range for the scans. A spin flipper was not available for all measurements. In the measurements performed with a spin flipper, only a narrow temperature range below T_C was investigated, since the measurement time doubled due to the measurement of both I_+ and I_- . The maximum temperatures used in these measurements were below the ordering temperature of the samples at several positions, which prevents the determination of T_C from these data.

Sample	x [%]	Date	Setup	Type	λ	T / steps	Results
crystal I	3.14	05/2007	#1, HZB, solid state bender polariser and analyser	T -scan	3.5 Å	24...59K/1K	$T_C = 45 \dots 55$ K, Fig. 5.2.3
crystal II	2.67	05/2007	#1, HZB, solid state bender polariser and analyser	T -scan	3.5 Å	5...40K/1K	$T_C = 6 \dots 20$ K, Fig. 5.2.3
crystal II	2.67	01/2009	#3, FRM II, 3 He polariser and analyser	T -scan	3.2 Å	3.5...29K/0.5K	$T_C = 6 \dots 25$ K, Fig. 5.2.5
crystal II	2.67	01/2009	#3, FRM II, 3 He polariser and analyser	Tomography	3.2 Å	8 K	Fig. 5.2.21
crystal II, slice 1	2.67	04/2009	#4, FRM II, 3 He polariser and analyser	T -scan	polychr.	4...30K/1K	$T_C = 5 \dots 24$ K, Fig. 5.2.6 (a)
crystal II, slice 2	2.67	10/2009	#4, FRM II, 3 He polariser and analyser	T -scan	polychr.	4...30K/1K	$T_C = 5 \dots 24$ K, Fig. 5.2.6 (b)
crystal II, slice 2	2.67	10/2009	#4, FRM II, 3 He polariser and analyser	Tomography	polychr.	12 K	Fig. 5.2.22
crystal III	3.24	05/2007	#1, HZB, solid state bender polariser and analyser	T -scan	3.5 Å	20...60K/1K	$T_C = 45 \dots 55$ K, Fig. 5.2.3
crystal IV	2.59	05/2007	#1, HZB, solid state bender polariser and analyser	T -scan	3.5 Å	5...25K/1K	$T_C = 11 \dots 20$ K, Fig. 5.2.3
crystal IV	2.59	11/2008	#3, FRM II, 3 He polariser and analyser	T -scan	3.2 Å	5...32.5K/2.5K	$T_C = 12 \dots 30$ K, Fig. 5.2.4
A2.5	2.50	01/2009	#3, FRM II, 3 He polariser and analyser	T -scan	3.2 Å	4...65 K	no ferromagnetism, Fig. 5.2.7
A5.0	5.00	01/2009	#3, FRM II, 3 He polariser and analyser	T -scan	3.2 Å	55...75K/1K	$T_C = 66 \dots 73$ K, Fig. 5.2.7

Table 5.1: Overview of the experiments and results on $\text{Pd}_{1-x}\text{Ni}_x$ samples. The setups are described in more detail in 4.2 and their numbers are defined in Tab. 4.1.

However, the experiments without a spin flipper have been performed up to higher temperatures and therefore, the beam polarisation after transmission of the sample was determined as shown in eq. (4.1.2) from calibration to the paramagnetic state of the sample.

A spatially resolved evaluation of the Curie temperature of the samples was done according to the discussion in 4.1 by locating the highest temperature at which the beam polarisation falls below $P = 0.8$. This rather low threshold which definitely yields a T_C lower than the true value was necessary due to the high noise in the acquired data. The resulting T_C maps are shown in Fig. 5.2.3 for all four samples. For each image, the colour code is displayed to the right of the image and the sample positions are indicated by red rectangles. Especially in the T_C images, the effect of stray fields outside of the sample is clearly observed, since these let the algorithm find a Curie temperature even outside of the sample due to the depolarisation of the beam.

Results

These first measurements revealed that all four crystals are highly inhomogeneous in their magnetic properties. Crystal I was investigated in a temperature range from 24 K to 59 K and shows variations of T_C between 45 K and 55 K. An additional measurement with a spin flipper was made, however, the temperature range from 44 K to 53 K was too narrow to determine T_C .

The measurements on crystal II were made without a spin flipper at temperatures from 5 K to 40 K and the obtained T_C varies from 6 K to 20 K. Furthermore, in many regions of the sample the Curie temperature could not be determined since the depolarisation of the beam was too small. This means that there might be regions of the sample which either show a $T_C < 6$ K or stay paramagnetic down to lowest temperatures. To clarify this, experiments with a cryostat with a base temperature as low as 500 mK are already planned.

As for the measurement on crystal I, the temperature range from 32 K to 52 K investigated with the possibility to flip the beam polarisation was too small to obtain a T_C map for crystal III. The map could, however, be obtained from the measurements of I_+ over the wider temperature range from 20 K to 60 K. As a result a variation of T_C from 45 K to 55 K was found.

No spin flipper was used for the measurement on crystal IV, which was carried out at temperatures from 5 K to 25 K. The evaluation of the data yields a T_C in the range from 11 K to 20 K, however, in contrast to the other samples, this crystal – which is the only single crystal – shows a rather linear variation of T_C from one end of the sample to the other and thus is the locally most homogeneous crystal.

Discussion

In conclusion, all four crystals show a variation of T_C of at least 9 K over the sample volume. A layered structure is observed for crystals I to III, which means that the Curie temperature is relatively constant along the x -direction at constant y . This could result from the Czochralski-type growth of the samples. With this method the samples are rotated and slowly drawn out of a melt of the desired composition for the resulting crystal. The growth direction was along the y -axis and the samples were also rotated about this axis during crystal growth. Changes in growth velocity were made during growth to maintain a constant thickness of the ingots [133], which could be responsible for the different compositions of

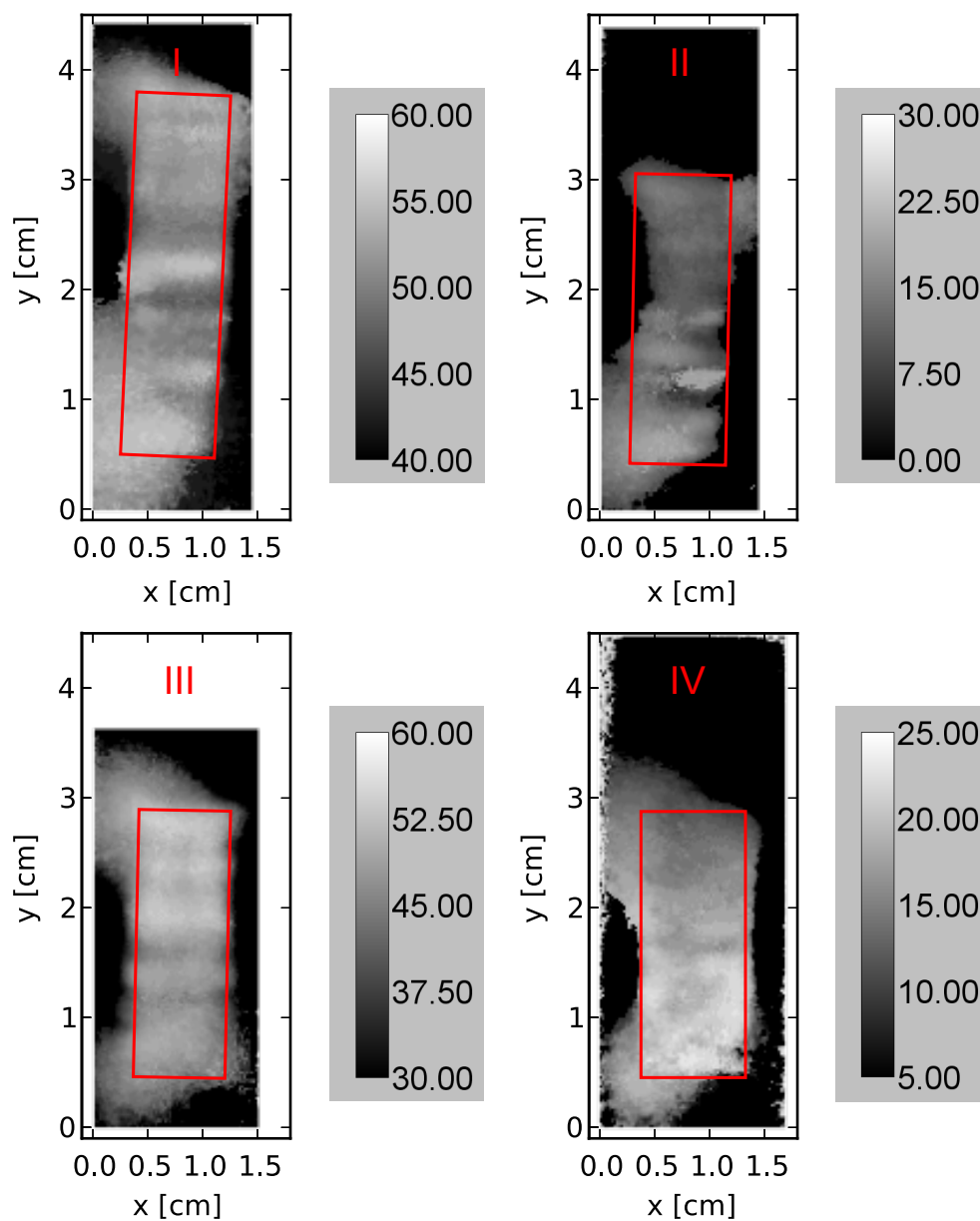


Figure 5.2.3: Resulting T_C maps (in K) for the four $\text{Pd}_{1-x}\text{Ni}_x$ crystals I to IV determined from the first NDI measurements performed at HZB, Berlin. The position of the samples is indicated by red rectangles. Strong artifacts resulting from stray fields around the samples are observed. The spatial resolution was approximately 0.75 mm.

the layers leading to variations of T_C . In contrast to this, crystal IV rather shows a gradient of the Curie temperature along the y -axis. This was the crystal with the lowest Ni concentration in the melt and the gradient might be caused by the crystallisation of $\text{Pd}_{1-x}\text{Ni}_x$ with a higher Ni concentration x in the beginning of the growth process, leaving less Ni in the melt and thus decreasing the Ni content in the subsequent regions of the ingot. Despite having a nominal Ni concentration which lies slightly below the critical concentration, the lowest ordering temperature found for this sample is 11 K.

Both crystals II and IV have a nominal Ni content close to the critical concentration $x_c = 2.6\%$. The results of these experiments show that these two crystals also have the lowest Curie temperatures of all samples. However, even though crystal IV has the lowest Ni concentration, its Curie temperatures are slightly higher than those of crystal II. But crystal II is at the same time much less homogeneous than crystal IV, exhibiting a wider variation of T_C . Crystals I and III have approximately the same nominal Ni content as well, and both show relatively similar Curie temperatures, which are higher than those of the other two crystals. This is also in agreement with their higher Ni content.

Further investigation at FRM II

Crystals II and IV were investigated in more detail at the ANTARES beam line at FRM II using ^3He polarisers and analysers (setup #3 in 4.2), which give much better spatial resolution and beam homogeneity than the solid state benders used for the experiments at HZB. Furthermore, the samples were mounted in a closed container filled with He exchange gas to reduce the temperature gradient over the samples.

For crystal IV a temperature scan of the depolarisation of the beam from 5 K to 32.5 K was measured at a wavelength of 3.2 \AA in temperature steps of 2.5 K. From the temperature dependence of the depolarisation, the Curie temperature of the sample was best determined by fitting the variation of the beam polarisation with temperature with a step function. Just as with the prior measurements strong effects of stray fields outside of the sample were observed. To obtain T_C only at the location of the sample, the calculation of the Curie temperature was restricted to the rectangular region where the sample was located. This region was determined from the transmission images at higher temperature where the sample was paramagnetic and only attenuation of the beam but no depolarisation occurs.

Results on crystal IV

The Curie temperature map obtained for crystal IV is shown in Fig. 5.2.4 in the left panel. The observed T_C ranges from 12 K to 30 K, which is in general agreement with the values observed in the measurements at HZB. However, from the present measurements we find that on a local scale the variation of the magnetic properties is stronger than expected from the low-resolution measurements at HZB.

Using the dependence of T_C on the Ni content x published in the article by Nicklas [36], it was possible to calculate the variations of the Ni concentration over the sample. The concentration dependence shown in this article and in Fig. 1.3.2 contains a compilation of most data published before 1999. All of these independent measurements turn out to be consistent with each other. The resulting concentration map for crystal IV is shown in the right panel of Fig. 5.2.4 and the concentration is found to vary by $\approx 0.8\%$ from 2.9% to 3.7%. We find that the lowest concentration of 2.9% found for this sample is higher than the nominal concentration of 2.59% used in the melt. This observation could either result from an

erroneous preparation of the melt or from the crystallisation of material with higher Ni concentration than the prepared melt. The latter explication would make it rather difficult to grow crystals of a defined Ni content with the Czochralski technique.

Results on crystal II

Measurements with higher spatial resolution have also been made with the same setup for crystal II. In this experiment the depolarisation of the beam by the sample was measured for temperatures from 3.5 K to 29 K in steps of 0.5 K at a wavelength of 3.2 Å. For this measurement a magnetic field of 80 G was applied at the sample position parallel to the guide field. This turned out to completely remove the fringes around the sample caused by field distortions. However, the application of a magnetic field magnetises the sample to a certain degree. Especially in the low T_C regions of the sample which show a very small ordered moment M_s this may have brought the sample close to saturation with a magnetisation pointing in the same direction as the beam polarisation. As a consequence no depolarisation of the beam can be observed in these regions and they seem to be paramagnetic.

The Curie temperatures were determined from the depolarisation measurements as the temperature at which the beam polarisation falls below 60%. This rather strict threshold was chosen as discussed in 4.1 because of the high statistical noise in the images. The T_C map obtained with this method is shown in Fig. 5.2.5. Variations of the ordering temperature between 6 K and 25 K were found but for vast regions of the sample, no T_C could be determined due to the small depolarisation of the beam by the sample. This means that the sample has a Curie temperature smaller than 5 K in these regions or might even be paramagnetic down to $T = 0$.

Slice 1 of Crystal II

All of the measurements described above have been performed on samples of a cylindrical shape. In neutron depolarisation measurements the total depolarisation along the transmission path of the neutron beam through the sample is measured. For a cylindrical sample, the transmission length is larger in the centre of the sample than at the sides. Therefore, higher depolarisation of the beam is expected in the centre of a homogeneous sample.

To determine the effect of the variation of the sample thickness on the depolarisation and the determination of the Curie temperature, after the measurements on the entire crystal described above, a first slice was cut from the middle of crystal II along the cylinder axis with a thickness of 1 mm and a rectangular cross section of $10 \times 26 \text{ mm}^2$. After spark erosion cutting, the slice was polished to remove any remnants from the cutting process from the surface.

This slice, a photo of which is shown in Fig. 5.2.2 (a), was once more analysed for its neutron depolarisation during a subsequent beam time. The depolarisation of the neutron beam was measured with setup #4 described in 4.2 using ^3He polariser and analyser and a polychromatic beam. The temperature was varied from $T = 4 \text{ K}$ up to $T = 29 \text{ K}$ in steps of 1 K. To avoid saturation of the sample, no additional field was applied at the sample position apart from the guide field of $B \approx 10 \text{ G}$.

With a variation of the Curie temperature between 4 K and 24 K as shown in Fig. 5.2.6 (a), this measurement once more confirmed the results already obtained on the entire crystal II and yielded even higher

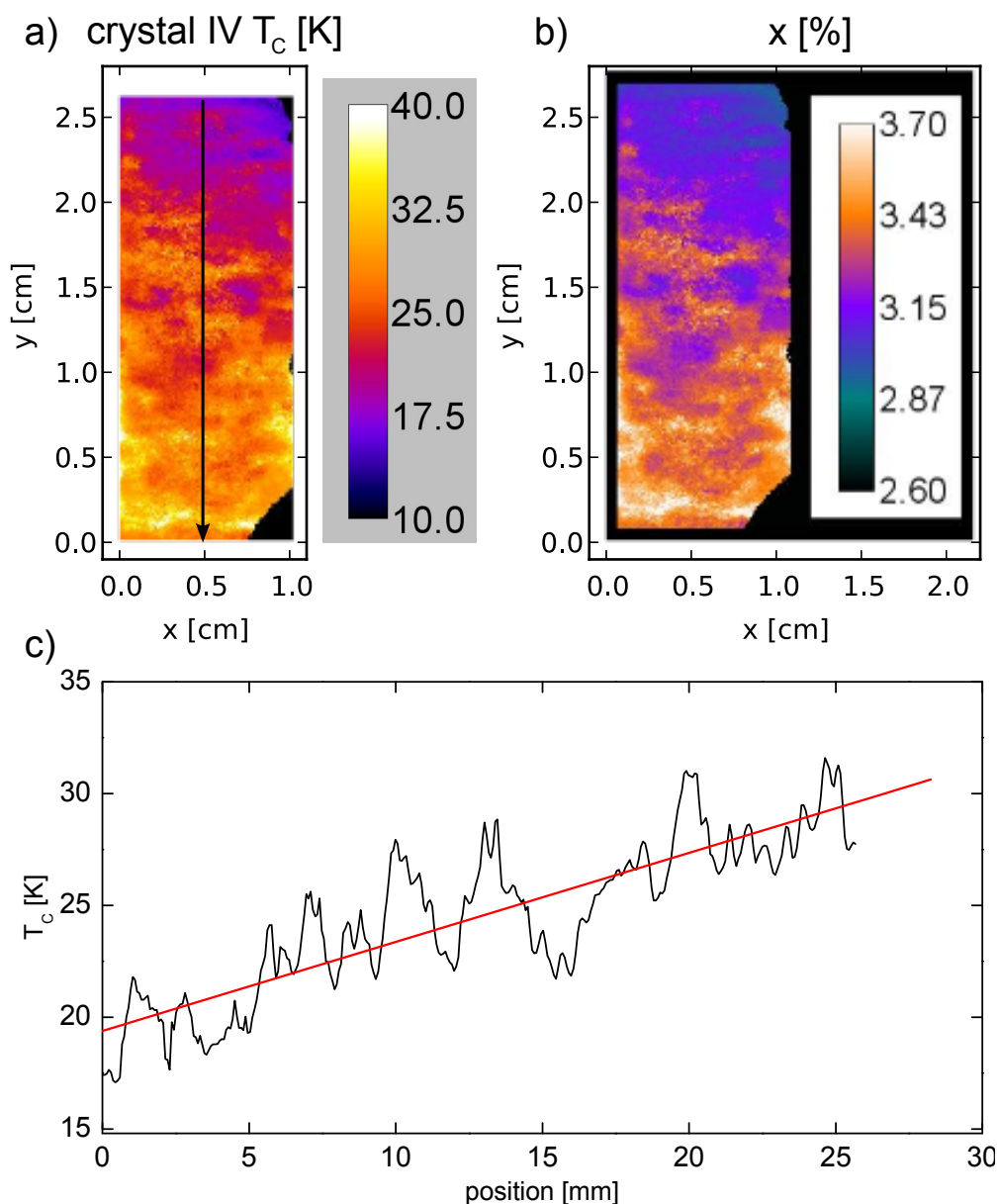


Figure 5.2.4: Spatial distribution of T_C over the cross section of crystal IV as obtained from the experiments at FRM II (a). A variation of the Curie temperature from 12 K to 30 K was found, which is in agreement with prior measurements at HZB. However, much better spatial resolution is achieved with this setup using a ^3He polariser and analyser. A plot of T_C along the arrow indicated in figure (a) is shown in figure (c) together with a linear fit of the data. The variation of the Ni concentration x (in %) was calculated from the Curie temperature using published data of the concentration dependence of T_C (b). The concentration varies from 2.9% to 3.7%.

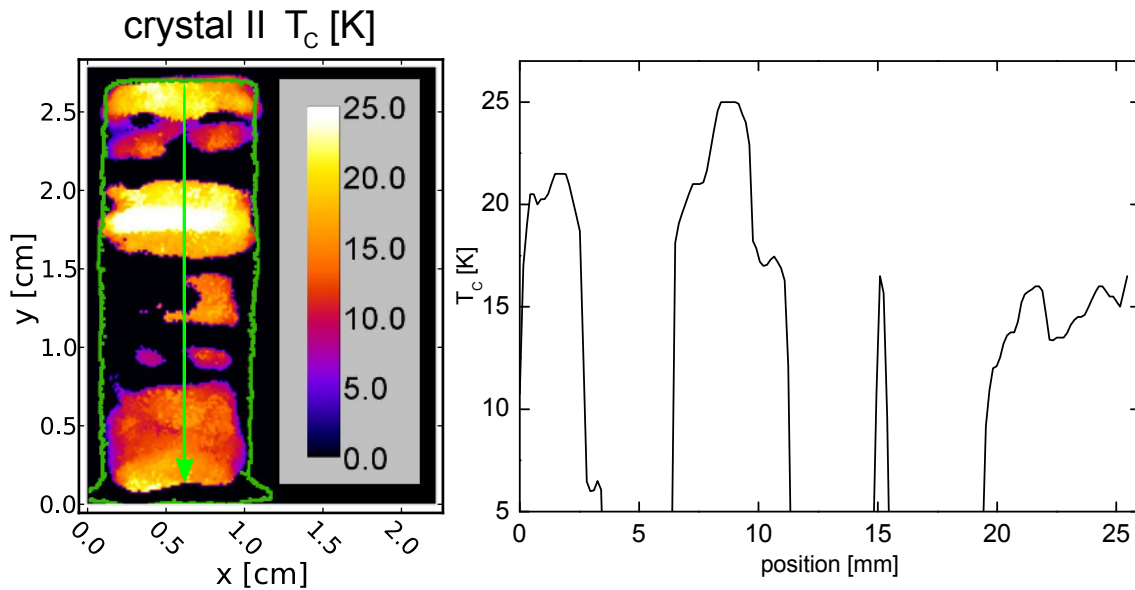


Figure 5.2.5: T_C -map obtained at FRM II for crystal II (left). The ordering temperature is found to lie in the range between 6K and 25K and the sample shows vast regions where the sample does not order ferromagnetically down to the lowest accessible temperature of 5 K. A plot of T_C along the arrow indicated in the left image is shown (right).

spatial resolution. Generally, the depolarisation of the beam by the slice is higher than for the entire crystal because a polychromatic beam with larger mean wavelength leading to higher depolarisation (c.f. eq. (2.4.9)) was used in this experiment. Despite of the higher depolarisation, several regions of the sample still show very small depolarisation of the beam even at the lowest temperatures we could reach. Thus, it is still not clear whether these regions eventually order ferromagnetically or stay paramagnetic down to $T = 0$. Furthermore, the effect of the sample thickness on the determination of the Curie temperature was found to be small for this particular sample because the sample shows similar magnetic properties for the thin slice as for the entire crystal. This underlines that the variations of the sample in the horizontal direction are small compared to those in the vertical direction.

Slice 2 of Crystal II

A second slice of similar dimensions (see Fig. 5.2.2 (b)) was cut from crystal II adjacent to the first slice and analysed with the same setup as the other slice in a temperature range from 4K to 30K. The resulting T_C -map is shown in Fig. 5.2.6 (b) and is in good agreement with the results obtained on the first slice. Both slices show a rather good homogeneity in the x -direction while there are strong variations of the observed magnetic properties in the y -direction. This is also in agreement with the measurements on the whole crystal II which were made before. This agreement gives further evidence that the variations in the horizontal layers of the crystals are small compared to those in the vertical direction.

Fig. 5.2.6 (c) shows plots of T_C along the centre lines for both slices. There is a general agreement of the main features of the plots. Especially the maxima at $x = 2$ mm and $x = 8$ mm and the minimum at $x \approx 16$ mm are present in both slices. However, the maximum values for slice 2 are up to 4 K higher than for slice 1 and the minimum values are up to 4 K lower for slice 1. Furthermore, the curve for slice 2 seems to be shifted slightly towards higher x -values, which is probably due to small differences in the alignment of the two plots with respect to the crystals. Despite these disagreements, the observed T_C

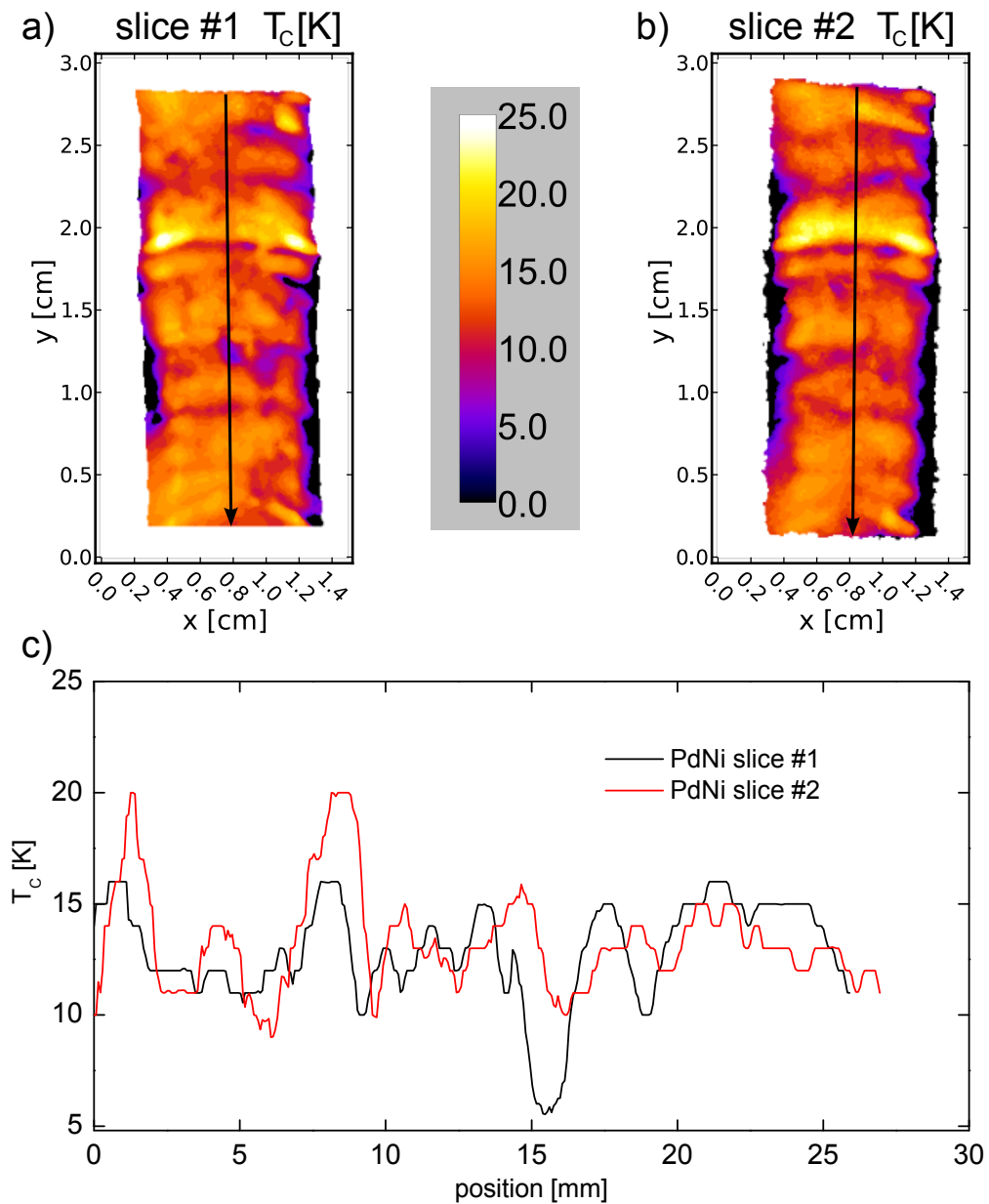


Figure 5.2.6: Distribution of the Curie temperature T_C over slice 1 (a) and slice 2 (b) cut from crystal II. The colour code is given in the right panel. Variations of T_C between 5 K and 24 K were found for both samples and for some regions, especially at the edges of the samples, the depolarisation of the beam was too small to determine the Curie temperature. Thus, in these regions T_C is either smaller than 5 K or the sample stays paramagnetic down to lowest temperatures. A horizontal layer structure is observed for both samples and they generally show a very similar structure, which further suggests that the variations in the horizontal direction are rather small compared to those in the vertical direction. A plot of T_C along the arrows indicated in images (a) and (b) is shown in (c).

values are in good agreement for the two slices.

Samples from the University of Augsburg

To compare the quality of the four $\text{Pd}_{1-x}\text{Ni}_x$ crystals obtained from the company Mateck with other samples, two crystals from University of Augsburg were additionally investigated. The crystals, which have a disc shape with a diameter of 10 mm and a thickness of 2 mm were prepared by arc melting in argon and quenched from the melt. In the following, the samples were remelted many times and later annealed at 1000 °C for five days. These two samples with a nominal Ni content of $x = 2.50\%$ (A2.5) and $x = 5.00\%$ (A5.0), respectively, have been prepared in exactly the same way as the samples used for the measurements published by Nicklas *et al.* [36]. The authors found an ordering temperature of $T_C = 75$ K for a similar sample with $x = 0.05$, whereas the sample with $x = 0.025$ is below the critical Ni concentration and was found not to order ferromagnetically. Both polycrystalline samples are shown on the photo in Fig. 5.2.7 (right).

These two crystals were investigated with setup #3 consisting of ^3He polarisers and analysers using a monochromatic beam of $\lambda = 3.2 \text{ \AA}$. The depolarisation of the beam at 4 K – the lowest temperature we could reach with the available cryostat – was measured. While sample A5.0 showed strong depolarisation of the beam, no depolarisation was found for sample A2.5. This is in agreement with the statement of Nicklas *et al.* [36] that this sample is below the critical concentration of $x_c = 2.6\%$ and consequently should stay paramagnetic down to $T = 0$. Neutron depolarisation measurements on this sample with a ^3He cryostat down to temperatures of 500 mK are already scheduled.

To determine the Curie temperature and homogeneity of sample A5.0, a temperature scan of the neutron depolarisation from 55 K to 75 K was made in steps of 1 K. The resulting T_C map shown in Fig. 5.2.7 is rather homogeneous compared to those of the Mateck crystals. However, we still find variations of T_C from 66 K to 73 K. This is in general agreement with the T_C of 75 K found by Nicklas *et al.*, since the authors determined the ordering temperature from magnetisation measurements on a macroscopic sample and thus – for an inhomogeneous sample – always find the total magnetisation of the sample to vanish at the highest ordering temperature found within the sample volume.

Magnetisation Measurements on Slice 1 of Crystal II

With the results of the depolarisation measurements on slice 1 described above, several interesting spots with different ordering temperatures were identified. At these spots ten small samples of $1 \times 1 \times 1 \text{ mm}^3$ were cut from the slice. For alignment, a 1 mm-grid was overlaid to the sample as shown in Fig. 5.2.8 where the obtained samples are marked by red squares. To reduce the time needed to cut the samples, all samples were arranged in a strip, which was cut from the sample by spark erosion. This strip was then cut into pieces with a diamond wire saw. The samples were named as indicated by the letters and numbers on the grid in Fig. 5.2.8. After cleaning and polishing of these samples, magnetisation measurements were made with a Quantum Design Physical Property Measurement System (PPMS) in collaboration with C. Franz for comparison with the results obtained from the radiography experiments described above.

Magnetic field sweeps were performed at different temperatures with fields up to $B = 9$ T. The results were plotted as Arrott plots (B/M vs. M^2) as discussed in 4.3 and M_s and T_C were determined from

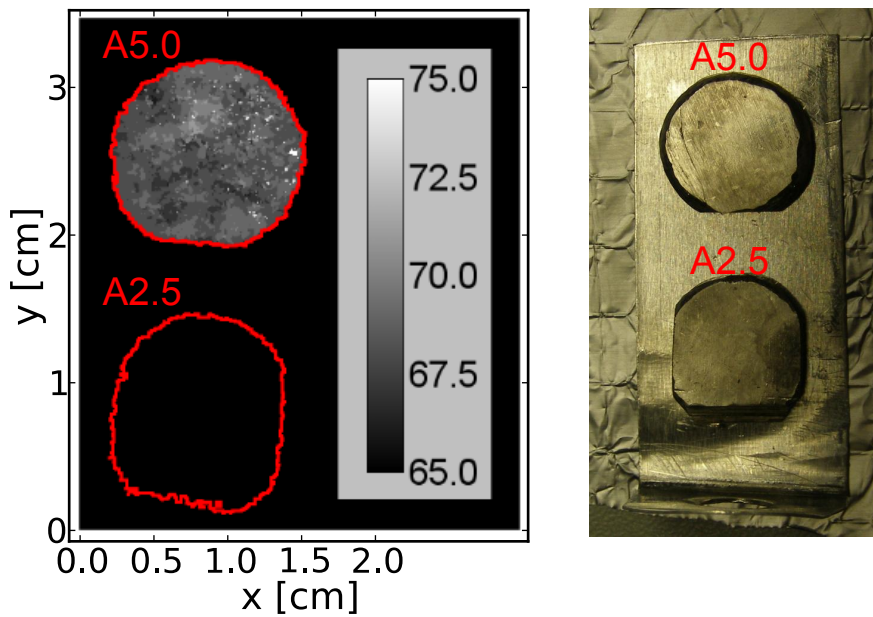


Figure 5.2.7: Distribution of the Curie temperature T_C over the PdNi samples from University of Augsburg (left). The shape of samples A5.0 and A2.5 is indicated on the top and bottom, respectively. Nicklas *et al.* [36] found an ordering temperature of $T_C = 75$ K for sample A5.0 (top), whereas sample A2.5 is below the critical concentration. A photo of the two samples as mounted in the sample holder is shown (right).

the data. An example of such an Arrott plot is given for sample D8 in Fig. 5.2.9. However, the Arrott plots are only found to be linear at high fields and high temperatures. For low fields and temperatures, a curvature of the Arrott plots is observed, which is of the same order of magnitude for all samples. The resulting T_C vs. M_s for all samples measured at the time of writing are plotted in Fig. 5.2.10. Generally, an increase of M_s with increasing T_C is observed. However, there exist several samples with very similar ordering temperature, showing different ordered moments. These differences might be caused by heterogeneities within the samples. The ordered moment is determined from the low temperature behaviour of the magnetisation data. Therefore, if the sample consists of several fractions with different ordering temperatures, all fractions will contribute to the ordered moment at $T = 0$. In contrast to that, T_C is determined as the temperature where the magnetisation vanishes. The condition $M = 0$ is fulfilled when the highest ordering temperature of all fractions of the sample is reached. Therefore, the obtained value of T_C represents the highest ordering temperature of all fractions of the sample.

Within the SCR theory framework M_s would be expected to track T_C down to zero as indicated by the blue line in Fig. 5.2.10. However, the data suggests that M_s vanishes discontinuously at $T_C = 0$ as shown by the dashed red line in the figure. This behaviour suggests a first order phase transition of $\text{Pd}_{1-x}\text{Ni}_x$ at $T = 0$ and not a second order transition as expected for a quantum critical point.

It turned out during the evaluation of the data that the ordering temperatures for the small samples determined from these magnetisation measurements were in poor agreement with the values obtained from NDI measurements performed before cutting. A more detailed investigation of the remaining pieces of the slice after cutting revealed that the grid marking the samples to be cut out was rotated by 180° by the sample preparation lab before the cutting process. Therefore not the samples originally intended were cut from the slice. Furthermore the exact position of the grid with respect to the sample boundaries during the cutting process was not exactly known. To determine the location of the grid and

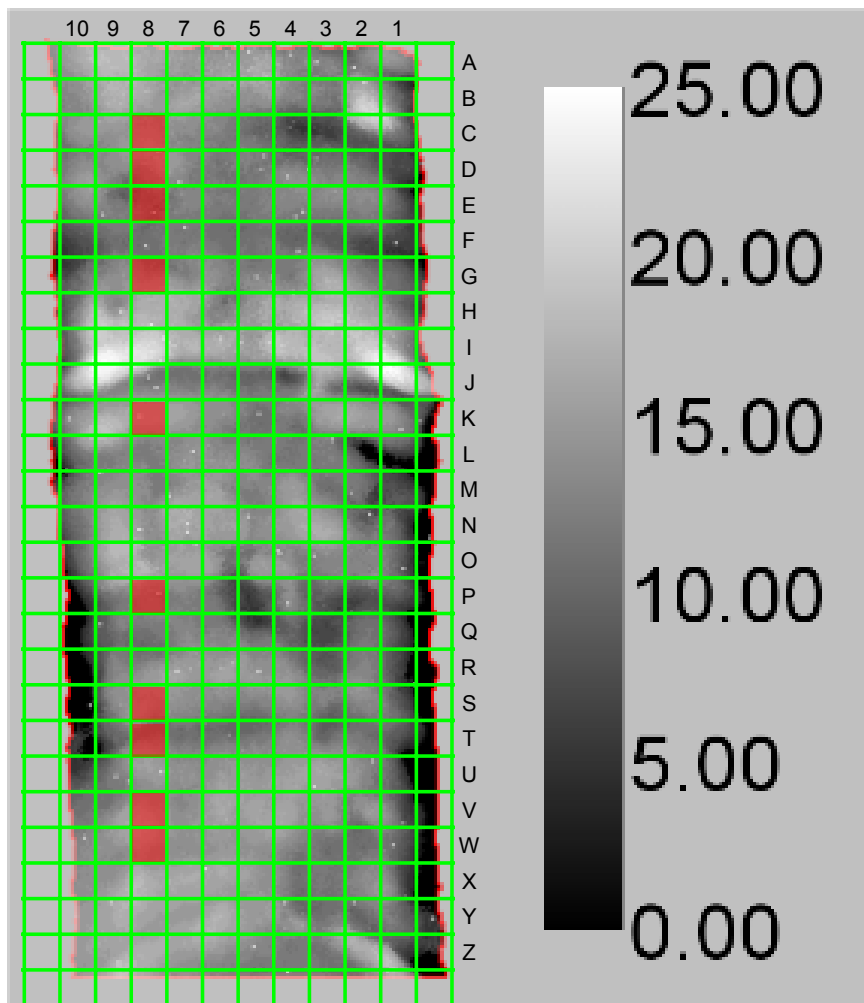


Figure 5.2.8: Location of the small samples cut from slice 1. These samples have a size of $1 \times 1 \times 1 \text{ mm}^3$ and were used for magnetisation measurements in a Quantum Design PPMS. The figure shows the correct positions of the samples after realignment of the grid .

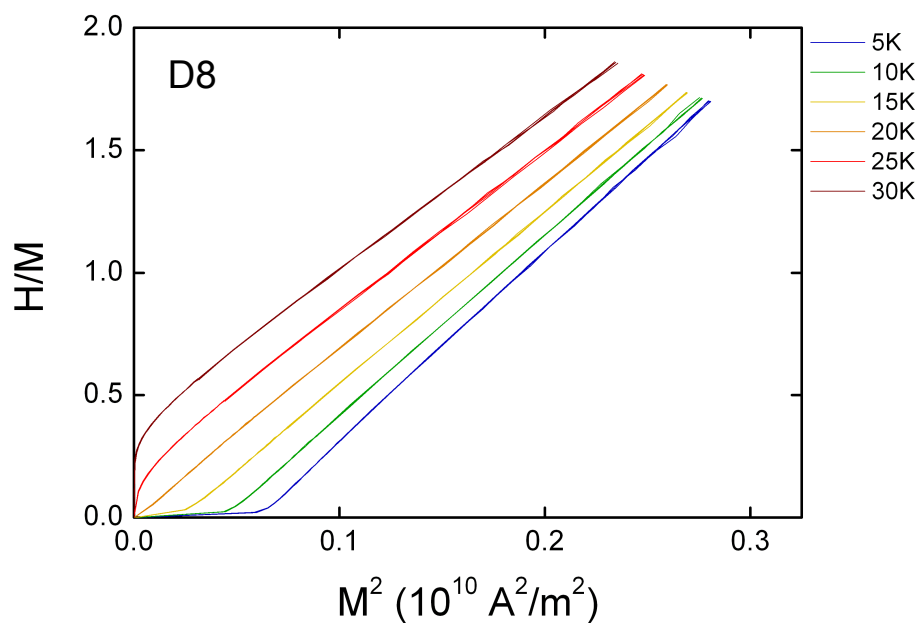


Figure 5.2.9: Arrott plots for $\text{Pd}_{1-x}\text{Ni}_x$ sample D8 as obtained from the magnetisation measurements at the PPMS magnetometer.

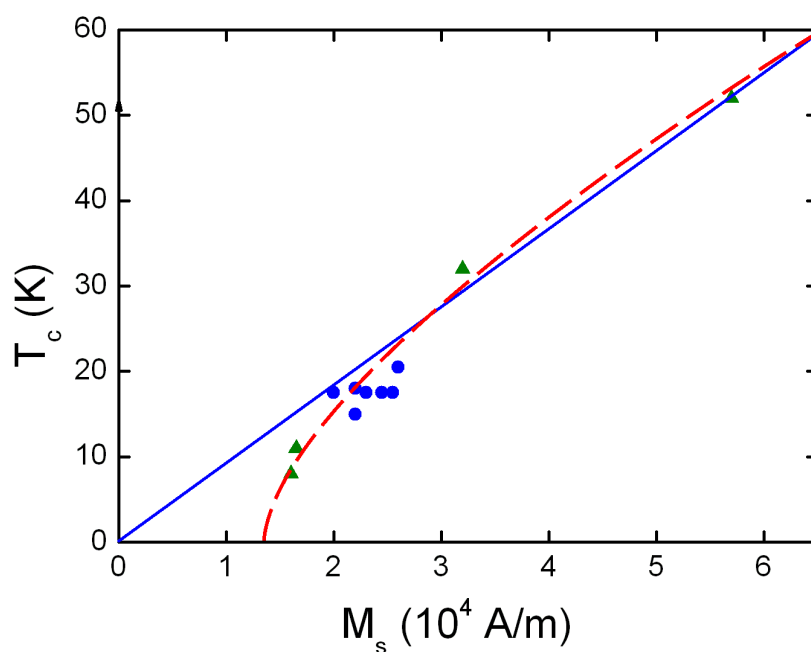


Figure 5.2.10: Plot of M_s vs. T_c obtained by C. Franz from magnetisation measurements on seven of the small samples cut from slice 1 (blue) and four other samples cut from the entire crystals I to IV (green) at a PPMS magnetometer. The latter datapoints have been obtained by C. Franz [53] in earlier measurements.

Sample	$T_{C,PPMS}[K]$	$T_{C,NDI}[K]$	$M_{s,PPMS}[A/m]$	$M_{s,NDI}[a.u.]$
C8	17.5	17.1	20000	0.75
D8	20.5	17.3	26000	0.64
E8	17.5	15.5	23000	0.45
G8	17.5	16.2	24500	0.60
K8	18	16.3	22000	1.08
P8	15	15.3	22000	0.68
W8	17.5	16.6	25500	0.76

Table 5.2: Comparison of the ordering temperatures and ordered moments obtained for the small samples cut from crystal II from magnetisation measurements on a PPMS with NDI measurements. The position of the grid with respect to the sample was optimised by minimising the mean square errors $\frac{1}{N} \sum_i (T_{C,PPMS} - T_{C,NDI})^2$ of both results with respect to each other. No good agreement is found for the values of M_s which might, however, be due to the completely different measurement procedures.

therefore the position of the small samples cut from the slice, the mean square error of the T_C values obtained from the NDI data and the bulk measurements was calculated for different shifts of the grid with respect to the sample boundaries. A minimisation of this mean square error ($\frac{1}{N} \sum_i (T_{C,PPMS} - T_{C,NDI})^2$) revealed the true position of the grid on the sample as shown in Fig. 5.2.8. A comparison of the final values of the ordering temperatures obtained with both methods is shown in Tab. 5.2.

The results of this optimisation yielded a shift of the grid with respect to the originally assumed position by approximately 0.5 mm both in the x and y direction, giving a very stable minimum of the mean square error. The ordered moment was determined from the NDI measurements using eq. (4.4.2):

$$M^2(T) = -\frac{1}{\alpha} \ln \frac{P(T)}{P_0}, \quad (5.2.1)$$

with $\alpha := \frac{1}{3} \gamma^2 \mu_0^2 d \delta / v^2$. The value of the scaling factor α was determined by first setting it to $\alpha = 1$ which yields the values for $M_{s,NDI}$ given in Tab. 5.2. Using an average value of the bulk and NDI values for the ordered moment and assuming a constant domain size throughout the sample we then determined α as

$$\alpha = \frac{M_{s,NDI}^2}{M_{s,PPMS}^2} = 7.44 \cdot 10^{-10}. \quad (5.2.2)$$

Plugging in the sample thickness $d = 10^{-3}$ m and the average neutron velocity $v = 890$ m/s for $\bar{\lambda} = 4.5$ Å into the definition of α yields an average domain size of $\delta = 33$ μm.

The agreement of the values for the ordered moment determined from the PPMS measurements and those from the NDI measurements is found to be rather poor. However, this might be attributed to the fact that both methods use a completely different technique to obtain these values and consequently inhomogeneities of the sample may have a completely different influence on the results. It is especially worth noting that the ordered moment found from magnetisation measurements is determined from the extrapolation of the high field behaviour towards zero field. In contrast to that NDI measurements are performed in very low magnetic fields. Here only the guide field of $B_g \approx 10^{-3}$ T is present.

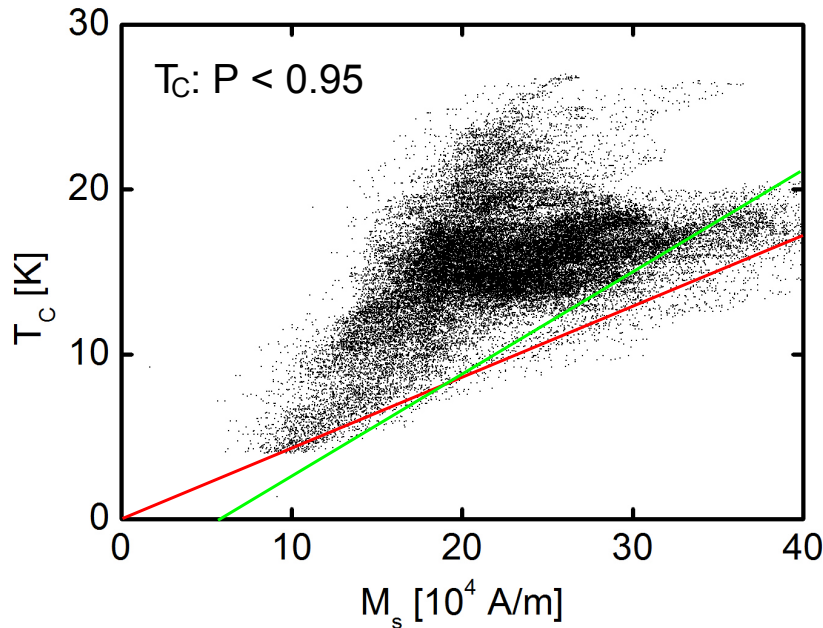


Figure 5.2.11: M_s vs. T_C dependence of $\text{Pd}_{1-x}\text{Ni}_x$ slice 1 determined from NDI measurements. Each point in the plot represents a pair of M_s and T_C values found at one pixel of the NDI data. The width of the plot is caused by inhomogeneities along the transmission path of the neutron beam through the sample. The intrinsic – homogeneous behaviour was shown by simulations to be given by the right edge of the cloud of points. However, the amount of data points especially at the low- T_C end of the plot is not sufficient to determine whether the phase transition is intrinsically first (green line) or second (red line) order.

Comparison with Neutron Depolarisation Data

As discussed in 4.4 it is possible to obtain the ordering temperature as well as the ordered moment from the temperature dependence of neutron depolarisation data. Here the ordered moment is determined from the extrapolation of the depolarisation data towards $T = 0$ and the ordering temperature is found as the temperature below which the polarisation falls below a certain threshold ($P < 0.95$ in this case). The values of M_s and T_C determined by this method for all pixels of the cross section of the $\text{Pd}_{1-x}\text{Ni}_x$ slice 1 were plotted in a single diagram shown in Fig. 5.2.11, similar to Fig. 5.2.10 obtained from bulk measurements. In contrast to the latter plot, the evaluation of the NDI data shows a much larger amount of data points resulting from the evaluation of M_s and T_C for each pixel of the NDI images.

As for the magnetisation data shown above, we also find different values of M_s for one value of T_C evaluated from the neutron depolarisation data. It was discussed in 4.4 that the broadening of the distribution of M_s values for one ordering temperature originates from inhomogeneities of the sample along the transmission path of the neutron beam through the sample. From comparison of the width of the measured data with simulations of an inhomogeneous sample we can deduce that the neutron beam traverses more than five regions of random ordering temperature. Since the sample thickness is only 1 mm the size of these regions must on the average be smaller than 0.2 mm. It is therefore obvious that the length scale of the inhomogeneities in the sample is of this order of magnitude and therefore smaller than the lateral spatial resolution achieved in the NDI measurements. We therefore conclude that the length scale of inhomogeneities in our particular sample is smaller than what can be resolved by these real space measurements.

As shown by the simulations in 4.4 the lower right edge of the cloud of points in Fig. 5.2.11 represents the case where the beam transmits the sample on a path with only one ordering temperature. Therefore, the sample is homogeneous along the transmission path of the beam for these points and the points represent the intrinsic behaviour of the sample unaffected by inhomogeneities. However, we furthermore showed that the shape of this edge depends crucially on the choice of the threshold for the determination of T_C especially at the low-temperature end of the plot. Decreasing this threshold leads to a shift of the curve towards lower T_C values and would lead to an erroneous identification of a first order phase transition of M_s for $T_C \rightarrow 0$. However, the statistical noise in the depolarisation data prevents the use of a threshold larger than 0.95. From the present data of a very inhomogeneous $\text{Pd}_{1-x}\text{Ni}_x$ sample we can therefore not conclude the intrinsic dependence of M_s on T_C . As indicated by the lines in Fig. 5.2.11, both a quantum critical (red) or a first order behaviour (green) may be seen in the data. However, it should be noted that a quantum critical behaviour would be contradictory with our magnetisation measurements shown in Fig. 5.2.10 which rather indicate a first order phase transition.

To solve the question whether the quantum phase transition of $\text{Pd}_{1-x}\text{Ni}_x$ is first or second order, samples with lower ordering temperatures would be necessary to increase the amount of data in the lower left corner of the plots, which contains the most valuable information on the phase transition. Furthermore, it would be helpful to have samples which are homogeneous along the transmission direction of the beam. Such samples yield only a single value of M_s for a certain T_C . It would be ideal to study gradient crystals for which the ordering temperature changes as a function of position perpendicular to the beam direction. A spatially resolved investigation of such a sample yields the entire $M_s(T_C)$ relation in a single NDI measurement run.

Additionally, the counting statistics in the measurements should be increased to allow for the choice of a higher threshold in the data evaluation, which will decrease the shifting effect of the plots as shown by our simulations. Furthermore a higher threshold also is required to determine the ordering temperature of regions of the sample with low T_C and therefore also low M_s , resulting only in a small depolarisation of the beam.

Conclusion: $\text{Pd}_{1-x}\text{Ni}_x$

In conclusion, all measurements on $\text{Pd}_{1-x}\text{Ni}_x$ discussed in this section demonstrate that it is extremely difficult to produce homogeneous samples of this material. The most homogeneous sample we investigated was sample A5.0 from the University of Augsburg which, however, still shows relatively large variations of the ordering temperature of approximately 7 K. Furthermore, this sample shows a high average ordering temperature of ≈ 65 K and is therefore far away from the quantum critical regime.

The comparison of our experiments on the 1 mm thick slice 1 cut from the low- T_C $\text{Pd}_{1-x}\text{Ni}_x$ crystal II with simulated neutron depolarisation data show that the inhomogeneities in this sample are even larger than expected from the neutron depolarisation images, where the limited spatial resolution of 0.3 mm hinders the verification of variations of the magnetic properties on a smaller length scale. The rounded shape of the temperature dependence of the measured depolarisation which is in good agreement with our simulations of an inhomogeneous sample indicates heterogeneities on an even smaller length scale.

The ultimate verification of the intrinsic nature of the quantum phase transition in $\text{Pd}_{1-x}\text{Ni}_x$ from the NDI data was at the time of writing not possible since the particular sample we have investigated turned

out to be too inhomogeneous and at the same time did not contain enough regions with very low ordering temperatures. To achieve a clarification whether the intrinsic phase transition is second or first order, and therefore whether or not a QCP exists in $\text{Pd}_{1-x}\text{Ni}_x$, a sample with lower ordering temperature which should additionally be more homogeneous should be used.

5.2.2 Ni₃Al

As discussed in 1.3.3, the Curie temperature of Ni₃Al can be reduced by application of hydrostatic pressure as well as by compositional doping. Niklowitz *et al.* [9] found T_C to vanish at a critical pressure of approximately $p_c = 80$ kbar. The same effect can be achieved by compositional doping with excess Al compared to the stoichiometric composition. The concentration dependence of T_C was studied by deBoer *et al.* [54]. These authors found by extrapolation of the T_C values observed for different Ni concentrations that in Ni_{75-x}Al_{25+x} the Curie temperature falls to zero at an excess Al concentration of $x = 0.4$, which shows the strong dependence of the magnetic properties of the material on compositional variations. As a consequence, especially for large size crystal growth, it is of paramount importance to minimise compositional inhomogeneities in the material.

The institute E21 at the Fakultät für Physik of Technische Universität München owns an optical image furnace in which single crystals can be grown with the optical float zoning technique (OFZ). This furnace has been remodeled to an all-metal-sealed UHV compatible setup by A. Neubauer as part of his PhD thesis. With these modifications, the entire image furnace can be evacuated, heated and afterwards filled with high purity argon inert gas atmosphere to reduce the evaporation of crystal material during the growth process. Being a crucible-free technique in combination with the high purity inert gas atmosphere makes the OFZ technique one of the cleanest techniques for single crystal growth and guarantees highest purity and perfection of the resulting crystals. High purity is especially important for weakly ferromagnetic materials in which even small contaminations with ferromagnetic materials can significantly alter the magnetic properties of the samples.

Attempts were made to grow large size Ni₃Al single crystals for bulk investigations as well as neutron scattering experiments with the OFZ technique. Especially neutron scattering experiments require large samples due to the increase of the intensity of the scattered neutrons with increasing sample size. The crystals were grown from starting rods which were prepared by inductive heating of the constituents in the desired amounts in a Cu crucible. The inductive heating leads to a stirring of the melt at the same time. The melt was then cast into a cylindrically formed water cooled crucible with a diameter of 6 mm which allows rapid quenching of the melt.

As discussed in 1.3.3, the phase diagram of Ni₃Al is not exactly known. Especially around the stoichiometric composition, the location of the peritectic point is uncertain. As a consequence, the preparation of a melt with the desired composition of the final crystal does not necessarily lead to the growth of a crystal with this composition. To study the influence of the starting composition on the resulting crystal composition, starting rods with different Ni concentrations between 75% and 76.5% were prepared.

Polarised neutron radiography was used as a sensitive tool to study the homogeneity and therefore the quality of the starting rods for crystal growth as well as the resulting crystals. Furthermore, this method offers the possibility to assess the effects of different growth conditions (i.e. growth velocity, temperature, annealing, ..) on the resulting crystal quality. An overview of all measurements performed on Ni₃Al samples and a summary of the results is given in Tab. 5.3. The starting rods are named “L##” and the OFZ grown crystals are named “OFZ##” and were all prepared by A. Neubauer at the E21 institute. Furthermore, four other samples obtained from other groups were investigated.

Sample	x [%]	Date	Setup	Type	λ	T / steps	Results
L54	75.5	07/2008	#2, FRM II, periscope polariser, ^3He analyser	T -scan	polychr.	10...80K/5K	very homogeneous, $T_C = 47 \dots 50\text{K}$, Fig. 5.2.12
L33	76.0	05/2008	#1, HZB, solid state bender polariser and analyser	T -scan	3.5 Å	5...70K/1K	very inhomogeneous on one end, $T_C = 55 \dots 65\text{K}$, Fig. 5.2.13
OFZ15	75.0	05/2008	#1, HZB, solid state bender polariser and analyser	T -scan	3.5 Å	30...60K/5K	stripe structure, $T_C = 42 \dots 52\text{K}$, Fig. 5.2.14 (a)
OFZ17	75.0	05/2008	#1, HZB, solid state bender polariser and analyser	T -scan	3.5 Å	5...55K/ $\geq 2.5\text{K}$	stripe structure, ferromagnetic grain, $T_C = 35 \dots 55\text{K}$, Fig. 5.2.14 (b)
OFZ20	75.5	07/2008	#2, FRM II, periscope polariser, ^3He analyser	T -scan	polychr.	10...70K/ $\geq 5\text{K}$	stripe structure, ferromagnetic grain, $T_C = 48 \dots 65\text{K}$, Fig. 5.2.14 (c)
OFZ20-L1	75.5	07/2008	#2, FRM II, periscope polariser, ^3He analyser	T -scan	polychr.	35...90K/ $\geq 2\text{K}$	three grains, $T_C = 72 \dots 90\text{K}$, Fig. 5.2.15
Jül-s	?	05/2008	#1, HZB, solid state bender polariser and analyser	T -scan	3.5 Å	65...85K/5K	strong stripe structure, $T_C = 75 \dots 85\text{K}$, Fig. 5.2.16 (right)
Jül-l	76.0	05/2008	#1, HZB, solid state bender polariser and analyser	T -scan	3.5 Å	53...90K/ $\geq 5\text{K}$	locally very homogeneous, $T_C = 65 \dots 90\text{K}$, Fig. 5.2.16 (left)
E5	75.0	04/2009	#3, FRM II, ^3He polariser and analyser	T -scan	3.2 Å	30...55K/ $\geq 1\text{K}$	inhomogeneous but within single crystalline grains relatively homogeneous, $T_C = 42 \dots 55\text{K}$, Fig. 5.2.17
E8	75.0	01/2009	#3, FRM II, ^3He polariser and analyser	T -scan	3.2 Å	20...50K/ $\geq 2\text{K}$	very homogeneous! $T_C = 37 \dots 39\text{K}$, Fig. 5.2.18

Table 5.3: Overview of the experiments and results on Ni_3Al samples. The setups are described in more detail in 4.2 and their numbers are defined in Tab. 4.1. The OFZ samples were grown before the development of the NDI technique. Therefore, the starting rods of these samples have not been investigated.

Starting Rods

Several starting rods with different Ni concentrations were investigated for their homogeneity and Curie temperature distribution at HZB Berlin with setup #1 (see 4.2) consisting of two solid state benders, followed by further investigations at FRM II with setup #2 using the periscope as a polariser. Both setups yield only mediocre spatial resolution and especially the periscope leads to severe stripe artifacts due to the imperfections discussed in 3.2.4. Therefore, a detailed evaluation of the data was often very difficult and for some samples only a visual evaluation of the depolarisation data could be made. In this work, we will only present the data of the samples for which a detailed analysis was possible.

The resulting T_C -maps for the starting rods L54 and L33 are shown in Fig 5.2.12 and Fig. 5.2.13, respectively. L54 turns out to be rather homogeneous along the cylinder axis with variations in T_C of only 2.5 K. The variation perpendicular to the cylinder axis can mainly be attributed to the shape of the crystal, which leads to higher depolarisation in the centre of the crystal, where it has a larger thickness, while at the edges the depolarisation is smaller due to the lower thickness. A constant threshold of $P < 0.5$ was used to determine T_C . Due to the higher depolarisation in the centre of the crystal, this threshold is reached at a higher temperature than at the sides of the sample, which show lower depolarisation.

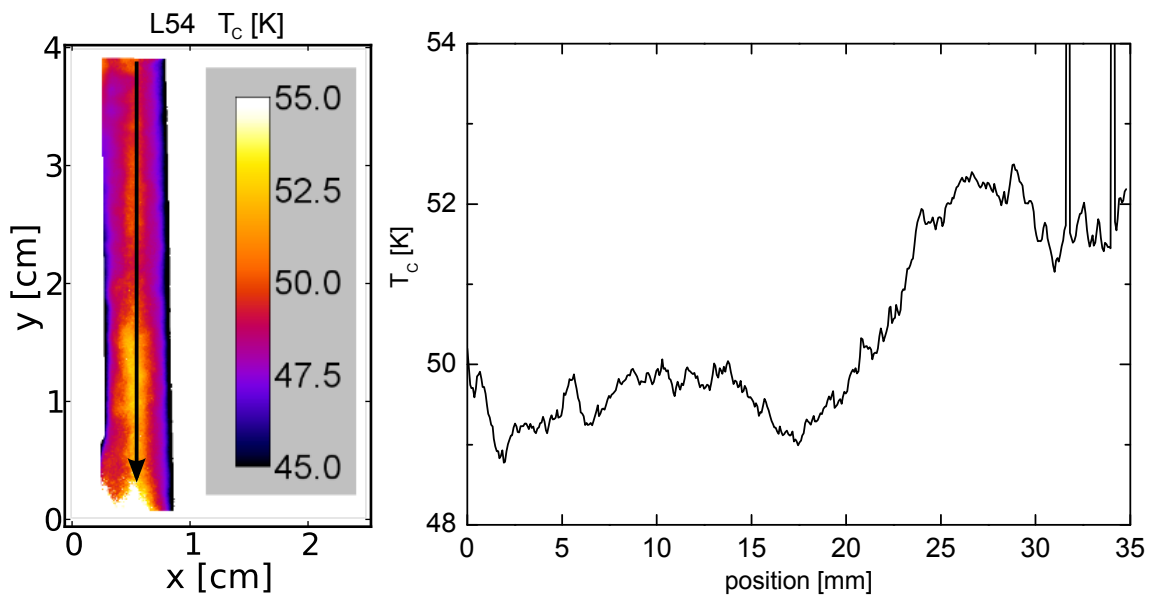


Figure 5.2.12: Distribution of the Curie temperature T_C for starting rod L54 (left) and a plot of the Curie temperature along the black arrow indicated in this figure (right). This sample is found to be very homogeneous along the cylinder axis. The variations perpendicular to the cylinder axis might mainly be an artifact introduced in the algorithm which determines the ordering temperature by the variation of the transmission length through the sample.

The starting rod L33 turns out to be much less homogeneous, showing variations of T_C along the cylinder axis between 55 K and 65 K. Here, the top part of the sample shows a region of higher ordering temperature than the rest of the sample. However, the region at the top, displayed in white in Fig. 5.2.13, was found to stay paramagnetic down to 5 K. The lower 2/3 part of the sample, in contrast, is very homogeneous, showing an ordering temperature of $T_C \approx 56$ K. These strong variations in the ordering temperature might have been caused by incomplete melting of the constituents. A shorter melting time was used for this sample than for sample L54 which does not show such inhomogeneities.

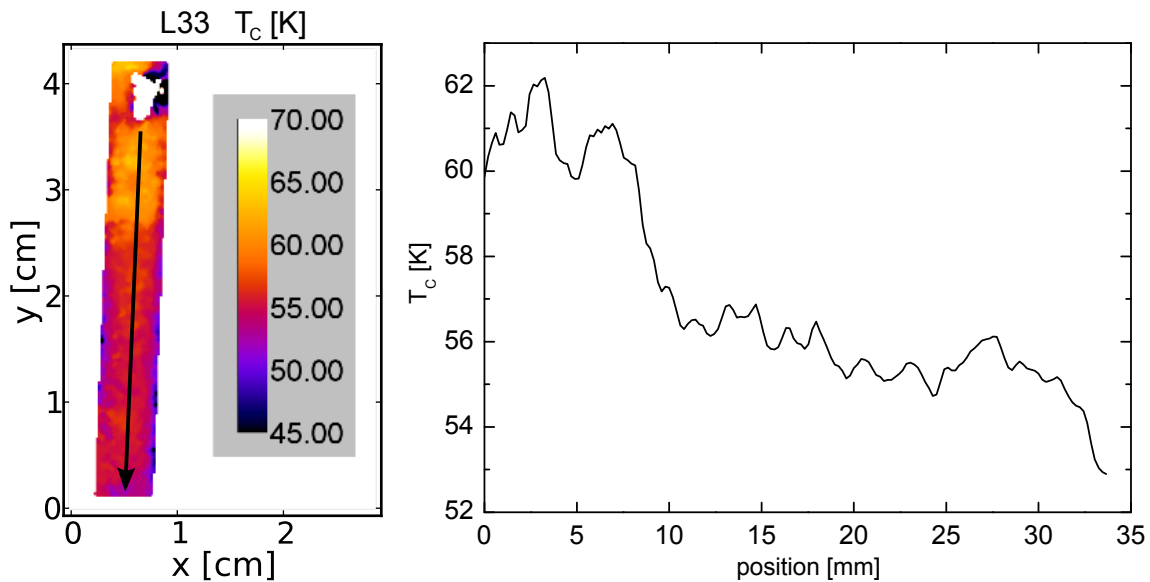


Figure 5.2.13: T_C -map for starting rod L33 (left) and plot along the black arrow shown in the left image (right). This sample shows strong variations of the ordering temperature especially at the top part of the sample, where a region with $T_C < 5$ K coexists next to a region with $T_C \approx 65$ K.

OFZ Grown Samples

Several crystals were analysed for their neutron depolarisation after OFZ growth. All samples were investigated optically for macroscopic single crystalline grains. For samples that seemed to have large grains, X-ray Laue images have been made, showing that none of the samples is entirely single crystalline. Since these samples were all grown before the development of the NDI technique, their starting rods could not be investigated.

The T_C -maps obtained from the temperature scans for crystals OFZ15, OFZ17 and OFZ20 are shown in Fig. 5.2.14. The measurements on samples OFZ15 and OFZ17 were carried out at HZB, Berlin with setup #1 (see 4.2) using two solid state benders as polariser and analyser, while the measurements on OFZ20 were performed at FRM II using setup #2 with the periscope as a polariser and a ^3He analyser.

Generally it is seen that the OFZ grown samples show much stronger gradients of T_C along the cylinder axis than the starting rods. Especially samples OFZ15 and OFZ17 show a pronounced layer structure which was not observed in any of the starting rods and consequently seems to arise during OFZ growth. However, the observed layer structure is not in agreement with the logged change of growth conditions. In our measurements, both OFZ15 and OFZ17 were oriented such that the growth direction was from bottom to top as indicated by the arrows in the images in Fig. 5.2.14 (a) and (b). The beginning of the floating zone (i.e. the point where OFZ growth was started) is indicated by a red line in the figures. OFZ17 shows a region at the beginning of the floating zone, which was found to be ferromagnetic up to room temperature displayed in white in the figure.

OFZ20 was grown from top to bottom in Fig. 5.2.14 (c) and shows a similar region which is ferromagnetic at room temperature at the beginning of the floating zone. However, these ferromagnetic regions do most likely not arise from the OFZ growth but from incomplete melting of the raw materials when preparing the starting rods. The ferromagnetic regions are probably due to unmolten Ni grains. For the starting rods prepared after these measurements, special care was taken to assure complete melting of

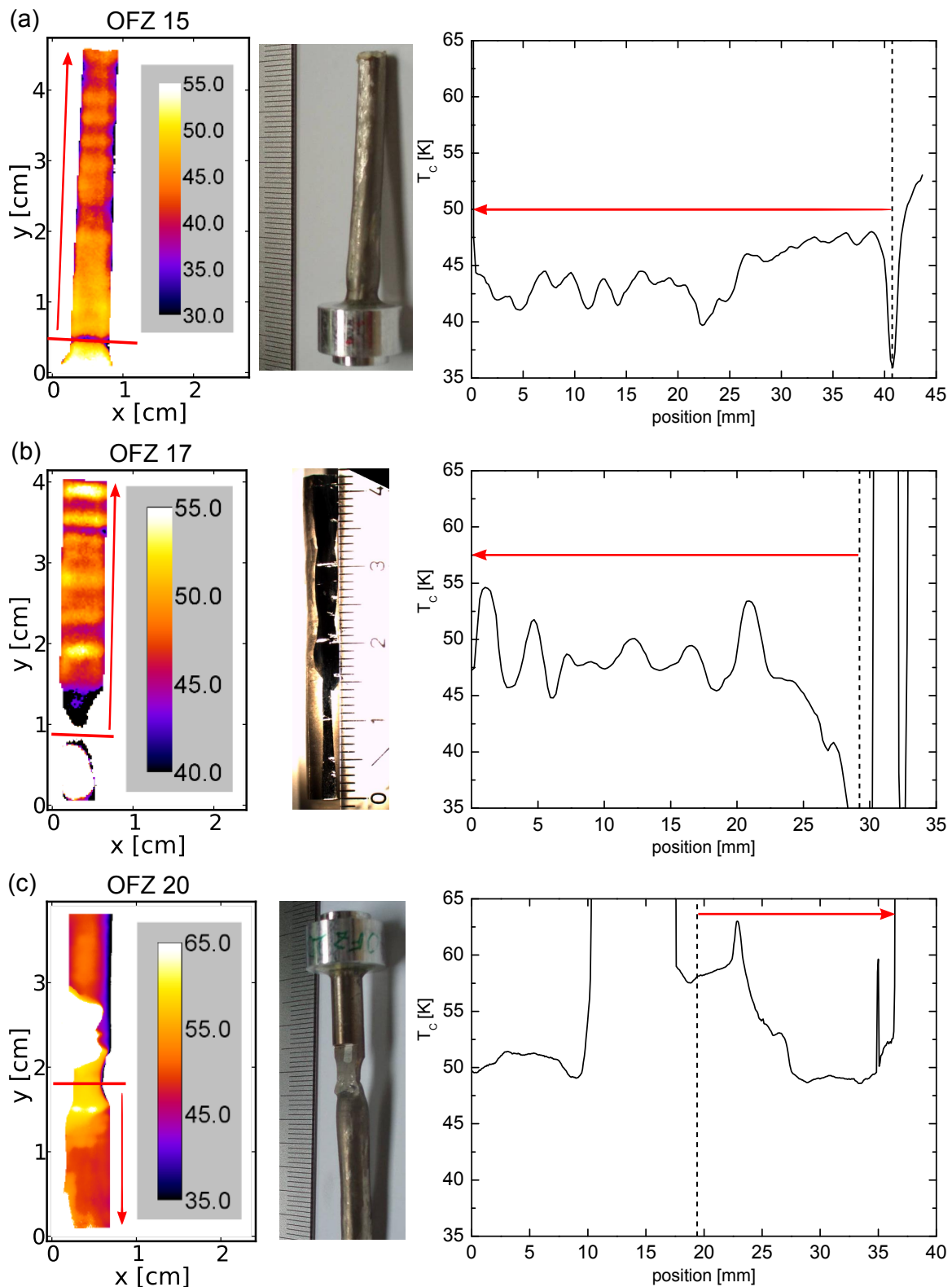


Figure 5.2.14: Distribution of the Curie temperature T_C and photos of samples grown in the optical image furnace at E21. (The photo of OFZ17 was taken after the NDI measurements and shows a surface which was polished for EDX measurements afterwards.) OFZ15 (a) and OFZ17 (b) were investigated at HZB, Berlin. The measurements on OFZ20 (c) were performed at FRM II. The red arrows indicate the growth direction and the red lines the point at which OFZ growth was started. Both OFZ17 and OFZ20 show a region which stays ferromagnetic up to room temperature and consequently must have a very high Ni content. The plots in the right panel show the variation of T_C along the centre of the crystals from top to bottom. The growth direction is once more indicated by red arrows and the end of the floating zone by dashed lines.

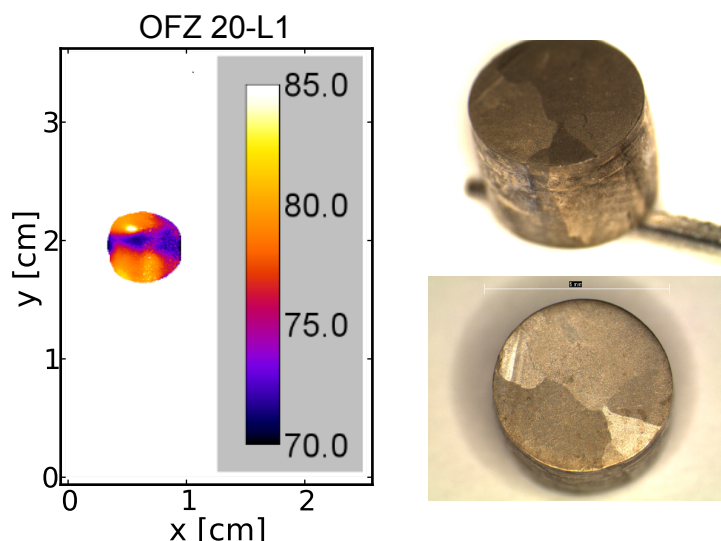


Figure 5.2.15: Curie temperature map for OFZ20-L1 (left). The crystal shows three large grains with different ordering temperatures. Furthermore, one spot was found which remains ferromagnetic at $T = 90\text{K}$. The grains can also be identified optically on the microscope photographs after etching of the surface (right).

the raw materials. No such high T_C ferromagnetic region was observed in OFZ15. Therefore it seems that the raw materials in the starting rod for this crystal have been entirely molten.

Crystal OFZ20 shows extended single crystalline regions. Thus, a cylindrical sample named OFZ20-L1 with a diameter of 7 mm and a length of 5 mm was cut from the large crystal. However, this sample still consists of several grains, three of which seem to occupy a major part of the sample volume. This sample was characterised by neutron depolarisation at ambient pressure as well as under pressures of up to 12 kbar (see 5.2.3). Additionally, magnetisation measurements were performed at ambient pressure at a Quantum Design PPMS magnetometer.

The results on the small sample OFZ20-L1 shown in Fig. 5.2.15 indicate that this sample consists mainly of three regions with different ordering temperature. This is in agreement with investigations of the sample in an optical microscope after etching of the surfaces, in which three large grains were found as observed from the photographs in the figure. Furthermore, there exists one small spot on the top left part of the sample which was found to stay ferromagnetic up to at least 90 K, which was the highest temperature at which the neutron depolarisation was measured for this sample.

Samples from Forschungszentrum Jülich

Further investigations were made on two crystals grown at Forschungszentrum Jülich. The first crystal is of cylindrical shape with a diameter of $\approx 16\text{mm}$ and a length of $\approx 60\text{mm}$ and was grown and borrowed to us by T. Chatterji. We will call this crystal Jül-1 in the following discussion. This single crystal had been used for the measurement of spin fluctuations in an article by Semadeni *et al.* [62] and has a Ni concentration of 76%, which was estimated by the authors from the observed Curie temperature. The second crystal, which we will call Jül-s, is of conical shape with a base diameter of $\approx 14\text{mm}$ and a length of $\approx 20\text{mm}$. Not much is known about the growth conditions of the crystal. It was grown by T. Reif in Jülich but it is not sure whether it is a single crystal or not.

These two samples were investigated at HZB Berlin using solid state benders as polariser and analyser (setup #1 in 4.2). The thickness of the sample covered quite exactly the width of the beam, however, the length of the crystal was larger than the beam height. Thus, only one end of the sample could be investigated. The black triangular region in the bottom right corner of Fig. 5.2.16 (left) is due to an edge which was cut from the crystal after alignment in prior neutron scattering measurements. No special care was taken in this neutron depolarisation experiment for alignment of the crystal axes with respect to the beam polarisation.

The Curie temperature distribution of these two crystals is shown in Fig. 5.2.16. Image (a) shows the results on the large crystal, while image (b) gives the T_C -map of the small crystal. In contrast to the results presented by Semadeni *et al.* [62], who reported $T_C = 72.5$ K for this sample, we found a strong variation of the ordering temperature over the size of the sample. Approximately 2.5 cm from the bottom of the sample a region with an ordering temperature of 90 K is found. The part of the sample above this region is very homogeneous and we found $T_C = 82$ K. The bottom part of the sample also turns out to be very homogeneous with an ordering temperature of 65 K. A plot of T_C along the centre line of the sample is shown in Fig. 5.2.16 (b).

These results are extremely important for the interpretation of the neutron scattering results presented in the article by Semadeni *et al.* since these measurements were performed on the entire crystal. This implies that the obtained results represent an average over regions of the sample with different magnetic properties.

Even though not much is known about the growth of the smaller crystal it seems to be grown with a different technique since it displays a layered structure similar to that also observed for the OFZ crystals grown at the institute E21. The Curie temperature of this crystal varies from ≈ 75 K to 85 K over the sample, and the highest ordering temperatures are found at the tip of the sample. Furthermore, the regions of homogeneous magnetic behaviour are much smaller than those in the larger crystal.

Samples from University of Cambridge

Two samples obtained from the group of G. G. Lonzarich at Cavendish Laboratory, University of Cambridge were investigated with high spatial resolution at FRM II using the setup #3 with ^3He polariser and analyser. These samples were prepared by N. Bernhoeft at the ILL, Grenoble by melting of Ni and Al in the desired amounts of the final crystal and rapid quenching of the melt. The obtained ingots were afterwards annealed for several months, which lead to the formation of large single crystalline grains, which can visually be well observed in the photos of the samples as mounted on the sample holder in Fig. 5.2.17 and Fig. 5.2.18. These crystals were named E5 and E8 by the producer and we will keep this scheme during this discussion. Several small samples for bulk measurements had already been extracted from sample E5 at various positions, the holes of which can be seen in the photo. Sample E8 consists of two parts. A large half-cylindrical part with a diameter of ≈ 15 mm and a length of ≈ 35 mm and a smaller circular part with a diameter of ≈ 15 mm. The orientation of the two parts with respect to each other during the growth process is unknown.

Sample E5 was found to be rather inhomogeneous with its ordering temperatures ranging from 42 K to more than 55 K, which was the highest temperature at which the neutron depolarisation was measured for this sample. Furthermore, a strong correlation between the visually observed grain structure and

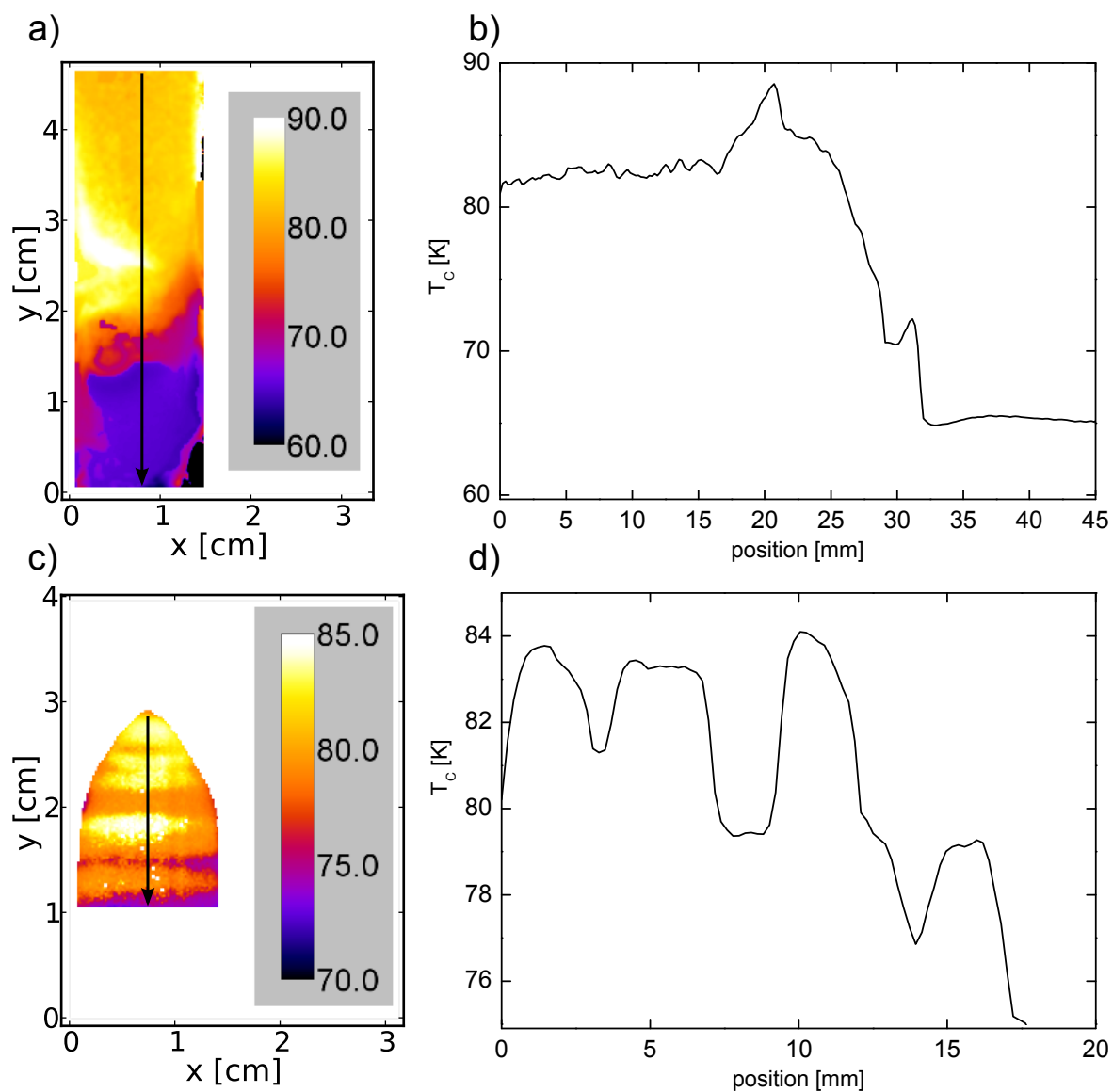


Figure 5.2.16: Distribution of the Curie temperature T_C for the large crystal Jül-l (a) and the small crystal Jül-s (c) both grown in Jülich. The large crystal shows essentially three regions: The top part has an ordering temperature of 82 K, the bottom part has a lower T_C of 65 K and the middle part is relatively inhomogeneous with a maximum T_C of 90 K. The small crystal shows a layered structure with variations of T_C between ≈ 75 K and 85 K. Plots of T_C along the arrows indicated in the figures are shown in images (b) and (d), respectively.

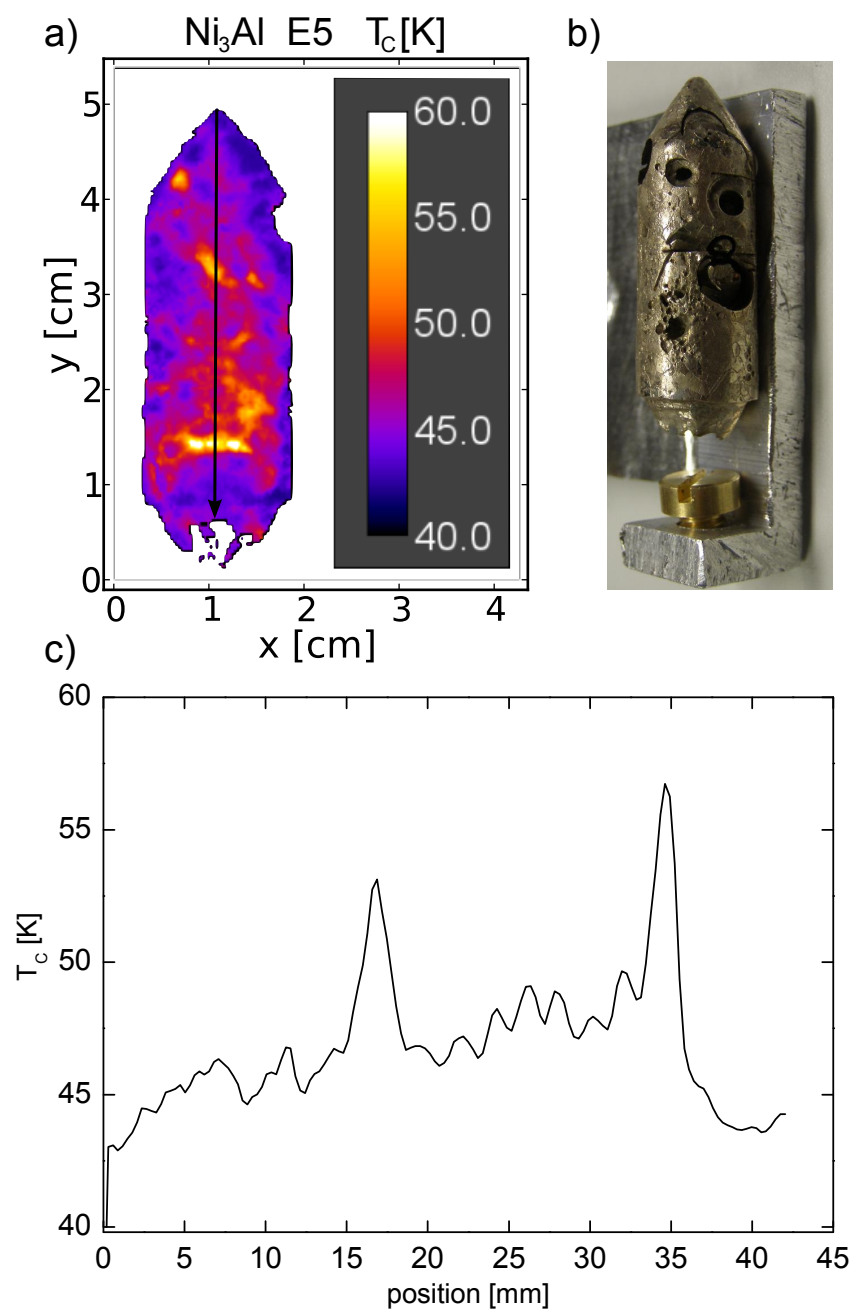


Figure 5.2.17: Distribution of the Curie temperature T_C for crystal E5 (a) and a photo of the crystal as mounted on the sample holder (b). The sample shows strong variations of T_C from 42 K to more than 55 K (highest temperature in the measurement). However, the single crystalline grains seem to be rather homogeneous. A plot of T_C along the arrow indicated in (a) is shown in (c).

the variations of T_C was observed. This suggests that the single crystalline grains of the sample might be relatively homogeneous and the variations of the magnetic properties might mainly occur from one grain to the other.

Sample E8 turned out to be very homogeneous over extended regions. The ordering temperature, which is displayed in Fig. 5.2.18 (left), shows only variations between 37 K and 39 K over the entire sample. Furthermore, most of the sample has a Curie temperature of 37 K and only several spots of the crystal, mainly located at the top of the larger part of the crystal and on the smaller crystal, show higher T_C .

Conclusion: Ni₃Al

Summarising the results of the many experiments performed on various Ni₃Al samples, it can be said that it seems to be extremely difficult to obtain large samples with high homogeneity of their magnetic properties. This difficulty arises especially for single crystalline samples in the case of OFZ growth, where a pronounced layer structure is introduced. In comparison to that, the polycrystalline starting rods used for float zoning were found to be much more homogeneous. This observation lets us conclude that the variations are introduced by the OFZ technique.

A comparison of the samples produced at the E21 institute with samples from other groups shows that not only OFZ grown samples exhibit variations of their magnetic properties. The only sample that was found to be of high homogeneity is sample E8 from the University of Cambridge.

The observation that many samples turn out to be of much lower quality than expected directly leads to the question of the homogeneity of the samples used for many of the publications on Ni₃Al. In case that inhomogeneous samples have been used for these experiments, the inherent averaging over these inhomogeneities might have lead to a wrong interpretation of the experimental data.

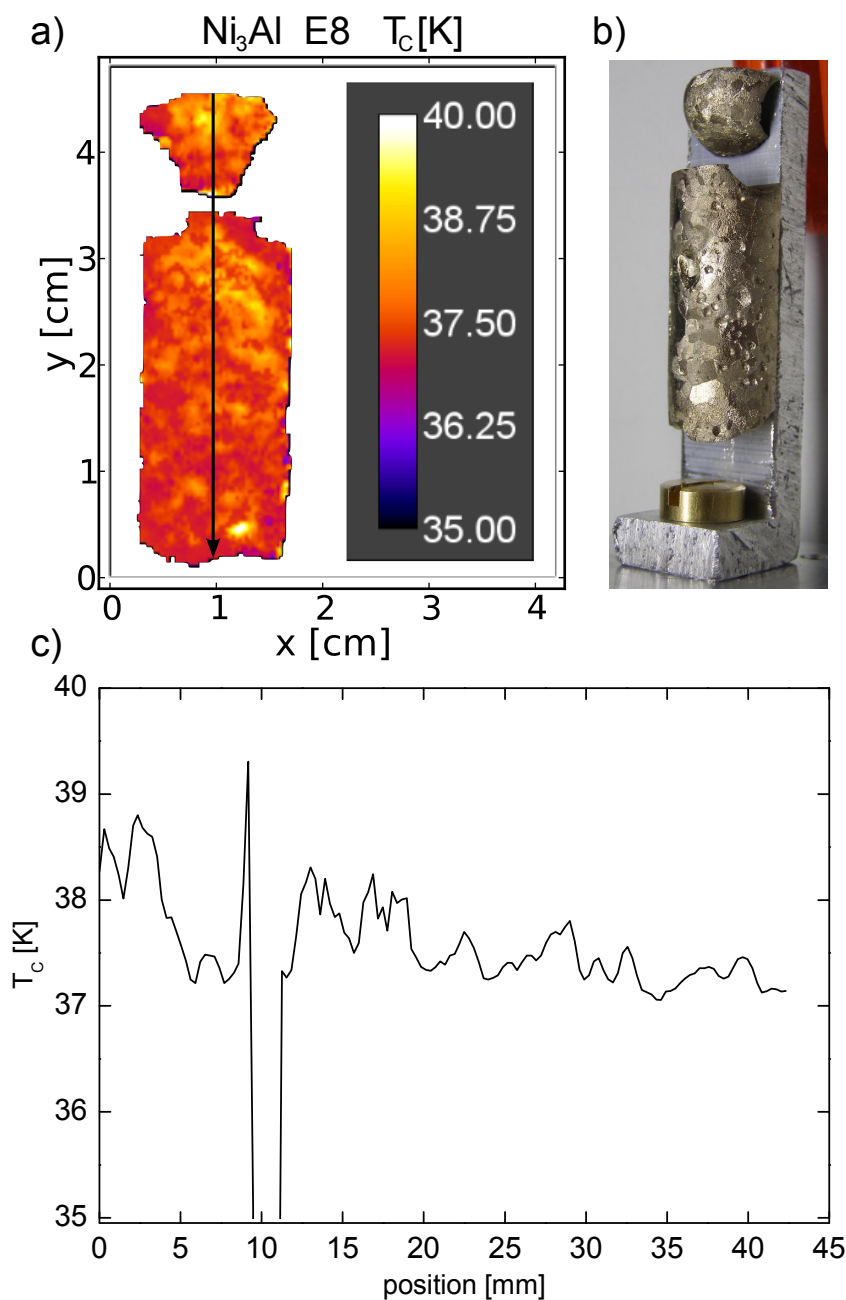


Figure 5.2.18: T_C -map for crystal E8 (a) and a photo of the two parts of the sample on the sample holder (b). Sample E8 was found to be extremely homogeneous over most parts of the sample with a variation of T_C of less than 1 K. Only several spots of the sample show an ordering temperature which is 2 K higher than the value of 37 K observed for the rest of the sample. A plot of T_C along the arrow indicated in (a) is shown in (c).

5.2.3 Pressure Dependence of Ferromagnetism

In many weakly ferromagnetic materials, ferromagnetism can be suppressed by application of hydrostatic pressure. In contrast to compositional doping, which can i.e. be used in $\text{Pd}_{1-x}\text{Ni}_x$ to tune the ordering temperature to zero, the application of pressure is a clean method, which does not introduce any compositional disorder in the material. Being neglected in the SCR theory framework, disorder effects might modify the free energy landscape and introduce new and complex physical behaviour in the systems. Therefore, pressure induced tuning of the ferromagnetic to paramagnetic phase transition is a very useful experimental technique to study quantum phase transitions close to $T = 0$ in the absence of disorder.

However, it turns out to be experimentally very difficult to perform accurate magnetisation measurements at high pressures. As a proof of principle measurement, the effect of hydrostatic pressure on the neutron depolarisation of the materials Ni_3Al and the Heusler alloy Fe_2VAl was studied by means of NDI. Both samples were placed together in one Cu:Be clamp type pressure cell with an inner diameter of 7 mm, a technical drawing of which is shown in Fig. 5.2.19 (a). To increase the neutron transmission of the pressure cell, the walls around the sample area were thinned to a thickness of 7 mm. The samples were placed in a Teflon cup filled with Fluorinert as a pressure medium, and maximum pressures of 10 kbar were applied in this modified pressure cell. The pressure in the cell was calculated from the applied force used to load the cell. In this thesis we will only discuss the experiments on the Ni_3Al sample, which show a strong pressure dependence of T_C .

The Ni_3Al sample used in these measurements is sample OFZ20-L1 on which neutron depolarisation measurements at ambient pressure have already been made as discussed in 5.2.2. These experiments have shown that this sample mainly consists of three large grains with different ordering temperatures. However, the sample orientation in this new experiment was different from the prior experiment, which prevents direct comparison of the results. An average ordering temperature of $T_C = 85$ K was found for this sample from susceptibility measurements.

The experiments were made with setup #4 shown in 4.2 with a ^3He polariser and analyser using a polychromatic ($\lambda \geq 4 \text{ \AA}$) neutron beam with a collimation ratio $L/D = 800$, which leads to a very high spatial resolution of 0.3 mm. Temperature dependent measurements of the neutron depolarisation were performed at two different pressures of ≈ 0.2 kbar and 10 kbar but otherwise using exactly the same experimental parameters. Extreme care was taken to maintain the orientation of the sample while changing the pressure. The low pressure measurement was performed at 0.2 kbar, which prevented loosening of the sample inside the pressure cell. The neutron depolarisation was investigated in a temperature range from 75 K to 90 K in steps of 1 K. At each temperature a total of 15 spin-up and spin-down images with an exposure time of 60 s each were taken, respectively.

Results and Discussion

Fig. 5.2.19 (b) – (d) show a typical set of images as obtained for each temperature step (here $T = 82$ K). A standard absorption neutron radiograph is shown in image (b). The contrast in this image is only due to the absorption of the neutrons by the sample and the pressure cell and not due to a magnetic interaction. The thinned shape of the pressure cell is clearly visible as well as the dark pressure stamp on the top. Furthermore, the Ni_3Al sample can be seen in the topmost third of the brighter pressure

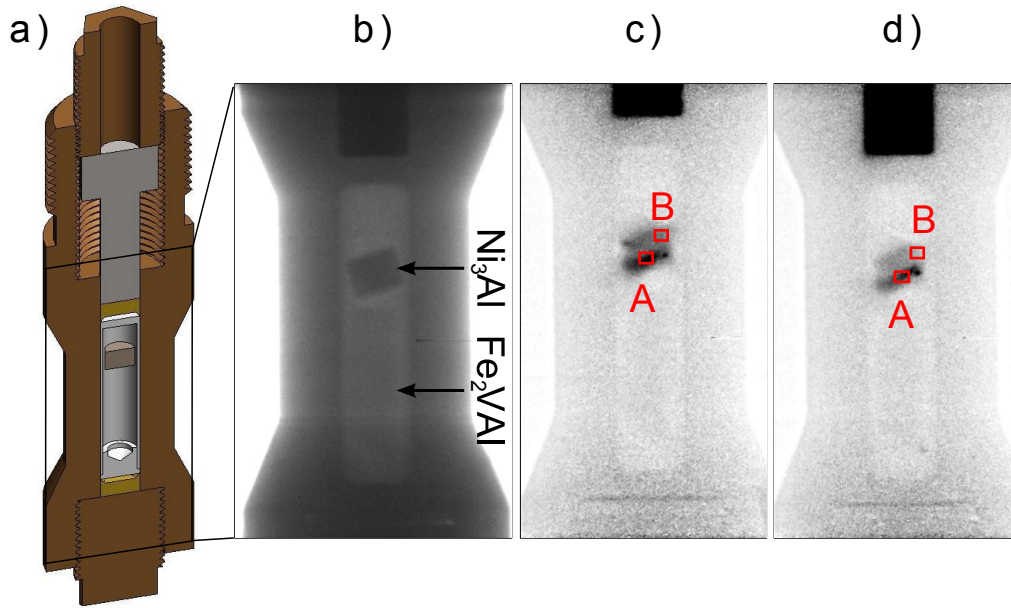


Figure 5.2.19: Technical drawing of the thinned Cu:Be pressure cell (a). The sample is placed inside a Teflon cup filled with Fluorinert as a pressure medium. Neutron absorption radiograph (b) of the pressure cell containing a Ni_3Al sample (top) and a Fe_2VAI sample (bottom), giving only weak absorption contrast. Polarisation of the neutron beam after transmission of the sample at $T = 82\text{K}$ for a pressure of $p = 0.2\text{kbar}$ (c) and 10kbar (d). The red rectangles mark the regions over which the temperature dependence of the beam polarisation is plotted in Fig 5.2.20. The Fe_2VAI sample is paramagnetic at this temperature, while for the Ni_3Al sample spatial variations in the neutron depolarisation can be observed.

volume. The Fe_2VAI sample, located directly below the Ni_3Al sample and separated from the latter by an (invisible) Al spacer is hardly visible. Images (c) and (d) show the neutron beam polarisation after transmission of the sample at $p = 0.2\text{kbar}$ and 10kbar , respectively. One can clearly observe the change of position of the (ferromagnetic and thus depolarising) pressure stamp with different pressure in these images. At a first glimpse one can already see the reduction of the darkened area at higher pressure, i.e the increase of the neutron beam polarisation with increasing pressure. Although the pressure cell is non-magnetic, it is slightly visible in the polarisation images (c) and (d) which is due to the statistical errors introduced by the strong neutron absorption of the material and the resulting low neutron counting statistics. This effect is most pronounced in the bottom part of the cell where it has its largest thickness.

The temperature dependence of the neutron depolarisation is plotted in Fig. 5.2.20, averaged over two different areas of the sample marked by red rectangles in Figs. 5.2.19 (c) and (d). From both plots it is obvious that the onset of neutron depolarisation, which coincides with the onset of ferromagnetic interaction in the sample, shifts towards lower temperatures at a hydrostatic pressure of $p = 10\text{kbar}$. The decrease of the ordering temperature is found to be approximately 2K , giving a $\frac{\partial T_c}{\partial p} \approx 0.2\text{K/kbar}$, which is lower than the value of $\approx 0.5\text{K/kbar}$ found by Niklowitz *et al.* [9] for a stoichiometric sample. Furthermore, we observe a constant depolarisation of the beam by the sample even at higher temperatures. This is due to a residual magnetisation of the sample, which was found to set in at 150K from ambient pressure susceptibility measurements on this sample.

The temperature dependence of the beam polarisation below the ferromagnetic transition shows a steeper decrease with applied pressure than at ambient pressure. This behaviour is intuitively unexpected since the application of pressure leads to a decrease of the magnetic moments and should consequently

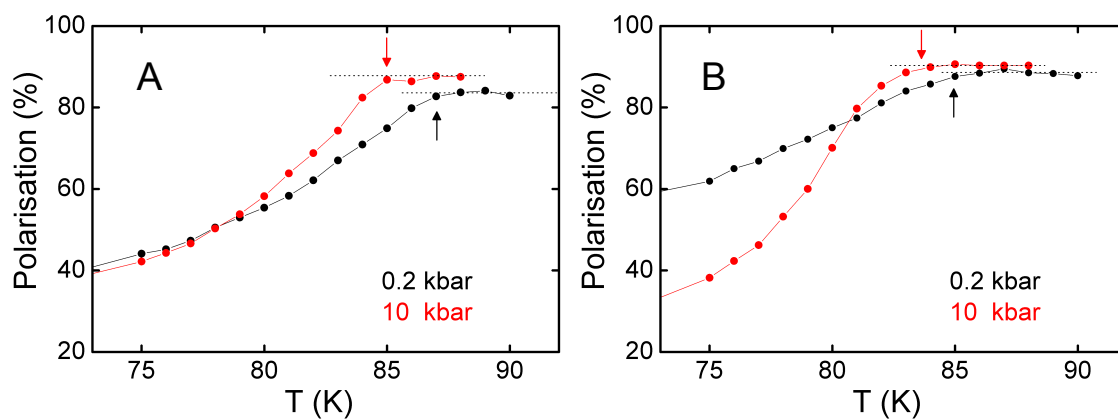


Figure 5.2.20: Temperature dependence of the neutron beam depolarisation by a Ni_3Al sample averaged over the red rectangles A and B shown in Fig. 5.2.19. The red circles give the data at 10kbar, while the low pressure data is shown in black. The reduction of the beam polarisation (marked by arrows) shows the onset of ferromagnetic interaction in the sample. Application of a hydrostatic pressure of 10kbar leads to a reduction of the ordering temperature of approximately 2K. Due to a residual magnetisation of the sample, which sets in at around 150K the beam polarisation does not quite reach 100%.

cause the beam polarisation to increase at a certain temperature compared to the ambient pressure value. Possible reasons for the reduction of the beam polarisation with pressure are an expansion of the ferromagnetic domains in the sample or a reorientation of the domains due to uniaxial pressure components introduced by the freezing of the pressure medium. Both effects could lead to a reduction of the beam polarisation. To clarify this question further experiments – preferably with a homogeneous sample – are necessary.

Conclusion

With these measurements we have shown the possibility to investigate the pressure dependence of the ferromagnetic phase transition with polarised neutron radiography. We obtained spatially resolved information about the pressure dependence of the magnetic properties of the material in a single measurement. NDI offers the possibility of a relatively fast investigation even of large and inhomogeneous samples with a non-destructive method, which can be of great interest in many fields of research.

To achieve higher pressures or perform measurements on larger samples, many different types of pressure cells are available, which could be adapted for the use in neutron radiography experiments. In addition further developments in neutron radiography and neutron optics (e.g focussing neutron optics) offer many possibilities for detailed investigation of a wide variety of problems from geophysics to superconductivity.

5.2.4 Tomographic Measurements

Tomography offers the possibility to non-destructively obtain three dimensional information about the spatial distribution of a material property within a sample. In standard neutron absorption tomography the transmission of a sample is measured under many different projection angles. These data are then reconstructed into a 3D model of the neutron absorption coefficient $\mu(x, y, z)$ using a filtered back projection algorithm.

As discussed in 2.6, measuring the polarisation of the neutron beam after transmission of the sample instead of the attenuation of the neutron beam under many projection angles yields 3D information about the neutron depolarisation density $\rho(x, y, z)$. The reconstruction of this depolarisation density can be performed with exactly the same algorithm, which is also used for neutron absorption tomography. The neutron depolarisation density contains volume information about the distribution of the spin flip probability within the sample. In comparison to the prior measurements, where only one projection angle was used, this method can retrieve 3D information about the variation of the magnetic properties within the sample. However, the procedure of acquiring many projections under different angles leads to very long measuring times. To limit the measurement time, the tomographic measurements described here have only been performed at a single temperature.

Experimental Details

A tomography of $\text{Pd}_{1-x}\text{Ni}_x$ crystal II was performed by mounting the cryostat in which the sample was mounted on a rotary stage, allowing to rotate the cryostat together with the sample over 180° . The experiments were made with a monochromatic beam of $\lambda = 3.2 \text{ \AA}$ employing setup #3 (cf. 4.2) with a ^3He polariser and analyser. During the measurement, which was performed at a temperature of 8 K, the sample was rotated in steps of 1° from 0° to 179° resulting in a total of 180 projections. At each projection angle, one spin-up and one spin-down image with an exposure time of 60 s was recorded. This procedure was repeated 5 times, resulting in a total of 5 spin-up and spin-down images at each projection angle yielding a total exposure time of 30 h. With this procedure we could avoid that the relaxation of the ^3He gas polarisation and consequently the higher statistical noise in the images affected especially the larger projection angles. In contrast to this, the ^3He relaxation was distributed more equally over all projections. Furthermore, 10 open beam images with the cryostat moved out of the beam were acquired for each polarisation direction, respectively.

Data evaluation

From each pair of spin-up and spin-down images the polarisation was calculated as $P_i = \frac{I_{\uparrow,i} - I_{\downarrow,i}}{I_{\uparrow,i} + I_{\downarrow,i}}$. All polarisations were then averaged while being weighted with the inverse of the standard deviation w_i , which was measured in a homogeneous area outside of the sample.

$$P = \frac{1}{\sum_{i=1}^5 w_i} \sum_{i=1}^5 w_i P_i \quad (5.2.3)$$

The standard deviation was taken as a measure for the statistical error due to the decreasing counting statistics resulting from the decreasing ^3He polarisation. This data was then reconstructed with a standard filtered back projection algorithm yielding the spatial distribution of the neutron depolarisation density $\rho(x, y, z)$.

Furthermore, the attenuation of the neutron beam by the sample was calculated as

$$A = \frac{\sum_{i=1}^5 I_{\uparrow,i} + I_{\downarrow,i}}{I_{\uparrow,\text{ob}} + I_{\downarrow,\text{ob}}}, \quad (5.2.4)$$

where $I_{\uparrow,\text{ob}}$ and $I_{\downarrow,\text{ob}}$ are the summed intensities of the open beam images. Just as the depolarisation data,

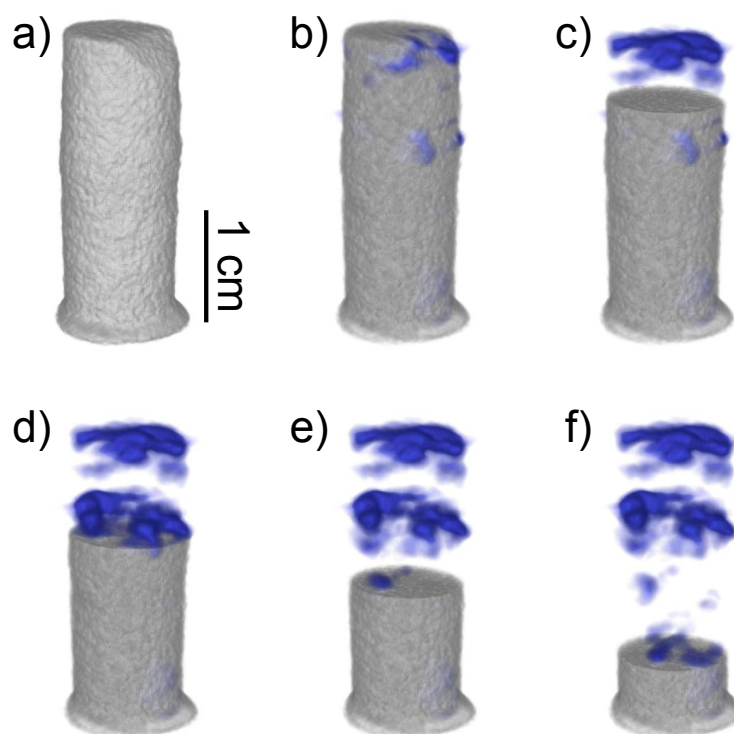


Figure 5.2.21: Tomographic reconstruction of the absorption (grey) and depolarisation (blue) data of $\text{Pd}_{1-x}\text{Ni}_x$ crystal II. Image (a) shows only the absorption data and images (b) – (f) show horizontal cuts through the absorption data at different heights for better visualisation of the depolarisation data.

this data was reconstructed with a filtered back projection algorithm, resulting in the spatial distribution of the neutron absorption coefficient $\mu(x, y, z)$.

Results & Discussion

The resulting 3D data sets were aligned and visualised with a 3D volume rendering software as shown in Fig. 5.2.21. The absorption data is shown in grey and the depolarisation data is displayed in blue. Image (a) shows only the absorption data, which gives an outside view of the shape of the crystal. At the top an inclined edge is visible which was cut from the crystal for bulk measurements. At the bottom of the sample, the glue is visible, which was used to fix the crystal on the sample holder and which shows high attenuation of the neutron beam. Images (b) to (f) show different horizontal cuts through the absorption data for better visualisation of the depolarisation data. Furthermore, in these images the absorption data is rendered more transparently to permit to see the depolarising parts of the sample close to the surface. It is clearly observed from the images that the sample has highly inhomogeneous magnetic properties and that the depolarising parts of the sample are oriented in horizontal layers.

Tomography of Slice 1 of Crystal II

Similar measurements as those on the entire crystal II described above have been performed on slice II after cutting of the two slices from this crystal. In contrast to the experiments on the entire crystal, this tomography has been performed with a polychromatic beam with $\lambda \geq 4 \text{ \AA}$ with setup #4 (cf. 4.2) using a ^3He polariser and analyser at a collimation ratio of $L/D = 800$. Thus, very high spatial resolution

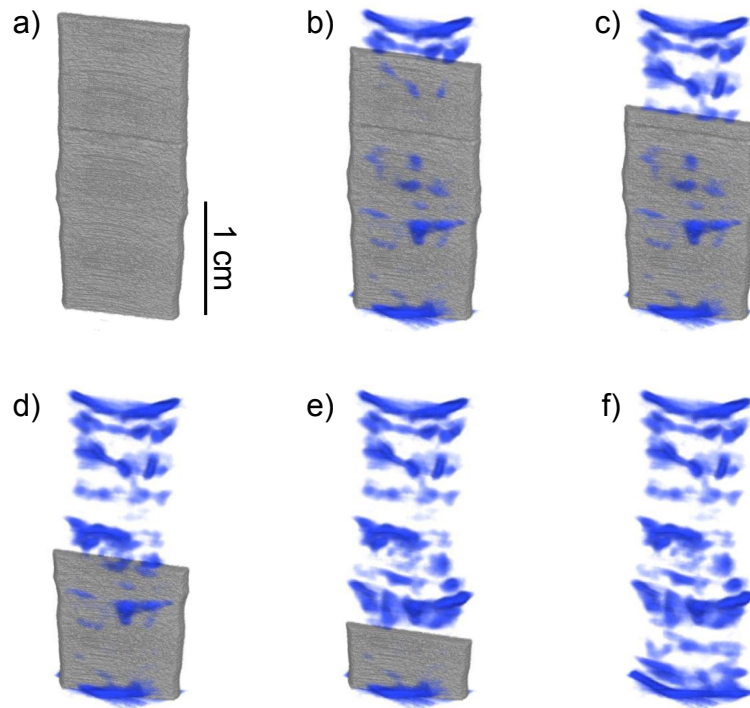


Figure 5.2.22: Tomographic reconstruction of slice 2 of $\text{Pd}_{1-x}\text{Ni}_x$ crystal II. The absorption data is displayed in grey and the depolarisation data in blue. (a) only the absorption data is shown. (b) – (e) several cuts through the absorption data are displayed for better visualisation of the depolarisation data. (f) only the depolarisation data is shown.

of ≈ 0.3 mm could be achieved. The sample was mounted as shown in Fig. 5.2.2 (right) between two Al sheets in a closed container filled with He exchange gas. The measurements were performed at a temperature of 12 K and 180 projections were acquired over 179° . At each projection angle 5 images with an exposure time of 60 s were recorded and processed as described above.

The reconstructed 3D data is shown in Fig. 5.2.22, where again the absorption data is displayed in grey and the depolarisation data in blue. In image (a) only the absorption data is displayed, showing that the shape of the slice can be accurately reconstructed from the projections. The absorption data of the sample is very homogeneous over the sample volume and from this data no variation of the sample composition is observed. There is a single horizontal streak visible where the object seems to have a scratch in $2/3$ of the height of the sample. However, this is a reconstruction artifact due to a pixel defect, which was visible at this position on the detector. Images (b) – (e) show both the absorption and the depolarisation data, where the absorption data is only displayed from the bottom of the sample up to different heights for a better visualisation of the depolarisation data. Image (f) shows only the depolarisation data. Despite the higher temperature in this measurement, there seem to be more depolarising regions in the sample than observed in the measurement on the entire crystal described above. However, this is due to the use of a polychromatic beam with larger mean wavelength, which leads to larger depolarisation.

It can be observed that especially at the top and bottom end of the sample, the depolarisation density extends to regions outside of the sample boundaries. This is mainly due to stray field effects, which often occur at the sample boundaries, and lead to a depolarisation of the beam even outside the sample. In the remaining parts of the sample the depolarisation extends in some places towards the surface of

the sample but not outside the sample.

It can be clearly observed from the data shown in Fig. 5.2.22 that the sample shows highly inhomogeneous magnetic properties, whereas its absorption is very homogeneous. This underlines that the variations in composition leading to a change in the magnetic properties are very small, which is in agreement with the strong composition dependence of the ordering temperature in $\text{Pd}_{1-x}\text{Ni}_x$. Also in good agreement with the radiographic measurements shown above is that at a temperature of 12 K there are vast paramagnetic regions in the sample, which show no depolarisation of the neutron beam.

Conclusion

These proof of principle measurements have shown the possibility to reconstruct neutron depolarisation data with standard filtered back projection algorithms and to obtain the spatial distribution of the neutron depolarisation density. Tomography can be an extremely helpful tool for quality control of samples and for locating small and homogeneous parts of a large sample, which can then be used for bulk measurements.

It would be ideal to perform temperature dependent tomographies of samples to obtain 3D information about the distribution of the Curie temperature T_C . The required beam time of nearly two days to perform such a measurement at a single temperature at currently available neutron sources, however, limits the application of this method to only a few temperature steps.

Chapter 6

Conclusion & Outlook

In this work we have developed a powerful new technique for the spatially resolved investigation of magnetic properties of bulk samples. This method, which we call Neutron Depolarisation Imaging (NDI), is based on the combination of a standard neutron radiography setup with equipment for neutron spin polarisation analysis. The interaction of the neutron's nuclear magnetic moment with the magnetic fields inside the domains of a ferromagnetic sample leads to the depolarisation of a polarised and collimated neutron beam after transmission of the sample. Analysing the depolarisation the neutron beam suffers by penetration of the sample yields valuable information about the domain structure of the sample. Most notably the average domain sizes, the ordering temperature of the sample and the ordered moment can be determined.

In contrast to the well known standard one dimensional neutron depolarisation technique, on which this method is based, we have used a collimated neutron beam on the radiography beam line ANTARES at FRM II in combination with neutron polarisers and analysers which do not affect the collimation. Employing a 2D position sensitive detector allows for the spatially resolved determination of the sample properties listed above. The requirements for the polarisers and analysers as well as further instrument components like a monochromator and spin flippers have been analysed in the context of optimising the performance of the NDI setup.

Experiments with this new technique have been performed on various samples of the weakly ferromagnetic (FM) materials $\text{Pd}_{1-x}\text{Ni}_x$ and Ni_3Al during which NDI has proven to be a valuable tool for the assessment of sample quality and homogeneity. For both substances the magnetic properties crucially depend on the concentration of the constituents and even small inhomogeneities lead to strong variations of these properties. The direct spatially resolved determination of the magnetic properties in contrast to the determination of the concentration of the constituents makes NDI superior to other methods like EDX. Furthermore, not being a surface sensitive method, NDI allows to measure the properties of bulk samples. The results of these experiments and experiments on other weakly ferromagnetic materials show that samples of good quality and homogeneity are extremely rare. Even samples which were found to be of high quality e.g. by residual resistivity measurements were found to show strong variations in the ordering temperature on a macroscopic scale.

The interest in weakly ferromagnetic materials is, however, not primarily based on the determination of sample homogeneity. More importantly, this material class shows ferromagnetic order at very low temperatures at which deviations from the standard Fermi liquid (FL) model of ferromagnetism are

observed. The detailed investigation of many weakly ferromagnetic systems has led to the view that this FL model is inappropriate to describe the ferromagnetism of these substances.

The transition temperature of weakly FM materials can be tuned towards $T = 0$ by application of hydrostatic pressure or by variation of the composition of the material. Tuning the ordering temperature towards low temperatures leads to a balancing of strong interactions leaving only weak interactions to determine the ground state of the material. These interactions can lead to completely new magnetic order as observed for example by the coexistence of superconductivity and ferromagnetism in UGe_2 or by the formation of a liquid crystal like phase of partial magnetic order in MnSi . In all systems investigated so far the phase transition was found to change from second to first order as coming sufficiently close to the suppression of the ordering temperature. For this reason there has been an extensive search going on in the past 20 years to find a material showing a quantum critical point for which the phase transition remains second order at $T = 0$.

We have therefore developed a method for the spatially resolved determination of the ordered moment M_s , which is the order parameter of the ferromagnetic to paramagnetic phase transition, as well as the ordering temperature T_C from the temperature dependence of NDI data. For an inhomogeneous sample containing regions with different M_s and T_C this method can yield the intrinsic relation between these two properties and can therefore reveal information, whether the phase transition is first or second order. A $\text{Pd}_{1-x}\text{Ni}_x$ sample was investigated in detail using this technique and the results were compared with simulations. For this particular sample, which does not contain areas with sufficiently low ordering temperatures we could, however, not ultimately successfully determine the nature of the phase transition.

We have proven the feasibility of pressure experiments at hydrostatic pressures of up to 12kbar in this work. As stated above, the application of hydrostatic pressure can lead to the suppression of the ordering temperature and the balancing of strong interactions. What remains are weaker interactions which normally do not play a significant role in the formation of the ground state of the material. New magnetic order was found to arise from these interactions at low temperatures. Especially high- T_C superconductors show significant heterogeneities and it is not known whether this disorder might eventually be responsible for the formation of the superconducting phase. Furthermore, it is not clear whether these heterogeneities arise from an intrinsic behaviour of the system or are caused by constitutional inhomogeneities of the sample. We have therefore developed a criterion to assess the amount of heterogeneity in a sample from the shape of the temperature dependence of its depolarisation signature. In the future we plan to perform NDI experiments under hydrostatic pressure down to lowest temperatures. These experiments will help to clarify whether the depolarisation signature shows the presence of heterogeneities and can therefore help to understand the origin of novel magnetic phases.

A further goal will be the extension of the NDI method to the three dimensional analysis of the beam depolarisation by the sample. This will require for compact polarisation rotators before and after the sample. The 3D analysis of the neutron depolarisation will provide even more information on the magnetic properties of the sample. Using this technique it will be possible to determine a net magnetisation and the mean square directions cosines of the magnetisation in the domains, i.e. it will be possible to identify easy axes of the system.

Chapter 7

Acknowledgements

As usual, an experimental PhD thesis is not the result of the work of a single person, but of the collaboration with many people. This work would not have been possible without the help of a number of colleagues and friends who spent much of their time and effort on its progress. At this point I wish to thank everybody who has supported me in one way or the other. My special thanks go to:

Prof. Peter Böni for giving me the opportunity to work on an interesting physical topic by supervising this thesis. Thank you for many fruitful and inspiring discussions with an innumerable amount of valuable ideas, many of which have helped to improve the method of neutron depolarisation imaging. Furthermore I wish to thank you for the friendly atmosphere with which I was received at your institute E21.

Prof. Christian Pfeiderer for introducing me to the topic of weak itinerant ferromagnetism and for many discussions on possible applications and improvements of neutron depolarisation imaging on this material class. I greatly appreciate the support you gave me in the development of this new technique and in bringing it together with real physical problems. Thank you as well for your concerns and open discussions about my career.

I am greatly indebted to **Elbio Calzada**, who did the construction work of most of the instrument components used for my setup. I always enjoyed your refreshingly different view of things! Thank you for helping and motivating me during the beam times and for sharing “mate” with me.

Also the rest of the **ANTARES team** has always had a helping hand for me when I really needed it. In particular I wish to thank **Dr. Burkhard Schillinger** for the huge amount of beam time I got at the beam line ANTARES to perform my experiments and for always supporting my ideas. Apart from that I appreciate his idea to build a polarising version of the periscope. Special thanks to **Martin Mühlbauer** for always being open to fruitful and interesting discussions, be it on physics or other topics. He has always been a great help planning and setting up my experiments. Thank you for the good time we had together! Furthermore, I wish to thank the former team members **Klaus Lorenz** and **Florian Grünauer** for their support and for the good atmosphere we enjoyed at ANTARES.

For their support of our first NDI experiments and for providing beam time at HZB, Berlin I wish to thank the team of the radiography beam line CONRAD (**Nikolay Kardjilov**, **André Hilger** and **Ingo Manke**). I would like to especially mention the fruitful discussions I had with André Hilger during our joint experiments at HZB.

First test measurements of the double crystal monochromator were performed at the ICON beam line at PSI, which was made available to me by **Eberhard Lehmann**. **Guido Kühne** and **Gabriel Frey** have performed the measurements together with me. I wish to thank the whole team for their help and for receiving me in such a friendly way!

I would like to express my appreciation for the perfect and fast work of the **FRM II workshop**. There was always a way to quickly build a part if it was urgently needed for my experiments. Most of the instrument components constructed during this thesis have been built in this workshop and still perform very well.

Andreas Neubauer spent a lot of time at the beam line ANTARES during our measurements on Ni₃Al. Thank you for always providing me with huge amounts of your “home-grown” samples and for helping me out on several weekend shifts!

Christian Franz has been of great help to me on the subject of Pd_{1-x}Ni_x. He performed the magnetisation measurements on the small samples cut from the slice and did the evaluation of the data. He was always a great source of knowledge about Pd_{1-x}Ni_x and magnetisation measurements.

I wish to thank **Sebastian Mühlbauer** for his support during the first proof of principle measurements on MIRA, for many very helpful discussions without which this work would not have been possible and for proof-reading of my manuscript. Thank you not only for all the help you provided on physical topics but also for the many free-time activities we shared – especially for the sailing trip to Croatia!

I very much appreciate the time **Marc Janoschek** took for helping me with data analysis, the many ideas he contributed to this work and most of all being an old friend who always had some helping words for me.

Despite working on the NDI technique for only a short time, **Philipp Schmakat** has become a great partner for discussions and a source of ideas for data evaluation. I am extremely grateful that he will continue my work as part of his diploma thesis.

The PANDA team (**Astrid Schneidewind**, **Dirk Etdorf** and **Peter Link**) has supported my work with many instrument components which I could borrow from their beam line. Thank you also for the great help installing the cryostat at ANTARES for the first time.

In this context I also wish to thank **Jürgen Peters** and **Heiner Kolb** from the sample environment team at FRM II for their support with the installation and operation of the cryostat.

Very special thanks to **Klaudia Hradil** for always having exactly the things I just needed. Thank you for providing your cryostat for so many times in such an uncomplicated manner.

I am also very grateful for the help of **Sergey Masalovich**, **Aleksander Lykvar** and **Hermann Schölderle** who have always provided polarised ³He for my experiments even on the weekends and for continuously improving the cells and magnetostatic cavities. Without their help, this work would not have been possible.

The TRISP team (**Thomas Keller**, **Kathrin Buchner** and **Nathalie Munnikes**) has always helped me when I needed materials or devices for my experiments. Especially I like to say thank you to **Thomas Keller** with whom I had many very interesting and fruitful discussions about many experimental techniques.

Furthermore, I wish to thank **Andi Bauer** for information on the SCR theory, **Christian Breunig** for characterisation of the waviness of the polarising supermirrors used in the periscope, **Robert Georgii** for his help with the first experiments on MIRA, **Jens Klenke** for discussions, literature and lending me his Helmholtz coils, **Jens Krüger** for his support with the taco system and other software related problems, **A. Loidl and A. Krimmel** from University of Augsburg for providing their $\text{Pd}_{1-x}\text{Ni}_x$ samples for my investigations, **G. G. Lonzarich** for providing Ni_3Al samples, **Martin Meven** for performing the measurements of the mosaic spread of the monochromator crystals and **Jürgen Neuhaus** for proof-reading of my manuscript and for being concerned about my work.

Financial support from **DFG Forschergruppe FOR 960** on quantum phase transitions is gratefully acknowledged.

Chapter 8

List of Publications

1. E. Calzada, F. Grünauer, M. Mühlbauer, B. Schillinger, and M. Schulz, “New design for the ANTARES-II facility for neutron imaging at FRM II,” *Nuclear Inst. and Methods in Physics Research, A*, vol. 605, no. 1-2, pp. 50–53, 2009.
2. M. Schulz, P. Böni, E. Calzada, M. Mühlbauer, A. Neubauer, and B. Schillinger, “A polarizing neutron periscope for neutron imaging,” *Nuclear Inst. and Methods in Physics Research, A*, vol. 605, no. 1-2, pp. 43–46, 2009.
3. M. Schulz, P. Böni, E. Calzada, M. Mühlbauer, and B. Schillinger, “Energy-dependent neutron imaging with a double crystal monochromator at the ANTARES facility at FRM II,” *Nuclear Instruments and Methods in Physics Research, A*, vol. 605, no. 1-2, pp. 33–35, 2009.
4. B. Schillinger, P. Böni, C. Breunig, E. Calzada, C. Leroy, M. Mühlbauer, and M. Schulz, “A neutron optical periscope used for neutron imaging,” *Nuclear Instruments and Methods in Physics Research, A*, vol. 605, no. 1-2, pp. 40–42, 2009.
5. A. Strzelec, D. Foster, H. Bilheux, C. Daw, C. Rutland, B. Schillinger, and M. Schulz, “Neutron Imaging of Diesel Particulate Filters,” *SAE international*, pp. 2009–01–2735, 2009.
6. M. Schulz, P. Böni, C. Franz, A. Neubauer, E. Calzada, M. Mühlbauer, B. Schillinger, C. Pfeleiderer, A. Hilger, and N. Kardjilov, “Comparison of Polarizers for Neutron Radiography,” Proceedings of the ICNS 2009, *Journal of Physics - Conference Series*, 2009. in press.
7. M. Schulz, A. Neubauer, M. Mühlbauer, E. Calzada, B. Schillinger, C. Pfeleiderer, and P. Böni, “Polarized Neutron Radiography with a Periscope,” Proceedings of the ICM 2009, *Journal of Physics - Conference Series*, 2009. in press.
8. M. Schulz, A. Neubauer, S. Masalovich, M. Mühlbauer, E. Calzada, B. Schillinger, C. Pfeleiderer, and P. Böni, “Towards a Tomographic Reconstruction of Neutron Depolarization Data,” Proceedings of the PNSXM 2009, *Journal of Physics - Conference Series*, 2009. in press.
9. C. Franz, C. Pfeleiderer, A. Neubauer, M. Schulz, B. Pedersen, and P. Böni, “Magnetisation of $\text{Pd}_{1-x}\text{Ni}_x$ near Quantum Criticality,” Proceedings of the ICM 2009, *Journal of Physics - Conference Series*, 2009. in press.

10. K. U. Hess, A. Flaws, B. Schillinger, M. Mühlbauer, M. Schulz, E. Calzada, and D. B. Dingwell, “Applications of a high to ultra-high resolution neutron computed tomography system for the geosciences,” *Geosphere*, 2009. submitted.

Appendix A

Further Experiments

A.1 Visualisation of magnetic field integrals

Not only magnetic domain structures of samples can be studied by radiography with polarised neutrons. The Larmor precession of the neutron spin around a magnetic field does not necessarily have to take place inside the sample. Any magnetic field perpendicular to the neutron polarisation between polariser and analyser will cause the neutron spin to precess around this field. The Larmor frequency of this precession is given by $\omega = \gamma B_{\perp}$, where $B_{\perp}(x, y, z)$ is the magnetic field perpendicular to the polarisation direction and γ is the gyromagnetic ratio. The total precession angle ϕ of the neutron spin after passing through the sample area is then given by the time the neutron spends within the field. With the neutron velocity v , this can be expressed as the field-integral along the flight path of the neutron

$$\phi = \gamma/v \int B_{\perp}(x, y, z) dz. \quad (\text{A.1.1})$$

The integral goes along the flight path of the neutron between polariser and analyser. The intensity measured at the detector is a product of the conventional attenuation law due to any neutron absorbing material between polariser and analyser

$$I_a = I_0 \exp\left(-\int \mu(x, y, z) dz\right) \quad (\text{A.1.2})$$

and a polarisation dependent part, which represents the projection of the resulting polarisation direction onto the analysing direction and is given by

$$I_p = 1/2(1 + PP_a \cos \phi). \quad (\text{A.1.3})$$

Here ϕ is the precession angle defined above, P_a is the analysing efficiency and P is the polarising efficiency. Using this equation, this technique can be used to determine the magnetic field integral of complex field geometries, like the stray field of electric coils or permanent magnets, or even trapped flux in superconductors [94]. However, not the absolute value of the field integral can be determined but only the variation of the precession angle modulo 2π .

As an example of the potential of this method we show the field integral image of a permanent ring magnet, which is a rotor of an electro motor. The magnet, which is shown in the inset of the plot on

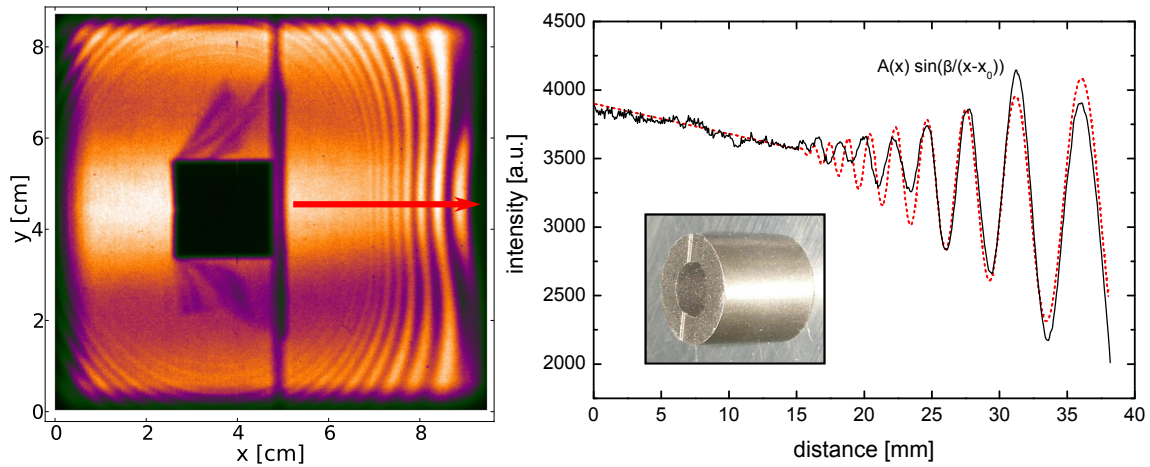


Figure A.1.1: Magnetic field integral image of a ring magnet (left) and a plot of the data along the red arrow in the left image (right). The ring magnet (shown in the inset in the plot on the right side) was mounted on a vertical Al slab with some Al tape, which is visible above and below the magnet. The direction of the beam was in z -direction and it was polarised in y -direction. A fit of the data with $A(x) \sin(\beta/(x-x_0))$ with a linearly increasing amplitude $A(x)$ is shown by the dashed red line.

the right hand side of Fig. A.1.1, has a diameter of ≈ 2 cm and approximately the same length. It was mounted on a vertical Al slab with some Al tape, which is visible due to its neutron absorption above and below the dark magnet in the middle of the left image.

The image was acquired at a wavelength of 3.2 \AA , using setup #3 described in 4.2 with a ^3He polariser and analyser as shown in Fig 3.2.1 b). This setup yields a spatial resolution of 0.4 mm , which is the highest value for magnetic field imaging reported so far. The cross section of the image is $\approx 9 \times 9 \text{ cm}^2$.

Coming from the outside of the left image one observes a fringe pattern with decreasing wavelength as going towards the centre of the magnet. This pattern originates from the variation of the detected intensity with the precession angle ϕ as discussed above and is in agreement with the increase of the magnetic field closer to the magnet. No more fringes are observed very close to the magnet due to the limited spatial resolution of the setup which does not allow to resolve the finer fringes. A plot of the detected intensity along the red line in the left image is shown on the right hand side of Fig. A.1.1. At the outer regions the fringes can be clearly resolved, but going closer to the centre of the image, the amplitude of the modulation decreases and the modulation vanishes at around 15 mm from the beginning of the arrow. The modulation that can still be resolved is in agreement with a spatial resolution of 0.4 mm . A comparison of the data with a $A(x) \sin(\beta/(x-x_0))$ fit with linearly increasing amplitude $A(x)$ is given by the dashed red line. Very good agreement of the peak positions is found for large x -values, whereas closer to the magnet a slower variation of the data is observed.

These measurements have shown that radiography with polarised neutrons allows to directly measure the magnetic field integral along the neutron flight path. This could for instance be used to determine the homogeneity of the magnetic field inside neutron spin manipulation components like precession coil spin flippers or B_0 coils used for neutron spin echo. A high field homogeneity over the cross section of these devices is essential for their performance and can be easily investigated with this method by aligning the components in a way that their magnetic field is perpendicular to the beam polarisation.

A.2 Magnetostriction in Ni foils

Here we will present first proof-of-principle measurements of a further interesting application of neutron depolarisation imaging. The magnetostriction effect leads to a change of the orientation of the domains within a sample, if a uniaxial force is applied on the sample. As a consequence, a change of the depolarisation which a neutron beam suffers after transmission of the sample is observed. In our experiments we used this effect on foils made of Ni, which has a negative magnetostrictive constant of $\lambda_s \approx -37 \cdot 10^{-6}$ [134], as a method for the spatially resolved measurement of the mechanical stress in the material. Non-spatially resolved 3D neutron depolarisation measurements of the magnetostrictive effect in Ni foils have already shown the possibility to use this effect as a measure of the stress applied on the foil [84].

High purity Ni foils (99.99%) with a thickness of $125 \mu\text{m}$ were cut to a concave shape as shown in Fig. A.2.1 (right) with a maximal width of 30mm and a minimal width of 10mm. After cutting, the foils were annealed in vacuum at 900°C for 8h to remove any remaining strain from the samples and then mounted in a frame, which was fixed at the top end, while the bottom end could be loaded with weights up to 25 kg. For the experiment, the foil was placed in the polarised neutron beam between the ^3He polariser and analyser of setup #3 (c.f. 4.2) with the direction of the tension applied by the weights being parallel to the beam polarisation. Spatially resolved measurements of the beam polarisation after transmission of the Ni foils were performed with three different loads from 5 kg to 25 kg on the setup. Five spin-up and spin-down images with an exposure time of 60s each were acquired per applied load, from which the transmitted beam polarisation was calculated.

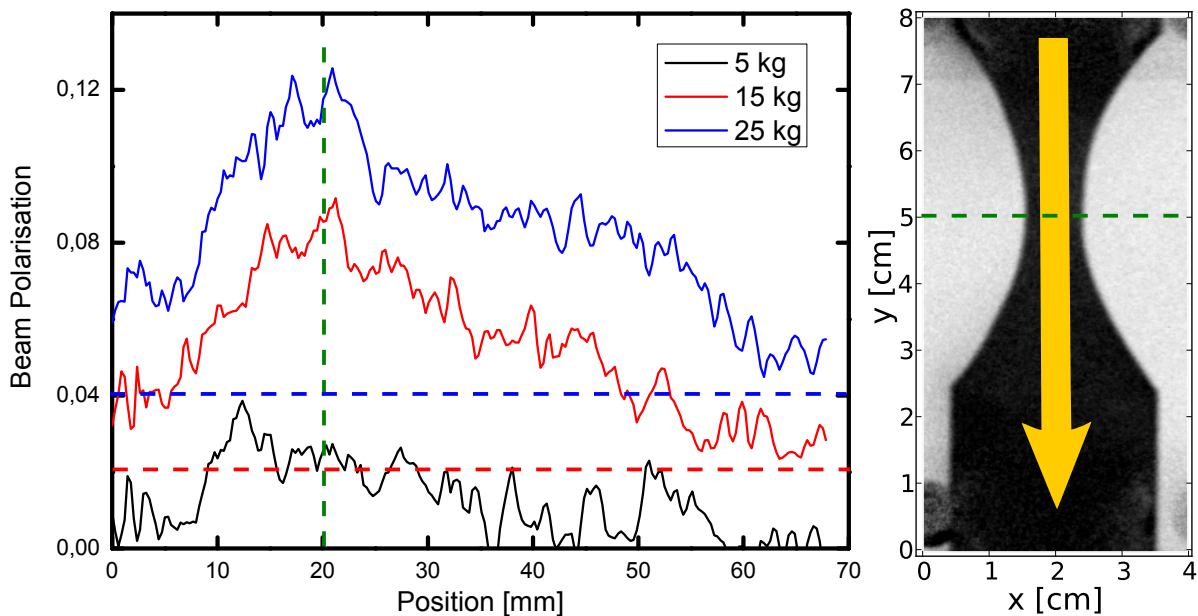


Figure A.2.1: Beam polarisation after transmission of a Ni foil along the line shown in the image on the right hand side (from top to bottom). The foil was loaded with different weights to modify the mechanical stress. Increasing stress leads to a reorientation of the domains and to increasing beam polarisation. For better visibility, the curves are shifted by a value of 0.02 along the y-axis as indicated by the red and blue baselines.

The beam polarisation after transmission of the foil is plotted in the left plot of Fig. A.2.1 along the yellow arrow shown in the right image. However, due to the strong depolarisation of the beam by the

Ni foil ($P \approx 0$), the statistical error in these measurements is very large. To reduce the statistical error, the polarisation was averaged over the horizontal extension of the arrow. For better visibility, the curves were shifted by a value of 0.02 with respect to each other along the y-axis.

Even though the statistical errors in these measurements are very high, it is still visible that the peak in the plot, which is located at the position where the sample has its smallest width (marked by the dashed green lines), increases with increasing stress. The beam polarisation increases due to the preferred alignment of the domains in the sample in parallel to the direction of the applied mechanical stress. A quantitative, spatially resolved evaluation of the mechanical stress in the foil was not possible due to the large errors in the measurements. These errors could, however, be decreased in future measurements by acquiring more images and also by using a polychromatic beam giving much improved counting statistics.

These proof-of-principle measurements have shown the possibility to use ferromagnetic foils with a high magnetostrictive constant as stress gauges for the spatially resolved determination of mechanical stress. The sensitivity of the method could be further improved by using foils with a higher magnetostrictive constant, e.g. FeCoV, for which the magnitude of the magnetostrictive constant $\lambda_s \approx 83.4 \cdot 10^{-6}$ is approximately twice as high as for Ni [135, 136]. Stress sensors could be built by mounting such foils on the surface of a (nonmagnetic) sample and measuring the depolarisation of the beam after transmission of the foil.

Bibliography

- [1] J. Hertz, “Quantum critical phenomena,” *Physical Review B*, vol. 14, no. 3, pp. 1165–1184, 1976.
- [2] A. Millis, “Effect of a nonzero temperature on quantum critical points in itinerant fermion systems,” *Physical Review B*, vol. 48, no. 10, pp. 7183–7196, 1993.
- [3] G. Lonzarich and L. Taillefer, “Effect of spin fluctuations on the magnetic equation of state of ferromagnetic or nearly ferromagnetic metals,” *J. Phys. C, Solid State Phys.*, vol. 18, no. 22, pp. 4339–4371, 1985.
- [4] T. Moriya, *Spin fluctuations in itinerant electron magnetism*. Springer Berlin, 1985.
- [5] H. Löhneysen, A. Rosch, M. Vojta, and P. Wölfle, “Fermi-liquid instabilities at magnetic quantum phase transitions,” *Reviews of Modern Physics*, vol. 79, no. 3, pp. 1015–1075, 2007.
- [6] M. Uhlarz, C. Pfleiderer, and S. M. Hayden, “Quantum Phase Transitions in the Itinerant Ferromagnet $ZrZn_2$,” *Physical Review Letters*, vol. 93, p. 256404, Dec 2004.
- [7] C. Pfleiderer and A. D. Huxley, “Pressure Dependence of the Magnetization in the Ferromagnetic Superconductor UGe_2 ,” *Physical Review Letters*, vol. 89, p. 147005, Sep 2002.
- [8] S. Barakat, D. Braithwaite, P. Alireza, K. Grube, M. Uhlarz, J. Wilson, C. Pfleiderer, J. Flouquet, and G. Lonzarich, “High-pressure investigations of the itinerant ferromagnet CoS_2 ,” *Physica B: Condensed Matter*, vol. 359-361, pp. 1216 – 1218, 2005. Proceedings of the International Conference on Strongly Correlated Electron Systems.
- [9] P. Niklowitz, F. Beckers, G. Lonzarich, G. Knebel, B. Salce, J. Thomasson, N. Bernhoeft, D. Braithwaite, and J. Flouquet, “Spin-fluctuation-dominated electrical transport of Ni_3Al at high pressure,” *Physical Review B. Condensed matter and materials physics*, vol. 72, no. 2, pp. 24424–24424, 2006.
- [10] A. Arrott, “Criterion for ferromagnetism from observations of magnetic isotherms,” *Physical Review*, vol. 108, no. 6, pp. 1394–1396, 1957.
- [11] E. Stoner, “Collective electron ferromagnetism,” *Proceedings of the Royal Society of London. Series A, Mathematical and Physical Sciences*, vol. 165, no. 922, pp. 372–414, 1938.
- [12] P. Weiss, “L’hypothèse du champ moléculaire et la propriété ferromagnétique,” *Journal de Physique theorique et appliquee*, vol. 6, no. 1, pp. 661–690, 1907.

- [13] D. Edwards and E. Wohlfarth, "Magnetic isotherms in the band model of ferromagnetism," *Proceedings of the Royal Society of London. Series A, Mathematical and Physical Sciences*, vol. 303, no. 1472, pp. 127–137, 1968.
- [14] R. White, *Quantum theory of magnetism*. Springer, 1983.
- [15] D. Belitz, T. R. Kirkpatrick, and T. Vojta, "First order transitions and multicritical points in weak itinerant ferromagnets," *Physical Review Letters*, vol. 82, pp. 4707–4710, Jun 1999.
- [16] T. Smith, J. Mydosh, and E. Wohlfarth, "Destruction of Ferromagnetism in $ZrZn_2$ at High Pressure," *Physical Review Letters*, vol. 27, no. 25, pp. 1732–1735, 1971.
- [17] J. Huber, M. Maple, D. Wohlleben, and G. Knapp, "Magnetic Properties of $ZrZn_2$ under pressure," *Solid-State Commun.*, vol. 16, no. 2, pp. 211–216, 1975.
- [18] F. Grosche, C. Pfleiderer, G. McMullan, G. Lonzarich, and N. Bernhoeft, "Critical behaviour of $ZrZn_2$," *Physica B: Physics of Condensed Matter*, vol. 206, pp. 20–22, 1995.
- [19] N. Kimura, M. Endo, T. Isshiki, S. Minagawa, A. Ochiai, H. Aoki, T. Terashima, S. Uji, T. Matsumoto, and G. Lonzarich, "de Haas–van Alphen Effect in $ZrZn_2$ under Pressure: Crossover between Two Magnetic States," *Physical Review Letters*, vol. 92, no. 19, p. 197002, 2004.
- [20] A. Huxley, I. Sheikin, and D. Braithwaite, "Metamagnetic behavior near the quantum critical point in UGe_2 ," *Physica B: Physics of Condensed Matter*, vol. 284, pp. 1277–1278, 2000.
- [21] S. S. Saxena, P. Agarwal, K. Ahilan, F. M. Grosche, R. K. W. Haselwimmer, M. J. Steiner, E. Pugh, I. R. Walker, S. R. Julian, P. Monthoux, G. G. Lonzarich, A. Huxley, I. Sheikin, D. Braithwaite, and J. Flouquet, "Superconductivity on the border of itinerant-electron ferromagnetism in UGe_2 ," *Nature*, vol. 406, pp. 587–592, Aug. 2000.
- [22] S. Saxena, P. Agarwal, K. Ahilan, F. Grosche, R. Haselwimmer, M. Steiner, E. Pugh, I. Walker, S. Julian, P. Monthoux, *et al.*, "Superconductivity on the border of itinerant electron ferromagnetism in UGe_2 ," *Journal of Magnetism and Magnetic Materials*, vol. 226, pp. 45–47, 2001.
- [23] T. Nishioka, G. Motoyama, S. Nakamura, H. Kadoya, and N. Sato, "Unusual Nature of Ferromagnetism Coexisting with Superconductivity in UGe_2 ," *Physical Review Letters*, vol. 88, no. 23, p. 237203, 2002.
- [24] T. Nishioka, N. Sato, and G. Motoyama, "Nishioka et al. Reply," *Physical Review Letters*, vol. 91, no. 20, p. 209702, 2003.
- [25] S. Sakarya, N. van Dijk, and E. Brück, "Determination of the magnetic domain size in the ferromagnetic superconductor UG_2 by three-dimensional neutron depolarization," *Physical Review B*, vol. 71, no. 17, p. 174417, 2005.
- [26] I. Dzyaloshinsky, "A thermodynamic theory of weak ferromagnetism of antiferromagnetics," *Journal of Physics and Chemistry of Solids*, vol. 4, no. 4, pp. 241–255, 1958.
- [27] T. Moriya, "Anisotropic superexchange interaction and weak ferromagnetism," *Physical Review*, vol. 120, no. 1, pp. 91–98, 1960.

- [28] Y. Ishikawa, K. Tajima, D. Bloch, and M. Roth, “Helical spin structure in manganese silicide MnSi,” *Solid State Commun*, vol. 19, pp. 525–528, 1976.
- [29] Y. Ishikawa and M. Arai, “Magnetic phase diagram of MnSi near critical temperature studied by neutron small angle scattering.,” *J. PHYS. SOC. JAPAN.*, vol. 53, no. 8, pp. 2726–2733, 1984.
- [30] S. Mühlbauer, B. Binz, F. Jonietz, C. Pfleiderer, A. Rosch, A. Neubauer, R. Georgii, and P. Böni, “Skyrmion lattice in a chiral magnet,” *Science*, vol. 323, no. 5916, p. 915, 2009.
- [31] C. Pfleiderer, G. McMullan, and G. Lonzarich, “Pressure induced crossover of the magnetic transition from second to first order near the quantum critical point in MnSi,” *Physica B: Physics of Condensed Matter*, vol. 206, pp. 847–849, 1995.
- [32] C. Pfleiderer, G. J. McMullan, S. R. Julian, and G. G. Lonzarich, “Magnetic quantum phase transition in mnsi under hydrostatic pressure,” *Physical Review B*, vol. 55, pp. 8330–8338, Apr 1997.
- [33] C. Pfleiderer, D. Reznik, L. Pintschovius, H. v. Lohneysen, M. Garst, and A. Rosch, “Partial order in the non-Fermi-liquid phase of MnSi,” *Nature*, vol. 427, pp. 227–231, Jan. 2004.
- [34] C. Pfleiderer, S. R. Julian, and G. G. Lonzarich, “Non-Fermi-liquid nature of the normal state of itinerant-electron ferromagnets,” *Nature*, vol. 414, no. 6862, pp. 427–430, 2001.
- [35] N. Doiron-Leyraud, I. R. Walker, L. Taillefer, M. J. Steiner, S. R. Julian, and G. G. Lonzarich, “Fermi-liquid breakdown in the paramagnetic phase of a pure metal,” *Nature*, vol. 425, pp. 595–599, Oct. 2003.
- [36] M. Nicklas, M. Brando, G. Knebel, F. Mayr, W. Trinkl, and A. Loidl, “Non-Fermi-Liquid Behavior at a Ferromagnetic Quantum Critical Point in $\text{Ni}_x\text{Pd}_{1-x}$,” *Physical Review Letters*, vol. 82, no. 21, pp. 4268–4271, 1999.
- [37] D. Gerstenberg, “Magnetische Untersuchungen an Pd-Mischkristallen mit Übergangselementen,” *Annalen der Physik*, vol. 457, pp. 236–262, 1958.
- [38] D. Shaltiel, J. H. Wernick, H. J. Williams, and M. Peter, “Paramagnetic Resonance of *S*-State Ions in Metals of High Paramagnetic Susceptibility,” *Physical Review*, vol. 135, pp. A1346–A1362, Aug 1964.
- [39] G. Chouteau, R. Fourneaux, K. Gobrecht, and R. Tournier, “Specific Heat and Susceptibility Enhancement in Dilute Pd:Ni Alloys,” *Physical Review Letters*, vol. 20, pp. 193–195, Jan 1968.
- [40] A. T. Aldred, B. D. Rainford, and M. W. Stringfellow, “Giant Moments in Pd(Ni) Alloys near the Critical Composition,” *Physical Review Letters*, vol. 24, pp. 897–900, Apr 1970.
- [41] A. Tari and B. Coles, “Electrical resistivity and the transition to ferromagnetism in the palladium-nickel alloys,” *Journal of Physics F: Metal Physics*, vol. 1, pp. L69–L71, 1971.
- [42] A. Murani, A. Tari, and B. Coles, “Critical concentration for the onset of ferromagnetism in Pd-Ni alloys,” *Journal of Physics F: Metal Physics*, vol. 4, pp. 1769–1781, 1974.

- [43] J. Beille, D. Bloch, and M. Besnus, "Itinerant ferromagnetism and susceptibility of nickel-platinum alloys," *Journal of Physics F: Metal Physics*, vol. 4, pp. 1275–1284, 1974.
- [44] J. Beille and G. Chouteau, "Giant moments and pressure effects in Pd-Ni alloys," *Journal of Physics F: Metal Physics*, vol. 5, pp. 721–731, 1975.
- [45] J. Beille and R. Tournier, "Critical pressure effects in PdNi alloys," *Journal of Physics F: Metal Physics*, vol. 6, pp. 621–629, 1976.
- [46] H. Fujiwara, H. Kadomatsu, K. Ohishi, and Y. Yamamoto, "Effects of Hydrostatic Pressure on the Curie Temperature of Ni-Based Alloys (Ni-V,-Cu,-Pd,-Pt and-Rh)," *Journal of the Physical Society of Japan*, vol. 40, no. 4, pp. 1010–1016, 1976.
- [47] D. Sain and J. Kouvel, "Giant moments in paramagnetic Pd-Ni alloys," *Physical Review B*, vol. 17, no. 5, pp. 2257–2261, 1978.
- [48] T. Cheung, J. Kouvel, and J. Garland, "Giant-moment clusters in paramagnetic and weakly ferromagnetic Pd-Ni alloys," *Physical Review B*, vol. 23, no. 3, pp. 1245–1251, 1981.
- [49] M. Yamada and S. Tanda, "Quantum critical behavior in itinerant ferromagnet $\text{Pd}_{1-x}\text{Ni}_x$," *Physica B: Condensed Matter*, vol. 284-288, no. Part 2, pp. 1305 – 1306, 2000.
- [50] M. Yamada and S. Tanda, "Observation of the crossover from quantum to classical critical behavior in ferromagnetic alloys of $\text{Pd}_{1-x}\text{Ni}_x$," *Physica B: Condensed Matter*, vol. 281-282, pp. 384 – 385, 2000.
- [51] L. Zhu, M. Garst, A. Rosch, and Q. Si, "Universally diverging grüneisen parameter and the magnetocaloric effect close to quantum critical points," *Physical Review Letters*, vol. 91, no. 6, p. 66404, 2003.
- [52] R. Küchler, P. Gegenwart, F. Weickert, N. Oeschler, T. Cichorek, M. Nicklas, N. Carocca-Canales, C. Geibel, and F. Steglich, "Thermal expansion and Grüneisen ratio near quantum critical points," *Physica B: Physics of Condensed Matter*, vol. 378, pp. 36–39, 2006.
- [53] C. Franz, "Experimentelle Untersuchung von ferromagnetischen Quantenphasenübergängen," Master's thesis, Physik Department E21, Technische Universität München, 2009.
- [54] F. R. de Boer, C. J. Schinkel, J. Biesterbos, and S. Proost, "Exchange-Enhanced Paramagnetism and Weak Ferromagnetism in the Ni_3Al and Ni_3Ga Phases; Giant Moment Inducement in Fe-Doped Ni_3Ga ," *Journal of Applied Physics*, vol. 40, no. 3, pp. 1049–1055, 1969.
- [55] J. Fluitman, B. D. Vries, R. Boom, and C. Schinkel, "Scattering of conduction electrons by paramagnons in Ni_3Al ," *Physics Letters A*, vol. 28, no. 7, pp. 506 – 507, 1969.
- [56] J. H. J. Fluitman, R. Boom, P. F. D. Chatel, C. J. Schinkel, J. L. L. Tilanus, and B. R. D. Vries, "Possible explanations for the low temperature resistivities of Ni_3Al and Ni_3Ga alloys in terms of spin density fluctuation theories," *Journal of Physics F: Metal Physics*, vol. 3, no. 1, pp. 109–117, 1973.
- [57] N. Buis, J. Franse, and P. Brommer, "The magnetic properties of Ni_3Al under high pressures," *Physica B+C*, vol. 106, no. 1, pp. 1 – 8, 1981.

- [58] T. I. Sigfusson, N. R. Bernhoeft, and G. G. Lonzarich, "The de Haas-van Alphen effect, exchange splitting and Curie temperature in the weak itinerant ferromagnetic Ni₃Al," *Journal of Physics F: Metal Physics*, vol. 14, no. 9, pp. 2141–2154, 1984.
- [59] J. J. M. Buiting, J. Kubler, and F. M. Mueller, "Weak itinerant ferromagnets: Ni₃Al," *Journal of Physics F: Metal Physics*, vol. 13, no. 9, pp. L179–L183, 1983.
- [60] N. R. Bernhoeft, G. G. Lonzarich, P. W. Mitchell, and D. M. Paul, "Magnetic excitations in Ni₃Al at low energies and long wavelengths," *Physical Review B*, vol. 28, pp. 422–424, Jul 1983.
- [61] S. K. Dhar, K. A. Gschneidner, L. L. Miller, and D. C. Johnston, "Low-temperature behavior of Ni₃Al alloys near the spin-fluctuator-ferromagnet phase boundary," *Physical Review B*, vol. 40, pp. 11488–11492, Dec 1989.
- [62] F. Semadeni, B. Roessli, P. Böni, P. Vorderwisch, and T. Chatterji, "Critical fluctuations in the weak itinerant ferromagnet Ni₃Al: A comparison between self-consistent renormalization and mode-mode coupling theory," *Physical Review B*, vol. 62, pp. 1083–1088, Jul 2000.
- [63] S. H. Kilcoyne and R. Cywinski, "A μ SR study of the magnetic ground state of Ni₃Al," *Physica B: Condensed Matter*, vol. 326, no. 1-4, pp. 577 – 580, 2003.
- [64] N. Buis, J. J. M. Franse, J. V. Haarst, J. P. J. Kaandorp, and T. Weesing, "Pressure dependence of the Curie temperature of some Ni₃Al compounds," *Physics Letters A*, vol. 56, no. 2, pp. 115 – 116, 1976.
- [65] M. Yoshizawa, H. Seki, K. Ikeda, K. Okuno, M. Saito, and K. Shigematsu, "Magnetic Field Effects on Electrical Resistivity and Ferromagnetism in Ni₃Al Alloys," *Journal of the Physical Society of Japan*, vol. 61, no. 9, pp. 3313–3321, 1992.
- [66] M. J. Steiner, F. Beckers, P. G. Niklowitz, and G. G. Lonzarich, "Non-Fermi liquid form of the low temperature resistivity in the low moment ferromagnets Ni₃Al and YNi₃," *Physica B: Condensed Matter*, vol. 329-333, no. Part 2, pp. 1079 – 1080, 2003. Proceedings of the 23rd International Conference on Low Temperature Physics.
- [67] C. Fuller, C. Lin, T. Mihalisin, F. Chu, and N. Bykovetz, "Thermodynamic, transport and magnetic properties of single crystal Ni₃Al," *Solid State Communications*, vol. 83, no. 11, pp. 863 – 866, 1992.
- [68] A. Aguayo, I. I. Mazin, and D. J. Singh, "Why Ni₃Al Is an Itinerant Ferromagnet but Ni₃Ga Is Not," *Physical Review Letters*, vol. 92, p. 147201, Apr 2004.
- [69] I. Mazin, D. Singh, and A. Aguayo, "Density Functional Calculations near Ferromagnetic Quantum Critical Points," *Arxiv preprint cond-mat/0401563*, 2004.
- [70] F. Bremer, M. Beyss, E. Karthaus, A. Hellwig, T. Schober, J. Welter, and H. Wenzl, "Experimental analysis of the Ni-Al phase diagram," *Journal of Crystal Growth*, vol. 87, no. 2-3, pp. 185–192, 1988.
- [71] H. Okamoto, "Al-Ni (aluminum-nickel)," *Journal of Phase Equilibria*, vol. 14, no. 2, pp. 257–259, 1993.

- [72] G. R. Stewart, "Non-fermi-liquid behavior in d - and f -electron metals," *Rev. Mod. Phys.*, vol. 73, pp. 797–855, Oct 2001.
- [73] T. Vojta, "Disorder-induced rounding of certain quantum phase transitions," *Physical Review Letters*, vol. 90, no. 10, p. 107202, 2003.
- [74] J. Sereni, T. Westerkamp, R. KÜchler, N. Caroca-Canales, P. Gegenwart, and C. Geibel, "Ferromagnetic quantum criticality in the alloy $\text{CePd}_{1-x}\text{Rh}_x$," *Physical Review B*, vol. 75, no. 2, p. 24432, 2007.
- [75] T. Westerkamp, M. Deppe, R. KÜchler, M. Brando, C. Geibel, P. Gegenwart, A. Pikul, and F. Steglich, "Kondo-cluster-glass state near a ferromagnetic quantum phase transition," *Physical Review Letters*, vol. 102, no. 20, p. 206404, 2009.
- [76] V. Dobrosavljević and E. Miranda, "Absence of conventional quantum phase transitions in itinerant systems with disorder," *Physical Review Letters*, vol. 94, p. 187203, May 2005.
- [77] H. Yashima and T. Satoh, "Nonmagnetic-magnetic transition in Ce–Si system," *Solid State Communications*, vol. 41, no. 10, pp. 723 – 727, 1982.
- [78] W. Lee, R. Shelton, S. Dhar, and K. Gschneidner Jr, "Competition between the Kondo effect and exchange interactions in the system CeSi_x ," *Physical Review B*, vol. 35, no. 16, pp. 8523–8527, 1987.
- [79] S. Drotziger, C. Pfeleiderer, M. Uhlarz, H. Löhneysen, D. Souptel, W. Löser, and G. Behr, "Pressure-induced magnetic quantum phase transition in $\text{CeSi}_{1.81}$," *Physica B: Physics of Condensed Matter*, vol. 359, pp. 92–94, 2005.
- [80] H. Löhneysen, H. Bartolf, S. Drotziger, C. Pfeleiderer, O. Stockert, D. Souptel, W. Löser, and G. Behr, "Rare-earth intermetallic compounds at a magnetic instability," *Journal of Alloys and Compounds*, vol. 408, pp. 9–15, 2006.
- [81] A. Kak and M. Slaney, "Principles of computerized tomographic imaging," *New York*, 1999.
- [82] O. Halpern and T. Holstein, "On the Passage of Neutrons Through Ferromagnets," *Physical Review*, vol. 59, no. 12, pp. 960–981, 1941.
- [83] M. Burgy, D. Hughes, J. Wallace, R. Heller, and W. Woolf, "Double Transmission and Depolarization of Neutrons," *Physical Review*, vol. 80, no. 6, pp. 953–960, 1950.
- [84] M. Rekveldt, "Study of ferromagnetic bulk domains by neutron depolarization in three dimensions," *Zeitschrift für Physik A Hadrons and Nuclei*, vol. 259, no. 5, pp. 391–410, 1973.
- [85] M. Rekveldt, "Neutron depolarization study of ferromagnetic domain structures (Neutron depolarization of ferromagnetic domain structures in three dimensions)," *Ph. D. Thesis*, 1972.
- [86] Maleev, S. V. and Ruban, V. A., "Critical Depolarization of Neutrons Traversing a Ferromagnetic Body," *Soviet Journal of Experimental and Theoretical Physics*, vol. 35, p. 222, 1972.
- [87] S. Maleev and V. Ruban, "Analysis of the Domain Structure of Uniaxial Ferromagnets by Neutron Depolarization," *Soviet Physics-Solid State*, vol. 18, no. 8, pp. 1331–1336, 1976.

- [88] R. Rosman and M. Rekveldt, “Neutron depolarization theory in the Larmor and the scattering approach,” *Zeitschrift für Physik B Condensed Matter*, vol. 79, no. 1, pp. 61–68, 1990.
- [89] T. Materna, S. Baechler, J. Jolie, B. Masschaele, M. Dierick, and N. Kardjilov, “The cold neutron tomography set-up at SINQ,” *Nuclear Inst. and Methods in Physics Research, A*, vol. 525, no. 1-2, pp. 69–73, 2004.
- [90] Giller, L. and Filges, U. and Kühne, G. and Wohlmuther, M. and Zanini, L., “Validation of Monte-Carlo simulations with measurements at the ICON beam-line at SINQ,” *Nuclear Instruments and Methods in Physics Research, A*, vol. 586, no. 1, pp. 59 – 63, 2008. Proceedings of the European Workshop on Neutron Optics - NOP '07.
- [91] A. Hilger, N. Kardjilov, M. Strobl, W. Treimer, and J. Banhart, “The new cold neutron radiography and tomography instrument CONRAD at HMI Berlin,” *Physica B: Physics of Condensed Matter*, vol. 385, pp. 1213–1215, 2006.
- [92] E. Calzada, B. Schillinger, and F. Grünauer, “Construction and assembly of the neutron radiography and tomography facility ANTARES at FRM II,” *Nuclear Inst. and Methods in Physics Research, A*, vol. 542, no. 1-3, pp. 38–44, 2005.
- [93] F. Grünauer, B. Schillinger, and E. Steichele, “Optimization of the beam geometry for the cold neutron tomography facility at the new neutron source in Munich,” *Applied Radiation and Isotopes*, vol. 61, no. 4, pp. 479–485, 2004.
- [94] N. Kardjilov, I. Manke, M. Strobl, A. Hilger, W. Treimer, M. Meissner, T. Krist, and J. Banhart, “Three-dimensional imaging of magnetic fields with polarized neutrons,” *Nature Physics*, vol. 4, no. 5, p. 399, 2008.
- [95] M. Janoschek, S. Klimko, R. Gähler, B. Roessli, and P. Böni, “Spherical neutron polarimetry with MuPAD,” *Physica B: Physics of Condensed Matter*, vol. 397, no. 1-2, pp. 125–130, 2007.
- [96] E. Jericha, R. Szeywerth, H. Leeb, and G. Badurek, “Reconstruction techniques for tensorial neutron tomography,” *Physica B: Physics of Condensed Matter*, vol. 397, no. 1-2, pp. 159–161, 2007.
- [97] F. Grünauer, *Design, optimization, and implementation of the new neutron radiography facility at FRM-II*. PhD thesis, Technische Universität München, 2005.
- [98] B. Schillinger, E. Lehmann, and P. Vontobel, “3D neutron computed tomography: requirements and applications,” *Physica B: Physics of Condensed Matter*, vol. 276, pp. 59–62, 2000.
- [99] W. Treimer, M. Strobl, N. Kardjilov, A. Hilger, and I. Manke, “Wavelength tunable device for neutron radiography and tomography,” *Appl. Phys. Lett*, vol. 89, no. 20, p. 203504, 2006.
- [100] S. Baechler, N. Kardjilov, M. Dierick, J. Jolie, G. Kühne, E. Lehmann, and T. Materna, “New features in cold neutron radiography and tomography Part I: thinner scintillators and a neutron velocity selector to improve the spatial resolution,” *Nuclear Inst. and Methods in Physics Research, A*, vol. 491, no. 3, pp. 481–491, 2002.

- [101] R. Hassanein, F. de Beer, N. Kardjilov, and E. Lehmann, "Scattering correction algorithm for neutron radiography and tomography tested at facilities with different beam characteristics," *Physica B: Physics of Condensed Matter*, vol. 385, pp. 1194–1196, 2006.
- [102] H. Friedrich, V. Wagner, and P. Wille, "A high-performance neutron velocity selector," *Physica B: Physics of Condensed Matter*, vol. 156, 1989.
- [103] V. Wagner, H. Friedrich, and P. Wille, "Performance of a high-tech neutron velocity selector," *Physica B: Physics of Condensed Matter*, vol. 180, 1992.
- [104] N. Kardjilov, "Further developments and applications of radiography and tomography with thermal and cold neutrons," *Ph. D. at Fakultät für Physik der Technischen Universität, München*, 2003.
- [105] N. Kardjilov, B. Schillinger, and E. Steichele, "Energy-selective neutron radiography and tomography at FRM," *Applied Radiation and Isotopes*, vol. 61, no. 4, pp. 455–460, 2004.
- [106] N. Kardjilov, S. Baechler, M. Bastürk, M. Dierick, J. Jolie, E. Lehmann, T. Materna, B. Schillinger, and P. Vontobel, "New features in cold neutron radiography and tomography Part II: applied energy-selective neutron radiography and tomography," *Nuclear Inst. and Methods in Physics Research, A*, vol. 501, no. 2-3, pp. 536–546, 2003.
- [107] C. J. Carlile and D. K. Ross, "Some aspects of the energy and momentum resolution of a cold-neutron rotating-crystal spectrometer," *Journal of Applied Crystallography*, vol. 8, pp. 292–296, Apr 1975.
- [108] M. Schulz, P. Böni, E. Calzada, M. Mühlbauer, and B. Schillinger, "Energy-dependent neutron imaging with a double crystal monochromator at the ANTARES facility at FRM II," *Nuclear Instruments and Methods in Physics Research, A*, vol. 605, no. 1-2, pp. 33 – 35, 2009.
- [109] M. Meven, V. Hutanu, and G. Heger, "HEiDi: single crystal diffractometer at the hot source of the FRM II," *Neutron News*, vol. 18, p. 19, 2007.
- [110] R. Hassanein, "Correction Algorithms for the Quantitative Evaluation of Neutron Tomography," *Dissertation at ETH Zürich*, 2006.
- [111] K. Lorenz, K. Lorenz, E. Calzada, M. Mühlbauer, B. Schillinger, M. Schulz, and K. Zeitelhack, "The new Multi-Filter at ANTARES: TOF Measurements and first Applications," in *Proceedings of the Eighth World Conference on Neutron Radiography, NIST, Gaithersburg, MD, USA*, vol. 16, p. 19, 2006.
- [112] H. Li, B. Schillinger, E. Calzada, L. Yinong, and M. Muehlbauer, "An adaptive algorithm for gamma spots removal in CCD-based neutron radiography and tomography," *Nuclear Inst. and Methods in Physics Research, A*, vol. 564, no. 1, pp. 405–413, 2006.
- [113] V. Hutanu, S. Masalovich, M. Meven, O. Lykhvar, G. Borchert, and G. Heger, "Polarized ^3He Spin Filters for Hot Neutrons at the FRM-II," *Neutron News*, vol. 18, no. 4, pp. 14 – 16, 2007.
- [114] K. Andersen, R. Chung, V. Guillard, H. Humblot, D. Jullien, E. Lelièvre-Berna, A. Petoukhov, and F. Tasset, "First results from Tyrex, the new polarized- ^3He filling station at ILL," *Physica B: Physics of Condensed Matter*, vol. 356, no. 1-4, pp. 103–108, 2005.

- [115] S. Masalovich, "Method to measure neutron beam polarization with 2×1 Neutron Spin Filter," *Nuclear Inst. and Methods in Physics Research, A*, vol. 581, no. 3, pp. 791–798, 2007.
- [116] F. Piegsa, B. van den Brandt, P. Hautle, J. Kohlbrecher, and J. Konter, "Quantitative radiography of magnetic fields using neutron spin phase imaging," *Physical Review Letters*, vol. 102, no. 14, p. 145501, 2009.
- [117] O. Schaerpf, "Properties of beam bender type neutron polarizers using supermirrors," *Physica B: Condensed Matter*, vol. 156-157, pp. 639 – 646, 1989.
- [118] B. Schillinger, "Neue Entwicklungen zu Radiographie and Tomographie mit thermischen Neutronen," *Doktorarbeit an der Technischen Universität München, Mensch und Buch Verlag*.
- [119] T. Krist, S. Kennedy, T. Hicks, and F. Mezei, "New compact neutron polarizer," *Physica B: Physics of Condensed Matter*, vol. 241, pp. 82–85, 1997.
- [120] W. Williams, *Polarized Neutrons*. Oxford University Press, USA, 1988.
- [121] P. Böni, "New concepts for neutron instrumentation," *Nuclear Instruments and Methods in Physics Research A*, vol. 586, no. 1, pp. 1 – 8, 2008. Proceedings of the European Workshop on Neutron Optics - NOP '07.
- [122] B. Schillinger, P. Böni, C. Breunig, E. Calzada, C. Leroy, M. Mühlbauer, and M. Schulz, "A neutron optical periscope used for neutron imaging," *Nuclear Instruments and Methods in Physics Research, A*, vol. 605, no. 1-2, pp. 40–42, 2009.
- [123] M. Schulz, P. Böni, E. Calzada, M. Mühlbauer, A. Neubauer, and B. Schillinger, "A polarizing neutron periscope for neutron imaging," *Nuclear Inst. and Methods in Physics Research, A*, vol. 605, no. 1-2, pp. 43 – 46, 2009.
- [124] B. Schillinger, E. Calzada, F. Grünauer, and E. Steichele, "The design of the neutron radiography and tomography facility at the new research reactor FRM-II at Technical University Munich," *Applied Radiation and Isotopes*, vol. 61, no. 4, pp. 653–657, 2004.
- [125] E. Calzada, F. Grünauer, M. Mühlbauer, B. Schillinger, and M. Schulz, "New design for the ANTARES-II facility for neutron imaging at FRM II," *Nuclear Inst. and Methods in Physics Research, A*, vol. 605, no. 1-2, pp. 50–53, 2009.
- [126] K. Nielsen and K. Lefmann, "Monte Carlo simulations of neutron-scattering instruments using McStas," *Physica B: Physics of Condensed Matter*, vol. 283, no. 4, pp. 426–432, 2000.
- [127] "McStas Software Homepage." <http://neutron.risoe.dk/mcstas>.
- [128] F. Mezei, "Neutron spin echo: a new concept in polarized thermal neutron techniques," *Zeitschrift für Physik A Hadrons and Nuclei*, vol. 255, no. 2, pp. 146–160, 1972.
- [129] J. Hayter, "Matrix analysis of neutron spin-echo," *Zeitschrift für Physik B Condensed Matter*, vol. 31, no. 1, pp. 117–125, 1978.

- [130] E. Babcock, A. Petoukhov, J. Chastagnier, D. Jullien, E. Lelièvre-Berna, K. Andersen, R. Georgii, S. Masalovich, S. Boag, C. Frost, and S. Parnell, “AFP flipper devices: Polarized ^3He spin flipper and shorter wavelength neutron flipper,” *Physica B: Condensed Matter*, vol. 397, no. 1-2, pp. 172 – 175, 2007. Proceedings of the Sixth International Workshop on Polarised Neutrons in Condensed Matter Investigations.
- [131] MaTecK - Material-Technologie & Kristalle GmbH. <http://www.mateck.de>.
- [132] B. Pedersen, F. Frey, W. Scherer, P. Gille, and G. Meisterernst, “The new single crystal diffractometer RESI at FRM-II,” *Physica B: Physics of Condensed Matter*, vol. 385, pp. 1046–1048, 2006.
- [133] H. Schlich. MaTecK - Material-Technologie & Kristalle GmbH, private communication, 2009.
- [134] G. Matsumoto, M. Kato, and A. Tasaki, “Magnetostriction Constant of Thin Ni Films Determined by Ferromagnetic Resonance,” *Journal of the Physical Society of Japan*, vol. 21, no. 5, pp. 882–885, 1966.
- [135] M. S. Kumar and P. Böni, “Influence of interstitial nitrogen on the structural and magnetic properties of FeCoV/TiN_x multilayers,” *Journal of Applied Physics*, vol. 91, no. 6, pp. 3750–3758, 2002.
- [136] S. Chikazumi and S. Charap, *Physics of magnetism*. Wiley New York, 1964.